

**DEVELOPMENT OF A RELATIVISTIC ATOMIC THEORY
FOR ACCURATE TREATMENT OF COMPLEX CORRELATIONS**

by

Charles Cheung

A dissertation submitted to the Faculty of the University of Delaware in partial fulfillment of the requirements for the degree of Doctor of Philosophy in Physics

Winter 2021

© 2021 Charles Cheung
All Rights Reserved

**DEVELOPMENT OF A RELATIVISTIC ATOMIC THEORY
FOR ACCURATE TREATMENT OF COMPLEX CORRELATIONS**

by

Charles Cheung

Approved: _____

Edmund R. Nowak, Ph.D.

Chair of the Department of Physics and Astronomy

Approved: _____

John Pelesko, Ph.D.

Dean of the College of Arts and Sciences

Approved: _____

Louis F. Rossi, Ph.D.

Vice Provost for Graduate and Professional Education
and Dean of the Graduate College

I certify that I have read this dissertation and that in my opinion it meets the academic and professional standard required by the University as a dissertation for the degree of Doctor of Philosophy.

Signed: _____

Marianna Safronova, Ph.D.
Professor in charge of dissertation

I certify that I have read this dissertation and that in my opinion it meets the academic and professional standard required by the University as a dissertation for the degree of Doctor of Philosophy.

Signed: _____

Krzysztof Szalewicz, D.Sc.
Member of dissertation committee

I certify that I have read this dissertation and that in my opinion it meets the academic and professional standard required by the University as a dissertation for the degree of Doctor of Philosophy.

Signed: _____

Stephen Barr, Ph.D.
Member of dissertation committee

I certify that I have read this dissertation and that in my opinion it meets the academic and professional standard required by the University as a dissertation for the degree of Doctor of Philosophy.

Signed: _____

Swati Singh, Ph.D.
Member of dissertation committee

I certify that I have read this dissertation and that in my opinion it meets the academic and professional standard required by the University as a dissertation for the degree of Doctor of Philosophy.

Signed: _____

Anderson Janotti, Ph.D.
Member of dissertation committee

I certify that I have read this dissertation and that in my opinion it meets the academic and professional standard required by the University as a dissertation for the degree of Doctor of Philosophy.

Signed: _____

Siu-Tat Chui, Ph.D.
Member of dissertation committee

ACKNOWLEDGEMENTS

First and foremost, I would like to extend my deepest gratitude to my advisor, Professor Marianna Safronova, for her guidance and mentoring during my years as a graduate student at the University of Delaware. It has been a great honor and privilege to work, study, and conduct research under her.

I must also thank the co-developers of the CI-MBPT code package, Dr. Sergey Porsev, Dr. Mikhail Kozlov, and Dr. Ilya Tupitsyn, for many useful discussions and advice on the projects I carried out throughout my graduate career. Without their guidance, my work developing a new parallel CI code package would have been infinitely more difficult. The computational aspects of my work was supported through the use of IT resources at UD, specifically the Caviness computing cluster. From the UD IT Research Computing group, I would like to thank Dr. Jeffrey Frey for his guidance, support and advice during the development of the codes.

I would like to thank my undergraduate advisor, Dr. Karl Unruh, without whom I would not have decided to advance to graduate school and progress to where I am today. I am also very grateful to Dr. Krzysztof Szalewicz, whose coursework in quantum mechanics and electronic structure theory helped me realize my research interests.

I gratefully acknowledge the financial support from the University of Delaware and the U.S. National Science Foundation, under Grant No. PHY-1620687.

Finally, I would like to thank my family and friends for their continuous support and encouragement, and accepting my occasional lack of communication. Thanks to all the mentors and friends I made during conferences and workshops, who gave me inspiration and motivation to continue my work.

TABLE OF CONTENTS

LIST OF TABLES	ix
LIST OF FIGURES	xiii
ABSTRACT	xiv
 Chapter	
1 INTRODUCTION	1
2 THEORY	8
2.1 Atomic structure	9
2.1.1 The non-relativistic Hamiltonian	10
2.1.2 The Hartree-Fock method	18
2.1.3 The relativistic Hamiltonian	21
2.1.4 The Breit interaction	26
2.1.5 The Second Quantization formalism	28
2.1.6 The Configuration Interaction method	31
2.1.7 Basis sets and basis set convergence	37
2.1.8 B-spline basis sets	38
2.1.9 The Davidson method	41
2.1.10 CI+MBPT	45
2.1.11 CI+all-order	51
2.1.12 Valence perturbation theory	57
2.2 Radiative transitions	59
2.2.1 The density matrix formalism	60
2.2.2 Multipole transition probabilities	66

3	CI/CI+MBPT/CI+ALL-ORDER CODE PACKAGE	75
3.1	Base computer package	75
3.1.1	hdf	76
3.1.2	bass	77
3.1.3	add	77
3.1.4	basc	77
3.1.5	conf	78
3.1.6	dtm	84
3.1.7	All-order part of the package	85
3.1.8	MBPT part of the package	85
3.1.9	conf_pt	86
3.2	Modernization of codes	88
3.3	Memory requirements	90
3.4	Parallelization of codes	91
3.4.1	conf - the CI code	92
3.4.1.1	Formation of CI Hamiltonian matrix	92
3.4.1.2	Formation of J^2 matrix	96
3.4.1.3	Davidson procedure	96
3.4.1.4	I/O	97
3.4.1.5	Inclusion of MBPT/all-order corrections	98
3.4.1.6	Achieved performance of parallelization	99
3.4.2	conf_pt - the valence PT code	100
3.4.2.1	Diagonal part of the Hamiltonian	101
3.4.2.2	Off-diagonal part of the Hamiltonian	102
3.4.2.3	Achieved performance of parallelization	104
3.4.3	dtm - the density (transition) matrix code	105
3.4.3.1	DM - density matrix	106
3.4.3.2	TM - transition matrix	106
3.4.3.3	Achieved performance of parallelization	107

4	DEVELOPMENT OF ATOMIC CLOCKS AND THE SEARCH FOR VARIATIONS OF FUNDAMENTAL CONSTANTS	108
4.1	Optical clocks based on Ir ¹⁷⁺	109
4.1.1	Method of calculation	110
4.1.2	<i>M1</i> and <i>E1</i> transition rates and energies	117
4.1.3	Selection of important configurations	120
4.2	Optical clocks based on the Cf ¹⁵⁺ and Cf ¹⁷⁺ ions	131
5	THE 3C/3D LINE INTENSITY RATIO IN FE XVII	139
6	THE LOWEST-LYING ODD-PARITY ATOMIC LEVELS IN Ac	144
7	PREDICTING ATOMIC PROPERTIES OF NEGATIVE IONS .	147
7.1	Identification of quasibound spectrum of La ⁻	148
7.2	Observation of an electric quadrupole atomic transition in Bi ⁻	157
8	CONCLUSION	164
	BIBLIOGRAPHY	167
	Appendix	
A	SLATER-CONDON RULES	182
B	ANGULAR MOMENTUM DIAGRAMS	184
C	HOUSEHOLDER'S METHOD OF DIAGONALIZATION	188
D	HIGH PERFORMANCE COMPUTING	192

LIST OF TABLES

2.1	Clebsch-Gordan coefficients for $\mathbf{J} = \mathbf{L} + \mathbf{S}$, with $s = 1$	67
3.1	The runtime of subroutines <code>FormH</code> and <code>Diag4</code> of the parallel <code>conf</code> program for increasing number of compute cores and the speedups of the parallel code are presented in seconds (s) for increasing number of cores N , relative to the serial code ($N=1$), as well as $N=50$	100
3.2	The runtime of subroutines <code>FormH</code> and <code>Diag4</code> of the parallel <code>conf</code> program for increasing number of compute cores and the speedups of the parallel code are presented in seconds (s) for increasing number of cores N , relative to the code ran with 50 cores ($N=50$)	101
3.3	Left: Diagonal and off-diagonal run times in seconds (s) correspond to the time it takes to calculate all diagonal and non-diagonal elements of the Hamiltonian in the PT space, respectively. Right: The speedups of the parallel code relative to the serial code. This run is done with Ir^{16+} with 14318 relativistic configurations and 83×10^6 determinants.	104
3.4	Left: Diagonal and off-diagonal run times in seconds (s) correspond to the time it takes to calculate all diagonal and non-diagonal elements of the Hamiltonian in the PT space, respectively. Right: The speedups of the parallel code relative to the serial code. This run is done with Ir^{16+} with 25588 relativistic configurations and 135×10^6 determinants.	105
4.1	Energies of Ir^{17+} (in cm^{-1}) obtained using CI with different number of electronic excitations.	115
4.2	Energy differences of Ir^{17+} (in cm^{-1}) obtained using CI with different sized basis sets.	116

4.3	Contribution of triple excitations (T) into energy levels of Ir ¹⁷⁺ calculated with single and double excitations (SD). Energy levels are calculated with [7 <i>spdfg</i>] basis set. Numbers under labels indicate the number of determinants used in the calculation in even parity runs. All values are given in cm ⁻¹	117
4.4	Contribution of full Breit interaction (Δ_{Br}) into energy levels of Ir ¹⁷⁺ calculated with Gaunt term. Energy levels are calculated with [7 <i>spdfg</i>] basis set. All values are given in cm ⁻¹	118
4.5	Contribution of QED corrections (Δ_{Br}) into energy levels of Ir ¹⁷⁺ . Energy levels are calculated with [7 <i>spdfg</i>] diagonalized basis set. All values are given in cm ⁻¹	119
4.6	Comparison of Ir ¹⁷⁺ M1 transition energies (in cm ⁻¹) with experimental results.	120
4.7	<i>E1</i> 4 <i>f</i> ¹² 5 <i>s</i> ² – 4 <i>f</i> ¹³ 5 <i>s</i> radiative transition rates A_{ab} of Ir ¹⁷⁺ (in s ⁻¹) obtained using CI with different number of electronic excitations: including excitations from the 4 <i>f</i> 5 <i>s</i> electrons, then adding excitations from 4 <i>d</i> and 4 <i>p</i> shells. The final numbers include correlation of all 60 electrons. Final values of the transition wavelengths λ (in nm) and reduced <i>E1</i> matrix elements D (in a.u.) are also listed.	121
4.8	Total number of non-relativistic configurations generated (total) compared with the number of non-relativistic configurations (non-rel) used in the valence CI space of the final CI and CI+PT runs. Numbers of relativistic configurations (rel) and determinants (dets) in millions taking part in the final CI valence space in final results are also shown.	123
4.9	Number of times an orbital appears in non-relativistic configurations with weights larger than the given threshold values. The system considered here is Ir ¹⁷⁺ with even parity. S, D and T excitations are allowed from basic configurations, 4 <i>f</i> ¹⁴ and 4 <i>f</i> ¹² 5 <i>s</i> ² . Other than 4 <i>f</i> and 5 <i>s</i> , all orbitals have minimum and maximum occupation numbers of 0 and 2, respectively, with 5 <i>f</i> being an exception, having 0 and 3, respectively.	127

4.10	List of the 10 most important configurations for calculation of Ir ¹⁷⁺ energy levels. Weights for 4 <i>f</i> ¹³ 5 <i>s</i> were calculated for the ³ <i>F</i> ₄ level, but ³ <i>F</i> ₃ , ³ <i>F</i> ₂ and ¹ <i>F</i> ₃ levels also have the approximately the same top configurations. Weights for 4 <i>f</i> ¹² 5 <i>s</i> ² were calculated for the ³ <i>H</i> ₆ level, but ³ <i>F</i> ₄ , ³ <i>H</i> ₅ and ³ <i>F</i> ₂ levels also have approximately the same top 10 configurations.	128
4.11	Comparison of top 5 most important configurations for Ir ¹⁷⁺ between short basis set [8 <i>spdfg</i>] and long basis set [10 <i>spdf</i>].	129
4.12	List of the 10 most important configurations for calculation of Ir ¹⁶⁺ energy levels <i>E</i> (cm ⁻¹) and their weights <i>W</i>	130
4.13	The energies of the excited states (in cm ⁻¹) of Cf ¹⁵⁺ and Cf ¹⁷⁺ , counted from the ground state, calculated in the CI and CI+MBPT approximations.	136
5.1	Contributions to the energies of Fe ¹⁶⁺ calculated with increased size basis sets and number of configurations. The results are compared with experiment. All energies are given in cm ⁻¹ with exception of the last line that shows the difference of the 3C and 3D energies in eV.	141
5.2	Contributions to the <i>E1</i> reduced matrix elements <i>D</i> (3 <i>D</i>) = <i>D</i> (2 <i>p</i> ⁶ ¹ <i>S</i> ₀ - 2 <i>p</i> ⁵ 3 <i>d</i> ³ <i>D</i> ₁) and <i>D</i> (3 <i>C</i>) = <i>D</i> (2 <i>p</i> ⁶ ¹ <i>S</i> ₀ - 2 <i>p</i> ⁵ 3 <i>d</i> ¹ <i>P</i> ₁) (in a.u.) and the ratio of the respective oscillator strengths <i>R</i>	143
6.1	The determined excitation energies and lifetimes, and comparison with theory and literature.	145
7.1	Quasibound levels of La ⁻ energy levels in meV. All energies are counted from the ³ <i>F</i> ₂ even ground state.	150
7.2	Identification of peaks of La ⁻ observed in experiments by Walter <i>et al.</i> (2020).	153
7.3	Calculated binding energies of Bi ⁻ bound states relative to the Bi ⁴ <i>S</i> _{3/2} ground state and transition energy for Bi ⁻ 6 <i>p</i> ⁴ ³ <i>P</i> ₂ → ³ <i>P</i> ₀ in cm ⁻¹	159
7.4	The energy levels of Po counted from the ground state.	161

7.5	Present results and previous calculations for the $\text{Bi}^- \ ^3P_2 \rightarrow \ ^3P_0$ $E2$ transition energy and upper-state lifetime.	162
-----	--	-----

LIST OF FIGURES

3.1	The scheme of the CI+MBPT/CI+all-order code package.	76
4.1	Low-lying energy levels of Ir ¹⁷⁺ based on past CI Dirac-Fock-Sturm (CIDFS) and Fock space coupled cluster (FSCC) calculations. . . .	111
4.2	Single and double excitations from the 4 <i>f</i> ¹³ 5 <i>s</i> configuration.	112
4.3	“Opening” the 4 <i>d</i> ¹⁰ shell - including it into the valence space.	114
4.4	The level scheme for low-lying odd-parity levels of Cf ¹⁷⁺	134
4.5	The level scheme for low-lying odd-parity levels of Cf ¹⁵⁺	135
7.1	Partial energy level diagram of relevant bound states of La ⁻ (black), neutral La (blue), and quasibound excited states of La ⁻ (red) in the a) ⁵ <i>G</i> and b) ⁵ <i>F</i> manifolds.	154
7.2	Measured La ⁻ photodetachment spectrum above the ground state threshold energy of 557.546 meV.	155
7.3	Measured photodetachment spectrum in the vicinity of the newly observed Peak 24, which is due to the La ⁻ ³ <i>F</i> ₂ → ⁵ <i>F</i> ₃ transition. . .	156

ABSTRACT

One of the central objectives of atomic, molecular and optical physics is describing complex correlations in atomic structure. There has been an increasing need for high quality high-precision atomic data and software in several scientific communities, including atomic, plasma and astrophysics. Having an accurate atomic theory is indispensable for experiments involving studies of fundamental interactions, astrophysics, atomic clocks, plasma science, quantum degenerate gases, quantum information, precision measurements, and others. The need for high-precision calculations of atomic properties of systems in the middle columns of the periodic table has become increasingly urgent due to its relevance in new experiments probing physics beyond the Standard Model.

The ultimate goal of the work described in this thesis is to develop methods and codes to enable accurate computation of atomic properties of atoms and ions with complex electronic structure. We apply our newly developed code package for reliable calculations of atomic properties of systems that were not possible before. This includes calculations correlating all 60 electrons in the highly charged Ir^{17+} ion, calculations predicting clock transitions and analyzing systemic effects that could affect the accuracy and stability of Cf^{15+} and Cf^{17+} ions, calculations predicting the $3C3D$ line intensity ratio in Fe^{16+} , calculations detecting the lowest lying odd parity atomic levels in neutral Ac, and calculating properties of negative ions La^- and Bi^- . The new code package will also be used to produce large volumes of atomic data for a new online portal being developed at the University of Delaware.

Chapter 1

INTRODUCTION

In this work, a new relativistic atomic code capable of very-large scale, high-precision calculations of atomic properties is developed and used for calculations of several complex ions that were not possible with previous codes. This atomic code utilizes the configuration interaction (CI) method, and allows to combine configuration interaction with either many-body perturbation theory (CI+MBPT) or the all-order method (CI+all-order), to analyze atoms and ions of interest. The main motivation for this work is the recent rapid development in experiments involving studies of fundamental interactions, astrophysics, atomic clocks, plasma science, quantum degenerate gases, quantum information, precision measurements, and others.

In the first part of this thesis, the theoretical frameworks that lay the foundation for the code package are discussed in enough detail to understand the functionalities of the code. The basics of atomic structure theory is briefly summarized, starting from the non-relativistic many-electron Hamiltonian and an N -electron antisymmetric wave function, we solve Schrödinger's equation to obtain the energy of the system of interest. This is extended to include relativistic effects by introducing the relativistic Hamiltonian. The Hartree-Fock method is introduced in the non-relativistic regime, and then extended to the Dirac-Hartree-Fock method when relativistic effects are taken into account. Then the CI method and the Davidson method [1] are introduced. Next, the hybrid approaches CI+MBPT and CI+all-order are introduced, treating core-core and core-valence correlations with MBPT/all-order and treating valence-valence correlations with CI. Valence perturbation theory (CI+PT) is introduced as an extension to the CI method, which is primarily used to treat very complicated open-shell systems where the usual CI+MBPT and CI+all-order methods would not work. The CI+PT

method allows for perturbative treatment of the valence correlations on top of the CI calculations. Finally, radiative transitions between states of an atomic system are discussed; the density matrix formalism is introduced, and then the expressions for multipole transition probability rates are derived.

In the second part of the thesis, the complete CI/CI+MBPT/CI+all-order code package is described. Here, the components of the complete set of codes are introduced, including codes that were not released in the initial CI+MBPT public distribution to Computer Physics Communications in 2015 [2]. These include 3 codes that realize the CI+all-order method, as well as a new code that realizes the CI+PT method for extreme-scale CI calculations. Next, we describe the code developments done in this work. This includes the modernization and parallelization of the main codes in the package, namely the CI code `conf`, the CI+PT code `conf_pt`, and the matrix element code `dtm`, which are the most computationally expensive portions of the entire code package. Memory usage, optimization, and parallelization schemes are discussed for these codes.

In the final part of the thesis, we showcase the recent calculations done with our newly developed parallel CI/CI+MBPT/CI+all-order code package. It is important to note that most of the calculations done here were not possible with the attained accuracy with previously existing codes. Highly charged ions (HCI) such as Ir^{17+} , Cf^{15+} , and Cf^{17+} are attractive candidates for the development of novel atomic clocks with very high sensitivity to the variation of the fine structure constant α . In our most demanding calculations, we correlate all 60 electrons in Ir^{17+} . $M1$ transition energies between same parity states have been measured to good agreement with previous calculations [3], and $E1$ transition rates between opposite parity states were found to be drastically lower than previously predicted [4]. Our calculations explain the lack of observed $E1$ transitions in the last 5 years, and provide a path towards detecting the corresponding clock transitions [4]. We also predicted properties of the Cf^{15+} and Cf^{17+} ions, including the wavelengths of clock transitions, and analyzed a number of systematic effects that affect the accuracy and stability of these optical clocks, including electric quadrupole,

micromotion, and quadratic Zeeman shifts of the clock transitions. Our calculation correlating all 10 electrons in Fe^{16+} , including full Breit and QED [5] corrections, predicted the transition rates of the resonance line $3D [2p^5 3d \ ^3D_1 - 2p^6 \ ^1S_0]$ and the intercombination line $3C [2p^5 3d \ ^1P_1 - 2p^6 \ ^1S_0]$ with 1-2% accuracy, ruling out basis set convergence in theoretical calculations as a potential explanation for the discrepancy of the observed intensity ratios with advanced plasma models. For the neutral Ac atom, we calculated the energy levels and lifetimes of the two lowest odd-parity states $7s^2 7p \ ^2P_{1/2}^o$ and $7s^2 7p \ ^2P_{3/2}^o$ with good agreement with experimental measurements, resolving discrepancy of other theory values with experiments. For La^- , we identified all of the 11 observed resonances in its photodetachment spectrum attributed to transitions to quasibound states [6], as well as predicted one more peak just outside the range of the prior experiment, which was validated after it was observed at the predicted wavelength. This is the first time our approach has been used to predict properties of quasibound states in any system. For Bi^- , our calculations found excellent agreement with recent experiments for the binding energies and $6p^4 \ ^3P_2 \rightarrow \ ^3P_0$ transition energies and rates [7].

The main motivation of the work done in this thesis is to develop a new modern atomic code package free of the limitations of existing available codes. This code package is capable of precise prediction of properties of even complicated systems and suitable to run on modern computational facilities. We plan to release the new code package to the user community. Here, we briefly summarize the atomic structure codes that have been available for public use in the last few decades. The NIST Multiconfiguration Hartree-Fock and Multiconfiguration Dirac-Hartree-Fock (MCHF/MCDHF) database contains collections of transition data from different relativistic theories by different computational methods, as well as the atomic structure codes used for the calculations of the data [8]. The MCHF/MCDHF database includes access to ATSP2K, a large scale, non-relativistic MCHF + Breit Pauli atomic structure package [9], and the GRASP2K package, which implements the fully relativistic MCDHF method for large-scale calculations [10, 11]. Some other generally applicable, documented atomic

structure codes include CIV3, which calculates configuration interaction (CI) wave functions and electric-dipole oscillator strengths [12]; SUPERSTRUCTURE, which calculates bound state energies in LS coupling and intermediate coupling as well as associated radiative data [13]; the COWAN code, which calculates atomic structures and spectra via the superposition-of-configuration method [14, 15]; HULLAC, which calculates atomic structure and cross sections for collisional and radiative atomic processes using methods such as CI and the parametric potential method [16]; the ATOM programs, which compute atomic processes, including photoionization, Auger and radiative decay, elastic scattering and ionization, using HF and its generalization to the random phase approximation (RPA) with exchange [17]; and the Flexible Atomic Code (FAC), which computes various atomic properties such as energy levels, radiative transitions, collisional excitations, ionization by electron impact, and photoionization [18]. All of these codes have been developed decades ago, with some more recent updates to some codes, including MPI parallelization. Modern applications require much more accurate treatment of the electronic correlations, and larger ranges of atomic properties that can be calculated with these codes. An initiative has been taken to develop much more modern codes with the release of the CI-MBPT code package in 2015 [2], and the AMBiT CI+MBPT code package in 2018 [19]. The AMBiT code package features hybrid MPI+OpenMP parallelization to take full advantage of modern high-performance computing (HPC) architectures, allowing for calculations of much more complicated systems than before.

The work done in this thesis resumes the development of the CI/CI+MBPT/CI+all-order code package, porting the previous serial code package to latest HPC architectures via modern computational methodologies, enabling the codes to run on large-scale computational facilities in order to treat complex systems, such as atomic systems with open d - and f -shells, beyond the original code's capabilities. Furthermore, the modern code package will be a part of a larger project: the development of an online portal that will provide the scientific community with access to a database of high-precision atomic properties and a package of application codes that can be used to compute

these properties.

A major motivation for this work is the development of atomic clocks, which is essential for the search for variation of fundamental constants. Modern theories aimed at unifying gravity with the other three fundamental interactions suggest that the fundamental constants could vary in an expanding universe [20]. Development of ultra-precise atomic clocks with fractional sensitivity $\delta\alpha/\alpha \sim 10^{-18} \text{ yr}^{-1}$ have already allowed for laboratory tests of the temporal variation of the fine structure constant $\alpha = e^2/\hbar c$, and novel clock schemes based on the ^{229}Th nuclear transition [21, 22] and optical transitions in highly-charged ions [23, 24, 25, 26, 27, 28] that may achieve the accuracy at the next decimal point, 10^{-19} , are being considered. Optical atomic clock transition energies ΔE depend on the fine-structure constant α as

$$\Delta E(\alpha) = \Delta E_0 + \Delta q \left[\left(\frac{\alpha}{\alpha_0} \right)^2 - 1 \right], \quad (1.1)$$

where α_0 is the current value of α [29], ΔE_0 is the transition energy corresponding to α_0 , and the differential sensitivity parameter Δq [30, 31] can be precisely calculated. The atomic clock maps out small fractional α deviations of any cause or type (temporal, spatial, slow drift, oscillatory, gravity-potential dependent, transient or other) to fractional frequency deviations

$$\frac{\Delta E - \Delta E_0}{\Delta E_0} = K \frac{\alpha - \alpha_0}{\alpha_0}, \quad (1.2)$$

where $K = 2\Delta q/\Delta E$ is the dimensionless enhancement factor. Experimentally, one can detect the variation of α by monitoring the ratio of two clock frequencies with different values of K . One would look for clocks with the best stability, total systematic uncertainty, and highest values of $\Delta K = K_1 - K_2$ for clocks 1 and 2. Highly charged ions (HCI) such as Ir^{17+} , Cf^{15+} , and Cf^{17+} are attractive candidates for the development of novel atomic clocks with very high sensitivity to the variation of the fine structure constant α [23, 28, 32]. Therefore, extensive theoretical and experimental studies must be done on highly charged ions (HCI) in order for these novel clocks to become a reality. For example, while the $M1$ transitions in Ir^{17+} between same parity states have been

measured to good precision [3], the clock transitions, or in fact any $E1$ transitions between opposite parity states have not yet been identified. These $E1$ transitions were expected to be observed in recent experiments since their predicted transitions rates [33] were well within the experimental capabilities. The lack of observations for the $E1$ transitions brought serious concerns about the accuracy of theoretical predictions. We have completed extensive work on several HCI, such as Ir^{17+} [4], Cf^{15+} [34], and Cf^{17+} [34] in this work. HCI have numerous long-lived optical transitions suitable for clock development with very low uncertainties, estimated to reach the 10^{-19} level [25, 35, 36]. Recent developments in quantum logic techniques for HCI spectroscopy in which a cooling ion provides sympathetic cooling, as well as control and readout of the internal state of the HCI ion, made rapid progress in the development of HCI clocks possible [37, 38].

Another motivation of this work is in astrophysics. Properties of Fe and Fe ions are essential for astrophysical studies [39, 40, 41, 42]. The code developed in this work will calculate energies and various multipole transition properties making it of use for plasma physics and astrophysics. The work done in this thesis enabled massive computations of a very large number of states (over 100) and their respective transitions. This scale of calculations were not previously possible, making the code usable for large-scale data production needed for astrophysics and plasma science. For example, for the last four decades, there has been a disagreement between the observed intensity ratios and advanced plasma models of the resonance line $2p^5 3d\ ^3D_1 - 2p^6\ ^1S_0$ and the intercombination line $3C\ 2p^5 3d\ ^1P_1 - 2p^6\ ^1S_0$ of Fe XVII ions [43]. These lines are crucial for plasma diagnostics of electron temperatures, elemental abundances, ionization conditions, velocity turbulences, and opacities. L -shell soft X-ray fluorescence of Fe^{16+} ions was recently measured in an electron beam ion trap following resonant photo-excitation using synchrotron radiation provided by the P04 beamline at PETRA III [43]. The experiment measured the $3C/3D$ oscillator strength in an attempt to explain this puzzle. We carried out a precision calculation using our newly developed parallel CI code to predict these transition rates with 1-2% accuracy.

We verified that the energies of all 18 states considered agree with the NIST database within the estimated experimental uncertainty of 0.05%, and the theoretical $3C - 3D$ energy difference of 13.44 eV is in agreement with the experiment to 0.3% [43].

The organization of the thesis is as follows: a summary of atomic structure theory and methods used in this work is given in Chapter 2; a description of the programs in the new parallel CI+MBPT/CI+all-order code package is given in Chapter 3; calculations done for the development of optical atomic clocks using highly charged ions Ir^{17+} , Cf^{15+} and Cf^{17+} are discussed in Chapter 4; calculations for the $3C/3D$ line intensity ratio in Fe^{16+} is discussed in Chapter 5; calculations for neutral Ac are done in Chapter 6; calculations done to predict quasibound states of negative ion La^- and bound states of Bi^- are done in Chapter 7; and a conclusion of the thesis is given in Chapter 8.

Chapter 2

THEORY

The study of atomic structure continues to be an exciting field, with increasingly precise measurements and improved computational methods allowing more and more detailed comparisons between experiment and theory. Accurate theory predictions are needed to propose, guide, and analyze experiments. The aim of this chapter is to give a brief overview of concepts that will be necessary for a better understanding of the contents of this work. The main focus will be computational methods for high-precision relativistic calculations for many-electron atomic systems. We will begin by describing a general many-electron system with a non-relativistic Hamiltonian. We'll find that for increasingly large systems, it will be impossible to write an analytical solution, making it necessary to introduce approximation methods, such as the configuration interaction method, many-body perturbation theory, and the coupled-cluster method. In this chapter, we will introduce major concepts and theory utilized in this work, leaving detailed discussion and derivations to the original sources. A detailed discussion on these topics can be found in references [44, 45, 46, 47]. Atomic units are used throughout the thesis, unless otherwise stated.

This chapter begins with a description of the methods used for atomic structure calculations, and ends with a description of radiative transitions relevant for determining transition rates, lifetimes, and branching ratios. In Sections 2.1.1 and 2.1.2, we introduce the non-relativistic theory of atomic structure; in Sections 2.1.3 and 2.1.4, we expand our understanding of atomic structure to include relativistic corrections; in Section 2.1.5, we introduce second quantization to describe many-electron systems in terms of creation and annihilation operators; in Section 2.1.6, we introduce the configuration interaction (CI) method, expanding the many-electron wave function as a linear

combination of Slater determinants constructed from a predetermined basis set; in Section 2.1.7, we describe basis sets and basis set convergence, particularly the B-spline basis set used in our calculations; in Section 2.1.9, we describe the Davidson method, which is an iterative diagonalization procedure used to find the low-lying energy eigenvalues and eigenvectors of the CI Hamiltonian matrix; in Sections 2.1.10 and 2.1.11, we describe methods combining CI with many-body perturbation theory (CI+MBPT) and the all-order method (CI+all-order), respectively, to treat core and valence interactions in different regimes (MBPT or all-order); in Section 2.1.12, a method combining CI with valence perturbation theory (CI+PT) is described to treat cases where the CI space is too large to run a full CI calculation, so second-order perturbation theory is used to calculate weights of configurations used to determine the most important configurations; in Section 2.2.1, we describe the density matrix formalism, used to express matrix elements between many-electron states using one-electron matrix elements; and in Section 2.2.2, we derive the expressions for the multipole transition rates.

2.1 Atomic structure

In quantum physics, the state of an N -electron atom or ion is described by a wave function $\Psi(\mathbf{x}_1, \dots, \mathbf{x}_N)$, where $\mathbf{x}_i = (\mathbf{r}_i, \sigma_i)$ represents the space and spin coordinates, respectively, of the i -th electron. This wave function is continuous in the range $(-\infty, \infty)$ for the space coordinates, and takes only values $\pm 1/2$ ($+1/2$ for “spin up” and $-1/2$ for “spin down”) for the spin coordinate. The wave function is a solution to the Schrödinger equation

$$H\Psi(\mathbf{x}_1, \dots, \mathbf{x}_N) = E\Psi(\mathbf{x}_1, \dots, \mathbf{x}_N), \quad (2.1)$$

where the Hamiltonian operator H is an operator that includes all the interactions relevant for the atomic system. Bound state solutions of this equation only exist if the wave function is square integrable, and only for discrete values of the total energy of the system E . The form of the Hamiltonian operator H depends on the quantum mechanical model used for the atomic system, and will be discussed in the upcoming sections.

2.1.1 The non-relativistic Hamiltonian

The starting point for non-relativistic calculations is often the time-independent Schrödinger's equation using an electronic Hamiltonian for an atom of the form

$$H = \sum_i^N h(i) + \sum_{i<j}^N \frac{1}{r_{ij}}, \quad (2.2)$$

where

$$h(i) = \sum_i^N \left(-\frac{1}{2} \nabla_i^2 - \frac{Z}{r_i} \right). \quad (2.3)$$

Here, H describes the i^{th} electron moving in the presence of the Coulomb field generated by the nucleus of charge Z , $r_{ij} = |\mathbf{r}_i - \mathbf{r}_j|$ is the distance between the i^{th} and j^{th} electrons, and r_i is the distance between the i^{th} electron and the nucleus. The one-electron terms describe the kinetic and potential energies of the electrons with respect to the nucleus, and the two-electron terms describe the Coulomb potential energy of the electrons.

This Hamiltonian assumes a couple of approximations described in Ref. [47]. First, the adiabatic approximation is assumed, such that the nuclear and electronic motion are separated due to the time-scale separation between the nucleus and electrons. This is a good approximation since the nucleus is at least about 2000 times heavier than an electron, and therefore moves about $\sqrt{2000}$ times slower. As the slow nucleus moves, the fast electrons follow it and their distribution around the nucleus is not much different than in the case of a stationary nucleus. Next, the Born-Oppenheimer approximation is assumed, such that the electrons move in a field generated by a point charge nucleus of infinite mass, with its location fixed at the origin of the coordinate system.

We seek solutions to the N -electron Schrödinger equation (Eq. 2.1) corresponding to electrons that are completely antisymmetric with respect to the interchange of any two coordinates

$$\Psi(\mathbf{r}_1, \dots, \mathbf{r}_i, \dots, \mathbf{r}_j, \dots, \mathbf{r}_N) = -\Psi(\mathbf{r}_1, \dots, \mathbf{r}_j, \dots, \mathbf{r}_i, \dots, \mathbf{r}_N). \quad (2.4)$$

It is also important to note that there is no exact analytical solution to Eq. 2.1 for atoms and ions more complex than hydrogen. If we consider the rubidium atom, with $Z = 37$, the wave function would depend on $3 \times 37 = 111$ variables. Using a basis set of only 10 functions for each variable, it would require 10^{111} functions to define the wave function of rubidium. Thus, it is more practical to look for approximations of the exact solutions and methods for systematically improving the accuracy of these approximations. These approximation methods build the framework for this work and are described in detail in Sections 2.1.2 – 2.1.12.

One straightforward approach to solving the many-electron Schrödinger equation is to assume the independent-particle approximation, where all interactions between electrons in the Hamiltonian are neglected, and each electron in the atom is assumed to move independently in the nuclear Coulomb field and in the average field of the remaining electrons. With this central field approximation, the N -body problem is separated into N one-body problems, separating the N -electron wave function into a product of N one-electron functions. We approximate the electron-electron interaction by a central potential $U(r)$, and construct an N -electron wave function as an anti-symmetric product of one-electron orbitals, with the constraint that the wave function remains normalized.

A completely asymmetric product wave function can be written in the form of a Slater determinant

$$\Psi(\mathbf{x}_1, \mathbf{x}_2, \dots, \mathbf{x}_N) = \frac{1}{\sqrt{N!}} \begin{vmatrix} \psi_{k_1}(\mathbf{x}_1) & \psi_{k_1}(\mathbf{x}_2) & \dots & \psi_{k_1}(\mathbf{x}_N) \\ \psi_{k_2}(\mathbf{x}_1) & \psi_{k_2}(\mathbf{x}_2) & \dots & \psi_{k_2}(\mathbf{x}_N) \\ \dots & \dots & \dots & \dots \\ \psi_{k_N}(\mathbf{x}_1) & \psi_{k_N}(\mathbf{x}_2) & \dots & \psi_{k_N}(\mathbf{x}_N) \end{vmatrix}. \quad (2.5)$$

From the properties of determinants, all spin-orbitals $\psi_i(\mathbf{x})$ have to be different, since the determinant vanishes if two columns are identical. It follows that the quantum numbers of the orbitals must be distinct (this is also known as the Pauli exclusion principle).

From here on, we follow closely Ref. [44] in describing the non-relativistic Hamiltonian and solving for its eigenvalues. In the independent-particle approximation, we write the Hamiltonian as $H = H_0 + V$, with

$$H_0(\mathbf{r}_1, \mathbf{r}_2, \dots, \mathbf{r}_N) = \sum_{i=1}^N h(\mathbf{r}_i) = \sum_{i=1}^N \left(-\frac{1}{2} \nabla_i^2 - \frac{Z}{r_i} + U(r_i) \right), \quad (2.6)$$

$$V(\mathbf{r}_1, \mathbf{r}_2, \dots, \mathbf{r}_N) = \frac{1}{2} \sum_{i \neq j} \frac{1}{r_{ij}} - \sum_{i=1}^N U(r_i), \quad (2.7)$$

where $U(r)$ is a mean field approximation to the electron interaction potential. In order to evaluate the matrix elements of many-particle operators between Slater determinants, the Slater-Condon (SC) rules (Appendix A) are utilized. With these rules, one can work out the expectation values of H for the closed-shell case, using Slater determinant wave functions:

$$E_0 = \sum_a (h_0)_{aa} + \sum_a U_{aa}, \quad (2.8)$$

$$V = \frac{1}{2} \sum_{ab} (g_{abab} - g_{abba}) - \sum_a U_{aa}, \quad (2.9)$$

$$E = \sum_a (h_0)_{aa} + \frac{1}{2} \sum_{ab} (g_{abab} - g_{abba}), \quad (2.10)$$

where we introduce the short-hand notation

$$h_{ij} = \langle \psi_i | h | \psi_j \rangle = \sum_{\sigma} \int d^3 \mathbf{x} \psi_i^*(\mathbf{x}) h(\mathbf{x}) \psi_j(\mathbf{x}), \quad (2.11)$$

and

$$g_{ijkl} = \langle \psi_i \psi_j | g | \psi_k \psi_l \rangle = \sum_{\sigma_1 \sigma_2} \iint d^3 \mathbf{x}_1 d^3 \mathbf{x}_2 \psi_i^*(\mathbf{x}_1) \psi_j^*(\mathbf{x}_2) g(r_{12}) \psi_k(\mathbf{x}_1) \psi_l(\mathbf{x}_2). \quad (2.12)$$

Here, g_{abab} is known as the direct matrix element and g_{abba} is known as the exchange matrix element of the Coulomb interaction $g(r_{12}) = 1/r_{12}$, respectively. In Eqs. 2.8 – 2.10, the sums over indices a and b extend over all one-electron spin-orbitals in the

set $\{\psi_a, \psi_b, \dots, \psi_n\}$. The sum over index a represents the sum over the entire set of quantum numbers $\{n_a, l_a, m_a, \sigma_a\}$ for all electrons, where n_a is the principle quantum number, l_a is the angular momentum quantum number, m_a is the magnetic quantum number, and σ_a is the spin quantum number, for the spin-orbital $\phi_a(\mathbf{x})$. The goal is then to determine the energy of the system via Eq. 2.10.

The one-electron spin-orbitals $\psi(\mathbf{x}) = \psi(r, \theta, \varphi, \sigma)$ are decomposed into radial, angular, and spin components

$$\psi_{nlm\sigma}(\mathbf{x}) = \psi_{nlm\sigma}(r, \theta, \varphi, \sigma) = \frac{1}{r} P_{nl}(r) Y_{lm}(\theta, \varphi) \chi_\sigma, \quad (2.13)$$

where $P_{nl}(r)$ is the radial function, $Y_{lm}(\theta, \varphi)$ is a spherical harmonic, and χ_σ is a spinor. The spinors χ_σ satisfy the orthonormality relations

$$\chi_\alpha^\dagger \chi_\beta = \delta_{\alpha\beta}. \quad (2.14)$$

The one-electron matrix elements in Eq. 2.10 can be evaluated as

$$(h_0)_{aa} = \int_0^\infty dr P_{n_a l_a} \left(-\frac{1}{2} \frac{d^2 P_{n_a l_a}}{dr^2} + \frac{l_a(l_a+1)}{2r^2} P_{n_a l_a} - \frac{Z}{r} P_{n_a l_a} \right). \quad (2.15)$$

This integral is often denoted by $I(n_a l_a)$, which after integrating by parts, can be expressed as

$$I(n_a l_a) = (h_0)_{aa} = \int_0^\infty dr \left[\frac{1}{2} \left(\frac{d^2 P_{n_a l_a}}{dr^2} \right)^2 + \frac{l_a(l_a+1)}{2r^2} P_{n_a l_a}^2 - \frac{Z}{r} P_{n_a l_a}^2 \right]. \quad (2.16)$$

To obtain expressions for the two-electron Coulomb matrix elements in Eq. 2.10, let us first derive the general expression for two-electron matrix elements

$$g_{abcd} = \iint d^3 \mathbf{r}_1 d^3 \mathbf{r}_2 \psi_a^*(\mathbf{r}_1) \psi_b^*(\mathbf{r}_2) \frac{1}{r_{12}} \psi_c(\mathbf{r}_1) \psi_d(\mathbf{r}_2). \quad (2.17)$$

We can expand $1/r_{12}$ in partial waves

$$\frac{1}{r_{12}} = \sum_k \frac{r_{<}^k}{r_{>}^{k+1}} P_k(\cos \omega), \quad (2.18)$$

where $r_<$ is the lesser of, and $r_>$ is the greater of, the two radial distances r_1 and r_2 separated by an angle ω . Next we can use the addition theorem for spherical harmonics

$$P_k(\cos \omega) = \frac{4\pi}{2k+1} \sum_{q=-k}^k Y_{kq}^*(\theta_1, \phi_1) Y_{kq}(\theta_2, \phi_2), \quad (2.19)$$

to write $1/r_{12}$ in terms of products of spherical harmonics

$$\frac{1}{r_{12}} = \sum_k^\infty \frac{4\pi}{2k+1} \frac{r_<^k}{r_>^{k+1}} \sum_{q=-k}^k Y_{kq}^*(\theta_1, \phi_1) Y_{kq}(\theta_2, \phi_2), \quad (2.20)$$

or in terms of products of C -tensors

$$\frac{1}{r_{12}} = \sum_k^\infty \frac{r_<^k}{r_>^{k+1}} \sum_{q=-k}^k (-1)^q C_q^k(\hat{r}_1) C_{-q}^k(\hat{r}_2), \quad (2.21)$$

where a C -tensor is defined as

$$C_q^k(\hat{r}) = \sqrt{\frac{4\pi}{2k+1}} Y_{kq}(\theta, \phi). \quad (2.22)$$

Expanding the many-electron wave functions into their individual components, we can then express the two-electron matrix element as

$$\begin{aligned} g_{abcd} &= \sum_{k=0}^\infty \int_0^\infty dr_1 \int_0^\infty dr_2 P_{n_a l_a}(r_1) P_{n_b l_b}(r_2) \frac{r_<^k}{r_>^{k+1}} P_{n_c l_c}(r_1) P_{n_d l_d}(r_2) \\ &\times \sum_{q=-k}^k (-1)^q \int d\Omega_1 Y_{l_a m_a}(\theta_1, \phi_1) C_q^k(\theta_1, \phi_1) Y_{l_c m_c}(\theta_1, \phi_1) \\ &\times \int d\Omega_2 Y_{l_b m_b}(\theta_2, \phi_2) C_{-q}^k(\theta_2, \phi_2) Y_{l_d m_d}(\theta_2, \phi_2). \end{aligned} \quad (2.23)$$

Here we can define a *Slater integral* $R_k(abcd)$ to be the double integral on the first line

$$R_k(abcd) = \int_0^\infty dr_1 \int_0^\infty dr_2 P_{n_a l_a}(r_1) P_{n_b l_b}(r_2) \frac{r_<^k}{r_>^{k+1}} P_{n_c l_c}(r_1) P_{n_d l_d}(r_2). \quad (2.24)$$

These Slater integrals can be written in terms of *multipole potentials* $v_l(a, b, r)$, defined by

$$v_k(a, b, r_1) = \int_0^\infty dr_2 P_a(r_2) P_b(r_2) \left(\frac{r_<^k}{r_>^{k+1}} \right). \quad (2.25)$$

This allows us to write the Slater integrals as

$$\begin{aligned} R_k(a, b, c, d) &= \int_0^\infty dr P_a(r) P_c(r) v_k(b, d, r) \\ &= \int_0^\infty dr P_b(r) P_d(r) v_k(a, c, r). \end{aligned} \quad (2.26)$$

Note that the functions $v_k(a, a, r)$ can be written in a simpler notation as $v_l(a, r)$, and that the function $v_0(a, r)$ is the potential at r due to a spherically symmetric charge distribution with radial density $P_a(r)^2$.

We can express the integrals on the second and third lines of Eq. 2.23 as matrix elements of C -tensors

$$\langle l_a m_a | C_q^k | l_c m_c \rangle = \int d\Omega_1 Y_{l_a m_a}(\theta_1, \phi_1) C_q^k(\theta_1, \phi_1) Y_{l_c m_c}(\theta_1, \phi_1), \quad (2.27)$$

$$\langle l_b m_b | C_{-q}^k | l_d m_d \rangle = \int d\Omega_2 Y_{l_b m_b}(\theta_2, \phi_2) C_{-q}^k(\theta_2, \phi_2) Y_{l_d m_d}(\theta_2, \phi_2). \quad (2.28)$$

We can then express the general two-electron matrix element, Eq. 2.23, as

$$g_{abcd} = \sum_{k=0}^{\infty} R_k(abcd) \sum_{q=-k}^k (-1)^q \langle l_a m_a | C_q^k | l_c m_c \rangle \langle l_b m_b | C_{-q}^k | l_d m_d \rangle. \quad (2.29)$$

Next, we can use the Wigner-Eckart theorem to express the two matrix elements as reduced matrix elements of the C -tensors:

$$\begin{aligned} g_{abcd} &= \sum_{k=0}^{\infty} R_k(abcd) \sum_{q=-k}^k (-1)^q \begin{array}{c} \uparrow l_a m_a \\ | \\ k q \\ | \\ l_c m_c \end{array} \begin{array}{c} \uparrow l_b m_b \\ | \\ k - q \\ | \\ l_d m_d \end{array} \langle l_a || C^k || l_c \rangle \langle l_b || C^k || l_d \rangle \\ &= \sum_{k=0}^{\infty} R_k(abcd) \sum_{q=-k}^k (-1)^k \begin{array}{c} \uparrow l_a m_a \\ | \\ k q \\ | \\ l_c m_c \end{array} \begin{array}{c} \uparrow l_b m_b \\ | \\ k q \\ | \\ l_d m_d \end{array} \langle l_a || C^k || l_c \rangle \langle l_b || C^k || l_d \rangle \\ &= \sum_{k=0}^{\infty} (-1)^k \begin{array}{c} \uparrow l_a m_a \\ | \\ \\ | \\ l_c m_c \end{array} \begin{array}{c} \\ | \\ \\ | \\ l_d m_d \end{array} + R_k(abcd) \langle l_a || C^k || l_c \rangle \langle l_b || C^k || l_d \rangle, \end{aligned} \quad (2.30)$$

where

$$\langle l_1 \| C^k \| l_2 \rangle = (-1)^{l_1} \sqrt{(2l_1 + 1)(2l_2 + 1)} \begin{pmatrix} l_1 & k & l_2 \\ 0 & 0 & 0 \end{pmatrix}, \quad (2.31)$$

$$\langle l_2 \| C^k \| l_1 \rangle = (-1)^k \langle l_1 \| C^k \| l_2 \rangle.$$

Here, diagrammatic techniques (Appendix B) were used to sum over magnetic quantum numbers q , going from line 2 to line 3.

With the general form of g_{abcd} , we can evaluate the direct matrix element term $\sum_{ab} g_{abab}$ and the exchange matrix element term $\sum_{ab} g_{abba}$ of the total energy, Eq. 2.10. The direct matrix element g_{abab} can be expressed as

$$g_{abab} = \sum_{k=0}^{\infty} (-1)^k \begin{array}{c} l_a m_a \\ \uparrow \\ - \\ \left| \begin{array}{c} \xrightarrow{k} \\ \left| \begin{array}{c} l_b m_b \\ \uparrow \\ l_b m_b \end{array} \right. \\ \downarrow \\ l_a m_a \end{array} \right. \\ \downarrow \\ l_a m_a \end{array} + R_k(abab) \langle l_a \| C^k \| l_a \rangle \langle l_b \| C^k \| l_b \rangle. \quad (2.32)$$

Next, we sum over magnetic quantum numbers m_b and spin quantum numbers σ_b

$$\begin{aligned} \sum_{m_b \sigma_b} g_{abab} &= \sum_{m_b \sigma_b} \sum_{k=0}^{\infty} (-1)^k \begin{array}{c} l_a m_a \\ \uparrow \\ - \\ \left| \begin{array}{c} \xrightarrow{k} \\ \left| \begin{array}{c} l_b m_b \\ \uparrow \\ l_b m_b \end{array} \right. \\ \downarrow \\ l_a m_a \end{array} \right. \\ \downarrow \\ l_a m_a \end{array} + R_k(abab) \langle l_a \| C^k \| l_a \rangle \langle l_b \| C^k \| l_b \rangle \\ &= 2 \sum_{k=0}^{\infty} (-1)^k \begin{array}{c} l_a m_a \\ \uparrow \\ - \\ \left| \begin{array}{c} \xrightarrow{k} \\ \left(\begin{array}{c} + \\ l_b \end{array} \right) \\ \downarrow \\ l_a m_a \end{array} \right. \\ \downarrow \\ l_a m_a \end{array} R_k(abab) \langle l_a \| C^k \| l_a \rangle \langle l_b \| C^k \| l_b \rangle \quad (2.33) \\ &= 2(2l_b + 1) R_0(abab) \\ &= 2(2l_b + 1) \int dr_1 \int dr_2 P_{n_a l_a}(r_1) P_{n_b l_b}(r_2) \frac{1}{r_{>}} P_{n_a l_a}(r_1) P_{n_b l_b}(r_2). \end{aligned}$$

Here, the sum over the spin quantum number σ_b gives an overall factor of 2. The sum over the magnetic quantum number m_b converges the right line of the diagram on line 1 into the loop on line 2.

Similarly, we can sum over the quantum numbers m_b and σ_b for g_{abba}

$$\begin{aligned}
\sum_{m_b \sigma_b} g_{abba} &= \sum_{m_b \sigma_b} \sum_{k=0}^{\infty} (-1)^{k+l_a+l_b+k} \begin{array}{c} \begin{array}{c} l_a m_a \\ \uparrow \\ - \\ \leftarrow k \\ \downarrow \\ l_b m_b \end{array} \\ + \\ \begin{array}{c} l_a m_a \\ \uparrow \\ + \\ \leftarrow k \\ \downarrow \\ l_b m_b \end{array} \end{array} R_k(abba) \langle l_a \| C^k \| l_b \rangle \langle l_b \| C^k \| l_a \rangle \\
&= \sum_{k=0}^{\infty} \delta_{\sigma_a \sigma_b} (-1)^{k+l_a+l_b} \begin{array}{c} l_a m_a \\ \leftarrow \\ \text{---} \circ \text{---} \\ \rightarrow \\ l_b m_b \end{array} R_k(abba) \langle l_b \| C^k \| l_a \rangle^2 \quad (2.34) \\
&= \sum_{k=0}^{\infty} \frac{\langle l_b \| C^k \| l_a \rangle^2}{2l_a + 1} R_k(abba).
\end{aligned}$$

We can then express the total energy, Eq. 2.10, as

$$\begin{aligned}
E &= \sum_a (h_0)_{aa} + \frac{1}{2} \sum_{ab} (g_{abab} - g_{abba}) \\
&= \sum_{n_a l_a} \sum_{m_a \sigma_a} (h_0)_{aa} + \frac{1}{2} \sum_{n_a l_a} \sum_{m_a \sigma_a} \sum_{n_b l_b} \sum_{m_b \sigma_b} (g_{abab} - g_{abba}) \quad (2.35) \\
&= \sum_{n_a l_a} \sum_{m_a \sigma_a} \left\{ I(n_a l_a) + \sum_{n_b l_b} (2l_b + 1) \left(R_0(abab) - \sum_{k=0}^{\infty} \Lambda_{l_a k l_b} R_k(abba) \right) \right\},
\end{aligned}$$

where we define

$$\Lambda_{l_a k l_b} = \frac{\langle l_b \| C^k \| l_a \rangle^2}{2(2l_a + 1)(2l_b + 1)} = \frac{1}{2} \begin{pmatrix} l_a & k & l_b \\ 0 & 0 & 0 \end{pmatrix}. \quad (2.36)$$

Since the term in the braces in the final line of Eq. 2.35 is independent of the quantum numbers m_a and σ_a , we can sum over these indices by multiplying by $2(2l_a + 1)$, resulting in

$$E = \sum_{n_a l_a} 2(2l_a + 1) \left\{ I(n_a l_a) + \sum_{n_b l_b} (2l_b + 1) \left(R_0(abab) - \sum_{k=0}^{\infty} \Lambda_{l_a k l_b} R_k(abba) \right) \right\}. \quad (2.37)$$

Expressing the Slater integrals in terms of multipole potentials (Eq. 2.25), we obtain

$$R_0(abab) = \int_0^{\infty} dr_1 P_a^2(r_1) \int_0^{\infty} dr_2 P_b^2(r_2) \frac{1}{r_{>}} = \int_0^{\infty} P_a^2(r) v_0(b, r), \quad (2.38)$$

$$R_k(abb a) = \int_0^\infty dr_1 P_a(r_1) P_b(r_1) \int_0^\infty dr_2 P_b(r_2) P_a(r_2) \frac{r_1^k}{r_2^{k+1}} = \int_0^\infty P_a(r) P_b(r) v_k(b, a, r), \quad (2.39)$$

where $v_k(a, a, r) \equiv v_k(a, r)$.

With these new designations, we can express the total energy as

$$E = \sum_a 2(2l_a + 1) \int_0^\infty dr \left\{ \frac{1}{2} \left(\frac{dP_a(r)}{dr} \right)^2 + \frac{l_a(l_a + 1)}{2r^2} P_a(r)^2 - \frac{Z}{r} P_a(r)^2 \right. \\ \left. + \sum_b (2l_b + 1) \left(P_a^2(r) v_0(b, r) - \sum_{k=0}^\infty \Lambda_{l_a k l_b} P_a(r) P_b(r) v_k(b, a, r) \right) \right\}. \quad (2.40)$$

2.1.2 The Hartree-Fock method

In this section, we will describe the Hartree-Fock method, restricting the derivation to atoms. To determine the best possible orbitals in the independent-particle model, we invoke the variational principle to look for Slater determinants Ψ that minimizes the expectation value of the Hamiltonian with respect to the orbitals, with the constraint that the wave function remains normalized:

$$E^{\text{HF}} = \min_{\Psi} \frac{\langle \Psi | H | \Psi \rangle}{\langle \Psi | \Psi \rangle} \geq E_0. \quad (2.41)$$

The Ritz variational principle guarantees that E^{HF} is always greater than or equal to the exact ground-state energy E_0 of the system of interest. We assume that the orbitals are orthonormal, so Ψ is normalized and

$$E^{\text{HF}} = \min_{\Psi} \langle \Psi | H | \Psi \rangle. \quad (2.42)$$

Using the Slater-Condon rules, we can write the expectation value of the Hamiltonian as

$$\langle \Psi | H | \Psi \rangle = \sum_{a=1}^N h_{aa} + \frac{1}{2} \sum_{ab}^N (g_{abab} - g_{abba}). \quad (2.43)$$

We add to the expectation value the orthonormalization condition using Lagrange's undetermined multipliers and minimize the energy functional \mathcal{L} with respect to the radial functions $P_{n_a l_a}(r)$ corresponding to a fixed value of l , i.e. $l_a = l_b$

$$\begin{aligned}\mathcal{L} &= \langle \Psi | H | \Psi \rangle - \sum_{n_a n_b l_a} \lambda_{n_a l_a, n_b l_a} N_{n_a l_a, n_b l_a} \\ &= E - \sum_{n_a n_b l_a} \lambda_{n_a l_a, n_b l_a} N_{n_a l_a, n_b l_a},\end{aligned}\tag{2.44}$$

where the normalization constant is expressed as

$$N_{n_a l_a, n_b l_a} = \int_0^\infty dr P_{n_a l_a}(r) P_{n_b l_a}(r) = \delta_{n_a, n_b}.\tag{2.45}$$

The variational principle can then be expressed as:

$$\delta \mathcal{L} = \delta \left(E - \sum_{n_a n_b l_a} \lambda_{n_a l_a, n_b l_a} N_{n_a l_a, n_b l_a} \right) = 0.\tag{2.46}$$

We require that energy functional \mathcal{L} be stationary with respect to variations $\delta P_{n_a l_a}$, and that the variations $\delta P_{n_a l_a}$ vanish at the origin and at infinity. With these constraints, we solve and obtain

$$\begin{aligned}-\frac{1}{2} \frac{d^2 P_{n_a l_a}}{dr^2} + \frac{l_a(l_a + 1)}{2r^2} P_{n_a l_a}(r) - \frac{Z}{r} P_{n_a l_a}(r) \\ + \sum_{n_b l_b} (4l_b + 2) \left(v_0(b, r) P_{n_a l_a}(r) - \sum_l \Lambda_{l_a l_b} v_l(b, a, r) P_{n_b l_b}(r) \right) \\ = \epsilon_{n_a l_a} P_{n_a l_a}(r) + \sum_{n_b \neq n_a} \epsilon_{n_a l_a, n_b l_a} P_{n_b l_a}(r),\end{aligned}\tag{2.47}$$

where

$$\epsilon_{n_a l_a} = \frac{\lambda_{n_a l_a, n_a l_a}}{4l_a + 2} \quad \text{and} \quad \epsilon_{n_a l_a, n_b l_a} = \frac{\lambda_{n_a l_a, n_b l_a}}{4l_a + 2}.\tag{2.48}$$

It can be shown that the orbitals associated with different principal quantum number n and the same angular quantum number l are orthogonal, no matter what value is chosen for the off-diagonal Lagrange multiplier $\lambda_{n_a l_a, n_b l_a}$ [44]. One can take advantage of this fact and choose $\epsilon_{n_a l_a, n_b l_a} = 0$ for all values of n_a , n_b and l_a .

Here we can define the Hartree-Fock potential V_{HF} by specifying its action on a radial orbital $P_a(r)$.

$$V_{\text{HF}}P_a(r) = V_{\text{dir}}P_a(r) + V_{\text{exc}}P_a(r), \quad (2.49)$$

where

$$V_{\text{dir}}(r)P_a(r) = \sum_b (4l_b + 2)v_0(b, r)P_a(r) \quad (2.50)$$

$$V_{\text{exc}}(r)P_a(r) = - \sum_b (4l_b + 2) \sum_l \Lambda_{bll_a} v_l(b, a, r)P_b(r). \quad (2.51)$$

Here the direct potential V_{dir} is a multiplicative operator describing the potential due to the spherically averaged charge distribution of all electrons. The exchange potential V_{exc} is an integral operator since it integrates over the function it acts upon. Using these operators and the choice of $\epsilon_{n_a l_a, n_b l_a} = 0$, one can rewrite the HF equations as

$$-\frac{1}{2} \frac{d^2 P_a}{dr^2} + \left(V_{\text{HF}} - \frac{Z}{r} + \frac{l_a(l_a + 1)}{2r^2} \right) P_a(r) = \epsilon_a P_a(r). \quad (2.52)$$

This set of radial equations, describing electrons moving in a central potential $V(r) = -Z/r + U(r)$, is known as the Hartree-Fock equations. Here, the optimal average central potential is the HF potential V_{HF} . To solve the HF equations, one typically expands the orbitals in terms of some known basis function, then solve the equations iteratively. One must solve the HF equations for some initial orbitals, solve the resulting eigenvalue problem, compute new operators using the resultant orbitals, then repeat the process. Once the HF equations are solved, the energy can be determined from Eq. 2.10, which can be written as

$$\begin{aligned} E &= \sum_a (h_0)_{aa} + \frac{1}{2} \sum_{ab} (g_{abab} - g_{abba}) \\ &= \sum_a \epsilon_a - \sum_a (V_{\text{HF}})_{aa} + \frac{1}{2} \sum_{ab} (g_{abab} - g_{abba}) \\ &= \sum_a \epsilon_a - \frac{1}{2} \sum_{ab} (g_{abab} - g_{abba}), \end{aligned} \quad (2.53)$$

where we have used the fact that $(V_{\text{HF}})_{aa} = \sum_b (g_{abab} - g_{abba})$. We can express the energy in terms of Slater integrals as

$$E = \sum_a (4l_a + 2) \left[\epsilon_a - \sum_b (2l_b + 1) \left(R_0(abab) - \sum_l \Lambda_{l_a l_b} R_l(abba) \right) \right]. \quad (2.54)$$

2.1.3 The relativistic Hamiltonian

Relativistic calculations follow closely with the non-relativistic methods described in the previous sections, with several modifications and caveats. First, the 2-component non-relativistic orbitals $\psi_{nlm\sigma}(\mathbf{r})$, which are products of radial functions $P_{nl}(r)$, spherical harmonics $Y_{lm}(\theta, \varphi)$, and 2-component spinors χ_σ , are replaced with 4-component relativistic orbitals $\varphi_{n\kappa m}(\mathbf{r})$, which are products of radial functions $(P_{nl}(r), Q_{nl}(r))$ and spherical spinors $\Omega_{\kappa m}(\theta, \phi)$, where $\kappa \equiv jl$ specifies the angular momentum quantum numbers n and j by $\kappa = \mp(j + 1/2)$ for $j = l \pm 1/2$. The advantages of having a relativistic theory include automatically accounting for the energy separation of nl leading into fine structure nlj with $j = l \pm 1/2$. This separation is typically not important in light atoms, but at the level of precision we need, relativistic methods are needed even in light atoms, just as they are important in heavy atoms or HCl where this separation is large [44]. Second, the Breit interaction is included along with the Coulomb interaction in the electron-electron contribution of the Hamiltonian. The Breit interaction results from transverse photon exchange between electrons, and is relatively smaller than the Coulomb interaction on the order of $\alpha^2 Z^2$. One major caveat is that the contributions from negative-energy states, which are associated with positron states, in the spectrum of the Dirac equation are omitted from the Hamiltonian and the MBPT sums entirely. In the expression for the relativistic Hamiltonian, the operators are restricted to be for positive-energy solutions associated with electron states for the Dirac equation (this Hamiltonian is also known as the *no-pair* Hamiltonian). Since positron states are not present, effects of virtual electron-positron pairs are omitted and must be found from a separate QED calculation [48].

In order to include relativistic effects, we typically start with the many-body non-relativistic Hamiltonian

$$H(\mathbf{r}_1, \mathbf{r}_2, \dots, \mathbf{r}_N) = \sum_{i=1}^N h_0(\mathbf{r}_i) + \frac{1}{2} \sum_{i \neq j} \frac{1}{r_{ij}}, \quad (2.55)$$

and choosing the one-electron Hamiltonian h_0 to be the Dirac Hamiltonian h_D

$$h_0(\mathbf{r}) = h_D(\mathbf{r}) = c\boldsymbol{\alpha} \cdot \mathbf{p} + \beta c^2 - \frac{Z}{r}. \quad (2.56)$$

Here, $\boldsymbol{\alpha}$ and β are the usual Dirac matrices:

$$\boldsymbol{\alpha} = \begin{pmatrix} 0 & \boldsymbol{\sigma} \\ \boldsymbol{\sigma} & 0 \end{pmatrix}, \quad \beta = \begin{pmatrix} I & 0 \\ 0 & -I \end{pmatrix}, \quad (2.57)$$

where $\boldsymbol{\sigma} = (\sigma_x, \sigma_y, \sigma_z)$ is a vector with components of 2×2 Pauli spin matrices and I is the 2×2 identity matrix given by

$$\sigma_x = \begin{pmatrix} 0 & 1 \\ 1 & 0 \end{pmatrix} \quad \sigma_y = \begin{pmatrix} 0 & -i \\ i & 0 \end{pmatrix} \quad \sigma_z = \begin{pmatrix} 1 & 0 \\ 0 & -1 \end{pmatrix} \quad I = \begin{pmatrix} 1 & 0 \\ 0 & 1 \end{pmatrix}. \quad (2.58)$$

Everything else follows as in the non-relativistic case. An average central field potential $U(r)$ is introduced, and we write our corresponding one-electron Hamiltonian as

$$h(\mathbf{r}) = c\boldsymbol{\alpha} \cdot \mathbf{p} + \beta c^2 - \frac{Z}{r} + U(r). \quad (2.59)$$

The resulting Dirac-Coulomb Hamiltonian and its expectation energy can then be written as in Eqs. 2.6 – 2.10. Although the expressions are the same as from the non-relativistic case, here we must use Dirac orbitals rather than the non-relativistic orbitals. The four-component one-electron Dirac orbital $\varphi_a(\mathbf{r})$ can be written in terms of radial functions and spherical spinors as

$$\varphi_a(\mathbf{r}) = \frac{1}{r} \begin{pmatrix} iP_a(r)\Omega_{\kappa_a m_a}(\theta, \phi) \\ Q_a(r)\Omega_{-\kappa_a m_a}(\theta, \phi) \end{pmatrix}, \quad (2.60)$$

where $a = n\kappa m$, and a short-hand notation $\Omega_{\kappa m} = \Omega_{jlm}$ is utilized with $\kappa = \mp(j + 1/2)$ for $j = l \pm 1/2$. The spherical spinors are given by

$$\Omega_{l\pm 1/2, l, m}(\theta, \phi) = \begin{pmatrix} \pm \sqrt{\frac{l\pm m+1/2}{2l+1}} Y_{l, m-1/2}(\theta, \phi) \\ \sqrt{\frac{l\mp m+1/2}{2l+1}} Y_{l, m+1/2}(\theta, \phi) \end{pmatrix}, \quad (2.61)$$

where $Y_{lm}(\theta, \phi)$ are spherical harmonics.

Analogously with the non-relativistic case, the goal is then to calculate the total energy

$$E = \sum_a (h_0)_{aa} + \frac{1}{2} \sum_{ab} (g_{abab} - g_{abba}), \quad (2.62)$$

now using Dirac orbitals $\varphi(\mathbf{r})$, given by Eq. 2.60, and using for the one-electron part of the Hamiltonian the Dirac Hamiltonian, given by Eq. 2.56.

The one-electron matrix element can be expressed by the radial integral

$$I(n_a \kappa_a) = (h_0)_{aa} = \langle a | h_0 | a \rangle = \int_0^\infty dr \left\{ P_a \left(-\frac{Z}{R} + c^2 \right) P_a + c P_a \left(\frac{d}{dr} - \frac{\kappa}{r} \right) Q_a - c Q_a \left(\frac{d}{dr} + \frac{\kappa}{r} \right) P_a + Q_a \left(-\frac{Z}{r} - c^2 \right) Q_a \right\}, \quad (2.63)$$

and the general two-electron matrix element can be expressed as

$$g_{abcd} = \sum_{kq} (-1)^q \langle \kappa_a m_a | C_q^k | \kappa_c m_c \rangle \langle \kappa_b m_b | C_{-q}^k | \kappa_d m_d \rangle R_k(abcd), \quad (2.64)$$

where we define a relativistic Slater integral as

$$R_k(abcd) = \int_0^\infty dr_1 [P_a(r_1)P_c(r_1) + Q_a(r_1)Q_c(r_1)] \times \int_0^\infty dr_2 \frac{r_1^k}{r_2^{k+1}} [P_b(r_2)P_d(r_2) + Q_b(r_2)Q_d(r_2)]. \quad (2.65)$$

The angular matrix elements in the two-electron matrix elements are given by

$$\begin{aligned} \langle \kappa_a m_a | C_q^k | \kappa_b m_b \rangle &= \int d\Omega \Omega_{\kappa_a m_a}^\dagger C_q^k(\hat{r}) \Omega_{\kappa_b m_b} \\ &= - \begin{array}{c} j_a m_a \\ | \\ k q \\ | \\ j_b m_b \end{array} \langle \kappa_a || C^k || \kappa_b \rangle, \end{aligned} \quad (2.66)$$

To find the optimal wave functions, we require that the total energy be stationary with respect to the radial functions, which are orthogonal for different principal quantum numbers n and same angular quantum number κ , just as in the non-relativistic case. We require that the radial functions follow the normalization condition

$$N_{n_a\kappa_a, n_b\kappa_a} = \int_0^\infty dr [P_{n_a\kappa_a}(r)P_{n_b\kappa_a}(r) + Q_{n_a\kappa_a}(r)Q_{n_b\kappa_a}(r)] = \delta_{n_a n_b}, \quad (2.75)$$

and invoke the variational principle,

$$\delta(E - \sum_{ab} \delta_{\kappa_a \kappa_b} \lambda_{n_a \kappa_a, n_b \kappa_a} N_{n_a \kappa_a, n_b \kappa_b}) = 0, \quad (2.76)$$

with respect to variations in the radial functions $\delta P_a(r)$ and $\delta Q_a(r)$. Again we require that these variations vanish at the origin and at infinity. The variational condition leads to the ‘‘Dirac-Hartree-Fock’’ (DF) equations

$$\left(V_{\text{HF}} - \frac{Z}{r} + c^2\right) P_a + c \left(\frac{d}{dr} - \frac{\kappa}{r}\right) Q_a = \epsilon_a P_a + \sum_{n_b \neq n_a} \epsilon_{n_a \kappa_a, n_b \kappa_a} P_{n_b \kappa_a}, \quad (2.77)$$

$$-c \left(\frac{d}{dr} + \frac{\kappa}{r}\right) P_a + \left(V_{\text{HF}} - \frac{Z}{r} - c^2\right) Q_a = \epsilon_a Q_a + \sum_{n_b \neq n_a} \epsilon_{n_a \kappa_a, n_b \kappa_a} Q_{n_b \kappa_a}, \quad (2.78)$$

where

$$\epsilon_a = \frac{\lambda_{n_a \kappa_a, n_a \kappa_a}}{2j_a + 1} \quad \text{and} \quad \epsilon_{n_a \kappa_a, n_b \kappa_a} = \frac{\lambda_{n_a \kappa_a, n_b \kappa_a}}{2j_a + 1}. \quad (2.79)$$

Here the DF potential V_{HF} is defined by its action of a radial function $R_a(r)$, which can either be the large component radial function $P_a(r)$ or the small component function $Q_a(r)$, by

$$V_{\text{HF}} R_a(r) = \sum_b (2j_b + 1) \left(v_0(b, r) R_a(r) - \sum_k \Lambda_{\kappa_a k \kappa_b} v_k(b, a, r) R_b(r) \right). \quad (2.80)$$

As in the non-relativistic case, the first term is the direct potential V_{dir} , which is a multiplicative operator that describes the potential due to the spherically averaged charge distribution of all electrons, and the second term is the exchange potential V_{exc} , which is an integral operator since it integrates over the radial function. Here, the relativistic screening potential is defined by

$$v_k(a, b, r) = \int_0^\infty dr' \frac{r'^k}{r^{k+1}} [P_a(r')P_b(r') + Q_a(r')Q_b(r')]. \quad (2.81)$$

As with the non-relativistic case, we choose $\epsilon_{n_a \kappa_a, n_b \kappa_a} = 0$ since the radial functions belonging to different principle quantum numbers n and the same angular quantum numbers κ are orthogonal for arbitrary values of the Lagrange multiplier $\epsilon_{n_a \kappa_a, n_b \kappa_a}$. Thus the HFD equations become a set of coupled, non-linear eigenvalue equations, which can be solved self-consistently to obtain the optimal orbitals and associated energy eigenvalues. Once the DHF equations are solved via Eq. 2.74, the total energy can be calculated in terms of DF eigenvalues as

$$E = \sum_a (2j_a + 1) \epsilon_a - \frac{1}{2} \sum_{ab} (2j_a + 1)(2j_b + 1) \left(R_0(abab) - \sum_k \Lambda_{\kappa_a k \kappa_b} R_k(abba) \right). \quad (2.82)$$

2.1.4 The Breit interaction

The Breit interaction results from transverse photon exchange between electrons and is included along with the Coulomb interaction in the electron-electron contribution of the Hamiltonian. The electron-electron Coulomb interaction is replaced by the sum of the Coulomb and Breit interaction,

$$\frac{1}{r_{12}} \rightarrow \frac{1}{r_{12}} + b_{12}, \quad (2.83)$$

where the “frequency-dependent” Breit operator associated with the exchange of a transverse photon between two electrons in states a and b is given by [49]

$$b_{12}(k_0) = -\frac{\boldsymbol{\alpha}_1 \cdot \boldsymbol{\alpha}_2}{r_{12}} \cos(k_0 r_{12}) + \boldsymbol{\alpha}_1 \cdot \nabla_1 \boldsymbol{\alpha}_2 \cdot \nabla_2 \left[\frac{\cos(k_0 r_{12}) - 1}{k_0^2 r_{12}} \right], \quad (2.84)$$

where $k_0 = |\epsilon_a - \epsilon_b|/c$. The static form ($k_0 = 0$) of the direct matrix element of the frequency-dependent Breit interaction is given by

$$b_{12} = -\frac{\boldsymbol{\alpha}_1 \cdot \boldsymbol{\alpha}_2}{r_{12}} + \frac{\boldsymbol{\alpha}_1 \cdot \boldsymbol{\alpha}_2 - (\boldsymbol{\alpha}_1 \cdot \hat{r}_{12})(\boldsymbol{\alpha}_2 \cdot \hat{r}_{12})}{2r_{12}}, \quad (2.85)$$

where the first term is referred to as the magnetic, or Gaunt, term [50], and the second term is referred to as the retardation term [51, 52, 53]. The magnetic term of the Breit operator is known to dominate in atomic calculations [54, 55] and is much simpler than the whole Breit operator. For this reason, the retardation term was neglected in the

original CI/CI+MBPT/CI+all-order code package. However, the full Breit operator has since been implemented in the latest version of our codes.

The lowest-energy shift associated with the Breit interaction is given by

$$\begin{aligned}
B^{(1)} = & -\frac{1}{2\pi^2} \int d^3r_1 \int d^3r_2 \sum_{ij} \int d^3k e^{i\mathbf{k}\cdot(\mathbf{r}_1-\mathbf{r}_2)} \left(\delta_{ij} - \frac{k_i k_j}{|\mathbf{k}|^2} \right) \\
& \times \left[\frac{1}{\mathbf{k}^2} \phi_a^*(\mathbf{r}_1) \alpha_i \phi_a(\mathbf{r}_1) \phi_b^*(\mathbf{r}_2) \alpha_j \phi_b(\mathbf{r}_2) - \frac{1}{\mathbf{k}^2 - k_0^2} \phi_a^*(\mathbf{r}_1) \alpha_i \phi_b(\mathbf{r}_1) \phi_b^*(\mathbf{r}_2) \alpha_j \phi_a(\mathbf{r}_2) \right].
\end{aligned} \tag{2.86}$$

The integral over d^3k can be carried out and the energy shift can be written in the form $B^{(1)} = b_{abab} - b_{abba}$, where b_{abab} is the two-particle direct matrix element, and b_{abba} is the two-particle exchange matrix element. The direct matrix elements b_{abab} and exchange matrix elements b_{abba} are evaluated using the static limit $k_0 \rightarrow 0$. The differences between the frequency-dependent Breit interaction and its static form are of relative order $\alpha^2 Z^2$ and therefore important for highly charged ions. Note that in our implementation of the full Breit operator in the CI/CI+MBPT/CI+all-order code package, we only use the static limit $k_0 \rightarrow 0$.

The two-particle matrix elements b_{ijkl} can be separated into the Gaunt interaction part m_{ijkl} and the retardation interaction part r_{ijkl} . This separation is convenient when considering angular reduction of the Breit interaction matrix elements.

The Gaunt interaction is given by

$$m_{ijkl} = - \iint \frac{d^3r_1 d^3r_2}{|\mathbf{r}_1 - \mathbf{r}_2|} \phi_i^*(\mathbf{r}_1) \boldsymbol{\alpha} \phi_k(\mathbf{r}_1) \cdot \phi_j^*(\mathbf{r}_2) \boldsymbol{\alpha} \phi_l(\mathbf{r}_2), \tag{2.87}$$

and the retardation interaction is given by

$$r_{ijkl} = \frac{1}{2} \iint \frac{d^3r_1 d^3r_2}{|\mathbf{r}_1 - \mathbf{r}_2|} \phi_i^*(\mathbf{r}_1) \boldsymbol{\alpha} \cdot \hat{r}_{12} \phi_k(\mathbf{r}_1) \phi_j^*(\mathbf{r}_2) \boldsymbol{\alpha} \cdot \hat{r}_{12} \phi_l(\mathbf{r}_2). \tag{2.88}$$

The matrix elements m_{ijkl} and r_{ijkl} are expanded in vector spherical harmonics, and then orthonormality properties are used to carry out angular integration. These matrix elements are complicated in form and are given in Refs. [44, 56].

It is found that for precision calculations of heavy atoms, it is sufficient to include only the exchange part of the Breit potential of the core and neglect valence-valence Breit interaction [54]. Interactions between electrons are typically reduced to

the valence-valence interaction, and the interaction of the valence electrons with the atomic core. The core-valence interaction is typically described by the HF potential, which includes direct and exchange Breit terms. The Breit correction to the interaction between valence electrons is on the order of α^2 , where α is the fine structure constant. For heavy atoms, this correction is usually below the accuracy of modern calculations. The Breit correction to the direct term of the HF potential turns to zero if the core includes only closed shells, since it is averaged to zero when summation over the closed shell is done. However, the Breit correction to the exchange interaction of the valence electrons with the core does not turn to zero, and is on the order of R^2 , where R is the overlap integral between the upper component of a valence orbital and the lower component of a core orbital. The largest integrals R correspond to the innermost core orbitals, where small components are on the order of αZ . Therefore, the dominant Breit correction is the one to the exchange core potential. The exchange interaction between valence electrons and the innermost core electrons is significantly screened if the core relaxation is allowed. Therefore, it is very important that the Breit correction to the core potential is calculated self-consistently. In some cases, the core relaxation can reduce the final Breit correction to the valence energies by an order of magnitude.

When solving the DHF equations with the Coulomb-Breit interactions, one has to keep in mind that the Breit approximation is not completely relativistic, so some caution may be necessary [54]. One can use projectors to the positive energy states, which can be done with the help of the kinetic balance condition for the small components of the Dirac orbitals. The resulting corrections in the DHF equations are not linear in the Breit interaction, but higher order terms can be eliminated using a scaling parameter λ . However, in practice, the higher order terms are usually small enough to be neglected.

2.1.5 The Second Quantization formalism

So far we have described the many-particle theory using the formulation of the Schrödinger equation, which is referred to as first quantization. It is often convenient

to replace this description of states using Slater determinants by the equivalent second quantization formalism, with which we express states and operators in terms of operators that create or annihilate particles. The rules of second quantization are similar to those of the harmonic oscillator studied in quantum mechanics [46, 57, 58]. Following closely to Ref. [44], the one-electron state $|i\rangle$, described by its wave function $\psi_i(\mathbf{r})$ in first quantization, is now represented in second quantization by an operator a_i^\dagger acting on the vacuum state $|0\rangle$

$$|i\rangle = a_i^\dagger|0\rangle. \quad (2.89)$$

The vacuum state $|0\rangle$ is the state in which there are no electrons, and is assumed to be normalized $\langle 0|0\rangle = 1$. The adjoint of the state $|i\rangle$ is given by

$$\langle i| = \langle 0|a_i. \quad (2.90)$$

The operators a_i^\dagger and a_i are called *creation* and *annihilation* operators, respectively, and are assumed to satisfy the following anticommutation relations

$$\{a_i^\dagger, a_j^\dagger\} = 0 \quad \{a_i, a_j\} = 0 \quad \{a_i, a_j^\dagger\} = \delta_{ij}. \quad (2.91)$$

A general N -particle state described by a Slater determinant wave function formed from an antisymmetric product of orbitals $\psi_a\psi_b\cdots\psi_n$, is represented in second quantization as

$$|ab\cdots n\rangle = a_a^\dagger a_b^\dagger \cdots a_n^\dagger |0\rangle. \quad (2.92)$$

A general one-particle operator is represented in second quantization as

$$F = \sum_{i=1}^N f(\mathbf{r}_i) \rightarrow \sum_{ij} \langle i|f|j\rangle a_i^\dagger a_j. \quad (2.93)$$

This operator acting on a state $|ab\cdots n\rangle$ gives

$$F|ab\cdots n\rangle = \sum_{ij} \langle i|f|j\rangle |ab\cdots j \rightarrow i\cdots n\rangle, \quad (2.94)$$

where the state $|ab\cdots j \rightarrow i\cdots n\rangle$ refers to the state $|ab\cdots n\rangle$ with the operator a_j^\dagger replaced with the operator a_i^\dagger . The state j is one currently occupied in $|ab\cdots n\rangle$ and

the state i can be one that is either identical to j or one not occupied in $|ab\cdots n\rangle$. The matrix element of F , between states $|a'b'\cdots n'\rangle$ and $|ab\cdots n\rangle$, vanishes if the states in the sets $\{ab\cdots n\}$ and $\{a'b'\cdots n'\}$ differ in more than one place, due to the Slater-Condon rules described in Appendix A.

A general two-particle operator is represented in second quantization as

$$G = \frac{1}{2} \sum_{i \neq j} g(r_{ij}) \rightarrow \frac{1}{2} \sum_{ijkl} g_{ijkl} a_i^\dagger a_j^\dagger a_l a_k, \quad (2.95)$$

where

$$g_{ijkl} = \langle \psi_i \psi_j | g | \psi_k \psi_l \rangle = \iint d^3 \mathbf{r}_1 d^3 \mathbf{r}_2 \psi_i^\dagger(\mathbf{r}_1) \psi_j^\dagger(\mathbf{r}_2) g(r_{12}) \psi_k(\mathbf{r}_1) \psi_l(\mathbf{r}_2). \quad (2.96)$$

As with the matrix elements of the one-particle operators, the matrix elements of the two-particle operators follow the Slater-Condon rules described in Section A.

We can also define the normal product of a set of operators to be the product rearranged such that core creation (excited state annihilation) operators are always on the right of core annihilation (excited state creation) operators. When rearranging, the product gains a phase $(-1)^N$, where N is the number of operator transpositions done. Normal products are designed by enclosing the operators between either a pair of colons $: a_i^\dagger a_j :$, a pair of brackets $\{a_i^\dagger a_j\}$, or a pair of brackets $n[a_i^\dagger a_j]$.

Under the formalism of second-quantization, we can write the Dirac-Hartree-Fock Hamiltonian described in Sections 2.1.3 – 2.1.4, in second quantization as

$$\begin{aligned} H &= H_0 + V, \\ H_0 &= \sum_i \epsilon_i \{a_i^\dagger a_i\}, \\ V &= \frac{1}{2} \sum_{ijkl} g_{ijkl} \{a_i^\dagger a_j^\dagger a_l a_k\} + \sum_{ij} (V_{\text{DF}} - U)_{ij} \{a_i^\dagger a_j\}. \end{aligned} \quad (2.97)$$

where ϵ_i is the eigenvalue of the Dirac equation $h_D(\mathbf{r})\phi_i(\mathbf{r}) = \epsilon_i\phi_i(\mathbf{r})$ with

$$h_D(\mathbf{r}) = c\boldsymbol{\alpha} \cdot \mathbf{p} + \beta c^2 - \frac{Z}{r} + U(r), \quad (2.98)$$

g_{ijkl} is a two-electron matrix element of the Coulomb + Breit potential $g(r_{12}) = 1/r_{12} + b_{12}$, $(V_{\text{DF}})_{ij} = \sum_a (g_{iaja} - g_{iaaj})$ is the one-electron matrix element of the Dirac-Fock

potential V_{HF} , and U_{ij} is the one-electron matrix element of the central potential $U(r)$. Here, the summation index a ranges over only core states, and the summation indices i, j, k, l range over all one-electron states. The $\{\dots\}$ designates normal products with respect to the closed core. The operators in the Hamiltonian are restricted to ones for positive-energy solutions to the Dirac equation, which are associated with electron states, and positron states are omitted from the Hamiltonian, resulting in the *no-pair* Hamiltonian. To account for the small effects of virtual electron-positron pairs, which are omitted in the atomic structure calculation, one must carry out a separate QED calculation [48].

2.1.6 The Configuration Interaction method

The basic idea of configuration interaction (CI) is to diagonalize the N -electron Hamiltonian in a basis of N -electron functions, or Slater determinants. Essentially what we're doing here is representing the exact wave function as a linear combination of N -electron trial functions and then using the variational method to minimize the energy. If a complete basis were used, we would obtain the exact energies to the ground state and all excited states of the system. In principle, this method provides an exact solution to the many-electron problem; however, in practice, only a finite set of N -electron trial functions are manageable so the CI wave function expansion is typically truncated at specific excited configurations. As a result of the size restrictions on practical CI calculations, CI always provides only upper bounds to the exact energies.

The CI wave function is constructed as a linear combination of known Slater determinants Φ_i with unknown expansion coefficients

$$|\Psi\rangle = \sum_i c_i |\Phi_i\rangle. \quad (2.99)$$

Typically, the Slater determinants are constructed from excitations of the Hartree-Fock “reference” determinant $|\Phi_0\rangle$. The CI wave function can be expanded as

$$|\Psi\rangle = c_0 |\Phi_0\rangle + \sum_{r,a} c_a^r |\Phi_a^r\rangle + \sum_{r<s,a<b} c_{ab}^{rs} |\Phi_{ab}^{rs}\rangle + \sum_{r<s<t,a<b<c} c_{abc}^{rst} |\Phi_{abc}^{rst}\rangle + \dots, \quad (2.100)$$

where $|\Phi_a^r\rangle$ represents the singly excited Slater determinants formed by replacing spin-orbital ϕ_a with ϕ_r , $|\Phi_{ab}^{rs}\rangle$ represents the doubly excited Slater determinants formed by replacing spin-orbital ϕ_a with ϕ_r and replacing spin-orbital ϕ_b with ϕ_s , and so on for higher excited states. In general, all N -electron Slater determinants can be formed by a set of N spin-orbitals $\{\phi_i\}_{i=1}^N$.

We can rewrite Eq. 2.100 in a more general form $|\Psi\rangle = \sum_{i=0} c_i |\Phi_i\rangle$, where $i = 0$ refers to the reference Hartree-Fock wave function, $i = 1$ refers to our singly excited state wave function, and so on. We now optimize our total CI wave function via the Ritz variational method by varying the coefficients of the wave functions

$$E = \frac{\langle \Psi | H | \Psi \rangle}{\langle \Psi | \Psi \rangle}. \quad (2.101)$$

If we expand the CI wave function in a linear combination of Slater determinants, we obtain

$$E = \frac{\sum_i \sum_j c_i^* c_j \langle \Phi_i | H | \Phi_j \rangle}{\sum_i \sum_j c_i^* c_j \langle \Phi_i | \Phi_j \rangle}. \quad (2.102)$$

The variational procedure corresponds to setting all the derivatives of our energy with respect to the expansion coefficients c_i equal to zero, i.e. $\partial E / \partial c_i = 0$.

Rearranging, we get

$$E \sum_i \sum_j c_i^* c_j \langle \Phi_i | \Phi_j \rangle = \sum_i \sum_j c_i^* c_j \langle \Phi_i | H | \Phi_j \rangle$$

$$\frac{\partial E}{\partial c_i} \sum_{ij} c_i^* c_j \langle \Phi_i | \Phi_j \rangle + 2E \sum_i c_i \langle \Phi_i | \Phi_j \rangle = 2 \sum_i c_i \langle \Phi_i | H | \Phi_j \rangle + \sum_{ij} c_i^* c_j \frac{\partial}{\partial c_i} (\langle \Phi_i | H | \Phi_j \rangle).$$

The first term vanishes from the minimization of the energy, and the last term vanishes since the matrix elements $\langle \Phi_i | H | \Phi_j \rangle$ do not depend on the expansion coefficients. Assuming that the basis functions are orthonormal, we obtain

$$E \sum_i c_i \delta_{ij} = \sum_i c_i \langle \Phi_i | H | \Phi_j \rangle$$

$$\sum_i H_{ij} c_i - \sum_i E \delta_{ij} c_i = 0,$$

where $H_{ij} = \langle \Phi_i | H | \Phi_j \rangle$. Since there is one equation for each j , we can transform this equation into a matrix equation

$$(\mathbf{H} - E\mathbf{I})\mathbf{c} = 0, \quad (2.103)$$

$$\mathbf{H}\mathbf{c} = E\mathbf{c}. \quad (2.104)$$

$$\begin{pmatrix} H_{00} - E & H_{01} & \dots & H_{0j} & \dots \\ H_{10} & H_{11} - E & \dots & H_{1j} & \dots \\ \vdots & \vdots & \ddots & \vdots & \dots \\ H_{j0} & \vdots & \dots & H_{jj} - E & \dots \\ \vdots & \vdots & \dots & \vdots & \ddots \end{pmatrix} \begin{pmatrix} c_0 \\ c_1 \\ \vdots \\ c_j \\ \vdots \end{pmatrix} = \begin{pmatrix} 0 \\ 0 \\ \vdots \\ 0 \\ \vdots \end{pmatrix} \quad (2.105)$$

Solving these secular equations is equivalent to diagonalizing the CI matrix. We use the Davidson method of diagonalization, which is described in Section 2.1.9. The CI Hamiltonian energy eigenvalues are then obtained as the lowest eigenvalues of the CI Hamiltonian matrix. The corresponding eigenvectors contain the set of expansion coefficients $\{c_i\}_{i=0}^N$ in front of the determinants in Eq. 2.100. In this case, the lowest eigenvalue corresponds to the ground state energy, the second lowest eigenvalue corresponds to the energy of the first excited state, the third lowest eigenvalue corresponds to the energy of the second excited state, and so on.

We have mentioned that the CI expansion is typically truncated at specific excited configurations. From the Slater-Condon rules, only singly and doubly excited states can interact directly with the reference state. Therefore, matrix elements with more than two differing spin-orbitals in the determinants vanish. Due to Brillouin's theorem [47], the matrix elements $\langle S | H | \Phi_0 \rangle$ are zero, where $|S\rangle$ refers to singly-excited

Slater determinants. The structure of the CI Hamiltonian matrix, under the basis set of HF Slater determinants and their excited states is then given as

$$\mathbf{H} = \begin{pmatrix} \langle \Phi_0 | H | \Phi_0 \rangle & 0 & \langle \Phi_0 | H | D \rangle & 0 & 0 & \dots \\ 0 & \langle S | H | S \rangle & \langle S | H | D \rangle & \langle S | H | T \rangle & 0 & \dots \\ \langle D | H | \Phi_0 \rangle & \langle D | H | S \rangle & \langle D | H | D \rangle & \langle D | H | T \rangle & \langle D | H | Q \rangle & \dots \\ 0 & \langle T | H | S \rangle & \langle T | H | D \rangle & \langle T | H | T \rangle & \langle T | H | Q \rangle & \dots \\ 0 & 0 & \langle Q | H | D \rangle & \langle Q | H | T \rangle & \langle Q | H | Q \rangle & \dots \\ \vdots & \vdots & \vdots & \vdots & \vdots & \vdots \end{pmatrix}, \quad (2.106)$$

where $|\Phi_0\rangle$ is the Hartree-Fock reference state, $|S\rangle$ is the singly excited state, $|D\rangle$ is the doubly excited state, and so on. The blocks $\langle X | H | Y \rangle$ which are not necessarily zero may still be sparse, meaning that most of its elements are zero. Let's look at the matrix element belonging to the block $\langle D | H | Q \rangle$. The matrix elements $\langle \Phi_{ab}^{rs} | H | \Phi_{cdef}^{tuvw} \rangle$ will be non-zero only if ϕ_a and ϕ_b are contained in the set $\{\phi_c, \phi_d, \phi_e, \phi_f\}$, and if ϕ_r and ϕ_s are contained in the set $\{\phi_t, \phi_u, \phi_v, \phi_w\}$.

The task at hand is then to calculate each matrix element and to diagonalize the CI matrix. As we include more and more excitations in the CI expansion, we capture more and more electron correlation. We can increase the size of the CI matrix by adding more excited configurations, or by increasing the basis set size. However, there's a problem with adding more and more excitations or basis sets - namely, it is very expensive to do so. If the number of spin-orbitals produced by HF is $2M$, then the number of determinants constructed is then $\binom{2M}{N}$, where N is the number of electrons. Taking into account all possible excitations in the expansion is known as Full CI (FCI), and this method goes with a complexity of $O(N!)$.

Due to the complexity of Full CI, what is usually done is to truncate the CI matrix, i.e. CI Doubles (CID) only takes into consideration CI with double excitations. Since the single excitations themselves do not correlate with the ground state directly, the most significant term for the correlation energy must come from the double excitations, since they are the first excitations coupled with the HF Slater determinant. This gives a reduced matrix which is much more feasible for practical computation;

however, the truncated CI will introduce errors in the wave function, which will in turn cause errors in the energy and all other properties. A particular result of truncating the N -electron basis is that the CI energies obtained are no longer size extensive [47].

It is clear that the fraction of the correlation energy recovered by a truncated CI will diminish as the size of the system increases, making it a progressively less accurate method. However, if we were to truncate CI, we should consider, for example, not exciting the inner shell orbitals since the computational complexity for those excitations can become huge for small effects on the correlation energy. We can neglect these orbitals by “freezing” the core orbitals and implementing CI in higher orbitals. This is also known as the *frozen-core* approximation. For some applications, such as the Ir^{17+} highly charged ion, we find that it is essential to open more orbitals for a more accurate treatment of the ion.

The Multi-Configurational Self-Consistent Field (MCSCF) method is another approach to the CI method, in which one decides on a set of determinants that can sufficiently describe the system of interest. Each of the determinants are constructed from spin-orbitals that are not fixed, but optimized as to lower the total energy as much as possible. The main idea here is to use the variational principle to not only optimize the coefficients in front of the determinants, but also to optimize the spin-orbitals used to construct the determinants. In a sense, the MCSCF method is a combination of the CI and HF methods (if the number of determinants chosen was just those of the reference HF Slater determinants, the method reduces back to the HF method).

The classical MCSCF approach follows very closely to the Ritz variational method described before. We start with the MCSCF wave function, which has the form of a finite linear combination of Slater determinants Φ_I

$$\Psi^{\text{MCSCF}} = \sum_I c_I \Phi_I, \quad (2.107)$$

where c_I are the variational coefficients. First, we calculate the coefficients for the determinants using the variational method, without varying the spin-orbitals, then we vary the coefficients of the determinants in the fixed CI space to obtain the best

determinants. And finally, we repeat by going back and expanding the MCSCF wave function in terms of the newly optimized determinants. In this way, the MCSCF method generates a qualitatively correct wave function, i.e., recovers the “static” part of the configurational space, where most of the dominant configurations reside. For many systems, this method can produce accurate results [8, 9, 10, 11]. The goal is usually not to recover a large fraction of the total correlation energy, but to recover all the changes that occur in the correlation energy for a given process. A major problem that this procedure faces is figuring out which configurations are necessary to include for the property of interest.

The Complete Active Space Self-Consistent Field (CASSCF) method is a special case of the MCSCF method. From the orbitals computed from HF, we partition the space of these orbitals into an active and inactive space. The inactive space of orbitals are chosen from the low energy orbitals, i.e. the doubly occupied orbitals in all determinants (inner shells). The remaining orbitals belong to the active space. Within the active space, we consider all possible occupancies and excitations of the active spin-orbitals to obtain the set of determinants in the expansion of the MCSCF wave function (hence, “complete”). For any full CI expansion, CASSCF becomes too large to be useful, even with small active spaces. To overcome this problem, a variation called the Restricted Active Space Self-Consistent Field (RASSCF) method is used.

In the RASSCF method, the active orbitals are divided into 3 subsections, RAS1, RAS2, and RAS3. Each of these subsystems have restrictions on the excitations allowed. A typical example is one where RAS1 includes occupied orbitals that are excited in the HF reference determinant, RAS2 includes orbitals limited to SD excitations, and RAS3 includes virtual orbitals that are empty in the HF determinant. The full CI expansion within the active space severely restricts the number of orbitals and electrons that can be treated by CASSCF methods. Any additional configurations to those from RAS2 space can be generated by allowing excitations from one space to another. For example, allowing 2 electrons to be excited from RAS1 to RAS3. In

essence, a typical example of the RASSCF method generates configurations by a combination of a full CI in a small number of orbitals in RAS2 and a CISD in a somewhat large orbital space in RAS1 or RAS3.

Excitation energies of truncated CI methods such as the ones described above are generally too high, since the excited states are not that well correlated as the ground state is. For equally correlated ground and excited states, one can use a method called Multi-Reference Configuration Interaction (MRCI), which uses more than one reference determinant from known singly, doubly, or higher excited states (this set of known determinants is called the model space). MRCI gives a better correlation of the ground state, which is important if the system under consideration has more than one dominant determinant since some higher excited determinants are also taken into the CI space. The CI expansion is then obtained by replacing the orbitals in the model space by other virtual orbitals.

2.1.7 Basis sets and basis set convergence

The standard wave functions used in solving Schrödinger's equations for atoms and molecules are constructed from antisymmetric products of spin-orbitals. In most methods, these spin-orbitals are generated by expanding them into a finite set of simple basis functions. The choice of basis functions for an atomic calculation is therefore always important. There are hundreds of basis sets that can be used, each optimized for a specific system. The basis sets used for the calculations done in this work are constructed on a case-by-case basis. DHF orbitals are typically always used for core or low-lying orbitals. In the case of the CI+all-order method, DHF orbitals are merged with B-splines for the rest of the orbitals (e.g. virtual orbitals). These basis sets created from B-splines will be discussed later in this section.

What we will need for carrying out accurate correlated calculations are not only a set of spin-orbitals that resemble as closely as possible the occupied orbitals of the atomic systems, but also a set of virtual correlating orbitals into which the correlated electrons can be excited. An obvious candidate here are the canonical orbitals from the

HF calculations; however, since the lowest virtual HF orbitals are very diffuse, they will not be well suited for correlating the ground-state electrons, except when the full set of orbitals is used. Another strategy is to try and generate correlating atomic orbitals for atomic calculations by relying on the energy criterion alone, i.e. adjust the exponents of the correlating orbitals as to maximize their contribution to the correlation energy. By doing this, we should be able to generate sets of correlating orbitals that are more compact, i.e. contains fewer primitive basis functions. This method will generate correlation-consistent basis sets, meaning that each basis set contains all correlating orbitals that lower the energy by comparable amounts, as well as all orbitals that lower the energy by larger amounts.

In these correlation consistent basis sets, each correlating orbital is chosen as to maximize its contribution to the correlation energy. All correlating orbitals that make similar contributions to the correlation energy are added simultaneously. The goal for these basis sets is to contain all correlating orbitals that lower the energy by comparable or larger amounts. The main advantage of this method is that it allows us to retrieve a larger number of correlations with a smaller basis set.

As the number of basis functions increase, the wave functions become better represented and the energy decreases to approach the complete basis set (CBS) limit. An infinite number of basis functions is impossible to employ practically, but we can try to estimate the energy at the CBS limit. By using hierarchical basis sets, i.e. correlating consistent sets with adjacent angular momenta, we can calculate the energy for a couple of points, then hope to extrapolate higher basis function energies or higher correlation energies.

2.1.8 B-spline basis sets

In the calculations done in this work, B-splines were utilized to construct the basis sets for the radial Dirac equation [44, 57]. Here we follow the Ref. [44] in describing these B-spline basis sets. Since correlation corrections in atoms have finite range, we restrict ourselves to a finite, but large cavity of radius R . To study the ground

state or low-lying excited states, we typically choose boundary conditions $P_{nl}(0) = P_{nl}(R) = 0$. The spectrum in this cavity is discrete, but infinite. The plan is then to expand solutions to the radial Schrödinger equation in a finite basis set of n B-splines of order k , following the work of deBoor [59].

We begin by dividing the interval $[0, R]$ into segments, where the endpoints of the segments are given by the knot sequence $\{t_i\}$, where $i = 1, 2, \dots, n+k$. The knots defining the grid have k -fold multiplicity at the endpoints, i.e. $t_1 = t_2 = \dots = t_k = 0$ and $t_{n+1} = t_{n+2} = \dots = t_{n+k} = R$. The knots $t_{k+1}, t_{k+2}, \dots, t_n$ are distributed on an exponential scale between 0 and R . B-splines of order k , $B_{i,k}(r)$, on this knot sequence are defined recursively by

$$B_{i,1}(r) = \begin{cases} 1, & t_i \leq r < t_{i+1}, \\ 0, & \text{otherwise,} \end{cases} \quad (2.108)$$

and

$$B_{i,k}(r) = \frac{r - t_i}{t_{i+k-1} - t_i} B_{i,k-1}(r) + \frac{t_{i+k} - r}{t_{i+k} - t_{i+1}} B_{i+1,k-1}(r), \quad (2.109)$$

where $B_{i,k}(r)$ is a piece-wise polynomial of degree $k-1$ inside the interval $t_i \leq r < t_{i+k}$, and vanishes outside this interval. The set of B-splines of order k on $\{t_i\}$ forms a complete basis for piece-wise polynomials of degree $k-1$ on the interval spanned by $\{t_i\}_{i=1}^{n+k}$.

We represent solutions to the radial Schrödinger equation as a linear combination of these B-splines and work with the B-spline representation of wave functions rather than the wave functions themselves. The radial wave function $P_l(r)$ satisfies the variational equation $\delta S = 0$, where the action S is given by

$$S = \int_0^R \left[\frac{1}{2} \left(\frac{dP_l(r)}{dr} \right)^2 + \left(V(r) + \frac{l(l+1)}{2r^2} \right) P_l(r)^2 \right] - \epsilon \int_0^R P_l(r)^2 dr. \quad (2.110)$$

Here we insure the normalization of the radial wave functions using the parameter ϵ . The variational principle leads to the radial Schrödinger equation for the radial wave function $P_l(r)$, which are expanded in terms of B-splines of order k as

$$P_l(r) = \sum_{i=1}^n p_i B_i(r), \quad (2.111)$$

where p_i is the expansion coefficient and we utilize a short-hand notation $B_i(r) = B_{i,k}(r)$. With this expansion, the variational principle leads to a system of linear equations for the expansion coefficients p_i . The system of linear equations can be written in the form of an $n \times n$ symmetric generalized eigenvalue equation

$$Av = \epsilon Bv, \quad (2.112)$$

where $v = (p_1, p_2, \dots, p_n)$ is the vector of expansion coefficients. The matrix elements of A and B are given by

$$A_{ij} = \int_0^R \left[\frac{dB_i(r)}{dr} \frac{dB_j(r)}{dr} + 2B_i(r) \left(V(r) + \frac{l(l+1)}{2r^2} \right) B_j(r) \right] dr, \quad (2.113)$$

$$B_{ij} = \int_0^R B_i(r) B_j(r) dr. \quad (2.114)$$

One obtains n real eigenvalues and eigenvectors, which satisfy orthogonality relations in the corresponding wave functions. The first few eigenvalues and eigenvectors in the cavity agree well with the first few bound-state eigenvalues and eigenvectors obtained by numerical integration, but the spectrum is expected to depart from the real spectrum as the principle quantum number increases.

To expand the usage of B-splines to the HF method, we must have the HF equations for the occupied orbitals of a closed-shell system solved, and have those resulting orbitals used to construct the HF potential. Once the HF potential has been determined, a complete set of one-electron orbitals can be constructed using B-splines. If we let V_{HF} be the HF potential, then its contribution to the action integral S for an orbital a will be

$$\int_0^R P_a(r) V_{\text{HF}} P_a(r) dr = \sum_b 2(2l_b + 1) \left(R_0(abab) - \sum_k \Lambda_{l_a k l_b} R_k(abba) \right), \quad (2.115)$$

where the sum over index b is over all occupied shells. This contribution to the action integral leads to the following modification of the potential contribution in the matrix

element A_{ij}

$$\int_0^R B_i(r) V_{\text{HF}} B_j(r) dr = \int_0^R dr B_i(r) \times \sum_b 2(2l_b + 1) \left[v_0(b, r) B_j(r) - \sum_k \Lambda_{l_a k l_b} v_k(b, B_j, r) P_b(r) \right]. \quad (2.116)$$

To solve the generalized eigenvalue problem, the occupied orbitals $P_b(r)$ are obtained first through numerical integration, then used to construct the matrix A . The eigenvalue problem can then be iteratively solved to give the complete spectrum of HF states to desired precision.

The relativistic case follows very closely with the non-relativistic method described above, with two major modifications. First, both the large component radial functions $P(r)$ and the small component radial functions $Q(r)$ are expanded in terms of B-splines

$$P(r) = \sum_{i=1}^n p_i B_i(r) \quad Q(r) = \sum_{i=1}^n q_i B_i(r), \quad (2.117)$$

leading to a $2n \times 2n$ generalized eigenvalue problem for the expansion coefficient vector $v = (p_1, p_2, \dots, p_n, q_1, q_2, \dots, q_n)$. The Dirac spectrum obtained include n electron bound and continuum states, and n positron states, which are omitted in sums over virtual states in expressions for the correlation energy. Second, the boundary condition $P(R) = 0$ is replaced with the MIT bag-model boundary condition $P(R) = Q(R)$ [60], in order to avoid problems associated with the Klein paradox that arise when one attempts to confine a particle to a cavity using an infinite potential barrier [58].

2.1.9 The Davidson method

In order to find the low-lying eigenvectors and eigenvalues of the CI Hamiltonian matrix, we use an iterative method suggested by Davidson [1]. Large scale CI calculations require construction of a few eigenvalues and eigenvectors of large, sparse, real-symmetric matrices. Davidson's method offers several advantages over widely

used eigenvalue solving procedures, such as the Lanczos algorithm [1, 61]. These include requiring only the matrix operation $\mathbf{A}\mathbf{b}$ and not sequential calculations of $(\mathbf{A}\mathbf{b})_i$, requiring only storage of two vectors at once regardless of the number of roots found, the ability to find higher eigenvalues without accurate values of lower eigenvalues, no difficulties of convergence for nearly degenerate eigenvectors, and a better chance for rapid convergence compared to methods such as the Lanczos algorithm [1]. The complexity of the Davidson algorithm comes mainly from the formation of matrix-vector products. For small matrices, these products are very cheap to compute, and it suffices to use direct diagonalization. For large matrices, the formation of the matrix-vector products are expensive, so it is more cost effective to utilize the Davidson algorithm.

Following Davidson's original paper in describing his iterative method [1, 61], we begin by constructing an initial approximation for the matrix of interest, and constructing trial eigenvectors from this initial approximation. An eigenpair is then constructed using the Rayleigh-Ritz (RR) procedure, and a residual vector is computed to measure convergence (convergence is typically met when the norm of the residual is reduced to 10^{-6}). Here, the bulk of the computation time is taken up by computing matrix-vector products. New trial eigenvectors are constructed, the associated trial space is diagonalized, and new eigenpairs are constructed again from the RR procedure. This procedure is repeated iteratively until convergence is met.

From the discussions in Section 2.1.6, we found that the variational method leads us to the CI Hamiltonian matrix equation (Eq. 2.104)

$$\mathbf{H}\mathbf{c} = E\mathbf{c}, \quad (2.118)$$

where \mathbf{H} is the CI Hamiltonian matrix, and \mathbf{c} is the wave function expressed as an array of expansion coefficients. The components of the wave function can be expressed as

$$\mathbf{c}^{(k)} = \sum_{i=0}^k \alpha_i^{(k)} \mathbf{b}_i, \quad (2.119)$$

where

$$\mathbf{b}_0 = \mathbf{c}^{(0)}, \quad (2.120)$$

$$\mathbf{b}_i = \frac{\mathbf{d}_i}{\|\mathbf{d}_i\|}, \quad (2.121)$$

$$\mathbf{d}_i = \left[\prod_{j=0}^{i-1} (\mathbf{1} - \mathbf{b}_j \mathbf{b}_j^T) \right] \boldsymbol{\xi}_i, \quad (2.122)$$

$$\|\mathbf{d}_i\| = \sqrt{\langle \mathbf{d}_i | \mathbf{d}_i \rangle}. \quad (2.123)$$

Here, the components of the vector $\boldsymbol{\xi}$ can be found by

$$\xi_{J,i+1} = (E(\mathbf{c}_{(i)}) - A_{JJ})^{-1} q_{J,i}, \quad (2.124)$$

where

$$\mathbf{q}_i = (\mathbf{H} - E(\mathbf{c}_{(i)})\mathbf{1}). \quad (2.125)$$

This method generates k approximate eigenvalues at each iterative step. The computational details of the original Davidson procedure are as follows (Note: This procedure is modified for usage in the CI/CI+MBPT/CI+all-order code package. These modifications along with our realization of the Davidson method is described below and in Section 3.1.5) [1]:

1. Select a zeroth-order orthonormal subspace $\mathbf{b}_1, \mathbf{b}_2, \dots, \mathbf{b}_l$, where $l \geq k$ spans the dominant components of the wave functions of the first k desired eigenvalues.
2. Form and save matrix-vector products $\mathbf{H}\mathbf{b}_1, \mathbf{H}\mathbf{b}_2, \dots, \mathbf{H}\mathbf{b}_l$, and $\tilde{H}_{ij} = \langle \mathbf{b}_i | \mathbf{H}\mathbf{b}_j \rangle$, where $1 \leq i \leq j \leq l$.
3. Diagonalize $\tilde{\mathbf{H}}$ using a standard method for small matrices, then select the k th eigenvalue $\lambda_k^{(l)}$ and the corresponding eigenvectors $\boldsymbol{\alpha}_k^{(l)}$.
4. Form the residual vector $\mathbf{q}_M = \sum_{i=1}^M \alpha_{i,k}^{(M)} (\mathbf{H}\mathbf{b}_i) - \sum_{i=1}^M \alpha_{i,k}^{(M)} \lambda_k^{(M)} \mathbf{b}_i$, where M is the dimension of $\tilde{\mathbf{H}}$ used to find $\boldsymbol{\alpha}$ and λ .
5. Compute the norm of the residual vector $\|\mathbf{q}_M\|$ and check convergence.
6. Form $\xi_{I,(M+1)} = (\lambda_k^{(M)} - H_{II})^{-1} q_{I,M}$, where $I = 1, \dots, N$.
7. Form $\mathbf{d}_{(M+1)} = \left[\prod_{i=1}^M (\mathbf{1} - \mathbf{b}_i \mathbf{b}_i^T) \right] \boldsymbol{\xi}_{(M+1)}$.

8. Form $\mathbf{b}_{(M+1)} = \mathbf{d}_{(M+1)} / \|\mathbf{d}_{(M+1)}\|$.
9. Form $\mathbf{H}\mathbf{b}_{(M+1)}$.
10. Form $\tilde{h}_{i,M+1} = \langle \mathbf{b}_i | \mathbf{H}\mathbf{b}_{(M+1)} \rangle$, where $i = 1, \dots, M + 1$.
11. Diagonalize $\tilde{\mathbf{H}}$ and return to step 4 with $\alpha_k^{(M+1)}$ and $\lambda_k^{(M+1)}$.

When looking for several eigenvalues, the first l of the $\sum_{i=1}^M \alpha_{ij} \mathbf{b}_i$ at the end of finding one root often provides for a good starting set for the next root. The slowest step in the Davidson procedure is the formation of the matrix-vector products $\mathbf{H}\mathbf{b}$. If M becomes inconveniently large, the current set of $\sum_{i=1}^M \alpha_{ij} \mathbf{b}_i$, where $j = 1, \dots, l$, can be taken as a new initial set and the calculation can be restarted from step 1.

With Davidson's method outlined above, we now discuss the realization of the method in our work. We define \mathbf{H} as the CI Hamiltonian matrix, and let $\mathbf{D} = \text{diag}(\mathbf{H})$. \mathbf{H} is an $N \times N$ matrix, and \mathbf{D} is an N -dimensional vector. We choose an initial approximation Hamiltonian \mathbf{Z} of size $N_0 \times N_0$, and diagonalize it using Householder's method (Appendix C). Next, the initial eigenvectors $\mathbf{B} = (\mathbf{B}_0^{(1)}, \mathbf{B}_0^{(2)}, \dots, \mathbf{B}_0^{(k)})$, each of dimension N , are chosen from the eigenvectors of \mathbf{Z} of dimension N_0 , with all other elements $\{B_{0,i}^{(k)}\}_{i=N_0+1}^N = 0$. Here, the (k) superscript represents the number k of desired eigenvalue and eigenvector.

After the initial approximation has been constructed, the iterative procedure begins with $j = 0$, incrementing by 1 until convergence is reached. First, the eigenvectors \mathbf{B}_j are orthonormalized, and the products $\mathbf{Q}_j = \mathbf{H}\mathbf{B}_j$ are evaluated. Next, we form the matrix $\mathbf{P} = \mathbf{B}_j^T \mathbf{Q}_j$. Due to technical complications, the construction of the matrix \mathbf{P} and its associated eigenvectors were done in two parts: First, the top left block of the matrix \mathbf{P} is formed, then the three other blocks are formed. Next, the residual vector \mathbf{C} is formed and the norm of the residual $\|\mathbf{C}\|$ is calculated and used to check for convergence. If not converged, a new set of eigenvectors \mathbf{B}_{j+1} is formed corresponding to the residual vectors. These eigenvectors are then orthonormalized, and the matrix \mathbf{P} is diagonalized using Householder's method for subsequent iterations. The products are then computed, and the process repeats until the convergence criteria

(10^{-6}) is reached. The technical details of the computational process is described in Section 3.1.5.

2.1.10 CI+MBPT

In this section, we describe a method combining configuration interaction with many-body perturbation theory developed in [62]. We can acquire benefits from both approaches to attain better accuracy for calculations for atoms with more than one valence electron. We follow closely from the original paper [62] to derive the CI+MBPT equation used in the code package.

We begin by dividing the many-electron Hilbert space into two subspaces: a model subspace P corresponding to the frozen-core electron states and a complementary subspace Q that includes all other states. The model subspace P is dealt with using the CI method, while the complementary subspace Q is dealt with using MBPT since projections of the wave functions of the lowest energy levels of the atom onto Q are assumed to be small. For the convergence of MBPT, it is important to separate the core and valence electrons so that their energies are well separated. We use Slater determinants $|I\rangle$ of the one-particle wave functions for the core electrons ϕ_i as a basis set in the many-electron space. We can define projection operators

$$\mathcal{P} = \sum_{I \in P} |I\rangle\langle I| \quad \text{and} \quad \mathcal{Q} = \sum_{I \in Q} |I\rangle\langle I| \quad (2.126)$$

to the subspaces P and Q , respectively, satisfying the completeness relation

$$\mathcal{P} + \mathcal{Q} = 1. \quad (2.127)$$

Using the CI method, we can introduce a CI model subspace $P^{\text{CI}} \subset P$ by defining a subset of configurations I associated with the lowest-lying states of the infinite-dimensional model subspace P . The wave function can then be represented as a linear combination of Slater determinants from P^{CI} ,

$$\psi = \sum_{I \in P^{\text{CI}}} C_I |I\rangle. \quad (2.128)$$

Varying the coefficients C_I leads to the matrix eigenvalue problem as before

$$\sum_{J \in P^{\text{CI}}} H_{IJ} C_J = E C_I. \quad (2.129)$$

The CI Hamiltonian matrix can be obtained as a projection of the exact Hamiltonian \mathcal{H} onto the model subspace P^{CI} :

$$\mathcal{H}^{\text{CI}} = \mathcal{P}^{\text{CI}} \mathcal{H} \mathcal{P}^{\text{CI}}. \quad (2.130)$$

For the sake of simplicity, we assume that it is possible to choose the configurations in P^{CI} such that we can obtain our desired accuracy for the solution of Schrödinger's equation in the P subspace. For this reason, we will not distinguish between P^{CI} and P . Since we chose P such that the core electrons are frozen, we can exclude them by averaging the Hamiltonian over the single-determinant wave function of the core electrons, giving

$$\mathcal{P} \mathcal{H} \mathcal{P} = E_{\text{core}} + \sum_{i > N_{\text{core}}} h_i^{\text{CI}} + \sum_{j > i > N_{\text{core}}} \frac{1}{r_{ij}}, \quad (2.131)$$

where E_{core} refers to the total core energy, defined as the matrix element of the exact Hamiltonian \mathcal{H} with the core wave function:

$$E_{\text{core}} = \langle \Psi_{\text{core}} | \mathcal{H} | \Psi_{\text{core}} \rangle, \quad (2.132)$$

$$|\Psi_{\text{core}}\rangle = a_1^\dagger a_2^\dagger \cdots a_{N_{\text{core}}}^\dagger |0\rangle. \quad (2.133)$$

E_{core} includes the kinetic energy of the core electrons, as well as the core-core and core-nucleus Coulomb interactions. The one-electron operator h^{CI} acts on the valence electrons and includes the kinetic term, as well as the core-valence and valence-nucleus Coulomb interactions. The last term accounts for the valence-valence Coulomb interaction.

Decomposing the Hamiltonian and the wave function into the P and Q subspaces,

$$\mathcal{H} = \mathcal{P} \mathcal{H} \mathcal{P} + \mathcal{P} \mathcal{H} \mathcal{Q} + \mathcal{Q} \mathcal{H} \mathcal{P} + \mathcal{Q} \mathcal{H} \mathcal{Q} \quad (2.134)$$

$$\Psi = \mathcal{P}\Psi + \mathcal{Q}\Psi \equiv \Phi + \chi, \quad (2.135)$$

the Schrödinger equation

$$\mathcal{H}\Psi = E\Psi \quad (2.136)$$

can be written in terms of Φ and χ :

$$(\mathcal{P}\mathcal{H}\mathcal{P})\Phi + (\mathcal{P}\mathcal{H}\mathcal{Q})\chi = E\Phi \quad (2.137)$$

$$(\mathcal{Q}\mathcal{H}\mathcal{Q})\chi + (\mathcal{Q}\mathcal{H}\mathcal{P})\Phi = E\chi. \quad (2.138)$$

Next we introduce the resolvent operator in the subspace \mathcal{Q} :

$$\mathcal{R}_{\mathcal{Q}}(E) = (E - \mathcal{Q}\mathcal{H}\mathcal{Q})^{-1}, \quad (2.139)$$

which will allow us to rewrite Eq. 2.138 as

$$\chi = \mathcal{R}_{\mathcal{Q}}(E)(\mathcal{Q}\mathcal{H}\mathcal{P})\Phi. \quad (2.140)$$

We can substitute this expression for χ into Eq. 2.137 to obtain an equation in the subspace \mathcal{P} , with an energy-dependent effective Hamiltonian

$$(\mathcal{P}\mathcal{H}\mathcal{P} + \Sigma(E))\Phi = E\Phi, \quad (2.141)$$

where

$$\Sigma(E) = (\mathcal{P}\mathcal{H}\mathcal{Q})\mathcal{R}_{\mathcal{Q}}(E)(\mathcal{Q}\mathcal{H}\mathcal{P}). \quad (2.142)$$

The orthonormality condition for the wave function then follows from

$$\langle \Phi_i | 1 + (\mathcal{P}\mathcal{H}\mathcal{Q})\mathcal{R}_{\mathcal{Q}}(E_i)\mathcal{R}_{\mathcal{Q}}(E_k)(\mathcal{Q}\mathcal{H}\mathcal{P}) | \Phi_k \rangle = \delta_{ik}. \quad (2.143)$$

Since the operators Σ and $\mathcal{R}_{\mathcal{Q}}$ depend on energy, the Schrödinger equation must be solved iteratively. If we only want the lowest-lying energy levels, then we can neglect the energy dependence and evaluate the operators for some average energy

$E_{\text{avg}} \cong E_i \cong E_k$. In this case, we can express the orthonormality condition in terms of the derivative of $\Sigma(E)$:

$$\langle \Psi_i | 1 - \frac{\partial \Sigma(E)}{\partial E} | \Phi_k \rangle_{E=E_{\text{avg}}} = \delta_{ik}. \quad (2.144)$$

With a properly chosen model space P , the energy derivative can become negligible, in which case the standard CI method can be used to solve Eq. 2.141, provided that the operator $\Sigma(E_{\text{avg}})$ is calculated beforehand with MBPT, and then added to the Hamiltonian. We use Brillouin-Wigner (BW) perturbation theory, resulting in an energy-dependent correction, as opposed to the typical Rayleigh-Schrödinger (RS) approach where the correction is independent of the energy. This is due to some disadvantages of using the RSPT approach, such as a non-symmetric matrix of the CI+MBPT eigenvalue problem due to differences in energy denominators and small denominators for highly excited configurations.

The operator $\Sigma(E)$ described by Eq. 2.142 connects the model subspace P of core electrons to the complementary subspace Q of core-excited states, so it accounts for core-valence correlations. The form of the operator $\Sigma(E)$ depends on the choice of the starting approximation h_0 , which in our case will be the one-electron DF operator given by Eq. 2.59 with central potential $U(r) = V^{N_{\text{DF}}}$, where N_{DF} corresponds to the number of electrons included in the HF self-consistent procedure. Here N_{DF} is chosen such that $N_{\text{core}} \leq N_{\text{DF}} \leq N$, with N being the total number of electrons in the atom or ion.

The DF operator in the many-electron space is given by

$$H_{\text{DF}} = E_{\text{core}} - \sum_{m=1}^{N_{\text{core}}} \epsilon_m b_m^\dagger b_m + \sum_{i>N_{\text{core}}} \epsilon_i a_i^\dagger a_i \equiv E_{\text{core}} + \tilde{H}_{\text{DF}}, \quad (2.145)$$

where $b_m^\dagger = a_m$ and $b_m = a_m^\dagger$ are the creation and annihilation operators of holes in the core, and a_m^\dagger and a_m are creation and annihilation operators, respectively [62].

It follows from Eq. 2.145 that

$$\mathcal{P} \mathcal{H}_{\text{DF}} \mathcal{Q} = \mathcal{Q} \mathcal{H}_{\text{DF}} \mathcal{P} = 0, \quad (2.146)$$

allowing us to write Eq. 2.142 as

$$\begin{aligned}\Sigma(E) &= (\mathcal{P}(\mathcal{H} - \mathcal{H}_{\text{DF}})\mathcal{Q})\mathcal{R}_{\mathcal{Q}}(E)(\mathcal{Q}(\mathcal{H} - \mathcal{H}_{\text{DF}})\mathcal{P}) \\ &= (\mathcal{P}(\mathcal{V} - \mathcal{V}^{\text{NDF}})\mathcal{Q})\mathcal{R}_{\mathcal{Q}}(E)(\mathcal{Q}(\mathcal{V} - \mathcal{V}^{\text{NDF}})\mathcal{P}),\end{aligned}\tag{2.147}$$

where $\mathcal{V} - \mathcal{V}^{\text{NDF}}$ is the residual two-electron Coulomb interaction. Since this expression has the usual MBPT form, we can treat $(\mathcal{V} - \mathcal{V}^{\text{NDF}})$ as a perturbation and expand the resolvent operator:

$$\begin{aligned}\mathcal{R}_{\mathcal{Q}}(E) &\equiv \mathcal{Q}(E - \mathcal{H})^{-1}\mathcal{Q} \\ &= \mathcal{Q}(E - \mathcal{H}_{\text{DF}})^{-1}\mathcal{Q} + \mathcal{Q}(E - \mathcal{H}_{\text{DF}})^{-1}\mathcal{Q}(\mathcal{V} - \mathcal{V}^{\text{NDF}})\mathcal{Q}(E - \mathcal{H}_{\text{DF}})^{-1}\mathcal{Q} + \dots.\end{aligned}\tag{2.148}$$

This allows us to rewrite $\Sigma(E)$ in matrix form as

$$\begin{aligned}\Sigma_{IJ} &= \sum_{M \in \mathcal{Q}} \frac{U_{IM}U_{MJ}}{E - E_M} + \sum_{M, L \in \mathcal{Q}} \frac{U_{IM}U_{ML}U_{LJ}}{(E - E_M)(E - E_L)} + \dots \\ &\equiv \Sigma^{(2)} + \Sigma^{(3)} + \dots.\end{aligned}\tag{2.149}$$

The code package take into account only second-order MBPT corrections. If we substitute $\Sigma^{(2)}$ into Eq. 2.141, we obtain the equation of the combined CI+MBPT method:

$$\sum_{J \in \text{PCI}} \left(H_{IJ} + \sum_{M \in \mathcal{Q}} \frac{U_{IM}U_{MJ}}{E - E_M} \right) C_J = EC_I.\tag{2.150}$$

It is important to note that only core excitations are treated by means of MBPT, and all valence excitations are accounted for directly from the matrix diagonalization. A complete evaluation of the MBPT term in Eq. 2.150 can be found in Ref. [62].

Following Refs. [63, 64], we can divide the core-valence correlations obtained from $\Sigma(E)$ into a one-electron part Σ_1 and a two-electron part Σ_2 . The CI+MBPT equation is written in the form of the standard CI method $(H^{\text{eff}} - E)\Psi = 0$, where $H^{\text{eff}} = H_1 + \Sigma_1 + H_2 + \Sigma_2$. Here, H_1 represents the one-body part of the Hamiltonian and H_2 represents the two-body Coulomb or Coulomb + Breit part of the Hamiltonian.

The second-order matrix elements of the one-electron correlation potential $(\Sigma_1^{(2)})_{yx}$ are given by [64]

$$(\Sigma_1^{(2)})_{yx} = \sum_{mab} \frac{g_{myab} \tilde{g}_{mxab}}{\epsilon_{ab} - \epsilon_{xm} + \tilde{\epsilon}_y - \epsilon_y} + \sum_{mna} \frac{g_{mnxa} \tilde{g}_{mnya}}{\tilde{\epsilon}_y + \epsilon_a - \epsilon_{mn}}, \quad (2.151)$$

and the second-order matrix elements of the two-electron correlation potential $(\Sigma_2^{(2)})_{mnnv}$ are given by [64]

$$\begin{aligned} (\Sigma_2^{(2)})_{mnnv} = & \sum_{cd} \frac{g_{vwcd} g_{mncd}}{\epsilon_{cd} - \epsilon_{mn} + \tilde{\epsilon}_v - \epsilon_v + \tilde{\epsilon}_w - \epsilon_w} \\ & + \left[\sum_{rc} \frac{\tilde{g}_{wrnc} \tilde{g}_{mrvc}}{\tilde{\epsilon}_v + \epsilon_c - \epsilon_{mr} + \tilde{\epsilon}_w - \epsilon_w} + \left(\begin{array}{c} m \iff n \\ v \iff w \end{array} \right) \right], \end{aligned} \quad (2.152)$$

where indices from the beginning of the alphabet a and b range over all occupied core states and indices from the middle of the alphabet m and n range over all possible virtual states, $\epsilon_{ij} = \epsilon_i + \epsilon_j$, the notation $\tilde{g}_{ijkl} = g_{ijkl} - g_{ijlk}$ is used to designate antisymmetrized two-particle matrix elements, and the energies $\tilde{\epsilon}_i$ are chosen to be the DF energy of the lowest orbital for the particular partial wave or approximated in other ways described in Ref [64].

In order to include the Breit interaction in the CI+MBPT method, it is necessary to include Breit corrections to the core potential, and to construct core orbitals from the DHF Hamiltonian with the Coulomb and Breit interactions included. Technically, the Breit interaction is included via one-electron and two-electron radial integrals, where the one-electron integrals describe the interaction of the valence electrons with the core, and the two-electron integrals describe interactions between valence electrons. All integrals depend not only on the potential, but also on the orbitals. It is important to account for the change of the orbitals caused by the inclusion of the Breit interaction. The one-electron integrals must explicitly include Breit, but the two-electron integrals can be calculated with Coulomb potential without Breit. Not including Breit in the two-electron integrals results in a difference on the order of $\sim 10^{-4}$, which introduces errors, which may be negligible in some cases [54]. If the MBPT in residual Coulomb interaction is used to account for the core-valence and core-core correlations, direct

and indirect Breit corrections have to be included in corresponding diagrams. Direct corrections refer to the substitution of the residual Coulomb interaction with the Breit interaction in the MBPT expressions, and the indirect corrections refer to using the DF+Coulomb+Breit equations as a zero-order approximation. Direct correlations are suppressed, and generally neglected altogether, due to huge energy denominators in the largest Breit radial integrals corresponding to virtual excitations from the innermost core shells [54]. The indirect corrections are accounted for simply by including the Breit interaction in the construction of the basis set.

2.1.11 CI+all-order

In this section, we follow Refs. [64, 65] in describing the relativistic all-order method and a method combining configuration interaction with the all-order method (CI+all-order). The relativistic all-order method is a linearized version of the coupled-cluster (CC) method, where all non-linear terms in the expansion of the exponential are omitted. This method was initially designed to treat monovalent systems by including all single and double excitations of the DHF wave functions to all orders of perturbation theory (also known as LCCSD). Extensions that include non-linear terms and valence triple excitations (also known as LCCSDvT) were developed in Refs. [66, 67], but significant cancellations of triples and non-linear terms make the SD version accurate and very efficient to use for most applications. For more complicated systems, a method combining configuration interaction and many-body perturbation theory was developed and described in the previous section. In the CI + all-order approach, corrections to the effective Hamiltonian described in Section 2.1.10 are calculated using the all-order method, in which the effective Hamiltonian contains dominant core-core and core-valence correlation corrections to all orders. The core-core and core-valence corrections are treated in the all-order method with the same accuracy as in the all-order approach for monovalent systems. The CI method is then used to evaluate valence-valence correlations.

We begin our description of the all-order method from the relativistic no-pair DHF Hamiltonian given by Eq. 2.97

$$H_0 = \sum_i \epsilon_i \{a_i^\dagger a_i\}, \quad (2.153)$$

$$V = \frac{1}{2} \sum_{ijkl} g_{ijkl} \{a_i^\dagger a_j^\dagger a_l a_k\} + \sum_{ij} (V_{\text{HF}} - U)_{ij} \{a_i^\dagger a_j\}. \quad (2.154)$$

In the coupled-cluster method, the exact many-body wave function is represented in the form

$$|\Psi\rangle = e^S |\Psi^{(0)}\rangle, \quad (2.155)$$

where $|\Psi^{(0)}\rangle$ is the reference atomic state vector, and S represents an operator for an N -electron atomic state consisting of the contribution from all excitations from the lowest-order state vector $|\Psi^{(0)}\rangle$. Here, $S = S_1 + S_2 + \dots + S_N$ represents one-electron, two-electron, ..., N -electron excitation operators. Note that if all excitations are considered, the full CC expansion would be identical to the full CI expansion. The general cluster operator can be expanded as

$$e^S = 1 + S_1 + \left(S_2 + \frac{1}{2} S_1^2 \right) + \left(S_3 + S_2 S_1 + \frac{1}{3!} S_1^3 \right) + \left(S_4 + S_3 S_1 + \frac{1}{2} S_2^2 + \frac{1}{2} S_2 S_1^2 + \frac{1}{4!} S_1^4 \right) + \dots, \quad (2.156)$$

where the general n -electron excitation operator is defined as

$$S_n = \frac{1}{(n!)^2} \sum_{m_1, m_2, \dots, m_n} \sum_{a_1, a_2, \dots, a_n} \rho_{m_1, m_2, \dots, m_n, a_1, a_2, \dots, a_n} \{a_{m_1}^\dagger a_{m_2}^\dagger \dots a_{m_n}^\dagger a_{a_n}^\dagger a_{a_{n-1}}^\dagger \dots a_{a_1}^\dagger\}. \quad (2.157)$$

Here the indices a_i with $i = 1, 2, \dots, n$ range over core states, and the indices m_i with $i = 1, 2, \dots, n$ range over all possible virtual states. Compared to the full CI expansion, the CC contributions from single excitations come from the term S_1 , double excitations come from the terms in the first parenthesis ($S_2 + \frac{1}{2} S_1^2$), triple excitations from the terms in the second parenthesis ($S_3 + S_2 S_1 + \frac{1}{3!} S_1^3$), and so on.

In the all-order method, we omit all non-linear terms in the expansion of the exponential, such that the all-order wave function takes the form

$$|\Psi\rangle = \{1 + S_1 + S_2 + S_3 + \cdots + S_N\}|\Psi^{(0)}\rangle. \quad (2.158)$$

Restricting the sum in Eq. 2.158 to single, double, and valence triple excitations yields the following expansion for the state vector of a monovalent atom in state v :

$$\begin{aligned} |\Psi_v\rangle = & \left[1 + \sum_{ma} \rho_{ma} a_m^\dagger a_a + \frac{1}{2} \sum_{mnab} \rho_{mnab} a_m^\dagger a_n^\dagger a_b a_a + \sum_{m \neq v} \rho_{mv} a_m^\dagger a_v \right. \\ & \left. + \sum_{mna} \rho_{mnva} a_m^\dagger a_n^\dagger a_a a_v + \frac{1}{6} \sum_{mnrab} \rho_{mnrwab} a_m^\dagger a_n^\dagger a_r^\dagger a_b a_a a_v \right] |\Psi_v^{(0)}\rangle, \end{aligned} \quad (2.159)$$

where the indices m , n , and r range over all possible virtual states, while indices a and b range over all occupied core states. The lowest-order wave function is given by

$$|\Psi_v^{(0)}\rangle = a_v^\dagger |\Psi_C\rangle, \quad (2.160)$$

where $|\Psi_C\rangle$ is the zeroth-order frozen-core wave function. The quantities ρ_{ma} and ρ_{mv} are single-excitation coefficients for core and valence electrons, respectively; ρ_{mnab} and ρ_{mnva} are core and valence double-excitation coefficients, respectively; and ρ_{mnrwab} are the valence triple excitation coefficients. In the single-double (LCCSD) implementation of the all-order method, only single and double excitations are included. In the single, double, and partial triple (LCCSDpT/LCCSDvT) variant of the all-order method, valence triple excitations are included perturbatively, as described in [65].

To derive the equations for the excitation coefficients of the LCCSD equations for a monovalent system, we substitute the state vector $|\Psi_v\rangle$ given by Eq. 2.159, omitting the last term, into the many-body Schrödinger equation $H|\Psi_v\rangle = E|\Psi_v\rangle$. We then project the Schrödinger equation onto the zeroth-order wave function $|\Psi_C\rangle$ and onto the functions obtained by operating the cluster operators on the zeroth-order frozen-core wave function. Terms on the left and right sides of the equation are then matched

based on the number and type of operators they contain, as done in perturbation theory. The resulting SD all-order equations for valence coefficients are

$$(\epsilon_v - \epsilon_m + \delta E_v) \rho_{mv} = \sum_{bn} \tilde{g}_{mbvn} \rho_{nb} + \sum_{bnr} g_{mbnr} \tilde{\rho}_{nrvb} - \sum_{bcn} g_{bcvn} \tilde{\rho}_{mnbc}, \quad (2.161)$$

$$\begin{aligned} (\epsilon_{vn} - \epsilon_{mn} + \delta E_v) \rho_{mnvb} &= g_{mnvb} + \sum_{cd} g_{cdvb} \rho_{mncd} + \sum_{rs} g_{mnrs} \rho_{rsvb} \\ &= \left[\sum_r g_{mnrb} \rho_{rv} - \sum_c g_{cnvb} \rho_{mc} + \sum_{rc} \tilde{g}_{cnrb} \tilde{\rho}_{mrvc} \right] + \left[\begin{array}{c} v \leftrightarrow b \\ m \leftrightarrow n \end{array} \right], \end{aligned} \quad (2.162)$$

where $\delta E_v = E_v - \epsilon_v$ is the valence correlation energy, $\epsilon_{ij} = \epsilon_i + \epsilon_j$, the notation $\tilde{g}_{ijkl} = g_{ijkl} - g_{ijlk}$ is used to designate anti-symmetrized two-particle matrix elements, and $\tilde{\rho}_{mnvb} = \rho_{mnvb} - \rho_{nmvb}$. The correlation correction to the energy of the state v is given in terms of the excitation coefficients by

$$\delta E_v = \sum_{ma} \tilde{g}_{vavm} \rho_{ma} + \sum_{mab} g_{abvm} \tilde{\rho}_{mvab} + \sum_{mna} g_{vbmn} \tilde{\rho}_{mnvb}. \quad (2.163)$$

Equations for the core excitation coefficients ρ_{ma} and ρ_{mnab} are obtained from the above equations by replacing the valence index v by a core index a and removing δE_v from the left-hand side of the equations. Equations for the correlation energy and all excitation coefficients are solved iteratively, where each iteration picks up correlation terms corresponding to the next higher order term in perturbation theory until the correlation energy converges to a sufficient numerical accuracy. Therefore, the all-order approach includes dominant MBPT terms to all orders.

Matrix elements for the one-body operator $Z = \sum_{ij} z_{ij} a_i^\dagger a_j$ are obtained in the framework of the all-order method as

$$Z_{wv} = \frac{\langle \Psi_w | Z | \Psi_v \rangle}{\sqrt{\langle \Psi_v | \Psi_v \rangle \langle \Psi_w | \Psi_w \rangle}}, \quad (2.164)$$

where $|\Psi_v\rangle$ and $|\Psi_w\rangle$ are given by the expansion in Eq. 2.159. In the SD approximation, the resulting expression for the one-body matrix element consists of the sum of the DF

matrix element z_{wv} and 20 other terms that are linear or quadratic functions of the excitation coefficients. The advantage of this approach is that this expression does not depend on the nature of the operator Z , only on its rank and parity.

The complexity of the all-order method for matrix elements increases drastically with the number of valence electrons. For divalent systems, the expression contains several hundred terms, instead of the 20 terms in the corresponding monovalent expression. Therefore, it is difficult to extend the all-order method to the case of complicated systems with more than 5-6 valence electrons.

To combine the all-order method with CI for calculating properties of atoms with a few valence electrons, we begin by expressing the all-order equations (Eqs. 2.161 – 2.163) in terms of matrix elements of Σ_1 and Σ_2 , and explicitly including energy dependence. We also need to add an all-order equation for the excitation coefficients ρ_{mnvw} to obtain Σ_2 .

Σ_1 and Σ_2 are essentially the all-order excitation coefficients ρ_{mv} and ρ_{mnvw} multiplied by the appropriate energy differences,

$$\begin{aligned}\Sigma_{ma} &= \rho_{ma} (\epsilon_a - \epsilon_m), \\ \Sigma_{mnab} &= \rho_{mnab} (\epsilon_{ab} - \epsilon_{mn}), \\ \Sigma_{mnva} &= \rho_{mnva} (\tilde{\epsilon}_v + \epsilon_a - \epsilon_{mn}), \\ \Sigma_{mv} &\equiv (\Sigma_1)_{mv} = \rho_{mv} (\tilde{\epsilon}_v - \epsilon_m), \\ \Sigma_{mnvw} &\equiv (\Sigma_2)_{mnvw} = \rho_{mnvw} (\tilde{\epsilon}_a + \tilde{\epsilon}_w - \epsilon_{mn}).\end{aligned}$$

The quantities Σ_{ma} , Σ_{mnab} , and Σ_{mnva} are used in the all-order iterative procedure but do not explicitly appear in the effective Hamiltonian. The excitation coefficients ρ_{ma} and ρ_{mnab} are multiplied by the appropriate energy differences to obtain the terms Σ_{ma} and Σ_{mnab} , and other all-order equations are re-written in terms of Σ , while terms that will otherwise be double counted by the CI part of the calculations are

removed. We obtain the following set of equations by writing the LCCSD equations given by Eq. 2.161 in terms of Σ :

$$\Sigma_{mv} \equiv (\Sigma_1)_{mv} = \sum_{nb} \frac{\tilde{g}_{mbvn}\Sigma_{nb}}{\epsilon_{bn} + \tilde{\epsilon}_v - \epsilon_v} - \sum_{bcn} \frac{\tilde{g}_{bcvn}\Sigma_{mnbc}}{\epsilon_{bc} - \epsilon_{mn} + \tilde{\epsilon}_v - \epsilon_v} + \sum_{bnr} \frac{\tilde{g}_{mbnr}\Sigma_{nrvb}}{\tilde{\epsilon}_v + \epsilon_b - \epsilon_{nr}}, \quad (2.165)$$

$$\begin{aligned} \Sigma_{mnvb} &= g_{mnvb} + \sum_{cd} \frac{g_{cdvb}\Sigma_{mncd}}{\epsilon_{cd} - \epsilon_{mn} + \tilde{\epsilon}_v - \epsilon_v} + \sum_{rs} \frac{g_{mnrs}\Sigma_{rsvb}}{\tilde{\epsilon}_v + \epsilon_b - \epsilon_{rs}} \\ &- \sum_c \frac{g_{cnvb}\Sigma_{mc}}{\epsilon_c - \epsilon_m + \tilde{\epsilon}_v - \epsilon_v} + \sum_r \frac{g_{mnvr}\Sigma_{rb}}{\epsilon_b - \epsilon_r + \tilde{\epsilon}_v - \epsilon_v} - \sum_c \frac{g_{mcvb}\Sigma_{nc}}{\epsilon_c - \epsilon_n + \tilde{\epsilon}_v - \epsilon_v} \\ &+ \sum_{cr} \frac{\tilde{g}_{cnrb}\Sigma_{mrvc}}{\tilde{\epsilon}_v + \epsilon_c - \epsilon_{mr}} - \sum_{cr} \frac{g_{cnrb}\Sigma_{rmvc}}{\tilde{\epsilon}_v + \epsilon_c - \epsilon_{mr}} - \sum_{cr} \frac{g_{mcrb}\Sigma_{rnvc}}{\tilde{\epsilon}_v + \epsilon_c - \epsilon_{nr}} \\ &+ \sum_{cr} \frac{\tilde{\epsilon}_{mcvr}\Sigma_{rncb}}{\epsilon_{cb} - \epsilon_{nr} + \tilde{\epsilon}_v - \epsilon_v} - \sum_{cr} \frac{g_{mcvr}\Sigma_{nrcb}}{\epsilon_{cb} - \epsilon_{nr} + \tilde{\epsilon}_v - \epsilon_v} - \sum_{cr} \frac{g_{cnvr}\Sigma_{mrcb}}{\epsilon_{cb} - \epsilon_{nr} + \tilde{\epsilon}_v - \epsilon_v}, \end{aligned} \quad (2.166)$$

$$\begin{aligned} \Sigma_{mnvw} \equiv (\Sigma_2)_{mnvw} &= \sum_{cd} \frac{g_{cdvw}\Sigma_{mncd}}{\epsilon_{cd} - \epsilon_{mn} + \tilde{\epsilon}_v - \epsilon_v + \tilde{\epsilon}_w - \epsilon_w} - \sum_c \frac{g_{cnvw}\Sigma_{mc}}{\epsilon_c - \epsilon_m + \tilde{\epsilon}_v - \epsilon_v + \tilde{\epsilon}_w - \epsilon_w} \\ &- \sum_c \frac{g_{mcvw}\Sigma_{nc}}{\epsilon_c - \epsilon_n + \tilde{\epsilon}_v - \epsilon_v + \tilde{\epsilon}_w - \epsilon_w} + \sum_{cr} \frac{\tilde{g}_{cnrw}\Sigma_{mrvc}}{\tilde{\epsilon}_v + \epsilon_c - \epsilon_{mr} + \tilde{\epsilon}_w - \epsilon_w} \\ &- \sum_{cr} \frac{g_{cnrw}\Sigma_{rmvc}}{\tilde{\epsilon}_v + \epsilon_c - \epsilon_{mr} + \tilde{\epsilon}_w - \epsilon_w} - \sum_{cr} \frac{g_{mcrw}\Sigma_{rnvc}}{\tilde{\epsilon}_v + \epsilon_c - \epsilon_{nr} + \tilde{\epsilon}_w - \epsilon_w} \\ &+ \sum_{cr} \frac{\tilde{g}_{mcvr}\Sigma_{rnvw}}{\epsilon_c + \tilde{\epsilon}_w - \epsilon_{nr} + \tilde{\epsilon}_v - \epsilon_v} - \sum_{cr} \frac{g_{mcvr}\Sigma_{rnvc}}{\epsilon_c + \tilde{\epsilon}_w - \epsilon_{nr} + \tilde{\epsilon}_v - \epsilon_v} \\ &- \sum_{cr} \frac{g_{cnvr}\Sigma_{rmvc}}{\epsilon_c + \tilde{\epsilon}_w - \epsilon_{mr} + \tilde{\epsilon}_v - \epsilon_v} \end{aligned} \quad (2.167)$$

The energy denominators are explicitly written out and the energy dependence is introduced in the formalism of the CI+MBPT approach. Next, we outline the CI+all-order method as used in this work [65]

1. A finite basis set is generated in a spherical cavity of radius R with which all calculations will be carried out. The terms $(\Sigma_1)_{vw}$ and $(\Sigma_2)_{mnvw}$, where m, n, v, w are any basis set functions, are then generated under second-order MBPT.

2. The all-order core ρ_{ma} and ρ_{mnab} excitation coefficients are obtained by the iterative solution of the corresponding equations in the appropriate potential. The core correlation energy is used as a convergence parameter and is generally required to converge to $10^{-5} - 10^{-6}$ relative accuracy. The core excitation coefficients are multiplied by the appropriate denominators as described earlier to obtain Σ_{ma} and Σ_{mnab} after the iterations are complete.
3. The core quantities Σ_{ma} and Σ_{mnab} are used to obtain Σ_{mv} and Σ_{mnva} by an iterative procedure for a large number of excited m , n , and v orbitals. The valence correlation energy for the state v is used as a convergence parameter here. The iterations of excitation coefficients result in the summation of the relevant classes of MBPT terms to all orders.
4. The all-order expression for $(\Sigma_2)_{mnvw}$ corrections to the effective Hamiltonian is calculated with previously stored fully converged values of Σ_{ma} , Σ_{mnab} , and Σ_{mnvb} .
5. CI calculations are carried out to generate accurate wave functions with the effective Hamiltonian constructed using Σ_1 and Σ_2 obtained in the previous steps in the same manner as in CI+MBPT described in Section 2.1.10.
6. The resulting wave functions are used to obtain various matrix elements and derived quantities.

2.1.12 Valence perturbation theory

Valence perturbation theory is discussed in great detail in [68] and will be briefly introduced here. It is a method for approximating and optimizing the CI space using weights of configurations. As usual, the goal is to find solutions of the many-body Schrödinger equation

$$H\Psi_n = E_n\Psi_n, \quad (2.168)$$

where E_n is the energy of the n -th level and Ψ_n is the corresponding wave function, which is described as a linear combination of Slater determinants

$$|\Psi_n\rangle = \sum_{i=1}^N c_i^{(n)} |\Phi_i\rangle, \quad (2.169)$$

where N corresponds to the dimensionality of the valence configuration space and Φ_i are Slater determinants constructed from basis orbitals. The basis orbitals are found by

solving HFD equations for the core and valence orbitals and then constructing virtual orbitals using B-splines.

Substituting Eq. 2.169 into Eq. 2.168 and varying over the coefficients $c_i^{(n)}$, we obtain the CI eigenvalue equation

$$\sum_k H_{ik} C_k^{(n)} = E_n C_i^{(n)}, \quad (2.170)$$

or in the matrix form

$$H\Phi_n = E_n\Phi_n, \quad (2.171)$$

where H is the energy matrix and $\Phi_n = (c_1^{(n)}, c_2^{(n)}, \dots, c_N^{(n)})$ is the desired wave function described in the basis of Slater determinants.

In valence perturbation theory, the valence space is divided into two subspaces: $N = N_0 + N_1$, where a smaller subspace of dimensionality $N_0 \times N_0$ is accounted for using CI and the complementary subspace of dimensionality $N_1 \times N_1$ is accounted for using PT. The Hamiltonian is rewritten in the form

$$H = H_0 + H_1, \quad (2.172)$$

where H_0 and H_1 correspond to the subspaces defined above for CI and PT, respectively. Here, H_0 is represented as

$$H_0 = H'_0 + D \quad (2.173)$$

where H'_0 is the upper left block of dimensionality $N_0 \times N_0$, and D is the diagonal of the block of dimensionality $N_1 \times N_1$ with elements $(H_{N_0+1N_0+1}, \dots, H_{NN})$. First, we solve the CI matrix equation

$$H_0\Phi_n^0 = E_n^0\Phi_n^0, \quad (2.174)$$

where $\Phi_n^0 = ((c_1^{(n)}, c_2^{(n)}, \dots, c_{N_0}^{(n)}), 0, \dots, 0)$ for $n \leq N_0$ and $\Phi_n^0 = (0, \dots, 0, 1, 0, \dots, 0)$ for $n > N_0$, where the unit occupies the n -th position. Solving Eq. 2.174, we find the energies and wave functions to initial approximation.

The weight of configurations is determined by the expression

$$W_k = \sum_{i=1}^{N_k} |c_i^{(k)}|^2, \quad (2.175)$$

where N_k is the number of determinants in the k th configuration and $c_i^{(k)}$ are the corresponding coefficients. Only weights above a certain threshold (typically above $10^{-5} - 10^{-6}$) are kept in the H'_0 subspace. All configurations with weights below the threshold are taken into account using PT in the next step.

After the CI matrix equation has been solved in the H_0 subspace, the corrections from the H_1 complementary subspace are added using PT. The first-order correction to the unperturbed energy E^0 is given by

$$E_i^{(1)} = \langle \Phi_i^0 | H_1 | \Phi_i^0 \rangle = 0, \quad (2.176)$$

and the second-order correction to the unperturbed energy E^0 is given by

$$E_i^{(2)} = \sum_{k=N_0+1}^N \frac{\langle \Phi_i^0 | H_1 | \Phi_k^0 \rangle \langle \Phi_k^0 | H_1 | \Phi_i^0 \rangle}{E_i^0 - E_k^0}, \quad (2.177)$$

where E_k^0 is the k -th element of the diagonal D . The first-order correction to the wave function is given by

$$\Phi_i^{(1)} = \sum_{k=N_0+1}^N \frac{\langle \Phi_k^0 | H_1 | \Phi_i^0 \rangle}{E_i^0 - E_k^0} | \Phi_k^0 \rangle. \quad (2.178)$$

All second-order corrections are taken into account and added to the energy calculated from CI to obtain the total energy, $E = E_0 + E_1$. The first-order corrections to the wave functions are stored for use in subsequent CI calculations.

2.2 Radiative transitions

In order to determine transition rates, lifetimes, and branching ratios of certain transitions, we need to study radiative transitions. Lifetimes are obtained by summing over all possible radiative transition rates:

$$\tau = \frac{1}{\sum_i A_i}. \quad (2.179)$$

The value of the branching ratios for a particular transition is determined as a ratio of the respective transition rate value and the sum of all possible radiative transition rates that are used to determine the lifetimes. The density matrix formalism is useful here as it greatly simplifies the treatment of transitions involving multiple states.

2.2.1 The density matrix formalism

We have thus far described the quantum state of a particle by a wave function $\Psi(\mathbf{x})$ in coordinate and spin space. Here, we will consider an alternative representation of the quantum state, called the density matrix. The density, or transition matrix was originally introduced in quantum statistical mechanics to describe a system for which the state was incompletely specified. Although describing a quantum system with the density matrix is equivalent to using the wave function, it has been shown that density matrices are more practical for certain time-dependent problems [69]. The formalism of the density, or transition matrix allows us to express the matrix elements between many-electron states using one-electron matrix elements. Here we follow Ref. [70] in introducing the density matrix formalism.

The general N -order density matrix is formally defined as

$$\gamma_N(\mathbf{x}'_1 \mathbf{x}'_2 \dots \mathbf{x}'_N, \mathbf{x}_1 \mathbf{x}_2 \dots \mathbf{x}_N) \equiv \Psi_N^*(\mathbf{x}'_1, \mathbf{x}'_2, \dots, \mathbf{x}'_N) \Psi_N(\mathbf{x}_1, \mathbf{x}_2, \dots, \mathbf{x}_N), \quad (2.180)$$

where $\mathbf{x}_i = \{\mathbf{r}_i, \sigma_i\}$ denote spatial and spin variables. Note that the density matrix contains two sets of independent quantities, $\{\mathbf{x}'_i\}$ and $\{\mathbf{x}_i\}$, that gives γ_N a numerical value. Equivalently, the general N -order density matrix can be viewed as the coordinate representation of the density operator,

$$\hat{\gamma}_N = |\Psi_N\rangle\langle\Psi_N| \quad (2.181)$$

since

$$\begin{aligned} \langle \mathbf{x}'_1 \mathbf{x}'_2 \dots \mathbf{x}'_N | \hat{\gamma}_N | \mathbf{x}_1 \mathbf{x}_2 \dots \mathbf{x}_N \rangle &= \langle \mathbf{x}'_1 \mathbf{x}'_2 \dots \mathbf{x}'_N | \Psi_N \rangle \langle \Psi_N | \mathbf{x}_1 \mathbf{x}_2 \dots \mathbf{x}_N \rangle \\ &= \Psi_N^*(\mathbf{x}'_1, \mathbf{x}'_2, \dots, \mathbf{x}'_N) \Psi_N(\mathbf{x}_1, \mathbf{x}_2, \dots, \mathbf{x}_N) \\ &= \gamma_N(\mathbf{x}'_1 \mathbf{x}'_2 \dots \mathbf{x}'_N, \mathbf{x}_1 \mathbf{x}_2 \dots \mathbf{x}_N). \end{aligned} \quad (2.182)$$

Note that $\hat{\gamma}_N$ can also be thought of as the projection operator onto the state Ψ_N . We then have for normalized Ψ_N ,

$$\text{Tr } \hat{\gamma}_N = \int \Psi_N^*(\mathbf{x}^N) \Psi_N(\mathbf{x}^N) d\mathbf{x}^N = 1,$$

where \mathbf{x}^N stands for the set $\{\mathbf{x}_i\}_{i=1}^N$. The trace of an operator \hat{A} is defined as the sum of the diagonal elements of the matrix representing \hat{A} , or the integral if the representation is continuous as above. It can also be verified that

$$\langle \hat{A} \rangle = \text{Tr} (\hat{\gamma}_N \hat{A}) = \text{Tr} (\hat{A} \hat{\gamma}_N).$$

From this, the density operator $\hat{\gamma}_N$ can be seen to carry the same information as the N -electron wave function Ψ_N . Note that while Ψ_N is defined only up to an arbitrary phase factor, $\hat{\gamma}_N$ for the state Ψ_N is unique, positive semi-definite and Hermitian. The state of the system is said to be *pure* if it can be described by a wave function, and *mixed* if it cannot. A system in a mixed state can be characterized by a probability distribution over all accessible pure states. If we set $\mathbf{x}'_i = \mathbf{x}_i$ for all i , we get the diagonal elements of the density matrix,

$$\gamma_N (\mathbf{x}_1 \mathbf{x}_2 \dots \mathbf{x}_N) \equiv \Psi_N^* (\mathbf{x}_1, \mathbf{x}_2, \dots, \mathbf{x}_N) \Psi_N (\mathbf{x}_1, \mathbf{x}_2, \dots, \mathbf{x}_N) = |\Psi_N (\mathbf{x}_1, \mathbf{x}_2, \dots, \mathbf{x}_N)|^2,$$

which is the N -order density matrix for a pure state. Note that this is also the probability distribution associated with a solution of the Schrödinger equation. We can express the Schrödinger equation in the density-matrix formalism by taking the time derivative of the density operator, and using Hermiticity and commutation relations to obtain

$$\begin{aligned} \frac{\partial}{\partial t} \hat{\gamma}_N &= \left(\frac{\partial}{\partial t} |\Psi_N\rangle \right) \langle \Psi_N| + |\Psi_N\rangle \left(\frac{\partial}{\partial t} \langle \Psi_N| \right) \\ &= \left(\frac{\hat{H}}{i\hbar} |\Psi_N\rangle \right) \langle \Psi_N| - |\Psi_N\rangle \left(\frac{\hat{H}}{i\hbar} \langle \Psi_N| \right) \end{aligned} \quad (2.183)$$

$$i\hbar \frac{\partial}{\partial t} \hat{\gamma}_N = [\hat{H}, \hat{\gamma}_N] \quad (2.184)$$

This equation is called the *von Neumann* equation and describes how the density operator evolves in time. We can generalize the density operator $\hat{\gamma}_N$ to the ensemble density operator

$$\hat{\Gamma} = \sum_i p_i |\Psi_i\rangle \langle \Psi_i|, \quad (2.185)$$

where p_i is the probability of the system being found in the state Ψ_i , and the sum is over the complete set of all accessible pure states. The coefficients p_i have the following properties since they are probabilities:

$$p_i \geq 0, \quad \sum_i p_i = 1.$$

We can then rewrite Eq. 2.184 in terms of the ensemble density matrix to obtain

$$i\hbar \frac{\partial}{\partial t} \hat{\Gamma} = [\hat{H}, \hat{\Gamma}], \quad (2.186)$$

which is true if $\hat{\Gamma}$ only involves states with the same number of particles, as is true in the canonical ensemble. This equation is also known as the *von Neumann* equation, the quantum mechanical analog of the Liouville equation. For stationary states, $\hat{\Gamma}$ is independent of time, which means that

$$[\hat{H}, \hat{\Gamma}] = 0,$$

implying that \hat{H} and $\hat{\Gamma}$ share the same eigenvectors.

The Hamiltonian operator, Eq. 2.2, is a sum of two symmetric one-electron operators and a symmetric two-electron operator, independent on spin. Along with the fact that the wave functions $\{\Psi_i\}_{i=0}^N$ are antisymmetric, the expectation values of the density operator can be systematically simplified by integrating the probability densities over $N - 2$ of its variables, giving rise to concepts of reduced density matrix and spinless density matrices.

The reduced density matrix of order k is defined as

$$\begin{aligned} \gamma_k(\mathbf{x}'_1 \mathbf{x}'_2 \dots \mathbf{x}'_k, \mathbf{x}_1 \mathbf{x}_2 \dots \mathbf{x}_k) = \\ \binom{N}{k} \int \dots \int \gamma(\mathbf{x}'_1 \mathbf{x}'_2 \dots \mathbf{x}'_k \mathbf{x}_{k+1} \dots \mathbf{x}_N, \mathbf{x}_1 \mathbf{x}_2 \dots \mathbf{x}_k \dots \mathbf{x}_N) d\mathbf{x}_{k+1} \dots d\mathbf{x}_N, \end{aligned} \quad (2.187)$$

where $\binom{N}{k}$ is a binomial coefficient, and γ_N is defined by Eq. 2.180. This is also known as taking the partial trace of the density matrix. For example, the first-order density matrix γ_1 is defined as

$$\gamma_1(\mathbf{x}'_1, \mathbf{x}_1) = N \int \dots \int \Psi^*(\mathbf{x}'_1 \mathbf{x}_2 \dots \mathbf{x}_N) \Psi(\mathbf{x}_1 \mathbf{x}_2 \dots \mathbf{x}_N) d\mathbf{x}_2 \dots d\mathbf{x}_N \quad (2.188)$$

and normalizes to

$$\text{Tr } \gamma_1(\mathbf{x}'_1, \mathbf{x}_1) = \int \gamma_1(\mathbf{x}_1, \mathbf{x}_1) d\mathbf{x}_1 = N.$$

Similarly, the second-order density matrix γ_2 is defined as

$$\gamma_2(\mathbf{x}'_1 \mathbf{x}'_2, \mathbf{x}_1 \mathbf{x}_2) = \frac{N(N-1)}{2} \int \cdots \int \Psi^*(\mathbf{x}'_1 \mathbf{x}'_2 \mathbf{x}_3 \cdots \mathbf{x}_N) \Psi(\mathbf{x}_1 \mathbf{x}_2 \mathbf{x}_3 \cdots \mathbf{x}_N) d\mathbf{x}_3 \cdots d\mathbf{x}_N \quad (2.189)$$

and normalizes to the number of electron pairs

$$\text{Tr } \gamma_2(\mathbf{x}'_1 \mathbf{x}'_2, \mathbf{x}_1 \mathbf{x}_2) = \iint \gamma_2(\mathbf{x}_1 \mathbf{x}_2, \mathbf{x}_1 \mathbf{x}_2) d\mathbf{x}_1 d\mathbf{x}_2 = \frac{N(N-1)}{2}.$$

The reduced density matrices γ_1 and γ_2 just defined are coordinate-space representations of operators $\hat{\gamma}_1$ and $\hat{\gamma}_2$, acting on the one- and two-particle Hilbert spaces, respectively. We can express the one-particle operator in terms of its eigenvalues and eigenvectors

$$\hat{\gamma}_1 = \sum_i n_i |\psi_i\rangle \langle \psi_i|,$$

where the eigenvalues n_i are the occupation numbers and the eigenvectors ψ_i are one-electron orbitals. Similarly, the two-particle operator can be expressed as

$$\hat{\gamma}_2 = \sum_i g_i |\theta_i\rangle \langle \theta_i|,$$

where the eigenvalues g_i are the occupation numbers and the eigenvectors θ_i are two-electron functions called geminals. It also follows from $n_i \geq 0$ and $g_i \geq 0$, that n_i is proportional to the probability of the one-electron state ψ_i being occupied and g_i is proportional to the probability of the two-electron state θ_i being occupied, after comparing these two operators with Eq. 2.185.

Now let us consider the expectation values of one- and two-electron operators with an antisymmetric N -body wave function Ψ . For a one-electron operator

$$\hat{O}_1 = \sum_{i=1}^N O_1(x_i, x'_i),$$

we have

$$\langle \hat{O}_1 \rangle = \text{Tr} (\hat{O}_1 \gamma_N) = \int O_1(\mathbf{x}_1 \mathbf{x}'_1) \gamma_1(\mathbf{x}'_1, \mathbf{x}_1) d\mathbf{x}_1 d\mathbf{x}'_1. \quad (2.190)$$

If the one-electron operator is local, i.e. $O_1(\mathbf{r}', \mathbf{r}) = O_1(\mathbf{r})\delta(\mathbf{r}' - \mathbf{r})$, we can conventionally write down only the diagonal part:

$$\langle \hat{O}_1 \rangle = \text{Tr}(\hat{O}_1 \gamma_N) = \int [O_1(\mathbf{x}_1) \gamma_1(\mathbf{x}'_1, \mathbf{x}_1)]_{\mathbf{x}'_1 = \mathbf{x}_1} d\mathbf{x}_1.$$

Similarly, if the two-electron operator is local, we have

$$\hat{O}_2 = \sum_{i < j}^N O_2(x_i, x_j)$$

and the corresponding expectation value

$$\langle \hat{O}_2 \rangle = \text{Tr}(\hat{O}_2 \gamma_N) = \int \int [O_2(\mathbf{x}_1, \mathbf{x}_2) \gamma_2(\mathbf{x}'_1, \mathbf{x}'_2, \mathbf{x}_1, \mathbf{x}_2)]_{\mathbf{x}'_1 = \mathbf{x}_1, \mathbf{x}'_2 = \mathbf{x}_2} d\mathbf{x}_1 d\mathbf{x}_2.$$

We thus obtain for the expectation value of the Hamiltonian, Eq. 2.2, in terms of density matrices

$$\begin{aligned} E &= \text{Tr}(\hat{H} \hat{\gamma}_N) = E[\gamma_1, \gamma_2] \\ &= \int \left[\left(-\frac{1}{2} \nabla_1^2 + v(\mathbf{r}_1) \right) \gamma_1(\mathbf{x}'_1, \mathbf{x}_1) \right]_{\mathbf{x}'_1 = \mathbf{x}_1} d\mathbf{x}_1 + \iint \frac{1}{|\mathbf{r}_1 - \mathbf{r}_2|} \gamma_2(\mathbf{x}_1 \mathbf{x}_2, \mathbf{x}_1 \mathbf{x}_2) d\mathbf{x}_1 d\mathbf{x}_2. \end{aligned} \quad (2.191)$$

We can further simplify this result by integrating over the spin variables.

The first-order and second-order spinless density matrices are defined by

$$\begin{aligned} \rho_1(\mathbf{r}'_1, \mathbf{r}_1) &= \sum_{\sigma_1 \sigma'_1} \gamma_1(\mathbf{r}'_1 \sigma'_1, \mathbf{r}_1 \sigma_1) \\ &= N \sum_{\sigma_1 \sigma'_1} \int \cdots \int \Psi^*(\mathbf{r}'_1 \sigma'_1, \mathbf{x}_2, \dots, \mathbf{x}_N) \Psi(\mathbf{r}_1 \sigma_1, \mathbf{x}_2, \dots, \mathbf{x}_N) d\mathbf{x}_2 \cdots d\mathbf{x}_N \end{aligned} \quad (2.192)$$

and

$$\begin{aligned} \rho_2(\mathbf{r}'_1 \mathbf{r}'_2, \mathbf{r}_1 \mathbf{r}_2) &= \sum_{\sigma_1 \sigma'_1, \sigma_2 \sigma'_2} \gamma_2(\mathbf{r}'_1 \sigma'_1 \mathbf{r}'_2 \sigma'_2, \mathbf{r}_1 \sigma_1 \mathbf{r}_2 \sigma_2) \\ &= \frac{N(N-1)}{2} \sum_{\sigma_1 \sigma'_1, \sigma_2 \sigma'_2} \int \cdots \int \Psi^*(\mathbf{r}'_1 \sigma'_1, \mathbf{r}'_2 \sigma'_2, \mathbf{x}_3, \dots, \mathbf{x}_N) \Psi(\mathbf{r}_1 \sigma_1, \mathbf{r}_2 \sigma_2, \mathbf{x}_3, \dots, \mathbf{x}_N) d\mathbf{x}_3 \cdots d\mathbf{x}_N. \end{aligned} \quad (2.193)$$

We can introduce a shorthand notation for the diagonal elements of ρ_1 ,

$$\rho_1(\mathbf{r}_1) = \rho_1(\mathbf{r}_1, \mathbf{r}_1) = N \sum_{\sigma_1} \int \cdots \int |\Psi(\mathbf{r}, \sigma)|^2 d\mathbf{x}_2 \cdots d\mathbf{x}_N$$

and similarly for ρ_2 ,

$$\rho_2(\mathbf{r}_1, \mathbf{r}_2) = \rho_2(\mathbf{r}_1 \mathbf{r}_2, \mathbf{r}_1 \mathbf{r}_2) = \frac{N(N-1)}{2} \sum_{\sigma_1 \sigma_2} \int \cdots \int |\Psi(\mathbf{r}, \sigma)|^2 d\mathbf{x}_3 \cdots d\mathbf{x}_N.$$

Note that from the above definitions, we can express the first-order density matrix in terms of the second-order density matrix

$$\begin{aligned} \rho(\mathbf{r}'_1, \mathbf{r}_1) &= \frac{2}{N-1} \int \rho_2(\mathbf{r}'_1 \mathbf{r}_2, \mathbf{r}_1 \mathbf{r}_2) d\mathbf{r}_2, \\ \rho(\mathbf{r}_1) &= \frac{2}{N-1} \int \rho_2(\mathbf{r}_1, \mathbf{r}_2) d\mathbf{r}_2. \end{aligned}$$

The expectation value of the Hamiltonian, Eq. 2.191, in terms of density matrices now becomes

$$\begin{aligned} E &= E[\rho_1(\mathbf{r}'_1, \mathbf{r}_1), \rho_2(\mathbf{r}_1, \mathbf{r}_2)] \\ &= \int \left[-\frac{1}{2} \nabla^2 \rho_1(\mathbf{r}', \mathbf{r}) \right]_{\mathbf{r}'=\mathbf{r}} d\mathbf{r} + \int v(\mathbf{r}) \rho(\mathbf{r}) + \iint \frac{1}{|\mathbf{r}_1 - \mathbf{r}_2|} \rho_2(\mathbf{r}_1, \mathbf{r}_2) d\mathbf{r}_1 d\mathbf{r}_2, \end{aligned} \tag{2.194}$$

where the three terms represent the electronic kinetic energy, the electron-nucleus potential energy, and the electron-electron potential energy, respectively. Note that since we can express the first-order density matrix in terms of the second-order, only the second-order density matrix is needed for the expectation value of the Hamiltonian.

When calculating the matrix elements of one-electron operators between many-electron states, the formalism of the density, or transition density matrix allows us to express the matrix elements between many-electron states in terms of one-electron matrix elements. Let us consider the matrix element $\langle J'M' | T_q^L | JM \rangle$, where $|JM\rangle$ and $|J'M'\rangle$ are the many-electron states with total angular momenta J and J' , with projections M and M' , respectively. T_q^L is the spherical component of the tensor

operator T of rank L . In terms of one-electron states $|nljm\rangle$ and $|n'l'j'm'\rangle$, the density matrix operator can be defined

$$\hat{\rho} = \rho_{nljm,n'l'j'm'}|nljm\rangle\langle n'l'j'm'|, \quad (2.195)$$

where

$$\rho_{nljm,n'l'j'm'} = \langle J'M'|a_{n'l'j'm'}^\dagger a_{nljm}|JM\rangle. \quad (2.196)$$

The many-electron matrix element can then be written

$$\langle J'M'|T_q^L|JM\rangle = \text{Tr} \rho_{nljm,n'l'j'm'} \langle n'l'j'm'|T_q^L|nljm\rangle, \quad (2.197)$$

where the trace sums over all quantum numbers $(nljm)$ and $(n'l'j'm')$. Using the Wigner-Eckart theorem, we can reduce the many-electron matrix element to

$$\langle J'\|T^L\|J\rangle = \text{Tr} \rho_{nlj,n'l'j'}^L \langle n'l'j'\|T^L\|nlj\rangle, \quad (2.198)$$

where

$$\rho_{nlj,n'l'j'}^L = (-1)^{J'-M'} \begin{pmatrix} J' & L & J \\ -M' & q & M \end{pmatrix}^{-1} \sum_{mm'} (-1)^{j'-m'} \begin{pmatrix} j' & L & j \\ -m' & q & m \end{pmatrix} \rho_{nlj,n'l'j'm'}^L. \quad (2.199)$$

2.2.2 Multipole transition probabilities

In this section, we will derive expressions for multipole transition probabilities as used in the `dtm` program, following Ref. [44]. The transition amplitude for a one-electron atom is

$$T_{ba} = \int d^3\psi_b^\dagger \boldsymbol{\alpha} \cdot \mathbf{A}(\mathbf{r}, \omega) \psi_a, \quad (2.200)$$

where $\mathbf{A}(\mathbf{r}, \omega)$ is the transverse-gauge vector potential

$$\mathbf{A}(\mathbf{r}, \omega) = e^{i\mathbf{k}\cdot\mathbf{r}} \hat{\boldsymbol{\epsilon}}. \quad (2.201)$$

Here, the vector $\mathbf{k} = k\hat{\boldsymbol{k}}$ is the propagation vector and the unit vector $\hat{\boldsymbol{\epsilon}}$ is the polarization vector. In the following derivation, it is useful to introduce vector spherical

harmonics $\mathbf{Y}_{JLM}(\theta, \phi)$, which is a combination of spherical harmonics and spherical basis vectors [44]:

$$\mathbf{Y}_{JLM}(\theta, \phi) = \sum_{\sigma} C(L, 1, J; M - \sigma, \sigma, M) Y_{LM-\sigma}(\theta, \phi) \boldsymbol{\xi}_{\sigma}, \quad (2.202)$$

where the Clebsch-Gordon coefficients $C(l, 1, j; m - m_s, m_s, m)$ for $\mathbf{J} = \mathbf{L} + \mathbf{S}$, with $s = 1$, are given in Table 2.1, Y_{lm} are the usual spherical harmonics, and $\boldsymbol{\xi}_{\sigma}$, with $\sigma = -1, 0, 1$, are spherical basis vectors defined by

$$\boldsymbol{\xi}_1 = -\frac{1}{\sqrt{2}} \begin{pmatrix} 1 \\ i \\ 0 \end{pmatrix}, \quad \boldsymbol{\xi}_0 = \begin{pmatrix} 0 \\ 0 \\ 1 \end{pmatrix}, \quad \boldsymbol{\xi}_{-1} = -\frac{1}{\sqrt{2}} \begin{pmatrix} 1 \\ -i \\ 0 \end{pmatrix}. \quad (2.203)$$

Table 2.1: Clebsch-Gordan coefficients for $\mathbf{J} = \mathbf{L} + \mathbf{S}$, with $s = 1$ [44].

	$m_s = 1$	$m_s = 0$	$m_s = -1$
$j = l + 1$	$\sqrt{\frac{(l+m)(l+m+1)}{(2l+1)(2l+2)}}$	$\sqrt{\frac{(l-m+1)(l+m+1)}{(2l+1)(l+1)}}$	$\sqrt{\frac{(l-m)(l-m+1)}{(2l+1)(2l+2)}}$
$j = l$	$-\sqrt{\frac{(l+m)(l-m+1)}{2l(l+1)}}$	$\frac{m}{\sqrt{l(l+1)}}$	$\sqrt{\frac{(l-m)(l+m+1)}{2l(l+1)}}$
$j = l - 1$	$\sqrt{\frac{(l-m)(l-m+1)}{2l(2l+1)}}$	$-\sqrt{\frac{(l-m)(l+m)}{l(2l+1)}}$	$\sqrt{\frac{(l+m+1)(l+m)}{2l(2l+1)}}$

One can expand the vector potential in a series of vector spherical harmonics

$$\mathbf{A}(\mathbf{r}, \omega) = \sum_{JLM} A_{JLM}(\mathbf{r}) \mathbf{Y}_{JLM}(\hat{r}), \quad (2.204)$$

where the expansion coefficients are given by

$$A_{JLM}(\mathbf{r}) = \int d\Omega (\mathbf{Y}_{JLM}(\hat{r}) \cdot \hat{\epsilon}) e^{i\mathbf{k} \cdot \mathbf{r}}. \quad (2.205)$$

Expanding the plane waves in terms of spherical Bessel functions $j_l(kr)$ via

$$e^{i\mathbf{k} \cdot \mathbf{r}} = 4\pi \sum_{lm} i^l j_l(kr) Y_{lm}^*(\hat{k}) Y_{lm}(\hat{r}), \quad (2.206)$$

one can carry out the angular integration and rewrite the expansion of the vector potential as

$$\mathbf{A}(\mathbf{r}, \omega) = 4\pi \sum_{JLM} i^L (\mathbf{Y}_{JLM}(\hat{k}) \cdot \hat{\epsilon}) \mathbf{a}_{JLM}(\mathbf{r}), \quad (2.207)$$

where

$$\mathbf{a}_{JLM}(\mathbf{r}) = j_L(kr)\mathbf{Y}_{JLM}(\hat{\mathbf{r}}). \quad (2.208)$$

One can express this expansion in terms of the vector spherical harmonics $\mathbf{Y}_{JM}^{(\lambda)}(\hat{\mathbf{r}})$ instead of $\mathbf{Y}_{JLM}(\hat{\mathbf{r}})$ using the relations

$$\mathbf{Y}_{JJ-1M}(\hat{\mathbf{r}}) = \sqrt{\frac{J}{2J+1}}\mathbf{Y}_{JM}^{(-1)}(\hat{\mathbf{r}}) + \sqrt{\frac{J+1}{2J+1}}\mathbf{Y}_{JM}^{(1)}(\hat{\mathbf{r}}), \quad (2.209)$$

$$\mathbf{Y}_{JJM}(\hat{\mathbf{r}}) = \mathbf{Y}_{JM}^{(0)}(\hat{\mathbf{r}}), \quad (2.210)$$

$$\mathbf{Y}_{JJ+1M} = -\sqrt{\frac{J+1}{2J+1}}\mathbf{Y}_{JM}^{(-1)}(\hat{\mathbf{r}}) + \sqrt{\frac{J}{2J+1}}\mathbf{Y}_{JM}^{(1)}(\hat{\mathbf{r}}), \quad (2.211)$$

leading to the *multipole expansion* of the vector potential

$$\mathbf{A}(\mathbf{r}, \omega) = 4\pi \sum_{JM\lambda} i^{J-\lambda} (\mathbf{Y}_{JM}^{(\lambda)}(\hat{\mathbf{k}}) \cdot \hat{\mathbf{e}}) \mathbf{a}_{JM}^{(\lambda)}(\mathbf{r}), \quad (2.212)$$

where the vector functions $\mathbf{a}_{JM}^{(\lambda)}(\mathbf{r})$ are referred to as *multipole potentials*, given by

$$\mathbf{a}_{JM}^{(0)}(\mathbf{r}) = \mathbf{a}_{JJM}(\mathbf{r}), \quad (2.213)$$

$$\mathbf{a}_{JM}^{(1)}(\mathbf{r}) = \sqrt{\frac{J+1}{2J+1}}\mathbf{a}_{JJ-1M}(\mathbf{r}) - \sqrt{\frac{J}{2J+1}}\mathbf{a}_{JJ+1M}(\mathbf{r}). \quad (2.214)$$

Only terms with $\lambda = 0, 1$ contribute to the multipole expansion since $\mathbf{Y}_{JM}^{(-1)}(\hat{\mathbf{k}}) = Y_{JM}(\hat{\mathbf{k}})\hat{\mathbf{k}}$ is orthogonal to $\hat{\mathbf{e}}$. The potentials with $\lambda = 0$ are the *magnetic* multipole potentials and those with $\lambda = 1$ are the *electric* multipole potentials. One can express the multipole potentials $\mathbf{a}_{JM}^{(\lambda)}(\mathbf{r})$ in terms of spherical Bessel functions as

$$\mathbf{a}_{JM}^{(0)}(\mathbf{r}) = j_J(kr)\mathbf{Y}_{JM}^{(0)}(\hat{\mathbf{r}}), \quad (2.215)$$

$$\mathbf{a}_{JM}^{(1)}(\mathbf{r}) = \left[j'_J(kr) + \frac{j_J(kr)}{kr} \right] \mathbf{Y}_{JM}^{(1)}(\hat{\mathbf{r}}) + \sqrt{J(J+1)} \frac{j_J(kr)}{kr} \mathbf{Y}_{JM}^{(-1)}(\hat{\mathbf{r}}). \quad (2.216)$$

The multipole expansion of the vector potential (2.212) leads to a corresponding multipole expansion of the transition operator

$$\begin{aligned}
T_{ba} &= \int d^3r \psi_b^\dagger \boldsymbol{\alpha} \cdot \mathbf{A}(\mathbf{r}, \omega) \psi_a \\
&= \int d^3r \psi_b^\dagger \boldsymbol{\alpha} \cdot \left[4\pi \sum_{JM\lambda} i^{J-\lambda} (\mathbf{Y}_{JM}^{(\lambda)}(\hat{k}) \cdot \hat{\epsilon}) \mathbf{a}_{JM}^{(\lambda)}(\hat{r}) \right] \psi_a \\
&= 4\pi \sum_{JM\lambda} i^{J-\lambda} [\mathbf{Y}_{JM}^{(\lambda)}(\hat{k}) \cdot \hat{\epsilon}] \int d^3r \psi_b^\dagger \boldsymbol{\alpha} \cdot \mathbf{a}_{JM}^{(\lambda)}(\hat{r}) \psi_a \\
&= 4\pi \sum_{JM\lambda} i^{J-\lambda} [\mathbf{Y}_{JM}^{(\lambda)}(\hat{k}) \cdot \hat{\epsilon}] [T_{JM}^{(\lambda)}]_{ba},
\end{aligned} \tag{2.217}$$

Upon squaring the amplitude, summing over polarization states, and integrating over photon directions, one obtains the transition probability rate (Einstein A coefficient)

$$\begin{aligned}
A_{ba} &= \frac{\alpha}{2\pi} \omega \sum_{\nu} \int d\Omega_k |T_{ba}|^2 \\
&= \frac{\alpha}{2\pi} \omega \int d\Omega_k 16\pi^2 \sum_{JM\lambda} \sum_{J'M'\lambda'} \sum_{\nu} [\mathbf{Y}_{JM}^{(\lambda)}(\hat{k}) \cdot \hat{\epsilon}_{\nu}] [\hat{\epsilon}_{\nu} \cdot \mathbf{Y}_{J'M'}^{(\lambda')}(\hat{k})] [T_{JM}^{(\lambda)}]_{ab} [T_{J'M'}^{(\lambda')}]_{ba} \\
&= 8\alpha\pi\omega \sum_{JM\lambda} \sum_{J'M'\lambda'} \int d\Omega_k [\mathbf{Y}_{JM}^{(\lambda)}(\hat{k}) \cdot \mathbf{Y}_{J'M'}^{(\lambda')}(\hat{k})] [T_{JM}^{(\lambda)}]_{ab} [T_{J'M'}^{(\lambda')}]_{ba} \\
&= 8\alpha\pi\omega \sum_{JM\lambda} \sum_{J'M'\lambda'} \delta_{JJ'} \delta_{MM'} \delta_{\lambda\lambda'} [T_{JM}^{(\lambda)}]_{ab} [T_{J'M'}^{(\lambda')}]_{ba} \\
&= 8\alpha\pi\omega \sum_{JM\lambda} \left| [T_{JM}^{(\lambda)}]_{ba} \right|^2,
\end{aligned} \tag{2.218}$$

where angular momentum selection rules limit the type and number of multipoles that contribute to the sum. Next, one can apply a gauge transformation to the multipole potentials

$$\begin{aligned}
\mathbf{a}_{JM}^{(\lambda)}(\mathbf{r}) &\rightarrow \mathbf{a}_{JM}^{(\lambda)}(\mathbf{r}) + \nabla \chi_{JM}(\mathbf{r}), \\
\phi_{JM}(\mathbf{r}) &\rightarrow i\omega \chi_{JM}(\mathbf{r}),
\end{aligned}$$

choosing the gauge function

$$\chi_{JM}(\mathbf{r}) = -\frac{1}{k} \sqrt{\frac{J+1}{J}} j_J(kr) Y_{JM}(\hat{r}).$$

The resulting gauge transformation has no effect on the magnetic multipole transitions, but the electric multipole potentials are transformed and reduced to the so-called *length-form* multipole potentials in the non-relativistic limit

$$\begin{aligned}\mathbf{a}_{JM}^{(1)}(\mathbf{r}) &= -j_{J+1}(kr) \left[\mathbf{Y}_{JM}^{(1)}(\hat{r}) - \sqrt{\frac{J+1}{J}} \mathbf{Y}_{JM}^{(-1)}(\hat{r}) \right] \\ \phi_{JM}^{(1)}(kr) &= -ic \sqrt{\frac{J+1}{J}} j_J(kr) Y_{JM}(\hat{r}).\end{aligned}\tag{2.219}$$

In the non-relativistic limit, the length-gauge electric multipole transition operator takes the form

$$T_{JM}^{(1)} = \boldsymbol{\alpha} \cdot \mathbf{a}_{JM}^{(1)}(\mathbf{r}) - \frac{1}{c} \phi_{JM}(\mathbf{r}).\tag{2.220}$$

Since the vector potential contributes less than the scalar potential by terms of order kr , the interaction can be approximated for small values of kr by taking the limit

$$T_{JM}^{(1)} = \lim_{k \rightarrow 0} \left[\boldsymbol{\alpha} \cdot \mathbf{a}_{JM}^{(1)}(\mathbf{r}) - \frac{1}{c} \phi_{JM}(\mathbf{r}) \right].\tag{2.221}$$

Using the asymptotic form of the spherical Bessel function

$$\lim_{x \rightarrow 0} j_l(x) = \frac{x^l}{(2l+1)!!},\tag{2.222}$$

one obtains for the limit of the first term

$$\lim_{k \rightarrow 0} \left[\boldsymbol{\alpha}(\mathbf{r}) \cdot \mathbf{a}_{JM}^{(1)} \right] = 0,\tag{2.223}$$

since

$$\begin{aligned}\lim_{k \rightarrow 0} j_{J+1}(kr) &= \lim_{k \rightarrow 0} \left[\frac{J}{kr} j_J(kr) - j_J'(kr) \right] \\ &= \frac{J}{kr} \frac{(kr)^J}{(2J+1)!!} - \frac{J}{(2J+1)!!} (kr)^{J-1} \\ &= \frac{J}{kr} \frac{(kr)^J}{(2J+1)!!} - \frac{J}{(2J+1)!!} \frac{(kr)^J}{kr} \\ &= 0,\end{aligned}$$

and for the second term

$$\begin{aligned}\lim_{k \rightarrow 0} \left[-\frac{1}{c} \phi_{JM} \right] &= \lim_{k \rightarrow 0} \left[-ic \sqrt{\frac{J+1}{J}} j_J(kr) Y_{JM}(\hat{r}) \right] \\ &= -ic \sqrt{\frac{J+1}{J}} \frac{(kr)^J}{(2J+1)!!} Y_{JM}(\hat{r}).\end{aligned}\tag{2.224}$$

Thus one obtains for the electric multipole transition operator

$$\begin{aligned}
T_{JM}^{(1)} &= \boldsymbol{\alpha} \cdot \mathbf{a}_{JM}^{(1)}(\mathbf{r}) - \frac{1}{c} \phi_{JM}(\mathbf{r}) \\
&= -\frac{1}{c} \left[-ic \sqrt{\frac{J+1}{J}} \frac{(kr)^J}{(2J+1)!!} Y_{JM}(\hat{r}) \right] \\
&= i \sqrt{\frac{(2J+1)(J+1)}{4\pi J}} \frac{(kr)^J}{(2J+1)!!} C_{JM}(\hat{r}) \\
&= i \sqrt{\frac{(2J+1)(J+1)}{4\pi J}} \frac{k^J}{(2J+1)!!} Q_{JM}(\mathbf{r}),
\end{aligned} \tag{2.225}$$

where the definition of a tensor operator in terms of spherical harmonics is used to get the third line, and in the last line,

$$Q_{JM}(\mathbf{r}) = r^J C_{JM}(\hat{r}) \tag{2.226}$$

is defined as the electric J -pole moment operator in a spherical basis.

In general, one can write the multipole interaction in terms of a dimensionless multipole-transition operator $t_{JM}^{(\lambda)}(\mathbf{r})$ as

$$\begin{aligned}
T_{JM}^{(\lambda)} &= \boldsymbol{\alpha} \cdot \mathbf{a}_{JM}^{(\lambda)}(\mathbf{r}) - \frac{1}{c} \phi_{JM}(\mathbf{r}) \\
&= i \sqrt{\frac{(2J+1)(J+1)}{4\pi J}} t_{JM}^{(\lambda)}(\mathbf{r}),
\end{aligned} \tag{2.227}$$

where the multipole-transition operators $t_{JM}^{(\lambda)}(\mathbf{r})$ are related to the frequency-dependent multipole-moment operators $q_{JM}^{(\lambda)}(\mathbf{r}, \omega)$ by

$$q_{JM}^{(\lambda)}(\mathbf{r}, \omega) = \frac{(2J+1)!!}{k^J} t_{JM}^{(\lambda)}(\mathbf{r}). \tag{2.228}$$

The multipole transition rates, or Einstein A -coefficients, giving the probability per unit time for emission of a photon with multipolarity $J\lambda$, from a state I with angular momentum J_I to a state F with angular momentum J_F , is obtained from

$$\begin{aligned}
A_{JM}^{(\lambda)} &= 8\pi\alpha\omega \sum_{JM\lambda} |[T_{JM}^{(\lambda)}]|^2 \\
&= 2\alpha\omega \frac{(2J+1)(J+1)}{J} |\langle F | T_{JM}^{(\lambda)} | I \rangle|^2.
\end{aligned} \tag{2.229}$$

Using the Wigner-Eckart theorem, one can express the transition rates in terms of reduced matrix elements

$$\begin{aligned} A_J^{(\lambda)} &= 2\alpha\omega \frac{(2J+1)(J+1)}{J} \frac{|\langle F \| T_J^{(\lambda)} \| I \rangle|^2}{2J_I+1} \\ &= \frac{2(2J+1)(J+1)(\alpha\omega)^{2J+1}}{J[(2J+1)!!]^2} \frac{|\langle F \| Q_J^{(\lambda)} \| I \rangle|^2}{2J_I+1}, \end{aligned} \quad (2.230)$$

Next, we introduce a new notation Tk to encapsulate the electric and magnetic multipole operators, Ek and Mk , expressed in a.u.. The following replacements were made from the previous notation: multipolarity $J \rightarrow k$, $\lambda \rightarrow T$, initial angular momentum $J_I \rightarrow J$ and final angular momentum $J_F \rightarrow J'$. In the new notation, the general expression for a multipole transition probability rate of order k is given by

$$W_{Tk}(J \rightarrow J') = \frac{2(2k+1)(k+1)}{k[(2k+1)!!]^2} \frac{(\alpha\omega)^{2k+1}}{2J+1} S_{Tk}(J \rightarrow J'), \quad (2.231)$$

where $\alpha \approx 1/137.036$, ω is the $J \rightarrow J'$ transition frequency expressed in a.u., and $S_{Tk}(J \rightarrow J')$ is the line strength obtained as the square of the corresponding multipole matrix element

$$S_{Tk}(J \rightarrow J') = |\langle J' \| Tk \| J \rangle|^2. \quad (2.232)$$

Using Eq. 2.231, we find

$$W_{T1}(J \rightarrow J') = \frac{4}{3(2J+1)} (\alpha\omega)^3 S_{T1}(J \rightarrow J'), \quad (2.233)$$

$$W_{T2}(J \rightarrow J') = \frac{1}{15(2J+1)} (\alpha\omega)^5 S_{T2}(J \rightarrow J'), \quad (2.234)$$

$$W_{T3}(J \rightarrow J') = \frac{8}{4725(2J+1)} (\alpha\omega)^7 S_{T3}(J \rightarrow J'). \quad (2.235)$$

Typically, probabilities are expressed in sec^{-1} , where the conversion between a.u. and sec^{-1} is given by

$$1 \text{ a.u.} \approx 6.57968 \times 10^{15} \text{ Hz} \approx 2\pi \cdot 6.57968 \times 10^{15} \text{ sec}^{-1}.$$

Additionally, it is convenient to use the energy difference ω expressed in cm^{-1} . Doing so, we transform the transition probabilities into a form convenient with our codes. The electric multipole transitions expressed in sec^{-1} are given by:

$$W_{E1}(J \rightarrow J') = 2.02613 \times 10^{-6} \frac{\omega^3}{(2J+1)} |\langle J' || E1 || J \rangle|^2, \quad (2.236)$$

$$W_{E2}(J \rightarrow J') = 1.11995 \times 10^{-22} \frac{\omega^5}{(2J+1)} |\langle J' || E2 || J \rangle|^2, \quad (2.237)$$

$$W_{E3}(J \rightarrow J') = 3.14441 \times 10^{-39} \frac{\omega^7}{(2J+1)} |\langle J' || E3 || J \rangle|^2, \quad (2.238)$$

where $E1 \equiv d$, $E2 \equiv Q$, $E3 \equiv O$, ω is given in cm^{-1} , and $\langle J' || Ek || J \rangle$, $k = 1, 2, 3$ is given in a.u..

For magnetic multipole transitions $S_{Mk}(J \rightarrow J') = |\langle J' || Mk || J \rangle|^2$, the matrix elements of the magnetic multipole operators are proportional to the Bohr magneton μ_0 . Taking into account that the Bohr radius is given by $a_0 = \hbar/mc\alpha$ in SI units, we have

$$\mu_0 = \frac{|e|\hbar}{2mc} = \frac{\alpha}{2}|e|a_0, \quad (2.239)$$

and correspondingly,

$$\langle J' || Mk || J \rangle \sim \mu_0 a_0^{k-1} = \frac{\alpha}{2}|e|a_0^k \text{ (SI units)} = \frac{\alpha}{2} \text{ (a.u.)} \quad (2.240)$$

Factoring out $\alpha/2$, we can write S_{Mk} in a.u. as

$$S_{Mk}(J \rightarrow J') = \frac{\alpha^2}{4} |\langle J' || Mk || J \rangle|^2. \quad (2.241)$$

The magnetic multipole transitions expressed in sec^{-1} are given by:

$$W_{M1}(J \rightarrow J') = 2.69735 \times 10^{-11} \frac{\omega^3}{(2J+1)} |\langle J' || M1 || J \rangle|^2, \quad (2.242)$$

$$W_{M2}(J \rightarrow J') = 1.49097 \times 10^{-27} \frac{\omega^5}{(2J+1)} |\langle J' || M2 || J \rangle|^2, \quad (2.243)$$

$$W_{M3}(J \rightarrow J') = 4.18610 \times 10^{-44} \frac{\omega^7}{(2J+1)} |\langle J' || M3 || J \rangle|^2, \quad (2.244)$$

where ω is given in cm^{-1} , and $\langle J' || Mk || J \rangle$, $k = 1, 2, 3$ is given in a.u..

After the transition probabilities of all allowed lower states are evaluated for a state a , the lifetime of the atomic state a can be determined as

$$\tau_a = \frac{1}{\sum_b A_{ab}}. \quad (2.245)$$

The branching ratio of a particular transition from state a to state b' is defined as

$$p_a = \frac{A_{ab'}}{\sum_b A_{ab}} = A_{ab'} \tau_a. \quad (2.246)$$

Chapter 3

CI/CI+MBPT/CI+ALL-ORDER CODE PACKAGE

The complete CI/CI+MBPT/CI+all-order code package allows one to carry out relativistic calculations for many-electron atoms and ions [2]. This suite of codes is based on a method combining the configuration interaction method with many-body perturbation theory and/or all-order coupled-cluster method, which were discussed in Chapter 2.

3.1 Base computer package

A version of the CI+MBPT code package was modified for public use and published in Computer Physics Communications in 2015 by M. Kozlov *et al* [2]. Although not published, the inclusion of the all-order part provides for accurate solutions for a large number of properties of atoms and ions with up to 4 – 5 valence electrons. The complete code package scheme is illustrated in Figure 3.1.

For the CI code, the computational time can span from an hour when studying very small systems of 1 – 2 valence electrons to up to weeks for more complex systems with 3 – 4 valence electrons. Some problems involving systems with more than 4 valence electrons were simply intractable with the previous code. One of the main objectives of this work was to parallelize the programs to reduce the computational time required for calculations of properties of atomic systems with more than 4 valence electrons. The results of this work will allow for future fast large-scale data production for an online portal project for systems with 2 – 4 valence electrons. Results of this effort is described in Section 3.4. Here we will give a summary of the CI/CI+MBPT/CI+all-order codebase. The following, as well as more detailed documentation about each code, as well as auxiliary codes, can be found in [2].

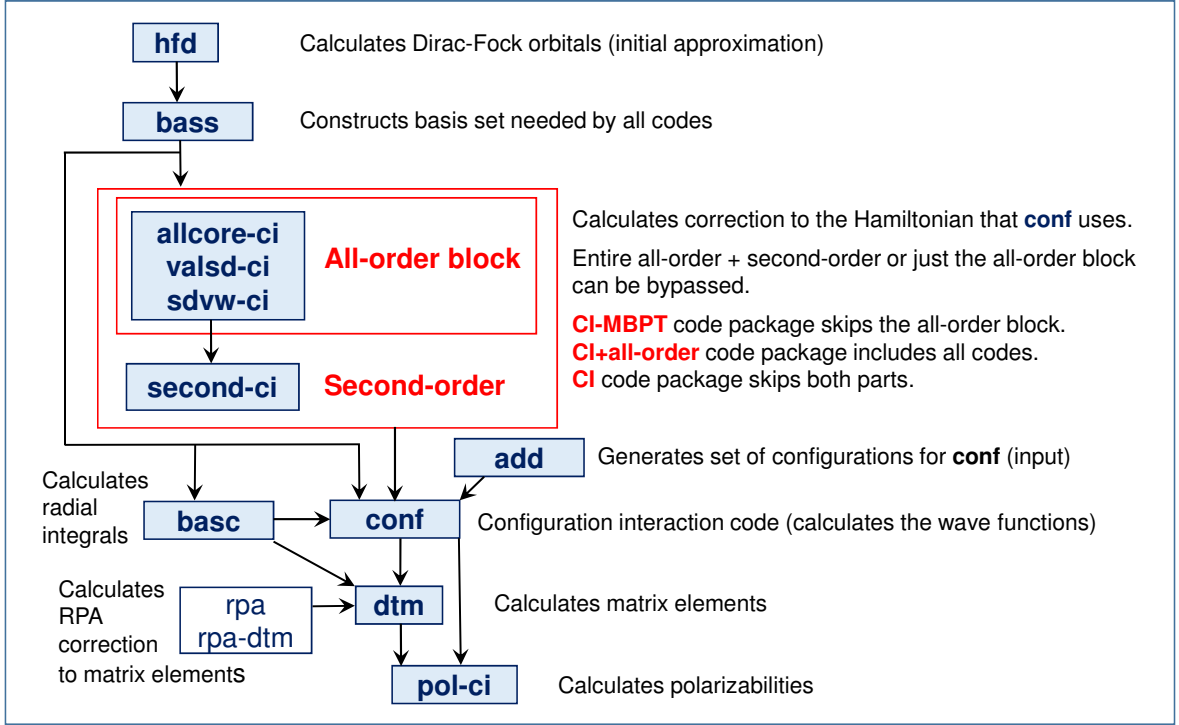


Figure 3.1: The scheme of the CI+MBPT/CI+all-order code package.

3.1.1 hdf

The `hdf` program solves restricted Hartree-Fock-Dirac (HFD) equations self-consistently under the central field approximation to find four-component Dirac-Fock (DF) orbitals and eigenvalues of the HDF Hamiltonian. These orbitals depend only on the principal, orbital, and total angular momentum quantum numbers n , l , and j . This program provides the initial approximation, storing both basis radial orbitals

$$\phi_{nlj} \equiv r \begin{pmatrix} f_{nlj} \\ -g_{nlj} \end{pmatrix}, \quad (3.1)$$

as well as the radial derivatives of the orbitals $\partial_r \phi_{nlj}$, to the file `HDF.DAT`. The run time of this program is only a few seconds, so parallelization of this code is not needed.

3.1.2 bass

The `bass` program is used for construction of the basis set, which is formed using DF orbitals for the core and valence shells, then adding virtual orbitals to account for correlations. A reasonable basis set should consist of orbitals mainly localized at the same distances from the origin as the valence orbitals [2]. This program reads in and updates the file `HDF.DAT`. This program typically takes under a minute to run, so parallelization of this code is not needed.

3.1.3 add

The `add` program constructs a list of configurations to define the CI space by exciting electrons from a set of reference configurations to a set number of active non-relativistic shells. It takes in the input file `ADD.INP`, which specifies the reference configurations, active non-relativistic shells, and minimum and maximum occupation numbers of each shell, and outputs the input file `CONF.INP`, which is subsequently used by the programs `basc`, `conf`, and `dtm`. This program takes only a few seconds to minutes to run, so parallelization of this code is not necessary.

3.1.4 basc

The `basc` program calculates one-electron and two-electron radial integrals, which are used by the `conf` program to form the Hamiltonian in the CI space. The one-electron radial integrals correspond to the HF potential of the core, and the two-electron radial integrals account for the Coulomb and Breit interactions between the valence electrons. The matrix element of the Coulomb interaction for the multipolarity k can be written as [2]:

$$\langle c, d | V_q^k | a, b \rangle \equiv G_q^k(ca) G_q^k(bd) R_{abcd}^k, \quad (3.2)$$

where the angular factors $G_q^k(fi)$ (known as relativistic Gaunt coefficients) are given by

$$G_q^k(fi) = (-1)^{m_f+1/2} \delta_p \sqrt{(2j_i+1)(2j_f+1)} \begin{pmatrix} j_f & j_i & k \\ -m_f & m_i & q \end{pmatrix} \begin{pmatrix} j_f & j_i & k \\ 1/2 & -1/2 & 0 \end{pmatrix}, \quad (3.3)$$

and R_{abcd}^k are the relativistic Coulomb radial integrals, and δ_p accounts for the parity selection rule:

$$\delta_p = \xi(l_i + l_f + k), \quad \xi(n) = \begin{cases} 1 & \text{if } n \text{ is even,} \\ 0 & \text{if } n \text{ is odd.} \end{cases} \quad (3.4)$$

The Breit interaction has the same form as Eq. 3.2, but without the parity selection rule (Eq. 3.4).

The `bas` program reads the file `CONF.INP` to determine which radial integrals are needed, then calculates these integrals and writes them to the file `CONF.INT`. The angular factors (Eq. 3.3) are stored in the file `CONF.GNT`. The file `CONF.DAT` is also formed, storing the basis radial orbitals ϕ_{nlj} , as well as functions $\chi_{nlj} = h_{\text{DF}}^r \phi_{nlj}$, where h_{DF}^r is the radial part of the Dirac-Fock operator.

The runtime of this code is only up to a few minutes for very small basis sets (e.g. `7spdfg` for Ir^{17+}), but can take over an hour for large basis sets needed for CI+all-order calculations (e.g. `22spdf18g` for Bi^-). This code produces output files measuring up to a few GB. Parallelization of this code is not urgent, and may be done using OpenMP in a future project.

3.1.5 `conf`

The `conf` program is based on the code described by Kotochigova and Tupitsyn in 1987 [71], and modified by Mikhail Kozlov, Sergey Porsev, Ilya Tupitsyn, and Andrey Bondarev. This program has been completely re-developed in this work. A major effort was made to port the original serial program into a parallel program capable of efficiently calculating atomic properties of much larger sizes. The parallel code now allows for computations of atomic systems of sizes larger by a factor of 100. From the

scaling tests done, we expect that much larger runs are also now possible on computational facilities outside the University of Delaware. We found great success in this effort, enabling precision modeling of complex atoms not currently possible with any other existing codes. The developments made in this program include modernization and implementation of MPI parallelization, which is discussed in the later sections of this chapter. One of the most significant problems to overcome was intrinsic to the CI method: uneven workload, in which a single configuration may result in one determinant or over 100 000 determinants, so a straightforward parallelization scheme has very poor scaling performance. Moreover, the number of non-zero Hamiltonian matrix elements vary drastically from case to case, and can not be adequately predicted. This is exacerbated by the procedure used to create a list of configurations, which tends to put simpler cases first.

The following are input and output files associated with `conf`:

Input Files:

- `CONF.INP` - List of relativistic configurations
- `CONF.GNT` - Relativistic Gaunt coefficients produced by *basc*
- `CONF.INT` - Relativistic Coulomb radial integrals produced by *basc*
- `CONF.DAT` - Basis radial orbitals ϕ_{nlj} and functions $\chi_{nlj} = h_{\text{HF}}^r \phi_{nlj}$, where h_{HF}^r is the radial part of the Dirac-Fock operator
- `SGC.CON` - One-electron effective radial integrals of the MBPT/all-order corrections
- `SCRC.CON` - Two-electron effective radial integrals of the MBPT/all-order corrections

Output Files:

- `CONF.DET` - Basis set of determinants
- `CONF.HIJ` - Indices and values of the Hamiltonian matrix elements
- `CONF.JJJ` - Indices and values of the matrix elements of the operator \mathbf{J}^2
- `CONF.XIJ` - Quantum numbers, eigenvalues and eigenvectors of the Hamiltonian

- `CONF.RES` - Final table of energy eigenvalues and the weights of all configurations contributing to each term

The `conf` program solves the CI matrix eigenvalue problem,

$$\sum_{J \in P^{CI}} H_{IJ} C_J = E C_I, \quad (3.5)$$

for the atomic system of interest. The computational details of the `conf` program can be summarized by the following:

1. `Input` - Read list of configurations, as well as other relevant parameters of atomic system of interest, from `CONF.INP` and `CONF.GNT`. These parameters, as well as keys for the run, are described in Ref. [2].
2. `Init` - Read basis set information from `CONF.DAT`.
3. `Rint` - Read radial integrals from `CONF.INT`.
4. `RintS` (*optional*) - Read in one-electron and two-electron effective radial integrals of the MBPT/all-order corrections from `SGC.CON` and `SCRC.CON`.
5. `Dinit` - Form list of determinants.
6. `Jterm` - Print table with number of levels with given J .
7. `Wdet` - Write determinants to file `CONF.DET` for subsequent density/transition matrix calculations.
8. `FormH` - Form CI Hamiltonian matrix (details below) and write it to `CONF.HIJ`.
9. `FormJ` - Form matrix of operator \mathbf{J}^2 and write it to `CONF.JJJ`.
10. `Diag4` - Calculate low-lying energy eigenvalues and eigenvectors using Davidson's method of diagonalization (details below). Energy eigenvectors are written to `CONF.XIJ` for subsequent density/transition matrix calculations.
11. `Print` - Print out table of energy levels and weights of configurations.

After the initialization of relevant atomic properties and parameters, the CI Hamiltonian matrix `H` is formed in the `FormH` subroutine. We define several variables: `Nd` is the total number of determinants, and `Nc` is the total number of configurations; and array `Iarr(1:Ne,i)` is the basis set of determinants associated with the i -th configuration.

The computational details of the formation of the CI Hamiltonian matrix are summarized as follows:

Loop index n over total number of determinants Nd.

Loop index ic over total number of configurations Nc.

1. **Gdet** - Generate **n**-th and **k**-th determinant and store them in arrays **idet1** and **idet2**, respectively.
2. **CompC** - Compare the determinants **idet1** and **idet2** and determine the difference between corresponding configurations **icomp**.
3. From the Slater-Condon rules described in Appendix A, if the number of differences **icomp** exceed 2, then the matrix element will be 0. If **icomp** ≤ 2, continue to the next step. Otherwise, move on to the next determinant **k+1**.
4. **Rspq** - Compare the determinants **idet1** and **idet2**, and determine the number of differences between determinants **nf**, and the differing indices of the determinants, **i1**, **i2**, **j1**, and **j2**.
5. **Hm1tn** - Calculate the value of the matrix element, following Slater-Condon rules described in Appendix A. If **nf=2**, the determinants differ by two functions, and therefore there is only a single two-electron integral that needs to be calculated. If **nf=1**, the determinants differ by one function, and therefore there are **Ne** number of two-electron integrals, as well as a single one-electron integral to calculate. If **nf=0**, the determinants are equal, and therefore there are **Ne*Ne** number of two-electron integrals, as well as **Ne** number of one-electron integrals to calculate. The one-electron integrals are calculated by the subroutine **Hint**, with one-electron effective radial integrals of the MBPT/all-order corrections calculated and added by the subroutine **HintS**. The two-electron integrals are calculated by the subroutine **Gint**, with two-electron effective radial integrals of the MBPT/all-order corrections added in by the subroutine **GintS**. The values of CI Hamiltonian matrix elements are computed, and the indices **n**, **k**, and value **t** of the matrix element are stored to arrays **H_n**, **H_k**, and **H_t**, respectively.

The **FormH** is the most expensive subroutine of the **conf** program. The challenge here is the exponential growth of the number of possible configurations with increasing number of valence electrons **Nv**, which exponentially increases the size of the CI Hamiltonian matrix, as well as the number of comparisons between determinants that has to be done during the **FormH** subroutine. Depending on the atomic system of interest, the user has to determine the size of the basis set, and the number of open shells used

in the calculations, which is inevitably limited by the computational complexity of the CI program. For complex systems, such as those with open d - or f -shells, the serial program would not suffice to accurately describe the system of interest. Therefore, the idea was to develop a parallel version of the CI code, as well as develop methods to accurately determine the most important configurations for a system of interest. With the parallel code, described later in Section 3.4, the size of the possible CI space has been increased by a factor of 100 over previous possible systems. In the present time (January 2021), the largest parallel CI runs executed have included about 150 million determinants. Accurate determination of the most important configurations for different systems remains an unsolved problem. Using CI+PT and the `conf_pt` code, known important configurations can be used to generate larger configuration sets, removing configurations that do not contribute much to the final results. The largest CI+PT run have included about 400 million determinants. This procedure can be automated for systems with a few valence electrons, but creating an efficient and reliable algorithm to do so for much larger systems requires a creative solution.

After the CI Hamiltonian matrix has been formed in the `FormH` subroutine, the `Diag4` subroutine iteratively computes the low-lying energy eigenvalues and eigenvectors using Davidson's method [1], as described in Section 2.1.9. We define several variables: `Nd0` is the number of determinants in the initial approximation, and `Nc4` is an input parameter that specifies the number of configurations in the initial approximation. The parameter `Nc4` can be increased to get a better initial approximation, leading to faster convergence, but the time for diagonalization will also grow very fast. It is typically better to put leading configurations at the beginning of the configuration list, rather than increasing `Nc4` too large. We diagonalize a block of a reasonable dimension (`Nd0`, `Nd0`) and use respective eigenvectors as a starting approximation for the Davidson iterative procedure.

The computational details of the Davidson procedure are as follows:

Initialization:

1. **Init4** - Construct the initial approximation by selecting the configurations specified by the **Nc4** parameter. **Nc4** also defines the number of determinants in the initial approximation. The initial approximation Hamiltonian is stored in the matrix **Z1** and is constructed by selecting the top-left block of the full CI Hamiltonian matrix **H**. The diagonal elements of **H** are stored in a separate array **Diag**.
2. **Hould** - Diagonalize the matrix **Z1** using Householder's method [72].
3. **FormB0** - Construct initial approximation eigenvectors stored in **B1**. The elements of **B1** in the initial approximation are chosen such that the first **Nd0** elements are eigenvectors of the matrix **Z1**, and all other elements are set to 0. The eigenvectors are stored in an array **ArrB** of dimension $(Nd, 3*Nlv)$, where **Nlv** is the number of energy levels to be calculated. The array is broken into 3 partitions, each with dimension (Nd, Nlv) : the first partition **ArrB(1)** stores the eigenvectors **B1**, the second partition **ArrB(2)** stores matrix-vector products $H*B1$, and the third partition **ArrB(3)** stores the residual vectors.

Davidson iterative procedure:

1. Check for convergence
2. **Ortn** - Orthonormalize the eigenvectors **B1** and store them in **ArrB(1)**.
3. **Mxmpy(1)** - Evaluate matrix-vector products $H*B1$ for **Nlv** eigenvalues and store them in **ArrB(2)**.
4. **FormP(1)** - Form upper-left block of matrix **P** of dimension (Nlv, Nlv) .
5. Average the diagonal **Diag** over configurations for first iteration.
6. **Dvdsn** - Form residual vector **C** and construct associated eigenvectors **B1**, storing them in **ArrB(2)**.
7. **Ortn** - Orthonormalize new **B1** vector in **ArrB(2)**.
8. **Mxmpy(2)** - Evaluate matrix-vector products $H*B1$ for new eigenvectors in **ArrB(2)** and store them in **ArrB(3)**.
9. **FormP(2)** - Form the other 3 blocks of matrix **P** of dimension $(2Nlv, 2Nlv)$.
10. **Hould** - Diagonalize the matrix **P** using Householder's method.
11. **FormB** - Construct eigenvectors **B2** for next Davidson iteration and store them in **ArrB(1)**.
12. *Repeat from Step 1 until convergence criteria is met.*

3.1.6 dtm

The `dtm` program calculates matrix elements of one-electron operators between many-electron states, under the density (or transition) matrix formalism. This formalism allows us to express the matrix elements between many-electron states via one-electron matrix elements. The `dtm` program forms these reduced density (or transition) matrices and calculates the reduced matrix elements. The following quantities can be calculated from this program:

- electronic g-factors
- magnetic dipole and electric quadrupole hyperfine structure constants A and B
- electric (Ek) and magnetic (Mk) multipole transition amplitudes, where $k = 1, 2, 3$ correspond to the dipole, quadrupole, and octupole transitions
- nuclear spin independent parity nonconserving (PNC) amplitude
- amplitude of the electron interaction with the P-odd nuclear anapole moment (AM)
- P, T-odd interaction of the electron electric dipole moment
- nucleus magnetic quadrupole moment

The program begins by reading the file `CONF.INP` for system parameters and the list of configurations. Next, basis radial orbitals are read from the file `CONF.DAT`, and radial integrals for all operators are calculated and written to the file `DTM.INT`. If this file already exists, `dtm` uses it and does not recalculate the radial integrals. For the diagonal matrix elements, the list of determinants and the eigenvectors corresponding to the state of interest are read from the files `CONF.DET` and `CONF.XIJ`, respectively. For the non-diagonal matrix elements, the initial state is read from the files `CONF.DET` and `CONF.XIJ`, and the final state is read from the files `CONF1.DET` and `CONF1.XIJ`. The results of the diagonal and non-diagonal matrix elements are written to the files `DM.RES` and `TM.RES`, respectively.

The runtime of `dtm` varies from a minute to hours or days, depending on the size of the system. Significant work has been done on this code, including modernization and parallelization. This process will be described in Section [3.4.3](#).

3.1.7 All-order part of the package

The all-order portion of the code package consists of three programs, `allcore-ci`, `valsd-ci` and `sdvw-ci`. These programs calculate corrections to the bare Hamiltonian for the `conf` program due to core shells using a variant of the LCCSD method, described in Section 2.1.11. A large number of terms in order-by-order MBPT are included by iteratively solving the all-order equations until sufficient numerical convergence is achieved. The `allcore-ci` program calculates core excitations, the `valsd-ci` program calculates core-valence excitations, and the `sdvw-ci` program calculates valence-valence excitations. In the future, these three programs would be restructured into a single program, modernized and parallelized using MPI. An OpenMP version is currently under development in our group, and an MPI version will be developed later in 2021.

3.1.8 MBPT part of the package

The MBPT portion of the code package consists of three programs, `sgc`, `scrc`, and `second-cis`. These programs calculate second-order MBPT corrections due to the core shells to the Hamiltonian. These programs calculate corrections to the bare Hamiltonian for the `conf` program due to core shells using second-order MBPT, but for a much larger part of the Hamiltonian than the all-order code. If the all-order calculation was carried out, it will overwrite the second-order results where applicable, drastically improving the efficiency of the method. The `sgc` program calculates one-electron effective radial integrals for the operator Σ (Eq. 2.142), and writes them to the file `SGC.CON`. The `scrc` program calculates two-electron matrix elements of the operator Σ , and writes them to the file `SCRC.CON`. The total number of two-electron diagrams may be very large, making the calculations much more time-consuming than for the one-electron diagrams. A fast variant of the `sgc/scrc` programs was also developed (`second-cis`), but it has more limited choice of the initial DHF potential. The CI+all-order package uses this `second-cis` program.

The `rpa` program solves RPA equations [2], calculates radial integrals of the effective operators and writes them to the files `RPA_n.INT`, where `n=1-13` numerates

one-electron operators, for use in the `dtm` program. The one-electron operators include:

1. `A_hf` - magnetic dipole hyperfine constant
2. `B_hf` - electric quadrupole hyperfine constant
3. `E1_L` - electric dipole transition amplitude in the length gauge
4. `EDM` - Parity (P)-odd, Time (T)-odd interaction of the electric dipole moment of the electron
5. `PNC` - P-odd nuclear spin-independent parity-nonconserving interaction
6. `E1_V` - electron dipole transition amplitude in the velocity gauge
7. `AM` - P-odd nuclear spin-dependent parity-nonconserving interaction, or the interaction with the P-odd nuclear anapole moment
8. `MQM` - P, T-odd interaction with the magnetic quadrupole moment of the nucleus
9. `M1` - magnetic dipole transition amplitude
10. `E2` - electric quadrupole transition amplitude
11. `E3` - electric octupole transition amplitude
12. `M2` - magnetic quadrupole transition amplitude
13. `M3` - magnetic octupole transition amplitude

3.1.9 `conf_pt`

The `conf_pt` program is an optional extension program that was not published with the standard CI+MBPT package. This code is used primarily in more complicated cases, such as atoms with more than 6 valence electrons or systems with holes in filled shells. It uses perturbation theory to quickly treat a much larger number of configurations than `conf` can, then analyzes the weights of each configuration and selects the most important configurations for a full `conf` run, with configurations of low weights removed from the configuration list. For these complex systems, `conf/conf_pt` is used to treat outer-core electrons, by allowing single and/or double excitations from as many core shells as needed to achieve convergence. One caveat to using this program is that the basis set should be diagonalized for efficient usage.

In the CI+MBPT method, the valence electrons are treated with CI, and the core-valence and core-core correlations are treated with MBPT. This method is very effective for atomic systems with a low number of valence electrons (1-3), where the valence CI space is not very large and can be easily saturated. However, for an increasing number of valence electrons, the size of the valence CI space grows exponentially and becomes impossible to solve the full CI problem. In this case, we can split the valence space into a smaller subspace for CI, and account for the corrections from the complementary valence space using second order Møller-Plesset (MP2) perturbation theory, as discussed in Section 2.1.12.

There are two main benefits acquired from using valence PT. First, we can use MP2 corrections to form an optimal CI subspace within the full valence space. This is done by first starting with a small CI space and calculating MP2 corrections for the rest of the valence space. The configurations that take part of this calculation are then weighted in the first order correction to the wave functions and re-ordered such that the CI subspace is filled with configurations with higher weights. Finally, we can repeat the CI procedure with this optimized CI space and then recalculate MP2 corrections for the rest of the valence space to improve our approximation. This procedure can be repeated until MP2 corrections decrease and results are obtained with good convergence.

The program begins the same way `conf` begins, reading in several input parameters and the list of configurations stored in the file `CONF.INP`, the basis set from `CONF.DAT`, and radial integrals from `CONF.INT`. The basis set of determinants is formed as it was done in `conf`. Next, the CI eigenvectors are read from `CONF.XIJ`, and weights of non-relativistic configurations are calculated for the CI eigenvectors. PT eigenvectors are then read from `CONF.XIJ`, and the Hamiltonian in PT space is constructed in two parts: the diagonal part and the non-diagonal part. Weights of the non-relativistic configurations are then calculated for the PT corrections, and configurations below a specified weight are removed. The remaining configurations with significant weights are sorted and written out to a new input file `CONF_new.INP`, which has the same form

as `CONF.INP`. This new `CONF_new.INP` file can be renamed `CONF.INP`, then subsequently used for a better approximation for the energy levels. `conf_pt` and `conf` can be ran repeatedly until the energy levels converge.

The runtime of `conf_pt` is similar to the runtime of `conf`, from a few minutes to several days depending on the number of valence electrons and the size of the basis set. Parallelization of this code was completed and is described in section 3.4.2.

3.2 Modernization of codes

The initial version of the CI/CI+MBPT/CI+all-order codes was developed with Fortran 77. For the first time, we try to take advantage of modern technologies and methodologies, such as applying parallelism with high performance computing (HPC). Common pre-F77 and F77 code hurt readability due to their `COMMON` blocks, implicit variables, arithmetic `IF` statements, and `GOTO` statements in place of `DO` loops.

The codes `conf`, `conf_pt`, and `dtm` were modernized in this work. We converted old Fortran 77 (F77) codes to Fortran 90 (F90), using modern design practices with the intent of optimizing and refactoring our code. Some of the major changes of the code include the removal of `COMMON` blocks, the removal of implicit variables, replacing old logical operators with modern notation, addition of modules to encapsulate logically related code, and refactoring from old fixed-style to modern free-form format.

The strategy is as follows. First, we add `implicit none` to each subroutine and fix every compile error. This removes all implicit variables from our code, which will be necessary for removing `COMMON` blocks. This process is very time consuming, but necessary. Next, we move all variables and arrays from `COMMON` blocks to modules. We do this to prevent having identical data in areas where they do not belong, and make sure no two variables are named the same thing. We use modules to package all physical constants and parameters together in a single file called `variables.f90`. We do the same with the "main" subroutines, packaging them in another module ending with `_aux.f90`. The goal is to have many, small, self-contained files.

Manually refactoring the code itself will also be a time-consuming process. To refactor the code itself, we would have to go through every subroutine and convert arithmetic IF statements to standard IF... ELSEIF... ELSE blocks, convert all GOTO's to `select case` blocks or DO loops, convert all DO loops to modern syntax, and convert equivalenced common block members to `allocatable` memory, allocated in a module. Refactoring and modernization is done in conjunction with running the old F77 code to ensure there are no differences in the final result between each version. Most of the debugging is done due to overlooking miscasted variables, e.g. setting a double precision variable to be real.

Dynamic allocation was done to remove the requirement of user input in defining array parameters and optimizing memory requirements, greatly improving the user experience. In the old F77 version of the code, users of the program would have to define the array parameters then recompile the program before each calculation. This also created issues of incompatibilities of old data files. After extended calculations, users would have files that could not be used since they do not know what parameters they were compiled with. There were several disadvantages with the way array parameters were dealt with. In the F77 version, several parameters (IP4, IPs, etc.) were defined to determine the size of several arrays in COMMON blocks. If a parameter for an array was set too low, then a segmentation fault would occur during code execution, requiring the user to re-define the array dimension parameters, re-compile the program, then re-run the calculation. If a parameter for an array was set too high, then there is a possibility that the required memory for the run would be too high, causing the program to stop before it finished. In this case, one would have to re-submit the job with more memory, or lower the array size. In order to avoid these issues, we attempt to remove all large array dimensions from the program, and have the code calculate exactly how much memory each array should have during code execution. With the modern F90 version of the code, the program calculates the exact required array sizes and allocates exactly enough memory for most arrays.

3.3 Memory requirements

The limit to the size of systems that can be ran with `conf` will depend on the memory requirements of the program. For this reason, it was essential to study the data structures again and try to minimize memory allocations. The serial version of the code utilized pre-allocated arrays with sizes set by specific parameters. In the Modern Fortran standard, it is best practice to implement dynamic allocations for all arrays.

The total memory requirements for the any program can be calculated by adding the sizes of all arrays. In the case of `conf`, this can be estimated roughly by the 3 largest arrays, `Iarr`, `ArrB`, `H_me`, and `J_me`, where `me` refer to the indices and value of the matrix elements. `Iarr` is an array storing the basis set of determinants, `ArrB` is an array storing eigenvectors, matrix-vector products, and residual vectors in the Davidson procedure, and `H_me` and `J_me` stores the matrix elements of the Hamiltonian and the operator \mathbf{J}^2 , respectively, in each core. `Iarr` stores `int*4` elements in a $N_d \times 2N_e$ dimensional array, where N_d is the total number of determinants and N_e is the total number of valence electrons. `ArrB` stores `double precision` in a $N_d \times N_e$ dimensional array. `H_me` and `J_me` stores `int*4` indices `n` and `k` for each determinant pair resulting in non-zero matrix elements, and the `double precision` value for the non-zero matrix element. `int*4` is stored with 4 bytes, and `int*8` and `double precision` are both stored with 8 bytes.

The total memory required by `Iarr` is then calculated to be $8 \times N_d \times N_e$. The total memory required by `ArrB` is also $8 \times N_d \times N_e$. The total memory required for `H_me` and `J_me` is calculated to be $16 \times \text{num_me}$, where `num_me` is the total number of non-zero matrix elements. Therefore, the `conf` program requires about $16 \times N_d \times N_e + 16 \times \text{num_me}$ bytes of memory, where `num_me` include matrix elements for both H and \mathbf{J}^2 . Note that `Iarr`, `ArrB`, and `J_me` are arrays that must be available on all cores, while the `H_me` array can be split among cores. For this reason, each core requires memory from `Iarr`, `ArrB`, and their chunk of `H_me`.

By studying the `conf` program more carefully, we realized that `Iarr` is only used

for the first half of the program setting up the formation of the Hamiltonian matrix, and `ArrB` is only used for the second half of the program in the Davidson procedure. For this reason, using dynamic allocation will reduce the amount of memory required for the `conf` program by $8 \times N_d \times N_e$. Effectively, all cores will require just the amount of memory for `Iarr/ArrB` and their chunk of `H_me`.

The largest parallel run done for this work involved a total number of determinants $N_d=66M$, a total number of valence electrons $N_e=60$, a total number of Hamiltonian non-zero matrix elements $H_num_me=100B$ and a total number of \mathbf{J}^2 non-zero matrix elements $J_num_me=987M$. Here, **M** refers to a million, and **B** refers to a billion. From this run, we can calculate the total per-core memory requirement using 310 cores to be about 40 GB. This is nearly the largest computation that we can currently run in our group with UD Caviness cluster resources of 12.7 TB of memory. Larger problems will need to be run on other large-scale computational facilities. Note that the total number of matrix elements is computed within the formation of the Hamiltonian matrix and the formation of the operator \mathbf{J}^2 and is not known before the program is initialized. Further optimizations to memory can be made and will be looked into more deeply in the future.

3.4 Parallelization of codes

So far, we've discussed modernization of some programs in the code package. Next, we implemented MPI parallelization for three of the CI+MBPT code package's major programs: `conf`, `conf_pt` and `dtm`. The parallelization schemes utilized depends on the structure of the problematic or time-consuming loops in the code. They will be discussed for each code in the next few sections. For each code, there are typically 3-4 blocks of these code that have to be parallelized. MPI calls have to be made to ensure that each core has the required global variables and arrays for subsequent calculations done by the parallelized blocks of code. To validate the final results, we simply compare our results from the parallel version to the results of the serial version. Speedup tests are also done using the timing data extracted from final testing runs. Specific details

regarding the MPI library and subroutines used in this work can be found in several textbooks and references [73][74]. We have outlined several essential MPI subroutines in Appendix D.

3.4.1 conf - the CI code

The parallelization of `conf` can be broken into 5 major problems:

- Modernization
- Formation of CI Hamiltonian matrix
- Formation of \mathbf{J}^2 matrix
- Davidson procedure
- I/O of matrix elements
- Inclusion of MBPT/all-order

We start this process with the bare serial `conf` program, without any subroutines that involve the all-order or MBPT parts. The MBPT/all-order sections of the code are added in after the main portions of the code is parallelized.

3.4.1.1 Formation of CI Hamiltonian matrix

The formation of the CI Hamiltonian matrix is the most computationally expensive algorithm in the `conf` program. The computational complexity of the calculation of CI Hamiltonian matrix elements stems from the differing number of comparisons done in the algorithm. The initial brute force algorithm is as follows: since the Hamiltonian is symmetric, we only need to calculate half of the entire matrix. Allowing index \mathbf{n} to run through rows and index \mathbf{k} to run through columns, we only need part of the Hamiltonian where $1 \leq \mathbf{n} \leq \mathbf{Nd}$ and $1 \leq \mathbf{k} \leq \mathbf{n}$. In this case, the total number of matrix elements is $\mathbf{Nd}^2/2$, where \mathbf{Nd} is the total number of determinants. However, many matrix elements will be reduced to zero when determinants differ by more than two electrons. This is due to the Slater-Condon rules, which are described in Appendix A. The `Rspq` subroutine compares determinants and returns the number of differences and the indices of differing orbitals. We split up the inner loop over determinants

into two (over N_c , the number of configurations and k_x , the number of determinants associated with a configuration). If it finds more than two differences, then nothing has to be done and it continues to the next pair of determinants. If the determinants belong to the configurations, which differ by more than two electrons, then it skips the whole configuration in the inner loop and jumps to the next one. The non-zero matrix elements are saved to memory and optionally to disc. In the F77 version of the code, we save an `integer*8` counter, the pair of `integer*4` indices, and the `double precision` value of the matrix element. In total, this requires 24 bytes of memory per non-zero matrix element. In the modern version, we do not save `integer*8` counter, reducing the memory required per core to 16 bytes per number of non-zero zero matrix elements, saving 33% of the memory requirements of the matrix elements.

In an initial brute force attempt of parallelizing the matrix element calculations, the outermost loop over N_d was distributed evenly across many cores (dividing N_d by `npes`, the total number of cores). While this did give a significant speedup with the amount of cores, it was severely limited due to an uneven workload distribution of matrix elements to each core. Cores assigned to the first blocks of the determinants had very few non-zero matrix elements and would finish very quickly while cores assigned the last blocks of determinants had many non-zero matrix elements and would take much longer. This uneven workload distribution eventually leaks through to the Davidson procedure. Since matrix elements have to be read for multiplication later in the program, each core would have big differences in the number of matrix elements they had to multiply. One way of combating this problem is by separating the Hamiltonian problem into two stages: a comparison stage to evenly distribute the total number of non-zero matrix elements, and a calculation stage to calculate the values of the non-zero matrix elements.

In the second implementation of MPI, the computational workload is first computed at the comparison stage. Here, we loop through all pairs of determinants for the total number of non-zero matrix elements. Once the total number of non-zero matrix elements is obtained, we divide the total workload by the number of cores, then

assign each core a starting index and an ending index for the outer loop determinant. This resulted in a more even workload distribution, which also accelerated the Davidson procedure utilized towards the end of the program. Each core allocates enough memory to hold their total workload, then the calculation stage begins. In the calculation stage, each core calculates an approximately equal number of non-zero matrix elements. However, we found that due to the nature of the problem, the calculation of each matrix element takes a different amount of time since each calculation depends on different numbers of comparisons. Because of this, it was not possible to perfectly distribute the workload evenly across all cores in matrix elements and time. With this implementation, an average speedup of about 50% was attained.

In another attempt to parallelize the Hamiltonian calculation, we introduce an **nk** array that stores the **n**, **k** pairs of indices with non-zero matrix elements in memory during the comparison stage. The **nk** matrix is populated during the comparison stage where non-zero matrix elements are found and require very minimal computation time. It is then duplicated to all cores, since it is not known which core will be assigned which determinants yet. Once each core has a copy of the **nk** matrix, each core will loop through their assigned range of **n** indices and calculate matrix elements where the **n**, **k** pair is non-zero. This is then used to drastically accelerate the calculation stage, reaching an average speedup of about 80%. However, the required memory of this method was beyond the scope of the group's currently accessible clusters and supercomputers so the idea was scrapped. The total memory required for the **nk** matrix is about $4 \times N_d \times N_c$, where N_d is the total number of determinants and N_c is the total number of configurations. The test case of a small CI space had $N_c=481$ and $N_d=15510$, resulting in a required memory of about 30 MB. The largest system tested with the **nk** array was with $N_c=24895$ and $N_d=17431323$, which resulted in a required memory of about 1.74 TB. This is not feasible for a final implementation since our group wants to be able to achieve much larger system sizes in the future.

One major issue we ran into when developing the parallel version of **FormH** was the size limitations of MPI restricting runs for large CI spaces. The limit during

this development phase was 2 billion non-zero matrix elements. This was due to the limitation of MPI message passing, where only a message of size 2 GB could be sent at once. In order to work around this, we had to find the right MPI subroutines to work with. The main problem was the use of the `MPI_Gatherv` subroutine, which required displacements, which go beyond the size `int*4`. One possible workaround is to replace these statements with `MPI_AllReduce` statements, sending required arrays to each core. The problem here is that this requires twice as much memory as before.

In the latest implementation, instead of dividing the outer loop of determinants into blocks like the previous methods, we split the total number of determinants based on their respective core ID `mype`. Each core is assigned determinants `mype+1`, `2*mype+1`, `...`, until `Nd` is reached. For example, with 4 cores and 13 determinants, core 0 would be assigned determinants `n=1,5,9,13`, core 1 with `n=2,6,10`, core 2 with `n=3,7,11`, and core 3 with `n=4,8,12`. Besides the new determinant assignment scheme, we also introduce so-called "chunks" to store non-zero matrix elements in dynamically allocated arrays. Each core has an array that accumulates each index and value of the matrix element in chunks, defined by the `vaGrowBy` parameter. This has a couple of advantages over the previous methods. First, the determinant assignment gives a very even workload distribution among the cores in terms of the number of saved non-zero matrix elements. The problem of uneven distribution due to blocks of determinants having varying numbers of non-zero matrix elements is resolved since each core takes a part of each block of determinant, however the problem of uneven distribution in time still persists, although it is reduced here. By dynamically allocating the arrays storing the indices and values of the non-zero matrix elements, each core will have exactly the amount of memory required. The main disadvantage of this method is that each core does not hold successive matrix elements, and therefore, the Davidson procedure becomes slower since arrays are not read successively during multiplication. Note that generally, the Davidson procedure takes much less time than the construction of the Hamiltonian matrix, so this was an acceptable trade off.

3.4.1.2 Formation of J^2 matrix

The formation of the J^2 matrix is done in a similar way to the formation of the Hamiltonian matrix. The subroutine `FormJ` follows a 3-loop structure. The outer loop ranges over the number of configurations, and the middle loop and inner loop range over the number of determinants associated with each configuration. The 3-loop structure is written in a way to skip configurations that will not contribute a non-zero matrix element, in a similar way to how it is done in the `FormH` subroutine. Since the outer loop ranges over the configurations and not the determinants, it will be necessary to make sure each core begin their work with the correct determinant indices. Thus, a preliminary count of the number of determinants per configuration is done for each core for their individual workload.

The current method of dividing the workload is by distributing the workload in equal areas. As with the Hamiltonian matrix, the J^2 matrix is also symmetric. Therefore, we consider a triangle with equal sides `Nc`. The total workload is the area of this triangle $Nc*Nc/2$, and the workload per core is $Nc*Nc/(2*num_cores)$. However, note that each matrix element here requires a vastly different amount of work to compute due to different numbers of comparisons leading to non-zero matrix elements. This results in a heavily uneven workload distribution. There are plans to optimize this subroutine, but since it is much smaller compared to the `FormH` subroutine, it is not as important. Since the master core requires all matrix elements for use in the Davidson procedure, a reduction is done to the master core, and the master core writes out `CONF.JJJ` serially.

3.4.1.3 Davidson procedure

The most expensive subroutine in the Davidson procedure is `Mxmpy`, so this was the only subroutine that was parallelized. In the `Mxmpy` subroutine, there is a single loop through each core's non-zero matrix elements for multiplication. In the Fortran 77 variant, this loop iteratively reads in the matrix elements from the `CONF.HIJ` file. In the modernization and parallelization processes, we remove the I/O since non-zero

matrix elements are stored in memory, and parallelize the loop by allowing each core to loop over the matrix elements they have stored from the `FormH` subroutine.

In the latest version of the parallel `FormH` subroutine described in the previous section, the total number of non-zero matrix elements is evenly distributed between all cores, but the successive indices have gaps determined by the number of cores. The number identifier, pair of indices, and the value of the non-zero matrix element is stored in arrays for each core in memory. Since the information for the CI matrix is already stored in memory and is readily available, `Mxmpy` no longer requires reading `CONF.HIJ` files, so it has been discarded. Each core reads matrix elements from memory for multiplication. The multiplications are done and stored in a new array called `ArrB`, which is then reduced using `MPI.Reduce` for the master core to do subsequent calculations.

The parallelization procedure for this is very simple since the workload was already distributed in the previous `FormH` subroutine. The matrix elements calculated by each core are saved in memory for each core to be re-used in the `Mxmpy` loop. In this way, matrix-vector multiplications are done in parallel by each core. This is done very efficiently since workload has been evenly distributed among cores.

3.4.1.4 I/O

The new parallel version of `conf` does not rely on file input and output (I/O) for any of the calculations. Subroutines such as `Init4` and `Mxmpy`, which involve the calculated matrix elements previously stored in `CONF.HIJ` files, now utilize the matrix elements stored in memory. This is faster since there is no time wasted in I/O. However, this does require higher memory consumption due to storage of matrix elements. The required memory to store the CI Hamiltonian matrix and the \mathbf{J}^2 matrix is given by

$$\text{Mem}_{\text{H,J}} = (4_{\text{n}} + 4_{\text{k}} + 8_{\text{t}}) \times \text{num_me}, \quad (3.6)$$

where 4 and 8 represent the amount of memory required in bytes, `n` and `k` are the indices for the non-zero matrix element, `t` is the value of the matrix element represented in

`double precision`, and `num.me` is the total number of matrix elements.

With the removal of all `CONF.HIJ` reading dependence from the `conf` code, a new key `Kw` has been added. `Kw` can take either one of two values: 0 or 1. If `Kw=0`, `CONF.HIJ` will not be written, and if `Kw=1`, `CONF.HIJ` will be written. The main advantages of this key are the following:

- If `CONF.HIJ` file does not need to be written for any reason, I/O can be completely eliminated from the execution by setting `Kw=0`, allowing for significant speedup of the code by removing potential writing of 1 GB – several TB files.
- If `CONF.HIJ` file is required for any reason, it can easily be obtained by setting `Kw=1`. This will require several minutes depending on the size of the CI matrix. Writing `CONF.HIJ` was a major computational bottleneck as previous version wrote `CONF.HIJ` serially. The latest version of the code utilizes MPI I/O to write a single `CONF.HIJ` file in parallel. Depending on the size of the constructed CI Hamiltonian matrix, the `CONF.HIJ` file is typically written to a HPC system's large-scale parallel distributed file system, such as Lustre [75].

A key `kXIj` has been added to define the intervals in which the wave functions are written to the file `CONF.XIJ`. If `kXIj=1`, the `CONF.XIJ` file will be written every Davidson iteration, and if `kXIj=10`, it will be written every 10 iterations. This is to reduce the total amount of serial writing of the file to a minimum to save computation time. From the parallelization of `conf`, some subroutines in the Davidson procedure were rewritten to utilize data stored in memory instead of in disc, including data stored in `CONF.XIJ`. This removed all serial reads from the program, and with the limited amount of serial writes, this resulted in a noticeable speedup for large runs.

3.4.1.5 Inclusion of MBPT/all-order corrections

Re-implementing the MBPT/all-order portion of the `conf` program simply required adding in two subroutines `RintS` and `FormD`, which were left out during the initial modernization and parallelization procedures. Most of the time spent on adding MBPT/all-order capabilities were on modernizing and fixing data structure compatibility when removing the `COMMON` blocks.

In addition to making MBPT/all-order compatible, memory requirements were increased due to the large number of additional integrals from new input files `SRC.CON` and `SCRC.CON`. The arrays storing these integrals have been designed with dynamic allocation, so when MBPT/all-order is not required, the program does not allocate any memory for them. Results for MBPT/all-order calculations were compared between serial and parallel versions of the code and were found to be identical.

3.4.1.6 Achieved performance of parallelization

The performance of the parallel `conf` program was tested with calculations for the Ir^{17+} ion. Our speedup tests are done for a small system with only the $4f$ shell open with small $[7spdfg]$ basis set. These calculations include $Nv=14$, $Nc=2351$, and $Nd=636892$. In Table 3.1, we compare runtimes of the `FormH` and `Diag4` subroutines for varying number of computing cores. For the `FormH` subroutine, we found that while there is an 80% speedup found going to 50 computing cores from the serial code, the parallel code scales perfectly linearly with increasing number of cores. One of the main bottlenecks of parallel code is the communication overhead, where data will need to be shared between processors for coordination. This communication between processors adds additional runtime, and may be the main reason for the imperfect scaling from 1 to 50 cores. The parallel code has been tested up to 550 cores, resulting in nearly perfect linear scalability for small systems. For the `Diag4` subroutine, which realizes the Davidson algorithm, we do not find great scalability since only the matrix-vector product subroutine `Mxmpy` was parallelized, and a large majority of the procedure is left serial. Since the Davidson procedure typically does not run as long as the `FormH` subroutine, the performance of the `Diag4` subroutine was deemed sufficient for our problems, leaving better optimization as a future project.

In Table 3.2, we compare runtimes of the `FormH` and `Diag4` subroutines for a much larger system. Here, the test system is Ir^{17+} with $4f$, $4d$, and $4p$ shells open with larger $[8spdfg]$ basis set. These calculations include $Nv=30$, $Nc=24895$, and $Nd=17431323$. Comparing large runs to the base $N=50$ case, we see that there is still

Table 3.1: The runtime of subroutines `FormH` and `Diag4` of the parallel `conf` program for increasing number of compute cores and the speedups of the parallel code are presented in seconds (s) for increasing number of cores N , relative to the serial code ($N=1$), as well as $N=50$. These small test runs were done with Ir^{17+} with 2351 relativistic configurations and 6.3×10^5 determinants. Note that the total times include all serial subroutines outside of `FormH` and `Diag`.

N	runtime (s)			speedup (from N=1)			speedup (from N=50)		
	FormH	Diag4	total	FormH	Diag4	total	FormH	Diag4	total
1	7097	288	7407	1	1	1	-	-	-
50	179	38	229	40	8	32	1	1	1
100	91	23	126	78	13	59	2	1.7	1.8
150	61	17	90	116	17	82	3	2.2	2.5
200	47	14	73	151	21	101	4	2.7	3.1
250	38	13	63	187	22	118	5	2.9	3.6
300	32	12	55	222	24	135	6	3.2	4.2
350	27	9	49	263	32	151	7	4.2	4.7
400	23	10	47	309	29	158	8	3.8	4.9
450	22	10	45	323	29	165	8	3.8	5.1
500	20	9	43	355	32	172	9	4.2	5.3
550	17	9	39	417	32	190	11	4.2	5.9

near perfect linear scalability up to 500 cores for the `FormH` subroutine, but see very small increased performance for `Diag` with 200 to 500 cores. Again as with the small system, the Davidson procedure takes much less time compared to the formation of the CI Hamiltonian, so the total computation time is not completely hindered by the performance of `Diag`, and we still see a modest total performance gain.

3.4.2 `conf_pt` - the valence PT code

Of the many subroutines in the `conf_pt` code, two subroutines: `DiagH`, which calculates the diagonal, and `PTE`, which calculates off-diagonal matrix elements, dominate in term of computational time and resource consumption, taking about 90% of the whole run time. These two subroutines are the main subjects of the MPI parallelization procedure. In order to parallelize both subroutines, we must first divide the total workload between the number of cores available. The entirety of the code is

Table 3.2: The runtime of subroutines `FormH` and `Diag4` of the parallel `conf` program for increasing number of compute cores and the speedups of the parallel code are presented in seconds (s) for increasing number of cores N , relative to the code ran with 50 cores ($N=50$). These large test runs were done with Ir^{17+} with 24895 relativistic configurations and 17.4×10^6 determinants. Note that the total times include all serial subroutines outside of `FormH` and `Diag`.

N	runtime (s)			speedup (from N=50)		
	FormH	Diag4	total	FormH	Diag4	total
50	22571	1343	24218	1	1	1
100	12843	1514	14593	1.8	0.9	1.7
200	5800	957	6927	3.9	1.4	3.5
300	3810	678	4610	5.9	2.0	5.3
400	2913	596	3646	7.8	2.3	6.6
500	2292	535	2958	9.9	2.5	8.2

ran by a master code and then forks for the duration of the diagonal and off-diagonal calculations; i.e. the code forks when it reaches the subroutine that calculates diagonal matrix elements then joins back when the calculation is complete, and the same is done for the calculation of the off-diagonal matrix elements. A fork refers to the master core splitting its workload to a number of cores, each working on a piece of the program simultaneously, and a join refers to when the individual cores are done working and the results are passed back to the master core. This is done differently for each subroutine, where the diagonal part is more straightforward due to comparing same determinants of the Hamiltonian matrix and the off-diagonal part is more complex due to it comparing different determinants.

3.4.2.1 Diagonal part of the Hamiltonian

The `DiagH` subroutine is responsible for computing the diagonal elements of the Hamiltonian matrix and storing the results in an array. This is parallelized by splitting a single sum over relevant determinants into many different parts; i.e. we are splitting a single loop into multiple loops depending on the number of cores available. To do this, we give each core a starting and ending value of the loop and let them do their

respective workload simultaneously until they are all done. When they are all done, each core must report its results to the master core using the MPI functions, specifically `MPI_Gatherv`, which takes in the individual sections of resultant array, computed by each individual core, and sends them to the master core.

3.4.2.2 Off-diagonal part of the Hamiltonian

The PTE subroutine computes all of the off-diagonal elements that are necessary to calculate MP2 corrections by looping through each configuration and the possible determinants, instead of traversing through the off-diagonal matrix elements by row and column. The main difference between the computational part of this code with the diagonal is that this subroutine has two main loops: an outer loop that traverses through the list of non-relativistic configurations, and an inner loop that traverses the number of determinants within each non-relativistic configuration. Several schemes were attempted to parallelize these loops and will now be discussed.

The first parallelization scheme attempted to split the outer loop into equal portions for each core to work on. This worked well for very small numbers of cores of about 1 to 8, but we quickly found that the speedup was not scalable to higher core counts. This was due to the varying number of determinants in each configuration, i.e. each configuration holds a different number of determinants so some cores had very little work to do while others had a lot more work to do. To take into account this we tried another scheme, where we evenly distribute the number of determinants between the cores.

The second scheme starts by first counting the total number of determinants in each individual configuration. Once this has been counted, the outer loop is split unevenly among the cores, but in such a way that the total number of determinants stayed relatively the same for each individual core. This worked very well for a modest number of cores of about 1 to 16. However, we quickly found that this also had a scalability issue when we tried to go up to 40+ cores. The main problem here was that we were trying to distribute the outer loop into equal workloads, but there are

some configurations that have such a big number of determinants that it would take more time to finish than cores that were required to take a sum of determinants that was less than the configuration with a high number of determinants. For example, if the total number of determinants is $N_d=135M$, and we want to split this into 100 cores, then we would need each core to work with, say 1.35 million determinants. However, since we parallelize the outer loop, there will eventually be cores that are working with a single configuration with maybe about 3 million determinants. The other cores with 1.35 million determinants will finish and they would have to wait for the last core with 3 million determinants. The other issue with this is that the number of iterations for the outer loop is a lot less than the number of iterations in the inner loop, i.e. we will not be able to scale this problem to much higher core counts of say 1000. If the total number of configurations in the PT space is less than the total number of cores, then there will be cores that will sit idle. This was the major bottleneck of this version of parallelization. In order to develop an algorithm to efficiently parallelize the total workload of both loops, we had to develop a method of parallelizing a 2-dimensional array with varying sizes as the second index. We then tried another parallelization scheme, which parallelizes the inner loop instead of the outer loop; i.e. splitting the workload for each individual configuration.

The current parallelization scheme also involves first counting the total number of determinants in each individual configuration. However, this time we work serially with the outer loop and parallelize only the inner loop. During the outer loop iterations, which is running in serial, we distribute the inner loop to multiple cores evenly and allow the cores to calculate the contributions of the single non-relativistic configuration and the first order eigenvectors. This method is similar to running the diagonal portion of the code inside another loop. After each core has completed their workload, we sum over all contributions to the energy correction from each core and gather all first order eigenvectors. By parallelizing the off-diagonal code this way, we avoid situations where some cores would have too much work to do, while others would sit idle. Instead, all cores are now able to work equally through the entire two-loop process. This scheme

Table 3.3: Left: Diagonal and off-diagonal run times in seconds (s) correspond to the time it takes to calculate all diagonal and non-diagonal elements of the Hamiltonian in the PT space, respectively. This also includes message passing times in the MPI procedures. The total run time is the total time it takes to complete both diagonal and off-diagonal run times. The total runtime of the *conf_pt* code adds a couple of minutes to the total time. Right: The speedups of the parallel code relative to the serial code (N=1). Speedups are presented for different number of cores N=1, 20, 40, 100, 200. This run is done with Ir¹⁶⁺ with 14318 relativistic configurations and 83×10^6 determinants.

Ir ¹⁶⁺	runtime (s)			speedup		
	N	diag	off-diag	total	diag	off-diag
1	539.7	2161.98	2878.24	1	1	1
20	36.64	111.31	147.95	19.55	19.42	19.45
40	19.32	55.73	75.05	37.07	38.79	38.35
100	8.18	23.21	31.39	87.56	93.15	91.69
200	4.59	12.85	17.44	156.05	168.25	165.04

has given us by far the best speedup, with speedups close to the number of cores for low numbers of cores and rounding off at higher core counts.

The main complication of these parallelization schemes was how to pass the results from each individual core to the master core. Passing the results from each individual core to the master core is done via the use of the `MPI_Gatherv` subroutine. This had to be done to send the individually calculated first order eigenvectors to the master core. `MPI_Gatherv` takes in an array of some size and data structure from each core and sends them individually to some node. The complication is with its requirement of two extra arrays, an array of the sizes of each array sent and an array of the displacements from the receiving buffer at the master code.

3.4.2.3 Achieved performance of parallelization

The MPI parallelization of *conf_pt* has been tested up to 15-valence electron systems. The number of electrons in the system significantly increases total computation time and required resources. The main tests were done with Ir¹⁶⁺, a highly-charged ion

Table 3.4: Left: Diagonal and off-diagonal run times in seconds (s) correspond to the time it takes to calculate all diagonal and non-diagonal elements of the Hamiltonian in the PT space, respectively. This also includes message passing times in the MPI procedures. The total run time is the total time it takes to complete both diagonal and off-diagonal run times. The total runtime of the *conf_pt* code adds a couple of minutes to the total time. Right: The speedups of the parallel code relative to the serial code (N=1). Speedups are presented for different number of cores N=1, 20, 40, 100, 200. This run is done with Ir¹⁶⁺ with 25588 relativistic configurations and 135×10^6 determinants.

Ir ¹⁶⁺	runtime (s)			speedup		
	N	diag	off-diag	total	diag	off-diag
1	922.68	5243.18	6165.86	1	1	1
20	57.10	331.50	388.60	16.16	15.82	15.87
40	31.20	166.51	197.71	29.57	31.49	31.19
100	12.54	68.52	81.06	73.58	76.52	76.06
200	6.71	36.62	43.33	137.51	143.18	142.30

with one hole in the $4f$ shell. Among the highest number of relativistic configurations and determinants tested so far, however, Ir¹⁷⁺ with 75446 configurations and 391×10^6 determinants took about 14 hours to run with 80 cores. In Table 3.3, computational run times of *conf_pt* are shown with different amounts of resources. Ir¹⁶⁺ was tested here with 14318 relativistic configurations and 83×10^6 Slater determinants. N represents the number of cores utilized in the computation, and if available, greatly speeds up the run time. Table 3.4 presents the computational run times testing Ir¹⁶⁺ with 25588 relativistic configurations and 135×10^6 Slater determinants. From the results of both tests, we see that increasing the size of the valence space (number of configurations and determinants) also decreases the amount of speedup. This is mainly due to the amount of message passing that is done within the code.

3.4.3 dtm - the density (transition) matrix code

As with the *conf* and *conf_pt* programs, the first objective before parallelization was to create a working modern F90 version and to validate the final results with those

of the old F77 version. Dynamic allocation has also been implemented for the main arrays in the program, to optimize memory requirements. With the `dtm` program, there are two major functionalities that need to be parallelized: the formation of the density matrix and evaluation of the expectation values, and the formation of the transition matrix and evaluation of the amplitudes. The DM part of the code and TM part of the code each require all cores to store all wave functions and determinants. The DM part requires same parity determinants and wave functions stored in the files `CONF.DET` and `CONF.XIJ`, respectively, whereas the TM part requires opposite parity determinants and wave functions stored in the files `CONF.DET` and `CONF.XIJ`, and `CONF1.DET` and `CONF1.XIJ`, respectively. The parallelization of these parts differ since the loop structure is different between the two subroutines, `FormDM` and `FormTM`.

3.4.3.1 DM - density matrix

The `FormDM` subroutine calculates the density matrix elements and expectation values. Wave functions and determinants from same parity states are first read from `CONF.XIJ` and `CONF.DET`. The loop structure of `FormDM` involves a 4-loop structure, but it can be thought of as two optimized loops: an outer loop that goes over configurations associated with the final state, and an inner loop that goes over configurations associated with the initial state. We split the total workload by splitting the outer loop into intervals of size $N_c/\text{num_cores}$, where N_c is the total number of configurations associated with the determinants, and `num_cores` is the total number of cores used in the calculation.

3.4.3.2 TM - transition matrix

The `FormTM` subroutine calculates the transition matrix elements and amplitudes of matrix elements. Wave functions and determinants from opposite parity states are first read in from `CONF.XIJ`, `CONF1.XIJ`, `CONF.DET`, and `CONF1.DET`. The loop structure of `FormTM` is similar to that of the `FormH` subroutine in the `conf` program: there is an outer loop goes over the determinants of the final state, and the inner loop is divided

over the configurations of the initial state. The parallelization scheme follows one of the older implementations of the `FormH` parallelization schemes, splitting up the outer loop into even chunks for distribution. We split the total workload into intervals of size `Nd2/num_cores`, where `Nd2` is the total number of determinants associated with the final state, and `num_cores` is the total number of cores used in the calculation.

3.4.3.3 Achieved performance of parallelization

Due to the already optimized algorithms used to compare configurations in the `FormDM` and `FormTM` subroutines, the scalability and performance of the parallelization was a great success. The average speedup achieved for the `dtm` program, for both density matrix and transition matrix calculations, was about 85% with the number of cores. Due to the already high speedup achieved, more optimized implementations have not been looked into and will be subject to a future project.

Chapter 4

DEVELOPMENT OF ATOMIC CLOCKS AND THE SEARCH FOR VARIATIONS OF FUNDAMENTAL CONSTANTS

The development of the CI/CI+MBPT/CI+all-order methods and codes are motivated by the development of atomic clocks, which is essential for the search for variation of fundamental constants. One of the main remaining stumbling blocks towards development of many HCI clock proposals is the large uncertainties in the theoretical predictions of the clock transitions, in particularly in cases with holes in the $4f$ shell (for example Ir^{16+} and Ir^{17+}) or mid-filled $4f$ shell (Ho^{14+}). While there are high-precision methods that allow for reliable prediction of HCI transitions in ions with 1-4 valence electrons to a few percent or better [24], the approaches for the $4f$ -hole systems are still in the development stage and theory accuracy has not been established. Lack of accurate theory predictions leads to years of delays in experimental efforts. Rapid development of current clock was in part possible due to the ability to accurately predict properties of monovalent and divalent systems, used in the present most precise clocks.

We note that this work serves as a basis for efficient treatment of systems with many valence electrons that can be used for a large variety of applications beyond HCI calculations. Numerous problems in astrophysics and plasma physics require accurate treatment of systems with many valence electrons, such as Fe. The lack of accurate theory predictions creates problems in applications involving almost all lanthanides and actinides as well as many other open-shell atoms and ions of the periodic table. There are many other problems, besides HCI where our results are useful, for example development of the neutral atom lattice clocks based on $4f^{14}6s6p\ ^3P_0^o - 4f^{13}6s^25d$ ($J = 2$) transition in Yb [76, 77]. None of the currently existing *ab initio* methods are

capable to reliably predict the atomic properties of this $J = 2$ state. In this chapter, we describe the calculations of atomic properties of Ir^{17+} , Cf^{15+} and Cf^{17+} .

4.1 Optical clocks based on Ir^{17+}

The work described in this chapter is published in Ref. [4]. The highly charged ion Ir^{17+} is of particular interest for the development of novel atomic clocks due to its very high sensitivity to the variation of the fine structure constant α and related dark matter searches. While the $M1$ transitions in Ir^{17+} between same parity states have been measured to good precision [3], the clock transitions, or in fact any $E1$ transitions between opposite parity states have not yet been identified despite over 6 years of experimental effort. While these $E1$ transitions are weak as they are only allowed due to the configuration mixing, i.e. no “one-electron” $E1$ transitions are allowed between these configurations (for example, $4f^{12}5s^2 - 4f^{13}5s$), strong allowed $E1$ transitions (between $4f^{12}5s^2 - 4f^{12}5s5p$ and $4f^{13}5s - 4f^{13}5p$ configurations) lie much higher on the spectrum, in the EUV and VUV rather than the optical range. These transitions were expected to be observed in recent experiments since their predicted transitions rates [33] were well within the experimental capabilities; especially since the $M1$ transitions with much smaller transition rates have been observed. The lack of observations for the $E1$ transitions brought serious concerns about the accuracy of theoretical predictions, even to the point of doubt of approximate spectral range, with over $10\,000\text{ cm}^{-1}$ differences. In this work, we resolved this problem and for the first time, definitively demonstrated the ability to converge the configuration interaction (CI) in systems with a few holes in the $4f$ shell and place uncertainty bounds on the results. Our results explain the lack of observations of the $E1$ transitions and provide a pathway towards detection of clock transitions.

Ir^{17+} ion has $[1s^2 \dots 4d^{10}]$ closed shells and complicated energy level structure with $4f^{12}5s^2$, $4f^{13}5s$ and $4f^{14}$ low-lying levels shown in Fig. 4.1. Prior calculations include the CI [32], CI Dirac-Fock-Sturm (CIDFS) [3], Fock space coupled cluster (FSCC) [3], and the COWAN code [78] calculations. There is a reasonable agreement,

from a few 100 cm^{-1} to 1500 cm^{-1} , for the energy levels of the lowest $4f^{13}5s$ states as all energies are counted from the ground state which has the same electronic configuration. However, there are very large, 5000 cm^{-1} to 13000 cm^{-1} differences for all other levels. For convenience, we have shown in Fig. 4.1 the positions of the $4f^{12}5s^2$ levels predicted using CIDFS [3] and FSCC [3] calculations which are the most elaborate from all prior approaches. The CI results of Ref. [32] place these levels much higher, by $5000 - 7000 \text{ cm}^{-1}$.

Berengut *et al.* [79] proposed to use the $4f^{12}5s^2\ ^3H_6 - 4f^{13}5s\ ^3F_4^o$ transition ($K = -22$) as a clock transition. It is a $E3/M2$ transition and can be enhanced via the hyperfine-mixing with the $\ ^3H_5$ state. They also note a possibility of using the $4f^{14}\ ^1S_0 - 4f^{13}5s\ ^3F_2^o$ transition which is a $M2$ transition and may be induced by the hyperfine mixing with the $4f^{12}5s^2\ ^3P_1$ level. The particular attraction of this possibility is very high (predicted to be $K = 143$) sensitivity to the variation of α . For comparison, all presently operating clocks have $K < 1$ with the exception of the Yb^+ octupole clocks with $K \sim -6$. A factor of 100 increase means that the sensitivity to the variation of α is 100 times higher than with $K = 1$, so the clocks with the same accuracy will set 100 times better limit. Fig. 4.1 illustrates the difficulty in predicting either one of these transition frequencies.

Nine of the $M1$ transitions in Ir^{17+} have been experimentally identified and measured at a ppm level [3]. The main puzzle is the lack of observation of two weak $E1$ transitions [33] between the even and odd levels, i.e. $4f^{12}5s^2\ ^3F_4 - 4f^{13}5s\ ^3F_{3,4}^o$ transitions. Theoretical determination of the odd level splittings is much more reliable in comparison with the odd-even energy difference and the observation of the $E1$ transitions would have allowed for the determination of the wavelength of the proposed $4f^{12}5s^2\ ^3H_6 - 4f^{13}5s\ ^3F_4^o$ clock transition with good precision.

4.1.1 Method of calculation

We start from the solutions of the Dirac-Hartree-Fock (DHF) equations in the central field approximation to construct the one-particle orbitals. We find that the

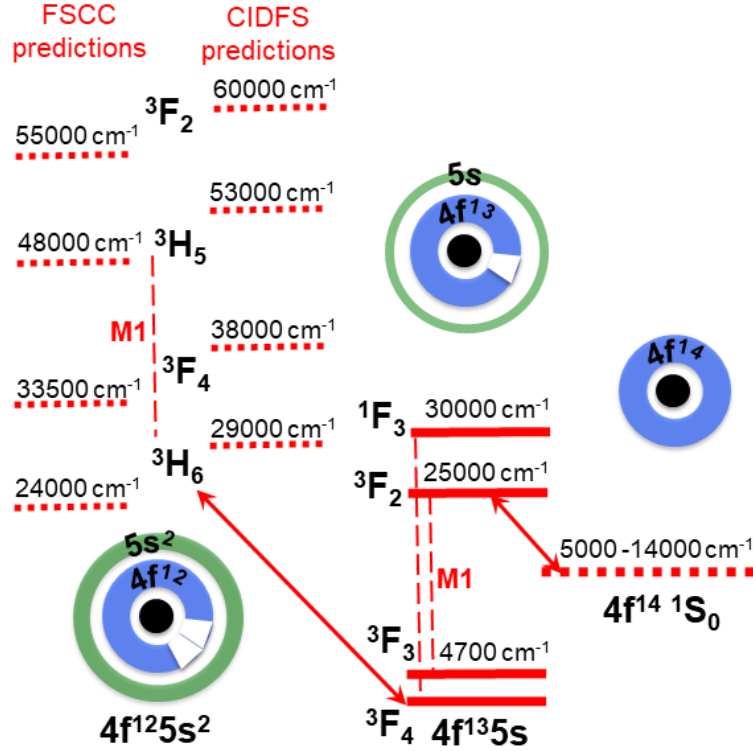


Figure 4.1: Low-lying energy levels of Ir¹⁷⁺ based on past CI Dirac-Fock-Sturm (CIDFS) and Fock space coupled cluster (FSCC) calculations [3]. Wavelengths of 3 M1 transitions shown by vertical dashed lines have been measured in [3]. The scheme is not to scale. From Ref. [4].

best initial approximation is achieved by solving the restricted DHF equations with the partially filled shells, namely $[1s^2 \dots 4d^{10}]4f^{13}5s$. Here, the hybrid approach that incorporates core excitations into the CI by constructing an effective Hamiltonian with the coupled-cluster method [64] cannot be used with such initial approximation. Therefore, the inner shells have to be treated using the CI method, as described in Section 2.1.6, leading to exponential increase in a number of required configurations. While the weights of most configurations are small, we find that the number of important configurations is still very large.

The increased size of the valence space imposes much higher computational demands. To resolve this problem, we developed a code utilizing MPI, as described in Section 3.1.9, that pre-estimates the weights of a very large number of configurations

using the perturbation theory (CI+PT approach [80] described in Section 2.1.12). We also developed codes to analyze the results and identify and sort the most important configurations. Finally, we developed a fast MPI version of the CI code, described in Section 3.4.1, as the resulting set of important configurations was still extremely large. Our new codes allowed us to increase the valence space from 14 electrons to all 60, and to include 250,000 configurations, resulting in 133 million Slater determinants, a factor of 20 increase to what was previously feasible.

In order to definitively ensure the reliability of the theoretical calculations, we considered all possible contributions that may affect the accuracy of the computations and ensure the convergence in all numerical parameters, including the number and type of configurations included in the CI, the size of the orbital basis set used to construct CI configurations, inclusion of the quantum electrodynamics (QED) corrections, and inclusion of the Breit corrections beyond the Gaunt term. We find that by far the largest effect comes from the inclusion of the inner electron shells into the CI and we studied this effect in detail.

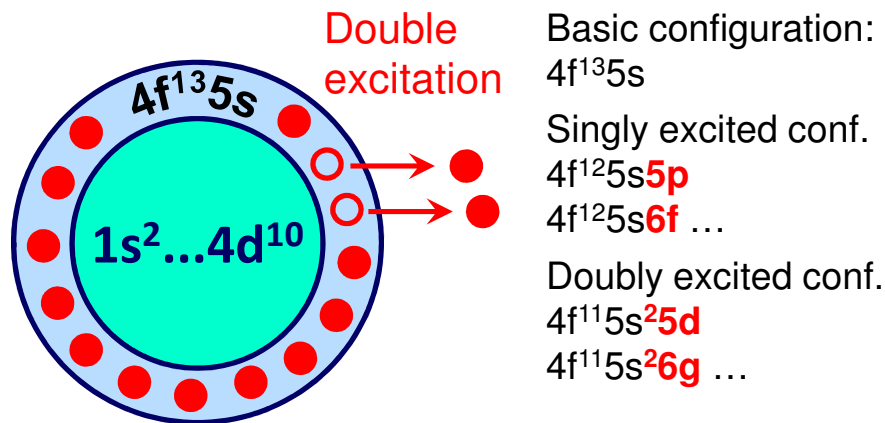


Figure 4.2: Single and double excitations from the $4f^{13}5s$ configuration. From Ref. [4].

We start with the most straightforward CI computation that includes single and double excitations from the $4f$ and $5s$ valence shells, similar to [32]. This is illustrated

in Fig. 4.2, which shows a few of the first configurations produced by exciting one and two electrons starting from the main $4f^{13}5s$ odd configuration. The excitations are allowed to each of the basis set orbitals. We begin with the basis set that includes all orbitals up to $7spdfg$ and discuss larger basis calculations below.

Next, we “open” a $4d$ shell as is illustrated in Fig. 4.3, i.e., allow all $4d$ electrons into the valence space and allow excitations of any of the 24 electrons from the $4d^{10}4f^{13}5s$ shells to the same basis set orbitals up to $7spdfg$. We find drastic changes in the frequencies of all of the (odd-even) $E1$ transitions and the position of the 1S_0 level. This effect accounts for the difference between previous CI calculations [32] which prohibited excitations from the $4d$ electrons, and CIDFS calculations [3] which allowed it. Due to such large contributions, we continued to include more and more electrons of the inner shells into the CI valence space, until all 60 electrons have been included. Both single and double excitations are allowed from the $4f, 4d, 4p, 4s$ and $3d$ shells, and only single excitations are included for all other shells. We tested that the double excitation contribution is small for these inner shells and can be omitted at the present level of accuracy. The results, obtained with different number of shells included into the CI valence space are given in Table 4.1. We note very large contributions of the excitations from the $4s$ shell, which is the main source of the difference between our results and the CIDFS calculations [3]. All calculations in Table 4.1 are carried out with the same $7spdfg$ basis set.

Three different basis sets of increasing sizes, including all orbitals up to $7spdfg$, $8spdfg$, and $10spdfg$ were used to test basis set convergence. The resulting energy differences between these different basis sets are shown in Table 4.2. The differences between results obtained with $7spdfg$ and $8spdfg$ basis sets do not exceed 262 cm^{-1} for any level. The difference between results obtained with $8spdfg$ and $10spdfg$ basis sets do not exceed 115 cm^{-1} for any level. Due to the decreasing difference with basis sets of higher principal quantum number, we concluded that the basis set has been reasonably converged at the present level of accuracy, and there was no need to include orbitals of higher principal quantum number at the time.

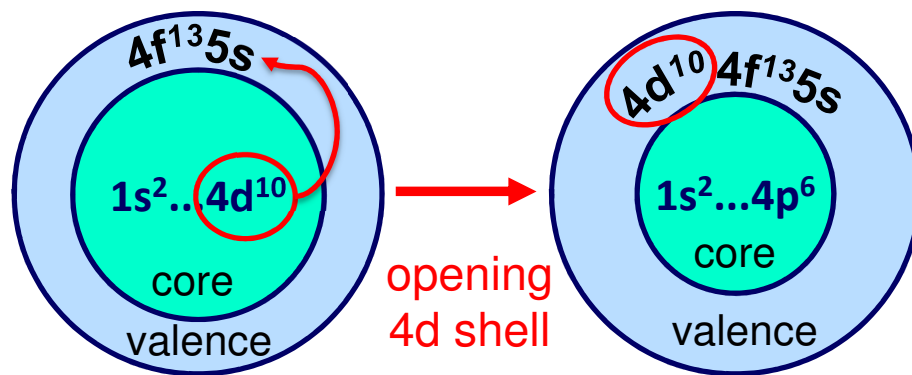


Figure 4.3: “Opening” the $4d^{10}$ shell - including it into the valence space. From Ref. [4].

Table 4.1: Energies of Ir^{17+} (in cm^{-1}) obtained using CI with different number of electronic excitations. Only configurations obtained by exciting $4f$ and $5s$ electrons are included in the “ $5s4f$ only” column. Excitation from the $4d$ shell are also included in the next column and the difference of the results is given in the column labeled “ $4d$ contr.”. Contributions of all other shells are given separately in the next columns. The results with all 60 electrons correlated by the CI are listed in the column “All shells open”. Sum of all other corrections is given in the column labeled “Other” - see text for explanation. From Ref. [4].

Configuration	5s4f only		5s4f4d		4d		4p		4s		3d		1s2s3s		3p		2p		All shells		Other	Final	
					contr.		contr.	contr.		contr.		contr.	contr.		contr.		contr.	open					
$4f^{13}5s$	${}^3F_4^o$	0	0	0	0	0	0	0	0	0	0	0	0	0	0	0	0	0	0	0	0	0	
	${}^3F_3^o$	4714	4745	31	15	14	14	15	14	14	8	8	-3	2	2	0	0	0	4781	-4	4777	0	
	${}^3F_2^o$	25170	25095	-75	14	13	13	14	13	13	75	75	-2	25	25	-4	-4	-4	25220	-34	25186	0	
	${}^1F_3^o$	30137	30253	116	51	33	33	51	33	33	73	73	-3	23	23	-4	-4	-4	30426	-31	30395	0	
$4f^{14}$	1S_0	9073	14870	5797	-931	-1994	1097	-240	183	294	144	144	143	143	143	143	143	143	143	143	143	143	143
$4f^{12}5s^2$	3H_6	36362	27813	-8549	460	1848	-403	183	294	144	144	144	143	143	143	143	143	143	143	143	143	143	143
	3F_4	46303	37623	-8680	-5	1858	-410	184	251	144	144	144	143	143	143	143	143	143	143	143	143	143	143
	3H_5	59883	51245	-8638	454	1858	-326	183	324	143	143	143	143	143	143	143	143	143	143	143	143	143	143
	3F_2	68786	60036	-8751	-188	1690	-384	253	191	64	64	64	64	64	64	64	64	64	64	64	64	64	64
	1G_4	69099	60056	-9043	165	1868	-322	184	304	143	143	143	143	143	143	143	143	143	143	143	143	143	143
	3F_3	71963	63068	-8894	146	1836	-332	179	266	146	146	146	146	146	146	146	146	146	146	146	146	146	146
3H_4	3H_4	91038	82254	-8784	78	1894	-245	187	340	142	142	142	142	142	142	142	142	142	142	142	142	142	142
	1D_2	97473	87855	-9618	-110	1735	-334	270	177	48	48	48	48	48	48	48	48	48	48	48	48	48	48
	1J_6	109332	99131	-10201	268	1809	-304	171	212	150	150	150	150	150	150	150	150	150	150	150	150	150	150

Table 4.2: Energy differences of Ir¹⁷⁺ (in cm⁻¹) obtained using CI with different sized basis sets. The differences shown are between the 8*spdfg* and 7*spdfg* basis sets, and the 10*spdfg* and 8*spdfg* basis sets. Due to the decreasing difference with larger basis sets of higher principal quantum number, we concluded that the basis set has been reasonably converged at the present level of accuracy.

		8 <i>spdfg</i> – 7 <i>spdfg</i>			10 <i>spdfg</i> – 8 <i>spdfg</i>		
Configuration		4 <i>f</i>	4 <i>d</i>	4 <i>p</i>	4 <i>f</i>	4 <i>d</i>	4 <i>p</i>
4 <i>f</i> ¹³ 5 <i>s</i>	³ F ₄ ^o	0	0	0	0	0	0
	³ F ₃ ^o	-3	-6	2	-7	-4	-1
	³ F ₂ ^o	-8	-20	-28	-3	-7	-12
	¹ F ₃ ^o	-11	-24	-28	-3	-7	-12
4 <i>f</i> ¹⁴	¹ S ₀	-86	-21	-169	28	90	115
4 <i>f</i> ¹² 5 <i>s</i> ²	³ H ₆	176	109	262	9	-50	96
	³ F ₄	142	93	242	-13	-70	76
	³ H ₅	171	97	239	8	-56	87
	³ F ₂	148	60	213	-6	-93	-34
	¹ G ₄	105	83	228	-32	-69	72
	³ F ₃	137	79	222	-9	-71	72
	³ H ₄	144	71	204	-11	-79	60
	¹ D ₂	82	37	184	-40	-104	-67
	¹ J ₆	118	34	180	-31	-101	40

In Table 4.3, we consider the contribution of the triple excitations from the 5*s*4*f* shells and found it to be small at the present level of accuracy: -600 cm⁻¹ for the ¹S₀ level and not exceeding -351 cm⁻¹ for all other levels. In Table 4.4, contributions from full Breit are computed: 420 cm⁻¹ for the ¹S₀ level and not exceeding -459 cm⁻¹ for all other levels. In Table 4.5, the contributions of QED are computed: -298 cm⁻¹ for the ¹S₀ level and not exceeding 299 cm⁻¹ for all other levels. The sum of the corrections for a large 10*spdfg* basis, triple excitations, Breit correction beyond the Gaunt term, and QED corrections [81, 82] is given in the column labeled “Other” in Table 4.1. We note that these unrelated corrections substantially cancel each other. Based on the size of the inner shell contributions and all other corrections, we estimate uncertainties of the final values for the even states to be on the order of 1000 cm⁻¹, similar for all states.

Table 4.3: Contribution of triple excitations (T) into energy levels of Ir¹⁷⁺ calculated with single and double excitations (SD). Energy levels are calculated with [7*spdfg*] basis set. Numbers under labels indicate the number of determinants used in the calculation in even parity runs. All values are given in cm⁻¹.

Conf.	Level	Energy (SD)		Δ_T
		0.86×10^6	49×10^6	
$4f^{13}5s$	3F_4	0	0	0
	3F_3	4714	4715	2
	3F_2	25170	25167	-3
	1F_3	30137	30138	1
$4f^{14}$	1S_0	9093	8493	-600
$4f^{12}5s^2$	3H_6	36361	36118	-243
	3F_4	46300	46050	-250
	3H_5	59883	59624	-259
	3F_2	68787	68521	-266
	1G_4	69098	68801	-297
	3F_3	71962	71677	-286
	3H_4	91039	90765	-274
	1D_2	97472	97121	-351
	1J_6	109332	108991	-341

4.1.2 M1 and E1 transition rates and energies

The M1 transition energies are compared with the experiment [3] in Table 4.6, and excellent agreement is observed with the exception of the ${}^1D_2 - {}^3F_3$ transition. It is unclear if there might be an issue with the experimental identification, or if the difference is due to the residual electronic correlations. The contribution of the inner shells (1*s* to 3*p*) is particularly large here, a factor of 4 larger than for any other M1 transition listed in Table 4.6, by about 200 cm⁻¹.

The E1 transition rates of Ir¹⁷⁺ (in s⁻¹) obtained using CI with different number of electronic excitations are given in Table 4.7. While opening of the 4*d* shell drastically changed the energy levels, we found only small effects on the matrix elements; the differences in transition rates were caused by differences in energies. When the

Table 4.4: Contribution of full Breit interaction (Δ_{Br}) into energy levels of Ir^{17+} calculated with Gaunt term. Energy levels are calculated with $[7spdfg]$ basis set. All values are given in cm^{-1} .

Conf.	Level	Gaunt	Full Breit	Δ_{Br}
$4f^{13}5s$	3F_4	0	0	0
	3F_3	4714	4714	1
	3F_2	25170	25159	-12
	1F_3	30137	30131	-6
$4f^{14}$	1S_0	9073	9493	420
$4f^{12}5s^2$	3H_6	36361	35910	-450
	3F_4	46300	45853	-447
	3H_5	59883	59426	-457
	3F_2	68787	68332	-455
	1G_4	69098	68650	-448
	3F_3	71962	71509	-453
	3H_4	91039	90579	-459
	1D_2	97472	97023	-449
	1J_6	109332	108875	-457

Table 4.5: Contribution of QED corrections (Δ_{Br}) into energy levels of Ir^{17+} . Energy levels are calculated with $[7spdfg]$ diagonalized basis set. All values are given in cm^{-1} .

Conf.	Level	Gaunt	Gaunt+QED	Δ_{QED}
$4f^{13}5s$	3F_4	0	0	0
	3F_3	4730	4726	-5
	3F_2	25407	25416	9
	1F_3	30376	30385	9
$4f^{14}$	1S_0	2327	2029	-298
$4f^{12}5s^2$	3H_6	42124	42401	277
	3F_4	52252	52530	278
	3H_5	65859	66149	291
	3F_2	74896	75188	292
	1G_4	75296	75580	285
	3F_3	78151	78444	293
	3H_4	97338	97640	302
	1D_2	103937	104232	294
	1J_6	115342	115641	299

excitations from the $4p$ shells were included, we found only modest changes in the energies (see Table 4.1), but drastic reduction of the values of the $E1$ matrix elements for a number of transitions. The multi-electron $E1$ transition rates are obtained from the one-body matrix elements, with the appropriate weights based on the mixing of the configurations. Allowing excitations from the $4p$ electrons accounted for previously omitted $4p - 5s$ one-electron matrix elements, whose role is particular important when the contributions from the one-electron $5s - 5p$ and $4d - 4f$ matrix elements are close in size, but have the opposite sign and, respectively, essentially cancel each other. The final numbers include correlation of all 60 electrons, but the effect of all other shells for stronger transitions was relatively small.

Previous calculations of transition rates in Ir^{17+} were only done with the FAC code [33] and did not include correlations besides the $4f5s$ electrons, leading to incorrect predictions. In particular, the ${}^3F_4 - {}^3F_4^o$ and ${}^3F_4 - {}^3F_3^o$ transition rates which should

Table 4.6: Comparison of Ir¹⁷⁺ M1 transition energies (in cm⁻¹) with experimental results [3]. Difference (in %) of the other theory (FSCC and CIDFS) values from experiment [3] are given in the last two columns. From Ref. [4].

Transition	Expt.	Present	Diff. %	FSCC	CIDFS	
4 <i>f</i> ¹³ 5 <i>s</i>	³ F ₂ ^o – ³ F ₃ ^o	20711	20409	1.5%	1.0%	2.6%
	¹ F ₃ ^o – ³ F ₄ ^o	30359	30395	-0.1%	0.5%	-0.6%
4 <i>f</i> ¹² 5 <i>s</i> ²	³ H ₅ – ³ H ₆	23640	23515	0.5%	0.8%	1.4%
	³ H ₄ – ¹ G ₄	22430	22263	0.7%	0.5%	1.9%
	¹ G ₄ – ³ F ₄	22949	22697	1.1%	1.2%	1.3%
	¹ D ₂ – ³ F ₃	23163	24093	-4.0%	-2.0%	-5.4%
	³ F ₃ – ³ F ₄	25515	25616	-0.4%	1.0%	-0.1%
	¹ D ₂ – ³ F ₂	27387	27844	-1.7%	-0.1%	-2.0%
	³ H ₄ – ³ H ₅	30798	30726	0.2%	-0.2%	1.7%

have been observable with previous predictions became extremely small, well outside of the detection range. We identified a number of other transitions for the future E1 transition search where the transition rates are above 100 s⁻¹. We have calculated all of the E1 transitions between the states listed in Table 4.1, also including ³P₂ states but only list the strongest transitions and a few representative examples where transition rate changes drastically with the opening of the 4*p* shell (these small values should be considered order-of-magnitude estimates due to large cancellations).

4.1.3 Selection of important configurations

It is necessary to be able to select the most important configurations for the valence CI space when the dimensionality of the CI problem is huge. We started with the computation of Ir¹⁶⁺, then switched to the more complicated Ir¹⁷⁺. In the case of Ir¹⁶⁺, which has 15 valence electrons, and Ir¹⁷⁺, which has 14 valence electrons, the complete basis set is limited to only a few principal quantum numbers *n* above closed core shells, e.g. [8*spdfg*]; this designation includes the orbitals 1-8*s*, 2-8*p*, 3-8*d*, 4-8*f* and 5-8*g*, where the numbers indicate principal quantum numbers and the letters *spdfg* indicate orbital angular momentum quantum numbers. Even with such a short basis

Table 4.7: $E1$ $4f^{12}5s^2 - 4f^{13}5s$ radiative transition rates A_{ab} of Ir^{17+} (in s^{-1}) obtained using CI with different number of electronic excitations: including excitations from the $4f5s$ electrons, then adding excitations from $4d$ and $4p$ shells. The final numbers include correlation of all 60 electrons. Final values of the transition wavelengths λ (in nm) and reduced $E1$ matrix elements D (in a.u.) are also listed. From Ref. [4].

Transition $a - b$	λ	D	Transition rate A_{ab}			
			$5s4f$	$+4d$	$+4p$	Final
${}^3P_2 - {}^3F_3^o$	91	4.1E-04	106	111	152	90
${}^3P_2 - {}^3F_2^o$	112	9.6E-04	727	458	276	269
${}^3P_2 - {}^1F_3^o$	118	1.2E-03	1432	1101	254	333
${}^3H_4 - {}^3F_4^o$	118	1.6E-03	798	479	366	358
${}^1D_2 - {}^3F_3^o$	118	5.2E-04	9	4	91	65
${}^3H_4 - {}^3F_3^o$	125	1.8E-03	1325	891	347	369
${}^3F_3 - {}^3F_4^o$	153	1.3E-03	379	201	140	137
${}^1D_2 - {}^3F_2^o$	155	9.9E-04	515	277	103	104
${}^1G_4 - {}^3F_4^o$	160	1.8E-03	677	362	181	184
${}^3F_3 - {}^3F_3^o$	165	1.2E-03	579	319	85	90
${}^1D_2 - {}^1F_3^o$	169	1.2E-03	498	276	105	122
${}^1G_4 - {}^3F_3^o$	174	1.7E-03	376	209	123	129
${}^3F_2 - {}^3F_3^o$	176	1.5E-04	101	60	6	1.7
${}^3H_4 - {}^1F_3^o$	184	7.2E-05	216	0.3	0.2	0.18
${}^3F_4 - {}^3F_4^o$	252	4.9E-05	57	25	0.2	0.03
${}^3F_2 - {}^3F_2^o$	274	1.6E-04	60	26	0.3	0.47
${}^3F_3 - {}^1F_3^o$	287	4.3E-04	48	19	2	2.3
${}^3F_4 - {}^3F_3^o$	287	4.9E-04	64	30	1.2	2.2
${}^1G_4 - {}^1F_3^o$	313	1.8E-04	34	15	0.02	0.2

set, the number of configurations and determinants that take part in the CI calculation is huge due to CI scaling exponentially with the number of valence electrons.

Initially, a configuration list with no weights is constructed by allowing excitations from select basic configurations. A very small subspace, consisting of about 500 relativistic configurations in our case, is used for a pre-initialization run to generate initial weights for each configuration. In this pre-initialization run, CI is ran for the very small subspace and then CI+PT is ran to obtain weights and re-order the initial configuration list by descending weights. CI is then re-ran using the re-ordered configuration list to obtain the energy levels. Several CI runs are done while increasing the number of configurations to see how energy levels are converging with increasing size of the CI space. The number of configurations selected is based on the weight of the configuration, i.e. all configurations above a weight of 10^{-3} would be selected for a small CI run, all configurations with weights above 10^{-4} would make up a medium run, and so on. Once the energy differences between subsequent CI calculations are relatively small, the CI+PT procedure is then used on the largest CI run to calculate the final energy levels. The final energy levels obtained from CI+PT are then compared with the corresponding CI result to check convergence. If PT corrections are still large, we can repeat this process from a newly re-ordered configuration list constructed from the previous largest CI+PT run. By repeating the CI and PT steps, second-order corrections iteratively decrease until convergence is met (in our case, until energy differences obtained from successive runs are below 1500 cm^{-1}), i.e., the CI space has been saturated as it has taken into account the most important configurations.

Table 4.8 displays the total number of configurations and determinants used for the largest CI+PT calculations of Ir^{16+} and Ir^{17+} energy levels. For both ions, about 3000-5000 relativistic configurations are taken into account using CI, while the remaining configurations are taken into account using CI+PT. We find that for our calculations, this is enough to reach saturation of CI. For the final calculations of Ir^{16+} energy levels, the total number of non-relativistic configurations for the odd parity was 2904, but 2030 non-relativistic configurations were used and expanded into 78156

Table 4.8: Total number of non-relativistic configurations generated (total) compared with the number of non-relativistic configurations (non-rel) used in the valence CI space of the final CI and CI+PT runs. Numbers of relativistic configurations (rel) and determinants (dets) in millions taking part in the final CI valence space in final results are also shown.

Ion	Parity	non-rel total	non-rel used	rel used	dets (10^6)
<u>CI</u>					
Ir ¹⁶⁺	even	3001	294	5112	11
	odd	2904	293	5890	6.6
Ir ¹⁷⁺	even	1633	214	3429	4.4
	odd	2281	185	3436	6.3
<u>CI+PT</u>					
Ir ¹⁶⁺	even	3001	1328	44649	365
	odd	2904	2030	78156	194
Ir ¹⁷⁺	even	1633	1633	38688	118
	odd	2281	1850	75446	391

relativistic configurations with 194×10^6 determinants. For the even parity, the total number of non-relativistic configurations was 3001, but only 1328 of them were included and expanded into 44649 relativistic configurations and 365×10^6 determinants. For the final CI+PT calculations of Ir¹⁷⁺ energy levels, 1633 non-relativistic configurations are expanded into 38688 relativistic configurations with 118×10^6 determinants for even parity. For the odd parity, a similar number of configurations and determinants are used if only expanding a single basic configuration $4f^{13}5s$, but allowing excitations from two basic configurations $4f^{13}5s$ and $4f^{12}5s5p$, there was a total of 2281 non-relativistic configurations, but only 1850 non-relativistic configurations were accounted for and expanded into 75446 relativistic configurations with 391×10^6 determinants. The selection procedure for the final configurations is explained below. The most computationally expensive run completed using this method was for the odd parity of Ir¹⁷⁺, which included 391×10^6 determinants. This run required 2 days of computation time to complete, while utilizing MPI with 40 cores.

To analyze the importance of configurations, we start from the configuration list generated by exciting electrons from a set of reference configurations to a number of non-relativistic shells. The initial list includes all possible relativistic configurations that can be obtained from the number of excitations, whether it is allowing singles (S), doubles (D), triples (T), or any combination of these excitations. The number of excitations and the number of non-relativistic shells determines the total number of configurations that will make up the list, and subsequently, the total number of determinants that will be used in the CI calculation. We take several steps in determining the importance of each configurations. First, the weight of each configuration is calculated. This is done in the CI and CI+PT routines described above. We can then count the number of times an orbital appears in non-relativistic configurations above some weight threshold and compare this data to the weighted configuration list constructed during the CI+PT routine.

Table 4.9 displays the number of times an orbital appears in the list of non-relativistic configurations for the even parity of Ir¹⁷⁺ with weights larger than threshold values of 1×10^{-3} , 1×10^{-4} , 1×10^{-5} and 1×10^{-6} . This data shows how important each orbital will be for the final CI+PT calculation. For Ir¹⁷⁺, we can see that for configurations above the 1×10^{-6} threshold value, besides the orbitals that show in the reference configurations $4f$ and $5s$, all $5p$ d f g will be important, but up to $8g$, all f and g subshells will also play an important role.

Table 4.10 shows the top 10 weighted configurations that take part of the calculations for the low-lying energy levels of Ir¹⁷⁺. For the $4f^{13} 5s$ configuration, we see that the most important configurations are those with double excitations to $4f^{11}$, and those with $5s$, $5f$, $6f$, $6g$, and $7g$ included. The $4f^{14}$ configuration have double excitations to $4f^{12}$, and those with $5f$, $6f$, $7f$, $6g$, and $7g$ as important configurations. The important configurations for the $4f^{12} 5s^2$ configuration include double excitations to $4f^{10}$, $5p$, $5f$, $6f$, $6g$ and $7g$. Configurations from triple excitations had weights less than 10^{-6} and were therefore not very important for the calculations. Due to the lower importance of triple excitations, we increase the basis set and allow just S and

D excitations in a calculation to be discussed later. We also see that in both Tables 4.9 and 4.10, the top configurations agree with the top appearances of orbitals in the configuration list.

Table 4.11 compares the top 5 weighted configurations for the Ir¹⁷⁺ calculations between a short basis set [8*spdfg*] and a longer basis set [10*spdf*]. It is clear that for the larger basis set calculation, the weights of the basic configurations decreased by a few thousandths and the top configurations remain mostly the same.

Table 4.12 shows the top 10 weighted configurations that take part of the calculations for the low-lying energy levels of Ir¹⁶⁺. For the 4*f*¹³ 5*s* configuration, we see that the most important configurations are those with double excitations to 4*f*¹¹, and those with 5*s*, 5*p*, 5*f*, 6*f*, 7*f*, 6*g*, and 7*g* included. The 4*f*¹⁴ configuration have double excitations to 4*f*¹², and those with 5*f*, 6*f*, 7*f*, 6*g*, and 7*g* as important configurations. The important configurations for the 4*f*¹² 5*s*² configuration include double excitations to 4*f*¹⁰, 5*p*, 5*f*, 6*f*, 6*g* and 7*g*. From this data, we can predict which shells must be allowed for an accurate description of the Ir¹⁶⁺ ion.

For the Ir¹⁷⁺ even parity calculations, every configuration was taken into account for, i.e. no configurations were left out in the final CI+PT calculation. The final energy levels converged after 2 runs of the CI+PT procedure for both even and odd parity runs after the pre-initialization run, i.e. CI saturated within 2 iterations of PT. However, for the Ir¹⁶⁺ and the odd parity of Ir¹⁷⁺, it was impractical to include every configuration as the inclusion of another valence electron grew the valence CI space to an unmanageable size. In this case, orbital importance must be taken into account by parts, by allowing excitations to specific shells one at a time and adding the weights to the configuration list by parts.

In summary, we have developed new MPI CI codes that for the first time allowed us to correlate all 60 electrons of Ir¹⁷⁺ in the framework of the CI approach. Our calculations explained the failed search for the *E1* transitions: the transition rates of the two transitions that were subject to search are well below detection threshold. We made reliable prediction of the *E1* and clock transition wavelengths, with the

evaluation of their uncertainties and provided predictions of the sufficiently strong $E1$ transitions for the experimental detection. As illustrated by Table 4.1, the energies of the $E1$ and clock ${}^3H_6 - {}^3F_4^o$ transitions are strongly correlated and as soon as any of the $E1$ transition wavelength is measured, we will be able to establish the clock transition energy with much higher precision. We developed a method of selecting the most important configurations of an atomic system using weights calculated during the CI and CI+PT procedures, and found them for the cases of Ir^{16+} and Ir^{17+} . The final large-scale Ir^{17+} calculations were done solely with the CI method.

The methods discussed here are very broadly applicable to many elements in the periodic table. Numerous problems in atomic physics, astrophysics, and plasma physics require accurate treatment of the open-shell systems similar to the one considered here. An exceptional speed up of the CI computations demonstrated in this work will allow one to perform computations for other systems where reliable predictions do not yet exist. Present computations were only limited by the computer memory resources presently available to us at the time this work was completed, about a year ago. At that time, the largest run took less than 3 days on 80 CPUs. This largest run was redone recently with 550 CPUs, lasting only about 13 hours, approximately 5 times faster with almost 7 times the number of CPUs. The work presented here, coupled with the development of new methods of efficiently selecting dominant configurations, and larger computational resources, will eventually lead to accurate theoretical predictions for most elements of the periodic table.

Table 4.9: Number of times an orbital appears in non-relativistic configurations with weights larger than the given threshold values. The system considered here is Ir^{17+} with even parity. S, D and T excitations are allowed from basic configurations, $4f^{14}$ and $4f^{12}5s^2$. Other than $4f$ and $5s$, all orbitals have minimum and maximum occupation numbers of 0 and 2, respectively, with $5f$ being an exception, having 0 and 3, respectively.

Orbital	1×10^{-3}	1×10^{-4}	1×10^{-5}	1×10^{-6}
$4f$	971	1963	3591	6459
$5s$	100	175	301	443
$5p$	20	38	86	134
$5d$	12	28	67	130
$5f$	15	33	69	126
$5g$	10	25	34	92
$6s$	3	9	32	64
$6p$	5	20	23	48
$6d$	6	19	36	80
$6f$	14	31	64	111
$6g$	13	27	50	109
$7s$	3	5	29	57
$7p$	6	20	24	42
$7d$	8	19	36	85
$7f$	14	27	55	105
$7g$	14	20	54	109
$8s$	4	5	27	53
$8p$	0	0	7	20
$8d$	0	0	3	16
$8f$	1	8	17	38
$8g$	13	22	39	76

Table 4.10: List of the 10 most important configurations for calculation of Ir¹⁷⁺ energy levels. Weights for $4f^{13} 5s$ were calculated for the 3F_4 level, but 3F_3 , 3F_2 and 1F_3 levels also have the approximately the same top configurations. Weights for $4f^{12} 5s^2$ were calculated for the 3H_6 level, but 3F_4 , 3H_5 and 3F_2 levels also have approximately the same top 10 configurations.

Conf.	Weight	Conf.	Weight
$4f^{13} 5s$	$J = 4, 3, 2$	$4f^{14}$	$J = 0$
$4f^{13} 5s$	0.9866	$4f^{14}$	0.9765
$4f^{11} 5s 7g^2$	0.0015	$4f^{12} 5s^2$	0.0075
$4f^{11} 5s 5f 6f$	0.0012	$4f^{13} 5f$	0.0038
$4f^{11} 5s 6g 7g$	0.0012	$4f^{12} 7g^2$	0.0017
$4f^{11} 5s 5f^2$	0.0009	$4f^{13} 6f$	0.0016
$4f^{11} 5s 6f 7f$	0.0009	$4f^{12} 6g 7g$	0.0015
$4f^{11} 5s 7f^2$	0.0008	$4f^{12} 5f 6f$	0.0015
$4f^{12} 5p 6g$	0.0008	$4f^{12} 5f^2$	0.0011
$4f^{11} 5s 5f 7f$	0.0008	$4f^{12} 7f^2$	0.0009
$4f^{11} 5s 7g 8g$	0.0006	$4f^{12} 6f 7f$	0.0009
		$4f^{12} 5s^2$	$J = 6, 4, 5, 2$
		$4f^{12} 5s^2$	0.9778
		$4f^{12} 5p^2$	0.0053
		$4f^{11} 5s^2 5f$	0.0022
		$4f^{10} 5s^2 7g^2$	0.0013
		$4f^{11} 5s 5p 6g$	0.0012
		$4f^{11} 5s^2 6f$	0.0011
		$4f^{11} 5s 5p 7g$	0.0009
		$4f^{10} 5s^2 6g 7g$	0.0009
		$4f^{12} 7f^2$	0.0009
		$4f^{10} 5s^2 5f 6f$	0.0008

Table 4.11: Comparison of top 5 most important configurations for Ir^{17+} between short basis set $[8spdfg]$ and long basis set $[10spdf]$.

Conf.	Weight	Conf.	Weight
<i>8spdfg</i>		<i>10spdf</i>	
$4f^{13} 5s$	$J = 4, 3, 2$		
$4f^{13} 5s$	0.9866	$4f^{13} 5s$	0.9848
$4f^{11} 5s 7g^2$	0.0015	$4f^{11} 5s 5f^2$	0.0039
$4f^{11} 5s 5f 6f$	0.0012	$4f^{11} 5s 5g^2$	0.0013
$4f^{11} 5s 6g 7g$	0.0012	$4f^{11} 5s 5p 5f$	0.00005
$4f^{11} 5s 5f^2$	0.0009	$4f^{12} 5s 5p$	0.00003
$4f^{14}$	$J = 0$		
$4f^{14}$	0.9765	$4f^{14}$	0.9750
$4f^{12} 5s^2$	0.0075	$4f^{12} 5s^2$	0.0055
$4f^{13} 5f$	0.0038	$4f^{13} 5f$	0.0050
$4f^{12} 7g^2$	0.0017	$4f^{12} 5f^2$	0.0045
$4f^{13} 6f$	0.0016	$4f^{12} 5g^2$	0.0017
$4f^{12} 5s^2$	$J = 6, 4, 5, 2$		
$4f^{12} 5s^2$	0.9778	$4f^{12} 5s^2$	0.9758
$4f^{12} 5p^2$	0.0053	$4f^{11} 5s^2 5f$	0.0037
$4f^{11} 5s^2 5f$	0.0022	$4f^{12} 5p^2$	0.0029
$4f^{10} 5s^2 7g^2$	0.0013	$4f^{10} 5s^2 5f^2$	0.0020
$4f^{11} 5s 5p 6g$	0.0012	$4f^{11} 5s 5p 5g$	0.0001

Table 4.12: List of the 10 most important configurations for calculation of Ir¹⁶⁺ energy levels E (cm⁻¹) and their weights W .

Configuration	J	E	W	Important Configurations
$4f^{13} 5s^2$	$7/2$	0	0.9775	$4f^{13} 5s^2$
			0.0057	$4f^{13} 5p^2$
			0.0016	$4f^{12} 5s 5p 6g$
			0.0015	$4f^{11} 5s^2 7g^2$
			0.0013	$4f^{11} 5s^2 5f 6f$
			0.0012	$4f^{11} 5s^2 6g 7g$
			0.0010	$4f^{11} 5s^2 5f^2$
			0.0010	$4f^{12} 5s 5p 7g$
			0.0008	$4f^{11} 5s^2 7f^2$
			0.0008	$4f^{11} 5s^2 5f 7f$
$4f^{13} 5s^2$	$5/2$	24770	0.9776	$4f^{13} 5s^2$
			0.0056	$4f^{13} 5p^2$
			0.0016	$4f^{12} 5s 5p 6g$
			0.0015	$4f^{11} 5s^2 7g^2$
			0.0013	$4f^{11} 5s^2 5f 6f$
			0.0012	$4f^{11} 5s^2 6g 7g$
			0.0010	$4f^{11} 5s^2 5f^2$
			0.0010	$4f^{12} 5s 5p 7g$
			0.0010	$4f^{12} 5s 5p 5g$
			0.0008	$4f^{11} 5s^2 7f^2$
$4f^{14} 5s$	$1/2$	37861	0.9778	$4f^{14} 5s$
			0.0039	$4f^{13} 5s 5f$
			0.0017	$4f^{12} 5s 7g^2$
			0.0016	$4f^{13} 5s 6f$
			0.0015	$4f^{12} 5s 5f 6f$
			0.0014	$4f^{12} 5s 6g 7g$
			0.0012	$4f^{12} 5s 5f^2$
			0.0010	$4f^{13} 5p 6g$
			0.0009	$4f^{12} 5s 5f 7f$
			0.0009	$4f^{12} 5s 6f 7f$

4.2 Optical clocks based on the Cf^{15+} and Cf^{17+} ions

The work described in this section is published in Ref. [34]. Here, we explore the possibility of developing optical clocks using the transitions between the ground and a low-lying excited state of the highly-charged Cf^{15+} and Cf^{17+} ions. Three out of eight main Cf isotopes have a long half-life: $A = 249, I = 9/2$ (351 y), $A = 250, I = 0$ (13.1 y), and $A = 251, I = 1/2$ (898 y), where A is the number of nucleons and I is the nuclear spin. Using the CI+all-order approach, we predicted the energies of clock transitions. Calculations of wavelengths of clock transitions and other relevant atomic properties, as well as an analysis of a number of systematic effects that affect the accuracy and stability of the optical clocks, including electric quadrupole, micromotion, and quadratic Zeeman shifts of the clock transitions, can be found in Ref. [34].

Both Cf^{15+} and Cf^{17+} ions have the $[1s^2, \dots, 5d^{10}, 6s^2]$ core. The former, Cf^{15+} , is a Bi-like ion with three valence electrons above the core, while Cf^{17+} has one valence electron above the core, allowing to consider it as a univalent element. But as a detailed analysis shows, more correct and accurate results are obtained if we consider Cf^{17+} as a trivalent ion including both 6s electrons into the valence field. This is particularly important for correct determination of the lowest-lying even-parity energy levels whose main configuration, according to our calculation, is $(6s 5f^2)$, which contains an unpaired 6s electron.

Both the Cf^{15+} and Cf^{17+} ions were studied previously in Refs. [83, 84] and found to be particularly good candidates for testing variation of the fine-structure constant. The calculation carried out in Ref. [84] identified the ground state $(5f6p^2 \ ^2F_{5/2}^o)$ and the first excited state $(5f^26p \ ^4I_{9/2}^o)$ of Cf^{15+} as the states with high sensitivity to α variation and convenient clock wavelength. The dimensionless sensitivity factor $|\Delta K|$ to a variation of α for the Cf^{17+} and Cf^{15+} clock pair was predicted to be 107 [28], while the largest $|\Delta K|$ factor for any of the currently operating clock pair is 7 (for $E3/E2$ transitions in Yb^+), with most others below 1.

We consider Cf^{15+} and Cf^{17+} as ions with three valence electrons above closed cores $[1s^2, \dots, 5d^{10}6s^2]$ and $[1s^2, \dots, 5d^{10}]$, respectively. We start from the solution of the

Dirac-Hartree-Fock (DHF) equations in the V^{N-3} approximation for both ions, where N is the total number of valence electrons. The initial self-consistency procedure was carried out for the core electrons and then the $5f, 6p, 6d, 7s$, and $7p$ orbitals (and also $6s$ in the case of Cf^{17+}) were constructed in the frozen-core potential. The remaining virtual orbitals were formed using a recurrent procedure described in [2, 85]. The newly constructed functions were then orthonormalized with respect to the functions of the same symmetry.

For both ions, the basis sets included in total 7 partial waves ($l_{\text{max}} = 6$) and orbitals with principal quantum number n up to 25. We included the Breit interaction on the same footing as the Coulomb interaction at the stage of constructing the basis set. QED corrections were also included following Ref. [5, 86].

We use the CI (as described in Section 2.1.6) and CI+MBPT (as described in Section 2.1.10) methods to see how large core correlations and higher-order effects were, and use the CI+all-order (as described in Section 2.1.11) method for final calculations. In general, we can express the effective Hamiltonian as

$$H_{\text{eff}}(E) = H_{\text{FC}} + \Sigma(E), \quad (4.1)$$

where H_{FC} is the Hamiltonian in the frozen-core approximation, and the energy-dependent operator $\Sigma(E)$ accounts for virtual excitations of the core electrons. We constructed this operator in three ways: using (i) second-order many-body perturbation theory (MBPT) over residual Coulomb interaction [87], (ii) the linearized coupled cluster single-double (LCCSD) method [64, 88], and (iii) the coupled cluster single double (valence) triple (CCSDT) method. In the last case, using the expressions for cluster amplitudes derived in Ref. [89], we included the non-linear (NL) terms and valence triple excitations into the formalism of the CI+all-order method developed in Ref. [64]. We note that the equations for the valence triples are solved iteratively. In the following we refer to these approaches, as the CI+MBPT, CI+LCCSD, and CI+CCSDT methods, respectively.

The sets of Cf^{15+} configurations for the odd- and even-parity states were constructed by allowing single and double excitations from the $5f6p^2$ and $5f^26p$ configurations and from the $6p^26d$, $5f6p6d$ and $5f^26d$ configurations, respectively, to $7 - 20s$, $7 - 20p$, $7 - 20d$, $6 - 19f$, and $5 - 13g$ shells (we designate it as $[20spd19f13g]$). The sets of Cf^{17+} configurations for the odd- and even-parity states were formed allowing single and double excitations from the $6s^25f$ and $6s^26p$ and from the $6s5f^2$ and $6s5f6p$ configurations, respectively, to $[20spd19f13g]$. We checked for both ions that if we allowed the single and double excitations to higher lying f and g shells and also triple excitations from the main configurations, the energies (counted from the ground state) changed only by few tens cm^{-1} .

The level schemes for low-lying levels of Cf^{17+} and Cf^{15+} are given in Fig. 4.4 and Fig. 4.5, respectively. The energies of the lowest-lying states of Cf^{15+} and Cf^{17+} obtained in different approximations are listed in Table 4.13. The energies of the excited states (in cm^{-1}) are counted from the ground state. The assignments of the Cf^{15+} odd levels are from Ref. [84]. For designation of all other terms we use the main configuration and the total angular momentum J of the state as a subscript.

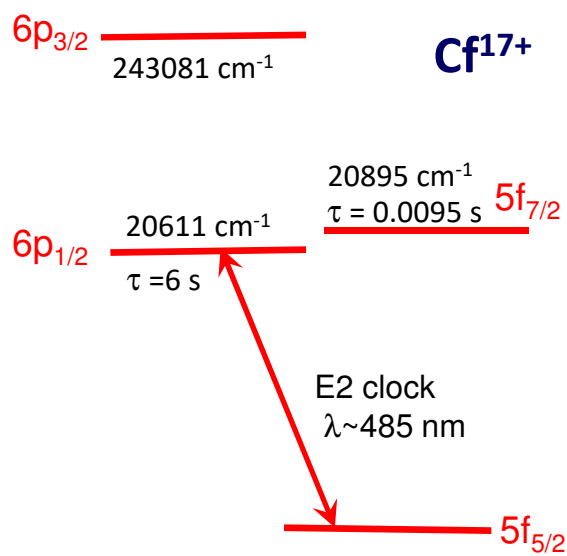


Figure 4.4: The level scheme for low-lying odd-parity levels of Cf^{17+} . From Ref. [34].

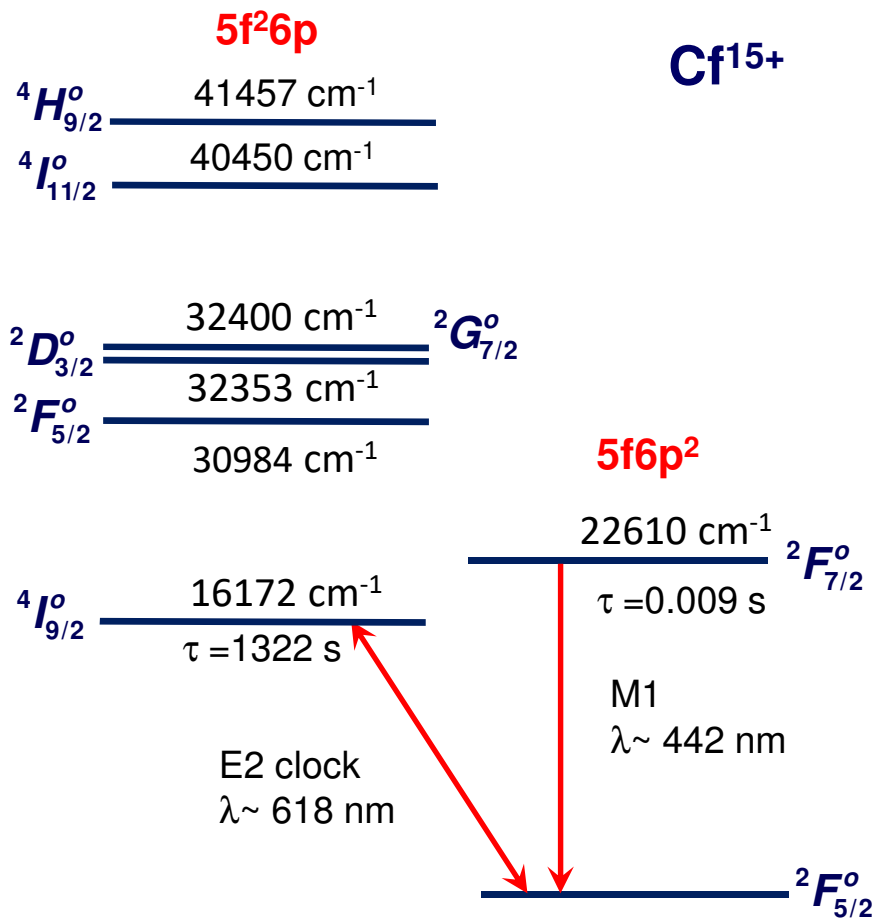


Figure 4.5: The level scheme for low-lying odd-parity levels of Cf¹⁵⁺. From Ref. [34].

Table 4.13: The energies of the excited states (in cm^{-1}), counted from the ground state, calculated in the CI and CI+MBPT approximations. Contributions from higher-order (HO) correlations (difference of the CI+LCCSD and CI+MBPT calculations.) and from the NL terms and triple excitations (difference of the CI+CCSDT and CI+LCCSD calculations) and estimated contributions of higher partial waves ($l > 6$) are given separately in columns HO, NLTr, and Extrp. The final values, given in the column labeled “Final”, are obtained as the sum of the CI+MBPT values and HO, NLTr, and Extrp corrections. We use the main configuration and the total angular momentum J as a subscript to designate the Cf^{15+} even-parity levels and the levels of Cf^{17+} . From Ref. [34].

	Level	CI	CI+MBPT	HO	NLTr	Extrp	Final	Ref. [83]	Ref. [5]	Ref. [84]
Cf^{15+}	$5f6p^2\ ^2F_{5/2}^o$	0	0	0	0	0	0	0	0	0
	$5f^26p\ ^4I_{9/2}^o$	28930	10549	2907	3675	-959	16172	12898	12898	12314
	$5f6p^2\ ^2F_{7/2}^o$	22269	22388	-107	486	-158	22610	22018	22018	21947
	$5f^26p\ ^2F_{5/2}^o$	43441	25803	2242	3741	-802	30984	27127	27127	26665
	$5f^26p\ ^2D_{3/2}^o$	45515	26984	2483	3855	-969	32353	27750	27750	27750
	$5f^26p\ ^2G_{7/2}^o$	43552	28809	1276	3081	-765	32400	29214	29214	28875
	$5f^26p\ ^4I_{11/2}^o$	51995	35979	1715	3717	-961	40450	37081	37081	36564
	$5f^26p\ ^4H_{9/2}^o$	52793	37304	1522	3564	-934	41457	37901	37901	37392
	$(6p^26d)_{3/2}$	520444	544228	-3419	-4383	1089	537515			
	$(5f6p6d)_{9/2}$	534519	545581	-1612	-2445	249	541773			
Cf^{17+}	$(5f6p6d)_{7/2}$	538082	548797	-1634	-2152	235	545245			
	$(5f6p6d)_{5/2}$	538863	549387	-1508	-2156	216	545939			
	$(5f6p6d)_{3/2}$	547123	556562	-1207	-1907	190	553637			
	$(6s^2\ 5f)_{5/2}^o$	0	0	0	0	0	0	0	0	0
	$(6s^2\ 6p)_{1/2}^o$	10104	22118	-1402	-1126	1021	20611	18686	18686	
	$(6s^2\ 5f)_{7/2}^o$	19682	22116	-1102	-152	33	20895	21848	21848	
	$(6s^2\ 6p)_{3/2}^o$	228778	245070	-1783	-1341	1136	243081	242811	242811	
	$(6s\ 5f^2)_{7/2}$	206421	202671	-496	-340	-945	200890			
	$(6s\ 5f^2)_{9/2}$	211719	208829	-707	-415	-942	206765			
	$(6s\ 5f^2)_{3/2}$	212749	210608	-860	-414	-833	208501			
$(6s\ 5f^2)_{5/2}$	219342	213728	-1663	-1524	-359	210182				
$(6s\ 5f\ 6p)_{5/2}$	206500	220621	-1855	-1252	-463	217050				

In the third and fourth columns, we present the pure CI and CI+MBPT values. Contributions from higher-order (HO) correlations (difference of the CI+LCCSD and CI+MBPT calculations) and from the NL terms and triple excitations (difference of the CI+CCSDT and CI+LCCSD calculations) are given separately in columns labeled “HO” and “NLTr”. Following an empiric rule obtained for Ag-like ions in Ref. [90] and applied for Cd-like and Sn-like ions in Ref. [91], we estimate the contribution of the higher ($l > 6$) partial waves as the contribution of the $l = 6$ partial wave obtained as the difference of two calculations where all intermediate sums in the all-order and MBPT terms are restricted to $l_{\max} = 6$ and $l_{\max} = 5$. This contribution is listed in Table 4.13 in the column labeled “Extrap”. The final theoretical results, listed in the Final column, are obtained as the sum of the CI+MBPT values and HO, NLTr, and Extrap corrections.

We find that the clock transition energies between the ground and first excited state are very sensitive to different corrections for both ions. The CI+MBPT value differs from the CI value by more than a factor of 2 for both ions, i.e., the contribution of the core-valence correlation corrections is as large as the CI result. An inclusion of the HO corrections, the NL terms and valence triples in the framework of the CI+LCCSD and CI+CCSDT methods further changed the energies by several thousands of cm^{-1} .

The Cf^{15+} clock transition energy found at the CI+LCCSD stage is in a reasonable agreement with the results of Refs. [5, 84]. The quadratic NL terms and valence triples, contributing 3675 cm^{-1} to the transition energy, were not taken into account in Refs. [5, 84], which explains the difference between the present result and the clock transition energy predicted in those works. Taking into account the importance of the NL terms and valence triple excitations, and also noting that the present calculation still omits the core triples and higher-order NL terms, we estimate the uncertainty of the clock transition energies as half of the difference between the CI+CCSDT and CI+LCCSD values.

This conservative estimate is based on a conclusion drawn from calculations for Na [92] and Cs [93], that the contribution from the valence triples and NL terms is

(much) larger than the contribution from core triples. Thus, the uncertainty of the clock transition energy is $\sim 1800 \text{ cm}^{-1}$ for Cf^{15+} , and $\sim 600 \text{ cm}^{-1}$ for Cf^{17+} . Taking these uncertainties into account, we neglect corrections to the transition energies due to effective three-particle interactions between valence electrons. These corrections were found to be at the level of 100 cm^{-1} or less for the low-lying states of Cf^{15+} [5].

Beyond the calculations of the energy levels, other properties of the low-lying states, such as wavelengths between the ground and excited states, and the lifetimes of the excited states for Cf^{15+} and Cf^{17+} , were obtained in the CI+CCSDT approximation and compared with other calculations where available [34]. A number of systematic effects that affect the accuracy and stability of the optical clocks were also analyzed in detail, including the electric quadrupole, micromotion, and quadratic Zeeman shifts of the clock transitions. The hfs magnetic dipole constants of the clock states and the BBR shifts of the clock transitions were also calculated. The calculations done here in Ref. [34] act as a guide for future experimental work, providing a detailed assessment of both ions for clock development.

Chapter 5

THE 3C/3D LINE INTENSITY RATIO IN FE XVII

The work described in this chapter is published in Ref. [43]. Space X-ray observatories, such as *Chandra* and *XMM-Newton*, resolve *L*-shell transitions of iron dominating the spectra of many hot astrophysical objects. Some of the brightest lines arise from Fe XVII (Ne-like iron) around 15 Å: the resonance line 3C ($[(2p^5)_{1/2}3d_{3/2}]_{J=1} \rightarrow [2p^6]_{J=0}$) and the intercombination line 3D ($[(2p^5)_{3/2}3d_{5/2}]_{J=1} \rightarrow [2p^6]_{J=0}$). They are crucial for diagnostics of electron temperatures, elemental abundances, ionization conditions, velocity turbulences, and opacities. However, for the past four decades, their observed intensity ratios persistently disagreed with advanced plasma models, diminishing the utility of high-resolution X-ray observations. *L*-shell soft X-ray fluorescence of Fe XVII ions was just measured in an electron beam ion trap following resonant photo-excitation using synchrotron radiation provided by the P04 beamline at PETRA III [43]. The experiment measured the most accurate 3C/3D oscillator strength ratio to date, in an attempt to explain the discrepancy between theory and experiment. We carried out a precision calculation correlating all 10 electrons, including full Breit and QED [5] corrections, to predict the transition rates with 1-2% accuracy. Our calculations ruled out incomplete inclusion of the electronic correlations in theoretical calculations as the potential explanation of the puzzle.

In this work [43], we start from the solution of the DHF equations in the central field approximation to construct the one-particle orbitals. The calculations are carried out using the CI method, as described in Section 2.1.6, correlating all 10 electrons. Breit interaction is included in all calculations, and the QED effects are included following Ref. [48]. The basis sets of increasing sizes are used to check for convergence of the values. The basis set is designated by the highest principal quantum number for each

partial wave included. For example, $[5spdf6g]$ means that all orbitals up to $n = 5$ are included for the $spdf$ partial waves and $n = 5, 6$ orbitals are included for the g partial waves. We find that inclusion of the $6, 7h$ orbitals does not modify the results of the calculations and omit higher partial waves.

We start with all possible single and double excitations to any orbital up to $5spdf6g$ from the $2s^22p^6$, $2s^22p^53p$ even and $2s^22p^53s$, $2s^22p^53d$, $2s2p^63p$, $2s^22p^54d$, $2s^22p^55d$ odd configurations, correlating 8 electrons. We verified that inclusion of the $2s2p^63s$, $2s^22p^54f$, $2s^22p^55f$ even and $2s2p^64p$, $2s^22p^54s$, and $2s^22p^55s$ odd configurations as basic configurations have negligible effect on either energies of relevant matrix elements.

The only unusually significant change in the ratio, by 0.07, is due to the inclusion of the $2s^22p^33d^3$ and $2p^53d^3$ configurations. These are obtained as double excitations from the $2s^22p^53d$ odd configuration, prompting the inclusion of the $2s^22p^54d$, $2s^22p^55d$ to the list of the basic configurations.

Contributions to the energies of Fe^{16+} calculated with different size basis sets and number of configurations are listed in Table 5.1. The results are compared with experimental data from the NIST database [94] and from a revised analysis of the experimental data [95]. We use LS coupling and NIST data term designations for comparison purposes, but note that jj coupling would be more appropriate for this ion. Contributions to the E1 reduced matrix elements $D(3D) = D(2p^6\ ^1S_0 - 2p^53d\ ^3D_1)$ and $D(3C) = D(2p^6\ ^1S_0 - 2p^53d\ ^1P_1)$ and the ratio of the respective oscillator strengths

$$R = \left(\frac{D(3C)}{D(3D)} \right)^2 \times \frac{\Delta E(3C)}{\Delta E(3D)}$$

are listed in Table 5.2. The energy ratio is 1.01655.

Table 5.1: Contributions to the energies of Fe¹⁶⁺ calculated with increased size basis sets and number of configurations. The results are compared with experiment. All energies are given in cm⁻¹ with exception of the last line that shows the difference of the 3C and 3D energies in eV. The basis set is designated by the highest quantum number for each partial wave included. For example, 12*spdfg* means that all orbitals up to $n = 12$ are included for *spdfg* partial waves. Contributions from triple excitations, excitations from the 1*s*² shells, and QED contributions are given separately. From Ref. [43].

Configuration	Expt. [94]	Expt. [95]	[5 <i>spdf6g</i>]	Triples	1 <i>s</i> ²	+ [12 <i>spdfg</i>]	+ [17 <i>dfg</i>]	QED	Final	Diff. [94]	Diff. [95]	Diff. [95]
2 <i>p</i> ⁶	0	0	0	0	0	0	0	0	0	0	0	0
¹ S ₀												
2 <i>p</i> ⁵ 3 <i>p</i>	6093450	6093295	6087185	6	254	3876	772	67	6092159	1291	1136	0.02%
³ S ₁												
2 <i>p</i> ⁵ 3 <i>p</i>	6121690	6121484	6116210	-21	24	2886	701	43	6119842	1848	1642	0.03%
³ D ₂												
2 <i>p</i> ⁵ 3 <i>p</i>	6134730	6134539	6129041	-23	25	3015	711	94	6132864	1866	1675	0.03%
³ D ₃												
2 <i>p</i> ⁵ 3 <i>p</i>	6143850	6143639	6138383	-11	41	2825	704	82	6142025	1825	1614	0.03%
¹ P ₁												
2 <i>p</i> ⁵ 3 <i>s</i>	5849490	5849216	5842248	-10	108	3408	735	787	5847276	2214	1940	0.03%
² P ₃												
2 <i>p</i> ⁵ 3 <i>s</i>	5864770	5864502	5857770	-10	70	3303	708	784	5862626	2144	1876	0.03%
¹ S ₀												
2 <i>p</i> ⁵ 3 <i>s</i>	5960870	5960742	5953697	-10	74	3364	717	1042	5958883	1987	1859	0.03%
³ P ₁												
2 <i>p</i> ⁵ 3 <i>d</i>	6471800	6471640	6466575	-11	16	2384	665	87	6469717	2083	1923	0.03%
³ P ₂												
2 <i>p</i> ⁵ 3 <i>d</i>	6486400	6486183	6481385	-13	16	2250	658	86	6484383	2017	1800	0.03%
³ F ₄												
2 <i>p</i> ⁵ 3 <i>d</i>	6486830	6486720	6482549	-12	27	1745	622	97	6485028	1802	1692	0.03%
³ F ₃												
2 <i>p</i> ⁵ 3 <i>d</i>	6493030	6492651	6488573	-14	26	1740	607	84	6491016	2014	1635	0.03%
¹ D ₂												
2 <i>p</i> ⁵ 3 <i>d</i>	6506700	6506537	6502481	-17	21	1696	627	88	6504895	1805	1642	0.03%
³ D ₃												
2 <i>p</i> ⁵ 3 <i>d</i>	6515350	6515203	6511163	-18	18	1762	604	87	6513617	1733	1586	0.02%
³ D ₁												
2 <i>p</i> ⁵ 3 <i>d</i>	6552200	6552503	6548550	-16	-3	1747	616	134	6551029	1171	1474	0.02%
³ F ₂												
2 <i>p</i> ⁵ 3 <i>d</i>	6594360	6594309	6589977	-16	22	1729	629	335	6592676	1684	1633	0.02%
³ D ₂												
2 <i>p</i> ⁵ 3 <i>d</i>	6600950	6600998	6596316	-17	14	1947	641	334	6599235	1715	1763	0.03%
¹ F ₃												
2 <i>p</i> ⁵ 3 <i>d</i>	6605150	6605185	6600744	-17	19	1803	610	343	6603501	1649	1684	0.03%
¹ P ₁												
2 <i>p</i> ⁵ 3 <i>d</i>	6660000	6660770	6656872	-8	-52	1743	619	288	6659462	538	1308	0.02%
3C-3D	13.3655	13.4234	13.4302	0.0009	-0.0061	-0.0005	0.0004	0.0191	13.4440	-0.0785	-0.0206	0.15%

We include a very wide range of configurations obtained by triple excitations from the basic configurations as well as excitations from the $1s^2$ shell and find negligible corrections to both energies and matrix elements as illustrated by Tables 5.1 and 5.2. These contributions are listed as “Triples” and “ $1s^2$ ” in both tables. Significant increase of the basis set from $[5spdf6g]$ to $[12spdfg]$ improves the agreement of energies with experiment but gives a very small, -0.009 , contribution to the ratio. We find that the weights of the configurations containing $12fg$ orbitals are several times higher than those containing $12spd$ orbitals, so we expand the basis to include more dfg orbitals. We also include $2s^22p^3nd^3$ and $2p^5nd^3$ configurations up to $n = 14$. The contributions to the energies of the orbitals with $n = 13 - 17$ are $3 - 5$ times smaller than those with $n = 6 - 12$, clearly showing the convergence of the values with the increase of the basis set. The effect on the ratio is negligible. The uncertainty of the NIST database energies, 3000 cm^{-1} is larger than our differences with the experiment. The energies from the revised analysis of Fe^{16+} spectra [95] are estimated to be accurate to about 90 cm^{-1} and the scatter of the differences of different levels with experiment is reduced. The last line of Table 5.1 shows the difference of the $3C$ and $3D$ energies in eV, with the final value $13.44(5)\text{eV}$. We explored several different ways to construct the basis set orbitals. While the final results with infinitely large basis set and complete configurations set should be identical, the convergence properties of the different basis sets vary, giving about 0.04 difference in the ratio and 0.04 eV in the $3C - 3D$ energy difference at the $12spdfg$ level. Therefore, we set an uncertainty of the final value of the ratio to be 0.05 . As an independent test of the quality and completeness of the current basis set, we compare the results for $D(3C)$ and $D(3D)$ obtained in length and velocity gauges for the $[12spdfg]$ basis, see rows L and V in Table 5.2. The difference of the results is only 0.001 .

Table 5.2: Contributions to the $E1$ reduced matrix elements $D(3D) = D(2p^6\ ^1S_0 - 2p^53d\ ^3D_1)$ and $D(3C) = D(2p^6\ ^1S_0 - 2p^53d\ ^1P_1)$ (in a.u.) and the ratio of the respective oscillator strengths R . See caption of Table 5.1 for designations. L and V rows compared results obtained in length and velocity gauges for the $[12spdfg]$ basis. All other results are calculated using the length gauge. Transition rates are listed in the last row in s^{-1} . From Ref. [43].

		$D(3C)$	$D(3D)$	Ratio
$[5spdf6g]$		0.33492	0.17842	3.582
$[5spdf6g]$	+Triples	0.33493	0.17841	3.583
	Triples	0.00001	-0.00001	
$[5spdf6g]$	+ $1s^2$	0.33480	0.17849	3.577
	$1s^2$	-0.00012	0.00007	
$[12spdfg]$	L	0.33527	0.17884	3.573
	V	0.33551	0.17894	3.574
$+ [12spdfg]$		0.00036	0.00042	
$+ [17dfg]$		-0.00001	0.00001	
QED		-0.00017	0.00030	
Final		0.33498	0.17921	3.552
Recomm.				3.55(5)
Transition rate		2.238×10^{13}	6.098×10^{12}	

Chapter 6

THE LOWEST-LYING ODD-PARITY ATOMIC LEVELS IN Ac

The work described in this chapter is published in Ref. [96]. Actinium ($Z = 89$) lends its name to the actinide series, of which it is the first member. The longest-lived isotope of actinium ^{227}Ac ($\tau_{1/2} \approx 22\text{y}$) is found in trace amounts as a member in the decay chain of natural ^{235}U . Actinium isotopes can be produced in nuclear reactors enabling their use in various applications based on their specific radioactivity. The isotope ^{225}Ac , an α -emitter with a half-life of 10 days, is used in cancer radiotherapy [97, 98, 99], while ^{227}Ac is considered for use as the active element of radioisotope thermoelectric generators. In combination with beryllium, ^{227}Ac is an effective neutron source [100], applied in neutron radiography, tomography and other radiochemical investigations. Moreover, ^{227}Ac is used as a tracer for deep seawater circulation and mixing [101]. On the fundamental-physics side, actinium can be considered as a possible system to study parity-nonconservation and time-reversal-invariance violation effects [102, 103]. Rare isotopes of actinium are produced and were studied at different on-line facilities worldwide. These research activities started at TRIUMF, Canada [104] and, together with contributions from the LISOL facility in Belgium [105], are still ongoing. At ISOLDE CERN, production of the isotope ^{229}Ac was investigated, acting as mother for the ^{229}Th isomer proposed as a nuclear clock [106]. Further rare isotopes will become available with high yield at the Facility for Rare Isotope Beams (FRIB) [107]. Studies of rare actinium isotopes contribute to deriving nuclear physics properties and trends in this region of the nuclear chart and help to decode astrophysical processes, to understand fundamental interactions, and to develop practical applications, for example, in nuclear medicine and material sciences.

Table 6.1: The determined excitation energies and lifetimes, and comparison with theory and literature. From Ref. [96].

State		Energy (cm ⁻¹)			τ (ns)			
		Exp.	Calc.	Lit.	Exp.	Calc. I	Calc. II	Lit. [116, 117]
$7s^27p$	$^2P_{1/2}^o$	7477.36(4)	7701(250)	7565 [116]	668(11)	647	707(53)	733(70)
$7s^27p$	$^2P_{3/2}^o$	12 276.59(2)	12 475(250)	12 345 [116]	255(7)	209	219(16)	238(20)
$7s7p6d$	$^4F_{3/2}^o$	13 712.74(3)	13 994(370)	13 712.90 [118]	352(11)	327	351(29)	317(30)

The atomic structure of actinium was elucidated by Judd who calculated the ordering and properties of low-lying levels of actinide atoms [108]. This work was extended by calculations of energy differences between the lowest states [109] and a prediction of the parameters of electric-dipole ($E1$) transitions in actinium [110] using the Hartree-Fock method, as well as other theoretical studies [111, 112, 113, 114, 115].

Recently, Dzuba, Flambaum, and Roberts calculated atomic parameters of 86 low-lying states of neutral actinium with energies below $36\,218\text{ cm}^{-1}$ [116]. Of these, only 28 levels had been confirmed experimentally prior to the present work. In particular, puzzling was the absence of the lowest-lying odd-parity levels $7s^27p\ ^2P_{1/2}^o$ and $7s^27p\ ^2P_{3/2}^o$, which should be directly accessible by $E1$ transitions from the $7s^26d\ ^2D_{3/2}$ even-parity ground state. Since these predicted strong transitions are of primary importance for spectroscopic applications (e.g., fluorescence and photoionization spectroscopy, optical pumping, cooling and trapping, etc.), experimental confirmation and determination of these states' parameters (e.g., accurate energies, lifetimes, hyperfine structure, etc.) are urgently needed. In this work, a new theoretical calculation of actinium levels is presented which allows the determination of several atomic level properties. Therefore, the present work also sets a benchmark of theoretical accuracy in Ac, tests methods to estimate theoretical uncertainties, and identifies future directions of theory development. Precise atomic calculations of Ac hyperfine constants and isotope shifts will be used for accurate extraction of nuclear properties from forthcoming laser-spectroscopy experiments.

A comparison of the calculated and experimentally determined energies and

lifetimes is shown in Table 6.1. While we list results for the three states of experimental interest, we calculated energies of 18 states using the CI+all-order approach, as described in Section 2.1.11, including 114 840 configurations, and demonstrated convergence of the results with increasing number of configurations. QED and full Breit corrections are included as described in Refs. [119, 34]. Our results for even and odd levels agree with previous experiments [118] to $40 - 120 \text{ cm}^{-1}$ and $200 - 350 \text{ cm}^{-1}$, respectively, with theory values being larger than the experimental ones in all cases. Such regular differences with experiment let us predict that we overestimate the energies of the 2P_J levels by about 200 cm^{-1} , with about 50 cm^{-1} uncertainties which is in excellent agreement with measured values. We list the lifetimes obtained using theoretical values of energies and electric-dipole ($E1$) matrix elements in the column labeled “Calc. I”. We use experimental energies and theoretical values of $E1$ matrix elements to calculate the final theoretical lifetimes listed in column labeled “Calc. II”. The uncertainties in the lifetimes are estimated from the size of the higher-order corrections to $E1$ matrix elements determined from the difference of the CI+LCCSD values and another calculation that combines CI with many-body perturbation theory [62].

Note that the lifetime values listed in [116] were recently corrected [117]; the corrected values are given in Table 6.1. Within the respective uncertainties, there is agreement between the two independent calculations and the experiment.

Chapter 7

PREDICTING ATOMIC PROPERTIES OF NEGATIVE IONS

Negative ions are important for both fundamental and practical reasons, such as medical applications [120, 121]. They are key constituents of terrestrial and space-based plasmas [122], and they play crucial roles in many chemical reactions, as highlighted, for example, in the very recent study of the astatine negative ion [121]. Beams of short-lived radioactive nuclei are needed for frontier experimental research in nuclear structure, reactions, and astrophysics, and negatively charged radioactive ion beams have unique advantages and can provide the highest beam quality with continuously variable energies [123]. Laser cooling of negative ions may allow for sympathetic cooling of antiprotons for the production of cold antihydrogen for tests of fundamental symmetries [124, 125]. From a fundamental standpoint, since the extra electron in a negative ion is not bound by a net Coulomb force, their properties critically depend on electron-electron correlation and polarization, giving valuable opportunities to gain insight into these important multibody interactions [126, 127, 128]. Therefore, negative ions serve as key test systems for state-of-the art atomic structure calculations.

Excited states of negative ions, both bound and quasibound states known as resonances, pose even more challenges and opportunities for both theory and experiment [120, 126, 129]. They are important in low energy electron scattering from atoms and molecules [130, 131, 132], electron attachment [131, 133], chemical reactions [134, 135], and photoabsorption [120, 126, 127, 136, 137]. Recent studies of negative ion excited states have focused on a diverse range of aspects, including the possibility of laser cooling negative ions [124, 125, 138, 139, 140, 141, 142], negative ion resonance spectroscopy using ultralong-range Rydberg molecules [143], and resonances in inner-shell photodetachment from small carbon molecular negative ions [144]. Clearly, progress

in theoretical calculations of negative ion excited states would be very valuable for a wide variety of both practical applications and fundamental insights.

We demonstrate for the first time that a high-precision relativistic hybrid approach that combines the configuration interaction and the coupled-cluster methods (CI+all-order) [64, 125] can be used to accurately predict the energies of quasibound states of negative ions. This method was designed for low-lying bound states and generally bound state approaches cannot be used to compute properties associated with levels beyond the ionization (or in this case photodetachment) threshold for reasons described below, but we have developed successful ways to extend this technique to quasibound states of complex negative ions.

7.1 Identification of quasibound spectrum of La^-

The work described in this section is submitted for publication [145]. Here, we demonstrated the accurate prediction of a quasibound spectrum of a negative ion using a novel high-precision theoretical approach. We used La^- as a test case due to a recent experiment done by collaborators from the Denison University that measured energies of 11 resonances in its photodetachment spectrum attributed to transitions to quasibound states [6]. We identified all of the observed resonances, and predicted one more peak just outside the range of the prior experiment. Following the theoretical prediction, the peak was observed at the predicted wavelength, validating the identification. The same approach is applicable to a wide range of negative ions. Moreover, theory advances reported in this work can be used for massive generation of atomic transition properties for neutrals and positive ions needed for a variety of applications. The work done in this section was done in collaboration with experimental group from the Denison University [6]. Our experimentalist collaborators performed the measurements done in this section, and we did the theoretical work to validate identifications.

The negative ion of lanthanum, La^- , is one of the most intriguing of all atomic negative ions. Whereas most negative ions only have a single bound state configuration because of the shallow, short-range nature of their binding potentials [126],

La⁻ possesses multiple bound states of opposite parity [138, 139]. Indeed, La⁻ has the richest spectrum of bound-bound electric-dipole transitions yet observed for any atomic negative ion [139], and it has emerged as one of the most promising negative ions for laser-cooling applications [125, 138, 139, 140, 146]. Beyond the complex bound structure of La⁻, very recent measurements of its photodetachment spectrum done by our collaborators from the Denison University have revealed a remarkably rich near-threshold spectrum including at least 11 prominent resonances due to excitation of quasibound negative ion states in the continuum [6]. This recent observation of its photodetachment spectrum allowed for an immediate test of our theoretical predictions of the quasibound state structure of La⁻. We were able to identify all of the 11 observed resonances (peaks), and predicted several peaks that were too weak to be observed in Ref. [6]. Our theoretical resonance energies agree with their experiment to 0.03 – 0.3% for “narrow” peaks and to 2.3 – 3% for “wide” peaks associated with higher energy levels. We also predicted that there should be a resonance peak just outside the photon energy range of the original experiment. Following our prediction, the peak was observed at exactly the predicted position, validating the identification; this new measurement done by our collaborators is reported here. We start with a description of the theoretical computations and specific solutions that allowed us to extract the quasibound states and identify the measured resonances.

While we used La⁻ as an example, the same approach is applicable to a wide range of negative ions. Moreover, we developed a way to reliably extract hundreds of states in the framework of the CI+all-order method, as described in Section 2.1.11, instead of just a few bound states. This advance will allow to significantly extend the applicability of the CI+all-order method for neutrals and positive ions, allowing for massive data generation (energies, transition rates, lifetimes, branching ratios, etc.) of a large part of the periodic table for a variety of applications.

In 2018, the CI+all-order approach was used to accurately predict energies of then unmeasured bound states of La⁻ as well as transition rates and branching ratios relevant to the laser cooling of La⁻ [125]. La⁻ is considered as a system with four

Table 7.1: Quasibound levels of La^- energy levels in meV. All energies are counted from the 3F_2 even ground state. Levels labeled A , B , C , and D in experimental work [6] are assigned terms. Calculated g -factors are compared with the non-relativistic values (NR) in the last two columns. From Ref. [145].

Level	Term	Theory	Expt.	Diff.(%)	g -factor	
					NR	CI+all
$6s^25d6p$	3P_1	567.0				
$6s^25d6p$	3P_2	643.2				
$6s5d^2(^4F)6p$	5G_2	725.0	723.34(4)	-0.2%	0.333	0.347
$6s5d^2(^4F)6p$	5G_3	763.0	761.26(7)	-0.2%	0.917	0.924
$6s5d^2(^4F)6p$	5G_4	814.1	811.27(4)	-0.3%	1.150	1.150
$6s5d^2(^4F)6p$	5G_5	877.7			1.267	1.266
$6s5d^2(^4F)6p$	5G_6	955.7			1.333	1.333
$6s5d^2(^4F)6p$	5F_1	900.4			0.000	0.083
$6s5d^2(^4F)6p$	5F_2	920.1			1.000	1.001
$6s5d^2(^4F)6p$	5F_3	953.3	979.3(11)	2.7%	1.250	1.231
$6s5d^2(^4F)6p$	5F_4	1005.9			1.350	1.312
$6s5d^2(^4F)6p$	5F_5	1068.0			1.400	1.386

valence electrons and Xe-like 54-electron core. The CI+all-order method, as described in Section 2.1.11, uses Dirac-Hartree-Fock one-electron wave functions for the low-lying valence electrons, $6s$, $5d$, $4f$, $6p$, $7s$, and $7p$ in the present work. We use a finite basis method to construct all other orbitals (up to $35spdfghi$) in a spherical cavity using B-splines. Such an approach discretizes the continuum spectrum: a sum over the finite basis is equivalent (to a numerical precision) to a sum over all bound states and integration over the continuum. The obvious downside of this approach is the limitation of its applicability to relatively low-lying bound states. For example, even for the largest practical size of the cavity (a few hundreds atomic units) the method is limited to the orbitals with the principal quantum number less than 20, so higher Rydberg, or other delocalized states cannot be treated accurately. The situation for negative ions is more favorable, where there are (if any) only a few bound states, no usual Rydberg series, and quasibound states (if any) are still highly localized.

There are two major problems in using the CI+all-order method to find quasi-bound states of negative ions. The first problem is the separation of true quasibound states from spurious “continuum-like” states that are artifacts of the finite basis (i.e. states containing orbitals with $n > 9$ that do not fit inside the cavity and represent near-continuum states). We solved this issue by running two set of calculations that were identical with the exception of the size of the cavity. We have theorized that the cavity size will affect the number and energies of the spurious states. The bound and quasibound states will not be affected as the smaller cavity size is chosen to fit them inside the cavity (we expect quasibound states to be well localized). We find that our supposition is correct and the energies of the quasibound states are indeed stable with the change in the cavity size from 60 a.u. to 85 a.u. The difficulty of this approach comes from the second problem: a large number of spurious states drastically affect convergence of the iterative procedure used by the CI, which is already very poor for negative ions making the computations prohibitively long. Furthermore, the convergence procedure was known to break down when some states reached convergence while other closely-lying states were still strongly varying. We separated the computation into seven different ones, each for a single value of the total angular momentum from $J = 0$ to $J = 6$ to improve convergence as well as resolved the issue of disparate convergence levels.

Building upon the MPI version of the CI code developed here, we improved both efficiency and memory use, allowing to run such a large number of already complicated computations in a short time. Each of the computations contained 110 000 – 186 000 configurations, corresponding to 4 – 6.6 million Slater determinants and requiring at least 100 iterations (where usual is under 20). We computed a total of 74 odd states with $J = 0 - 6$ and identified eight of these states as known bound states and twelve more states as quasibound states. We verified that the bound states agree with experiment to 0.1 – 2%. We find that dominant configurations for “spurious” states contain a large fraction of the np electrons with $n > 8$, unlike the quasibound states where configurations with $6p$ and $7p$ dominate.

The energies of quasibound states are listed in Table 7.1 relative to the 3F_2 even ground state (detachment threshold is 557.546(20) meV [147, 148]). Two of the quasibound states complete the 3P_J triplet, with the 3P_0 state being the last bound state. We classify the remaining 10 states as 2 quintets, $6s5d^26p$ 5G and 5F . Both quintets can be formed by attachment of a $6p$ electron to the $6s5d^2({}^4F)$ excited states of La. To verify our term assignments, we compute the g -factors for all states and compare them to the g -factors obtained from the non-relativistic Landè formula. We find a near perfect agreement of the calculated g -factors with the non-relativistic values (see the last two columns of Table 7.1), unambiguously confirming our term identification.

The dipole selection rules allow for eight transitions from the three lowest-lying $6s^25d^2$ ${}^3F_{2,3,4}$ even states to the 5G odd levels and nine transitions to the 5F odd levels. There are no allowed transitions involving the 5G_6 level. The transition energies for these 17 transitions are listed in Table 7.2, along with the identification of peaks observed by our collaborators in Ref. [6] and their measured energies. All “narrow” (<1 meV width) peaks 13-19 observed in Ref. [6] involve the 5G levels. Due to excellent agreement of the theoretical predictions with the measured energies, all of these peaks were straightforward to identify. All of the transition energies agree to 0.03 – 0.3%. The only allowed transition that was not observed by our collaborators in Ref. [6] is ${}^3F_4 \rightarrow {}^5G_3$, which is expected to be weaker than the observed ${}^3F_{2,3} \rightarrow {}^5G_3$ transitions. All observed transitions are illustrated in Fig. 7.1 a) which shows a partial energy level diagram of relevant states of La^- and La showing quasibound excited states in the 5G manifold. The numbered arrows indicate resonance transitions that have been assigned in this study.

The remaining “wide” (>1 meV width) peaks 20-23 in the spectrum are associated with transitions to the 5F multiplet. Peaks 20 and 23 have to involve the same 5F_J level, as they are separated by 89 meV, which matches the energy difference of the 3F_3 and 3F_4 even states [139, 147, 148]. However, complete identification of the peaks 20-23 is more complicated as there are multiple ways to match these observed transitions to theory predictions. We expect theory to be less accurate for these higher

Table 7.2: Identification of peaks observed in [6]. Transition energies are given in meV. The recommended values given in “recomm.” column are shifted by 22 meV from the *ab initio* values. Last column gives the difference between the experimental and theoretical values in meV. From Ref. [145].

Transition	Theory		Expt.	Peak	Diff.
	<i>ab initio</i>	recomm.			
${}^3F_2 \rightarrow {}^5G_2$	725.0		723.34(6)	17	1.7
${}^3F_3 \rightarrow {}^5G_2$	640.5		639.41(5)	14	1.1
${}^3F_2 \rightarrow {}^5G_3$	763.0		761.24(9)	19	1.8
${}^3F_3 \rightarrow {}^5G_3$	678.5		677.36(5)	15	1.1
${}^3F_4 \rightarrow {}^5G_3$	587.5		not observed		
${}^3F_3 \rightarrow {}^5G_4$	729.6		727.32(3)	18	2.3
${}^3F_4 \rightarrow {}^5G_4$	638.6		638.41(3)	13	0.2
${}^3F_4 \rightarrow {}^5G_5$	702.2		701.01(4)	16	1.2
${}^3F_2 \rightarrow {}^5F_1$	900.4	876.4	not observed		
${}^3F_2 \rightarrow {}^5F_2$	920.1	898.1	blended with 23		
${}^3F_3 \rightarrow {}^5F_2$	835.6	813.6	not observed		
${}^3F_2 \rightarrow {}^5F_3$	953.3	931.3	predicted observed 930.5(9)*		
${}^3F_3 \rightarrow {}^5F_3$	868.8	846.8	847.8(9)	21	21.0
${}^3F_4 \rightarrow {}^5F_3$	777.8	755.8	not observed		
${}^3F_3 \rightarrow {}^5F_4$	921.4	899.4	895.6(19)	23	25.8
${}^3F_4 \rightarrow {}^5F_4$	830.4	808.4	806.3(13)	20	24.1
${}^3F_4 \rightarrow {}^5F_5$	892.5	870.5	872.1(12)	22	20.4

*Present work

states due to stronger configuration mixing. The study of the fine-structure splittings within the 5F quintet shows these to be regular, i.e. matching non-relativistic values to within a few meV. Therefore, we expect similar differences between theory and experiment for all 4 measured transitions, with the deviation not exceeding a few (~ 5) meV. This requirement leaves only one possible identification of peaks 20-24 given in Table 4.6 in which all 4 measured energies differ from the theory by 20-25 meV. We predict that 3 transitions where total angular momentum J is lower for the quasibound state than for the even state were too weak to be observed. Two of the transitions, ${}^3F_3 \rightarrow {}^5F_4$ and ${}^3F_2 \rightarrow {}^5F_2$, have nearly the same energy, resulting in blending of two

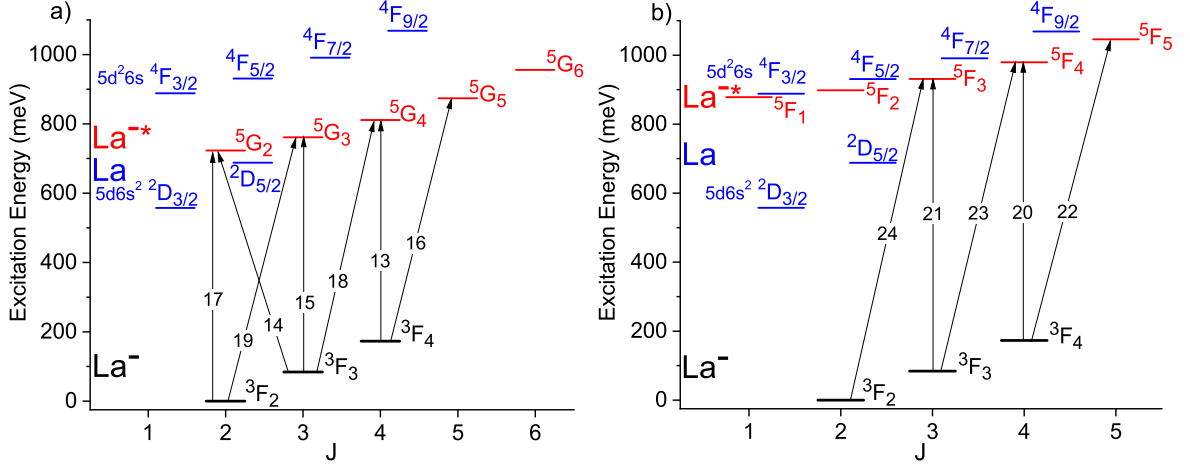


Figure 7.1: Partial energy level diagram of relevant bound states of La^- (black), neutral La (blue), and quasibound excited states of La^- (red) in the a) 5G and b) 5F manifolds. Numbered arrows indicate resonance transitions observed previously by the Denison University group [6] (Peaks 13-23) and in the present study (Peak 24) that have been identified in the present study. From Ref. [145].

transitions in Peak 23; note that the expected separation of these two transitions of only 1.3 meV is substantially less than Peak 23’s width of 8.8(18) meV [6]. To improve theory prediction for other peaks, we shift the calculated energies by 22 meV and list these recommended values in the “recomm.” column, with expected uncertainties of less than 5 meV.

Importantly, from our identification of the quasibound state structure, we expect a new resonance photodetachment peak associated with the $^3F_2 \rightarrow ^5F_3$ transition at slightly higher energy than the previously measured spectrum of Walter *et al.* [6]. Its predicted resonance energy can be calculated based on the energy of Peak 21, which is due to transition to the same 5F_3 upper state but from a different lower state, 3F_3 . Thus, the predicted energy of new Peak 24 is the energy of Peak 21 (847.8(9) meV) plus the La^- ($^3F_2 - ^3F_3$) fine structure splitting (83.941(20) meV [139, 147, 148]), yielding a predicted energy for Peak 24 of 931.7(9) meV. Peak 20-23 identification and new Peak 24 are illustrated in Fig. 7.1 b), which shows transitions to the 5F manifold.

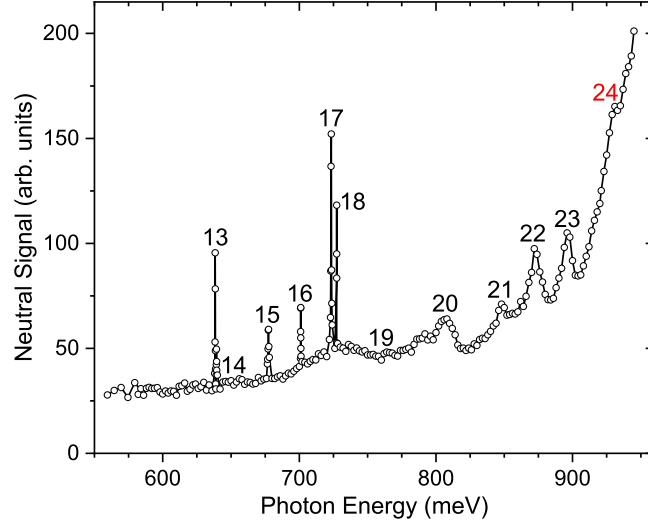


Figure 7.2: Measured La^- photodetachment spectrum above the ground state threshold energy of 557.546 meV. Data below 920 meV are from previous work [6, 139]; data above 920 meV are from the present study. The numbered peaks are due to resonant detachment via excitation of quasibound negative ion states; the newly observed Peak 24, which was predicted and verified in the present study, is indicated in red. From Ref. [145].

To test the theoretical interpretation of the La^- resonance spectrum, previous measurements [6] were extended to slightly higher photon energies to search for the predicted resonance due to the $\text{La}^- \ ^3F_2 \rightarrow \ ^5F_3$ transition near 931 meV. The relative photodetachment cross section was measured as a function of photon energy using a crossed ion-beam-OPO laser-beam system described in detail in Refs. [6, 149, 150]. In the present study, the tuning range of the OPO was extended beyond its nominal short wavelength limit of 1350 nm by manually controlling its crystal in order to measure photodetachment from 920 - 948 meV (1350 - 1310 nm).

Figure 7.2 shows the La^- photodetachment spectrum from Walter *et al.* [6], together with the present measurements above 920 meV. The continuum photodetachment cross section rapidly rises above 920 meV in a nearly linear fashion due to the opening of photodetachment channels from bound states of La^- to the $\text{La} \ ^4F$ manifold. Most importantly, the new measurements reveal an additional resonance peak, Peak 24, which appears as a weak hump in the cross section at an energy near 931 meV. The

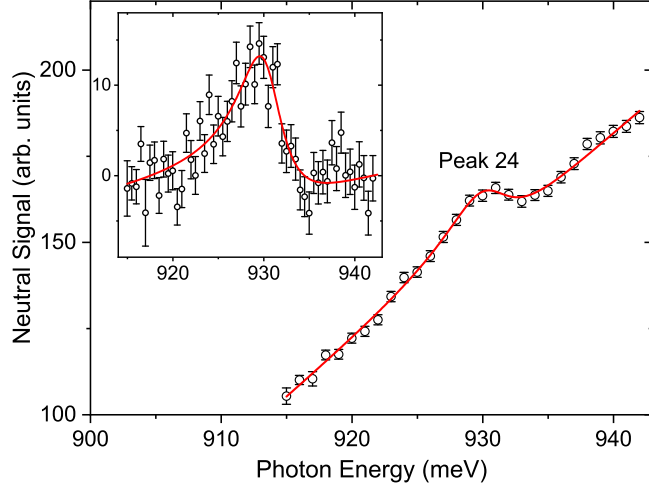


Figure 7.3: Measured photodetachment spectrum in the vicinity of the newly observed Peak 24, which is due to the $\text{La}^- \ ^3F_2 \rightarrow \ ^5F_3$ transition. The solid line is a fit to the data of a Fano profile with a linear background. The inset shows the remaining peak after the linear background has been subtracted from the measured neutral signal. From Ref. [145].

measured photodetachment spectrum in the vicinity of the newly observed Peak 24 is shown in Fig. 7.3, together with a fit of the Fano resonance formula [151] with a linear background continuum cross section. The Fano profile provides an excellent fit to the data, yielding a resonance energy of 930.5(9) meV and peak width of 5.8(10) meV.

The measured energy of Peak 24 of 930.5(9) meV agrees with the predicted value of 931.7(9) meV based on its theoretical identification as the $\ ^3F_2 \rightarrow \ ^5F_3$ transition. Furthermore, the measured widths of Peaks 21 and 24 (6.2(10) meV and 5.8(10) meV, respectively) are the same within uncertainties, as expected since the peak width depends on the lifetime of the $\ ^5F_3$ upper state which is the same for both peaks. The agreement between the predicted and measured energy and width of the newly observed Peak 24 clearly verifies the present theoretical interpretation of the La^- quasisubbound resonance spectrum and demonstrates the power of the methods used in these calculations. It is important to note that the theoretical calculations were absolutely necessary in finding the new peak, since it is very weak ($< 8\%$ of the background signal) and situated on a steep slope due to a rapidly increasing continuum photodetachment

cross section.

7.2 Observation of an electric quadrupole atomic transition in Bi^-

The work described in this section is submitted for publication [7]. Electric quadrupole atomic transitions are of great interest due to applications such as tests of fundamental physics [23, 84, 152], optical clocks [153], and quantum information [154], and they provide important benchmarks for detailed state-of-the-art theoretical calculations [155]. The properties of negative ions crucially depend on electron correlation effects [120, 126, 128, 156, 157], and $E2$ transitions in negative ions provide uniquely valuable opportunities to gain insights into these subtle but important interactions. Accurate theoretical computations are very difficult for negative ions with complex electronic structure due to large configuration mixing in comparison with neutral or positive ions [9, 126].

There is a great urgency for studying forbidden transitions in negative ions with the advent of new cryogenic storage ring facilities, such as DESIREE [158, 159] and the CSR [160, 161], that can measure lifetimes of excited states of negative ions over unprecedentedly long scales of up to hours [159]. While most of the negative ion excited state lifetime experiments to date have involved $M1$ transitions, one recent study at DESIREE measured the $E2$ decay of an excited state of Pt^- [162].

In this work, we investigate an $E2$ transition in the negative ion of bismuth with experimentalist collaborators from Denison University. The hyperfine-averaged binding energy of the Bi^- ($6p^4 \ ^3P_2$) ground state relative to the Bi ($6p^3 \ ^4S_{3/2}$) ground state was previously measured by Bilodeau and Haugen to be 942.369(13) meV [163]. While there have not been any previous measurements of the fine structure of Bi^- , Su *et al.* very recently reported calculations that indicated an interesting inversion in the ordering of the excited fine structure levels, with 3P_0 being bound and 3P_1 unbound [164]. Although there have been previous observations of transitions in negative ions that had both $M1$ and $E2$ contributions [165, 166], to our knowledge, this is the first transition observed in a negative ion with $E2$ as the lowest-order allowed interaction.

The Bi^- fine structure and $E2$ transition properties were independently calculated using a high-precision hybrid theoretical approach to account for the strong multi-level electron interactions and relativistic effects. The experiment and theoretical results are in excellent agreement, providing valuable new insights into this complex system and testing the accuracy of the theoretical approach.

We carried out calculations of the Bi^- binding energies and the $\text{Bi}^- 6p^4\ ^3P_0 - ^3P_2$ transition energy and transition rate using the CI+all-order method, as described in Section 2.1.11 [64]. Alternatively, we carry out identical computation constructing the entire effective Hamiltonian using the second-order MBPT [2] to evaluate the importance of the higher-order corrections; we refer to such results as the CI+MBPT.

We treat Bi as a system with 3 valence electrons and a $[\text{Xe}]4f^{14}5d^{10}6s^2$ core. The core is the same as for the Bi^- calculation. The difference between the Bi^- and Bi calculation is in the CI part, which contains 4 valence electrons for Bi^- . There is an exponential growth in the number of possible configurations with the addition of extra valence electrons and care must be taken to ensure a sufficiently large set of configuration for Bi^- . The problem is exacerbated for the weakly-bound negative ion which exhibits very strong configuration mixing. All calculations incorporate the Breit interaction as described in Ref. [34].

Table 7.3: Calculated binding energies of Bi⁻ bound states relative to the Bi ⁴S_{3/2} ground state and transition energy for Bi⁻ $6p^4 \ ^3P_2 \rightarrow \ ^3P_0$ in cm⁻¹. Bi experimental values are from NIST [94]. Contributions of the higher orders (HO) are calculated as the differences of the CI+all-order (CI+all) and the CI+MBPT calculations. QED correction, contribution of the higher particle wave ($l = 6$) are listed separately. The column “Extra conf” list the difference of the results of the large and medium CI calculations, see text for more explanation. Final results are obtained with including all of these corrections in the same computation. See text for more explanations. From Ref. [7].

	J	Expt.	CI+MBPT	CI+All	HO	$l = 6$	QED	Extra conf.	Final	Diff.	Diff.%
Bi	$6p^3$	0	0	0	0	0	0	0	0	0	0
	$3/2$	0	0	0	0	0	0	0	0	0	0
	$3/2$	11419	11183	11180	3	28	9	-34	11184	235	2.1%
	$5/2$	15438	15079	15117	-38	35	8	-83	15079	359	2.3%
	$1/2$	21661	22259	21769	490	39	12	-105	21714	-53	0.2%
	$3/2$	33165	33332	32596	736	74	24	-86	32601	564	1.7%
	$1/2$	41125	41983	41248	735	45	20	307	41623	-498	1.2%
	$3/2$	42941	43730	43010	720	46	20	360	43439	-499	1.2%
	$1/2$	49998	51149	50437	712	51	20	162	50673	-675	1.3%
	$3/2$	50595	51738	51030	708	52	21	141	51246	-652	1.3%
Bi -	$6p^4 \ ^3P$	2	7600.66(10) ^a	7343	7348	5	17	215	7597	4	0.05%
	$6p^4 \ ^3P$	0	3009 ^b	2590	2763	172	8	210	2992	17	0.6%
	$^3P_2 \rightarrow \ ^3P_0$		4591 ^b	4752	4585	-167	9	5	4605	-14	0.3%

^a Ref. [163], hyperfine-averaged.

^b Present measurements.

The results of the CI+all-order and CI+MBPT calculations and specific contributions to the energies are summarized for neutral Bi, and the electron affinity and the $6p^4\ ^3P_2 \rightarrow\ ^3P_2$ transition energy are presented for Bi^- in Table 7.3. Binding energies are shown relative to the Bi $6p^3\ ^4S_{3/2}$ ground state. Contributions of the higher orders (HO) are calculated as the differences of the CI+all-order (CI+all) and the CI+MBPT calculations. To evaluate the accuracy of the calculations, we calculated several smaller corrections separately. We originally ran CI+all-order and CI+MBPT calculations allowing excitations to all partial waves up to $l = 5$, with maximum principal quantum number $n = 35$ for each (relativistic) partial wave. The contribution of the $l = 6$ partial wave is listed in the column “ $l = 6$ ”. From the extrapolations carried out for simpler systems, we find that the contribution of all other partial waves is on the same order as the $l = 6$ contribution. QED corrections are calculated following Ref. [5]. Both the contributions of the $l = 6$ partial wave and the QED corrections are relatively small. Next, we increase the number of CI configurations allowing excitations up to $23spdf18g$ and $22spdf18g$ orbitals for Bi and Bi^- , respectively, an increase from the initial $22spd18f14g$ set. All single, double and a large subset of triple excitations are included. These changes increase the number of included configurations for the Bi^- from 73 719 to 126 168, with corresponding increase in the number of Slater determinants from 3 090 923 to 4 952 692. Finally, we carry out a complete CI+all-order run that incorporates all corrections (QED, $l = 6$, and larger number of configurations) simultaneously. These results are listed as “Final” in Table 7.3.

Our final calculated binding energy of the $\text{Bi}^- \ ^3P_2$ ground state is in excellent agreement with the measured value of Bilodeau and Haugen [163], differing by only 0.05% (see Table 7.3). We find that the binding energy of the ground state, or the electron affinity (EA), is strongly affected by the inclusion of more configurations, but not by the inclusion of the higher orders. This is expected as Bi and Bi^- computations share the same core, and differences in its treatment is expected to cancel to a degree. A sensitivity to extra configurations is also expected as configuration mixing for Bi^- is much stronger than for Bi. There is also excellent agreement for the binding energy

Table 7.4: The energy levels of Po counted from the ground state. The experimental values are from NIST [94]. From Ref. [7].

Level	Expt.	CI+MBPT	CI+All	HO	Final	Diff.	Diff.%
$6p^4 \ ^3P_2$	0	0	0	0	0	0	
$6p^4 \ ^3P_0$	7515	8022	7739	-283	7717	-202	-2.6%
$6p^4 \ ^3P_1$	16832	16508	16189	-318	16272	560	3.4%
$6p^4 \ ^1D_2$	21679	21370	21183	-187	21181	499	2.4%

of the fine structure excited state 3P_0 , with our calculated value of 2992 cm^{-1} being within 17 cm^{-1} or 0.6% of the measured value of 3009 cm^{-1} . However, in contrast to the ground state, the higher orders contribute significantly (5.7%) to the binding energy of the 3P_0 state and therefore affect the $^3P_2 \rightarrow ^3P_0$ transition energy. Finally, our calculations indicate that the $\text{Bi}^- \ ^3P_1$ state is not bound, which is in agreement with the calculations of Su *et al.* [164].

We find it interesting to also explore if Po, which has the same two lowest electronic states as Bi^- , may be used as a homologue system to improve prediction for a negative ion. We carried out a Po computation with all parameters identical to Bi^- . The results are listed in Table 7.4. We find that the difference with experiment is actually larger in Po than in Bi^- . This is most likely due to uneven cancellation of some omitted effects, such as core triple excitations and non-linear terms that tend to strongly cancel. We also find as expected that there is much stronger configuration mixing in a negative ion, for example, only 11 non-relativistic configurations contribute a total of 99% for the ground state of Po, but 22 for Bi^- . Our results demonstrate the significant fact that an isoelectronic neutral system cannot always be used as a homologue for a negative ion.

The present theoretical results for the $\text{Bi}^- \ ^3P_2 \rightarrow ^3P_0$ $E2$ transition is given in Table 7.5, together with previous calculations. Our calculated transition energy (4605 cm^{-1}) is in excellent agreement with the experimental value (4591 cm^{-1}), differing by only 14 cm^{-1} or 0.3%. In contrast, the calculated transition energy from Su *et al.* [164] is 444 cm^{-1} larger than the recent measurement, while the earlier calculation of Konan

Table 7.5: Present results and previous calculations for the $\text{Bi}^- \ ^3P_2 \rightarrow \ ^3P_0$ $E2$ transition energy and upper-state lifetime. From Ref. [7].

Study	Method	$\ ^3P_2 \rightarrow \ ^3P_0$ Energy (cm^{-1})	Lifetime (s)
Present	Experiment	4591	-
Present	Theory	4605	16.5(7)
Su [164]	Theory	5033	15.20
Konan [168]	Theory	8872	-

et al. is even farther away. Our computations include higher-order inner-shell electronic correlations and, therefore, are expected to be more accurate than Multiconfigurational Dirac-Hartree-Fock calculations [164, 168] for both energies and transition rates.

Turning now to the transition rate, we calculate the electric quadrupole $6p^4 \ ^3P_2 \rightarrow \ ^3P_0$ reduced matrix element to be $16.30(33)ea_0^2$ using the CI+all-order method. There is only a 1% difference between the CI+all-order and the CI+MBPT results, and there is a 1.7% difference between the results obtained with medium and large sets of CI configurations. We add these in quadrature to estimate the final uncertainty of the matrix element to be 2%. Using the experimental value of the transition energy, we obtain $0.0607(24) \text{ s}^{-1}$ for the transition rate, corresponding to a $\ ^3P_0$ lifetime of 16.5(7) s. At first glance, the previous calculated lifetime by Su *et al.* of 15.20 s appears to be fairly close to our value. However, it is important to consider that Su *et al.*'s quoted lifetime was obtained using their calculated transition energy for $\ ^3P_2 \rightarrow \ ^3P_0$, which is larger than the precisely measured energy by 10%. Since the $E2$ lifetime scales inversely with transition energy to the fifth power, revising their lifetime using our measured energy would yield an adjusted lifetime of 24.05 s, which is significantly longer than our value. Finally, note that although our calculated lifetime of the $\ ^3P_0$ upper state of 16.5(7) s indicates that the transition is far too narrow ($2 \times 10^{-14} \text{ meV}$) for a direct measurement of the lifetime from the peak width in the present experiment, the theoretically predicted lifetime could be rigorously tested in storage ring experiments using established techniques [159, 162].

In summary, we have calculated the binding energies of the Bi^- bound states

and transition energy for $6p^4\ ^3P_2 \rightarrow\ ^3P_0$ in cm^{-1} . We have confirmed the fine structure of Bi^- and the $E2$ character of the transition through detailed theoretical calculations including the transition rate. The measured and calculated energies are in excellent agreement, demonstrating the power of the theoretical methods used to account for the important correlation and relativistic effects in this complex multielectron system. Similar theoretical methods can be applied to study $E2$ transitions in other negative ions that have appropriate excited bound state structures, opening a new avenue for investigations of forbidden transitions in atomic systems. Such studies can be combined with the new ability of accurately measuring lifetimes of excited negative ions over long time scales, recently developed at cryogenic storage ring facilities such as DESIREE and the CSR, to give further insights into many-body correlation effects and decay dynamics.

Chapter 8

CONCLUSION

We have developed a broadly-applicable approach that drastically increases the ability to accurately predict properties of complex atoms. The computational advances demonstrated in this work are widely applicable to most elements in the periodic table and will allow one to solve numerous problems in atomic physics, astrophysics, and plasma physics.

Our systematic study of the atomic properties of highly charged Ir^{17+} demonstrates new capabilities for high precision relativistic atomic calculations required for modern experiments relevant for the development of novel atomic clocks with high sensitivity to the variation of the fine-structure constant. Previously predicted $E1$ transitions have eluded observation despite years of effort raising the possibility that theory predictions are grossly wrong. We provide accurate predictions of transition wavelengths and $E1$ transition rates, explaining the lack of observation and providing a pathway towards detection of clock transitions.

In the Cf^{15+} and Cf^{17+} highly charged ions, we have carried out a systematic study of properties needed for the development of optical clocks using the hybrid approach combining the CI and coupled cluster methods. We analyzed a number of systematic effects, including electric quadrupole- micromotion-, and quadratic Zeeman shifts, of the clock transitions that affect the accuracy and stability of the optical clocks. We also calculated the hfs magnetic dipole constants of the clock states and the BBR shifts of the clock transitions.

In the neutral Ac atom, we collaborated with experimentalists from the University of Mainz to locate the two lowest-lying odd-parity states, and measure the energies

and lifetimes, as well as hyperfine parameters of the $^2P_{3/2}^o$ state, finding excellent agreement between theoretical predictions and experimental measurements, implying good understanding of the atomic structure of the actinium atom. Our theoretical findings aid in developing techniques for cooling and trapping of actinium, of potential interest for measuring the nuclear Schiff moment enhanced in Ac, as well as in optimization of specific resonance-ionization processes. The results will be useful for production of ^{225}Ac for nuclear medicine, and may support the design of fundamental physics experiments such as investigations of fundamental symmetries with this atom. Precise atomic calculations of Ac hyperfine constants and isotope shifts will be used for accurate extraction of nuclear properties from forthcoming laser-spectroscopy experiments.

In the Fe^{16+} ion, we carried out a precision calculation all 10 electrons, including full Breit and QED corrections, to predict the transition rates with 1-2% accuracy. Our calculations ruled out incomplete inclusion of the electronic correlations in theoretical calculations as the potential explanation of the puzzle. We saturated the computation in all possible numerical parameters, including over 230 000 configurations in the largest basis set $12sp17dfg$. We verified that all the energies of all 18 states considered, counted from the ground state, agree with the NIST database well within the experimental uncertainty of 0.05%. The theoretical $3C - 3D$ energy difference of 13.44 eV is in agreement with the experimental value to 0.3%.

We demonstrated the ability to accurately predict the quasibound spectrum of negative ions with our calculations of atomic properties of La^- and Bi^- . The CI+all-order method was designed for low-lying bound states and generally bound state approaches cannot be used to compute properties associated with levels beyond the ionization threshold, but we developed successful ways to extend this technique to quasibound states of complex negative ions. In La^- , we identified all of the observed resonances, and predicted one more peak just outside the range of the prior experiment. Following the theoretical prediction, the peak was observed at the predicted wavelength, validating the identification. In Bi^- , we calculated the binding energies of the Bi^- bound states and transition energy for $6p^4 \ ^3P_2 \rightarrow ^3P_0$ in cm^{-1} . We have

confirmed the fine structure of Bi^- and the $E2$ character of the transition through detailed theoretical calculations including the transition rate. The measured and calculated energies are in excellent agreement, demonstrating the power of the theoretical methods used to account for the important correlation and relativistic effects in this complex multielectron system.

BIBLIOGRAPHY

- [1] E. R. Davidson, “The iterative calculation of a few of the lowest eigenvalues and corresponding eigenvectors of large real-symmetric matrices,” *Journal of Computational Physics*, vol. 17, pp. 87–94, Jan. 1975.
- [2] M. G. Kozlov, S. G. Porsev, M. S. Safronova, and I. I. Tupitsyn, “CI-MBPT: A package of programs for relativistic atomic calculations based on a method combining configuration interaction and many-body perturbation theory,” *Computer Physics Communications*, vol. 195, pp. 199–213, 2015.
- [3] A. Windberger, J. R. Crespo López-Urrutia, H. Bekker, N. S. Oreshkina, J. C. Berengut, V. Bock, A. Borschevsky, V. A. Dzuba, E. Eliav, Z. Harman, U. Kaldor, S. Kaul, U. I. Safronova, V. V. Flambaum, C. H. Keitel, P. O. Schmidt, J. Ullrich, and O. O. Versolato, “Identification of the predicted $5s-4f$ level crossing optical lines with applications to metrology and searches for the variation of fundamental constants,” *Phys. Rev. Lett.*, vol. 114, p. 150801, Apr. 2015.
- [4] C. Cheung, M. S. Safronova, S. G. Porsev, M. G. Kozlov, I. I. Tupitsyn, and A. I. Bondarev, “Accurate Prediction of Clock Transitions in a Highly Charged Ion with Complex Electronic Structure,” *Phys. Rev. Lett.*, vol. 124, p. 163001, Apr. 2020.
- [5] I. I. Tupitsyn, M. G. Kozlov, M. S. Safronova, V. M. Shabaev, and V. A. Dzuba, “Quantum electrodynamic shifts in multivalent heavy ions,” *Phys. Rev. Lett.*, vol. 117, p. 253001, 2016.
- [6] C. W. Walter, N. D. Gibson, N. B. Lyman, and J. Wang, “Photodetachment spectroscopy of quasibound states of the negative ion of lanthanum,” *Phys. Rev. A*, vol. 102, Oct. 2020.
- [7] C. W. Walter, S. E. Spielman, R. Ponce, N. D. Gibson, J. N. Yukich, C. Cheung, and M. S. Safronova, “Observation of an electric quadrupole transition in a negative ion: Experiment and theory,” *arXiv:2011.10872*, 2020. submitted to *Phys. Rev. Lett.* (2020).
- [8] *NIST Multiconfiguration Hartree-Fock and Multiconfiguration Dirac-Hartree-Fock Database*, Charlotte Froese Fischer and Georgio Tachiev, <http://nlte.nist.gov/MCHF>.

- [9] C. F. Fischer, G. Tachiev, G. Gaigalas, and M. R. Godefroid, “An MCHF atomic-structure package for large-scale calculations,” *Computer Physics Communications*, vol. 176, pp. 559–579, Apr. 2007.
- [10] P. Jönsson, X. He, C. F. Fischer, and I. Grant, “The grasp2k relativistic atomic structure package,” *Computer Physics Communications*, vol. 177, pp. 597–622, Oct. 2007.
- [11] P. Jönsson, G. Gaigalas, J. Bieroń, C. F. Fischer, and I. Grant, “New version: Grasp2k relativistic atomic structure package,” *Computer Physics Communications*, vol. 184, pp. 2197–2203, Sept. 2013.
- [12] A. Hibbert, “CIV3 — a general program to calculate configuration interaction wave functions and electric-dipole oscillator strengths,” *Computer Physics Communications*, vol. 9, pp. 141–172, Mar. 1975.
- [13] W. EISSNER, “SUPERSTRUCTURE - AN ATOMIC STRUCTURE CODE,” *Le Journal de Physique IV*, vol. 01, pp. C1–3–C1–13, Mar. 1991.
- [14] R. D. Cowan, “Theory of atomic structure and spectra.” University of California Press, Berkeley, 1981. <http://www.tcd.ie/Physics/People/Cormac.McGuinness/Cowan/>.
- [15] R. D. Cowan, *The theory of atomic structure and spectra*. Berkeley: University of California Press, 1981.
- [16] A. Bar-Shalom, M. Klapisch, and J. Oreg, “HULLAC, an integrated computer package for atomic processes in plasmas,” *Journal of Quantitative Spectroscopy and Radiative Transfer*, vol. 71, pp. 169–188, Oct. 2001.
- [17] M. Amusia, *Computation of atomic processes : a handbook for the ATOM programs*. Bristol, UK Philadelphia, Pa: Institute of Physics Pub, 1997.
- [18] M. F. Gu, The flexible atomic code, *Canadian Journal of Physics*, 86, 675–689 (2008).
- [19] E. V. Kahl and J. C. Berengut, “AMBiT: A programme for high-precision relativistic atomic structure calculations,” *Computer Physics Communications*, vol. 238, p. 232, May 2019.
- [20] J.-P. Uzan, “The fundamental constants and their variation: observational and theoretical status,” *Reviews of Modern Physics*, vol. 75, pp. 403–455, Apr. 2003.
- [21] E. Peik and C. Tamm, “Nuclear laser spectroscopy of the 3.5 eV transition in Th-229,” *Europhysics Letters (EPL)*, vol. 61, pp. 181–186, Jan. 2003.
- [22] M. Safronova, “In search of the nuclear clock,” *Nature Physics*, vol. 14, pp. 198–198, Feb. 2018.

- [23] J. C. Berengut, V. A. Dzuba, and V. V. Flambaum, “Enhanced laboratory sensitivity to variation of the fine-structure constant using highly charged ions,” *Phys. Rev. Lett.*, vol. 105, Sept. 2010.
- [24] M. S. Safronova, V. A. Dzuba, V. V. Flambaum, U. I. Safronova, S. G. Porsev, and M. G. Kozlov, “Highly charged ions for atomic clocks, quantum information, and search for α variation,” *Phys. Rev. Lett.*, vol. 113, p. 030801, 2014.
- [25] A. Derevianko, V. A. Dzuba, and V. V. Flambaum, “Highly charged ions as a basis of optical atomic clockwork of exceptional accuracy,” *Phys. Rev. Lett.*, vol. 109, Oct. 2012.
- [26] V. A. Dzuba, A. Derevianko, and V. V. Flambaum, “Ion clock and search for the variation of the fine-structure constant using optical transitions in Nd^{13+} and Sm^{15+} ,” *Phys. Rev. A*, vol. 86, Nov. 2012.
- [27] V. A. Dzuba, V. V. Flambaum, and H. Katori, “Optical clock sensitive to variations of the fine-structure constant based on the Ho^{14+} ion,” *Phys. Rev. A*, vol. 91, Feb. 2015.
- [28] M. G. Kozlov, M. S. Safronova, J. R. Crespo López-Urrutia, and P. O. Schmidt, “Highly charged ions: optical clocks and applications in fundamental physics,” *Rev. Mod. Phys.*, vol. 90, p. 045005, 2018.
- [29] E. Tiesinga, P. J. Mohr, D. B. Newell, and B. N. Taylor, “The 2018 CODATA recommended values of the fundamental physical constants,” 2020. Database developed by J. Baker, M. Douma, and S. Kotochigova. Available at <http://physics.nist.gov/constants>. National Institute of Standards and Technology, Gaithersburg, MD 20899.
- [30] V. A. Dzuba, V. V. Flambaum, and J. K. Webb, “Space-time variation of physical constants and relativistic corrections in atoms,” *Phys. Rev. Lett.*, vol. 82, pp. 888–891, Feb. 1999.
- [31] V. A. Dzuba, V. V. Flambaum, and J. K. Webb, “Calculations of the relativistic effects in many-electron atoms and space-time variation of fundamental constants,” *Phys. Rev. A*, vol. 59, pp. 230–237, Jan. 1999.
- [32] J. C. Berengut, V. A. Dzuba, V. V. Flambaum, and A. Ong, “Electron-hole transitions in multiply charged ions for precision laser spectroscopy and searching for variations in α ,” *Phys. Rev. Lett.*, vol. 106, p. 210802, May 2011.
- [33] H. Bekker, private communication.
- [34] S. G. Porsev, U. I. Safronova, M. S. Safronova, P. O. Schmidt, A. I. Bondarev, M. G. Kozlov, I. I. Tupitsyn, and C. Cheung, “Optical clocks based on the Cf^{15+} and Cf^{17+} ions,” *Phys. Rev. A*, vol. 102, p. 012802, July 2020.

- [35] V. A. Dzuba, A. Derevianko, and V. V. Flambaum, “High-precision atomic clocks with highly charged ions: Nuclear-spin-zero f^{12} -shell ions,” *Phys. Rev. A*, vol. 86, Nov. 2012.
- [36] V. A. Dzuba, A. Derevianko, and V. V. Flambaum, “Erratum: High-precision atomic clocks with highly charged ions: Nuclear-spin-zero f^{12} -shell ions [phys. rev. a86, 054501 (2012)],” *Phys. Rev. A*, vol. 87, Feb. 2013.
- [37] L. Schmoger, O. O. Versolato, M. Schwarz, M. Kohlen, A. Windberger, B. Piest, S. Feuchtenbeiner, J. Pedregosa-Gutierrez, T. Leopold, P. Micke, A. K. Hansen, T. M. Baumann, M. Drewsen, J. Ullrich, P. O. Schmidt, and J. R. C. Lopez-Urrutia, “Coulomb crystallization of highly charged ions,” *Science*, vol. 347, pp. 1233–1236, Mar. 2015.
- [38] T. Leopold, S. A. King, P. Micke, A. Bautista-Salvador, J. C. Heip, C. Ospelkaus, J. R. C. López-Urrutia, and P. O. Schmidt, “A cryogenic radio-frequency ion trap for quantum logic spectroscopy of highly charged ions,” *Review of Scientific Instruments*, vol. 90, p. 073201, July 2019.
- [39] S. Johansson, A. Derkach, M. P. Donnelly, H. Hartman, A. Hibbert, H. Karlsson, M. Kock, Z. S. Li, D. S. Leckrone, U. Litzén, H. Lundberg, S. Mannervik, L.-O. Norlin, H. Nilsson, J. Pickering, T. Raassen, D. Rostohar, P. Royen, A. Schmitt, M. Johannig, C. M. Sikström, P. L. Smith, S. Svanberg, and G. M. Wahlgren, “The FERRUM project: New f -value data for Fe II and astrophysical applications,” *Physica Scripta*, vol. T100, no. 1, p. 71, 2002.
- [40] N. C. Deb and A. Hibbert, “Electric-dipole allowed and intercombination transitions among the $3d^5$, $3d^44s$ and $3d^44p$ levels of Fe IV,” *Atomic Data and Nuclear Data Tables*, vol. 96, pp. 358–480, July 2010.
- [41] N. C. Deb and A. Hibbert, “Strong infrared lines among the lowest three even configurations of Fe II,” in *APS Division of Atomic, Molecular and Optical Physics Meeting Abstracts*, vol. 40 of *APS Meeting Abstracts*, p. OPM.10, May 2009.
- [42] C. Reynolds, “Fluorescent iron lines as a probe of astrophysical black hole systems,” *Physics Reports*, vol. 377, pp. 389–466, Apr. 2003.
- [43] S. Kühn, C. Shah, J. R. C. López-Urrutia, K. Fujii, R. Steinbrügge, J. Stierhof, M. Togawa, Z. Harman, N. S. Oreshkina, C. Cheung, M. G. Kozlov, S. G. Porsev, M. S. Safronova, J. C. Berengut, M. Rosner, M. Bissinger, R. Ballhausen, N. Hell, S. Park, M. Chung, M. Hoesch, J. Seltmann, A. S. Surzhykov, V. A. Yerokhin, J. Wilms, F. S. Porter, T. Stöhlker, C. H. Keitel, T. Pfeifer, G. V. Brown, M. A. Leutenegger, and S. Bernitt, “High resolution photoexcitation measurements exacerbate the long-standing Fe XVII oscillator strength problem,” *Phys. Rev. Lett.*, vol. 124, June 2020.

- [44] W. R. Johnson, *Atomic Structure Theory*. Springer Berlin Heidelberg, 2007.
- [45] G. Drake, *Springer Handbook of Atomic, Molecular, and Optical Physics*. New York: Springer, 2006.
- [46] I. Lindgren and J. Morrison, *Atomic Many-Body Theory*. Springer Berlin Heidelberg, 1986.
- [47] K. Szalewicz, “PHYS838: Advanced Molecular Science,” Dec. 2017.
- [48] I. I. Tupitsyn, M. G. Kozlov, M. S. Safronova, V. M. Shabaev, and V. A. Dzuba, “Quantum electrodynamical shifts in multivalent heavy ions,” *Phys. Rev. Lett.*, vol. 117, p. 253001, 2016.
- [49] H. A. Bethe and E. E. Salpeter, *Quantum Mechanics of One- and Two-Electron Atoms*. Springer Berlin Heidelberg, 1957.
- [50] J. A. Gaunt, “The triplets of helium,” *Proceedings of the Royal Society of London. Series A, Containing Papers of a Mathematical and Physical Character*, vol. 122, pp. 513–532, Feb. 1929.
- [51] G. Breit, “The effect of retardation on the interaction of two electrons,” *Physical Review*, vol. 34, pp. 553–573, Aug. 1929.
- [52] G. Breit, “The fine structure of He as a test of the spin interactions of two electrons,” *Physical Review*, vol. 36, pp. 383–397, Aug. 1930.
- [53] G. Breit, “Dirac’s equation and the spin-spin interactions of two electrons,” *Physical Review*, vol. 39, pp. 616–624, Feb. 1932.
- [54] M. Kozlov, S. Porsev, and I. Tupitsyn, “Breit interaction in heavy atoms,” *arXiv:physics/0004076*, May 2000.
- [55] I. Grant, “Relativistic calculation of atomic structures,” *Advances in Physics*, vol. 19, pp. 747–811, Nov. 1970.
- [56] J. B. Mann and W. R. Johnson, “Breit interaction in multielectron atoms,” *Phys. Rev. A*, vol. 4, pp. 41–51, July 1971.
- [57] W. R. Johnson, S. A. Blundell, and J. Sapirstein, “Finite basis sets for the dirac equation constructed from B-splines,” *Phys. Rev. A*, vol. 37, pp. 307–315, Jan. 1988.
- [58] J. J. Sakurai, *Modern quantum mechanics*. Boston: Addison-Wesley, 2011.
- [59] C. D. Carl de Boor, *A Practical Guide to Splines*. Springer-Verlag GmbH, 2001.
- [60] A. Chodos, R. L. Jaffe, K. Johnson, C. B. Thorn, and V. F. Weisskopf, “New extended model of hadrons,” *Phys. Rev. D*, vol. 9, pp. 3471–3495, June 1974.

- [61] R. B. Morgan and D. S. Scott, “Generalizations of Davidson’s method for computing eigenvalues of sparse symmetric matrices,” *Journal on Scientific and Statistical Computing*, vol. 7, pp. 817–825, July 1986.
- [62] V. A. Dzuba, V. V. Flambaum, and M. G. Kozlov, “Combination of the many-body perturbation theory with the configuration-interaction method,” *Phys. Rev. A*, vol. 54, pp. 3948–3959, Nov. 1996.
- [63] V. A. Dzuba and J. S. M. Ginges, “Calculations of energy levels and lifetimes of low-lying states of barium and radium,” *Physical Review A*, vol. 73, Mar. 2006.
- [64] M. S. Safronova, M. G. Kozlov, W. R. Johnson, and D. Jiang, “Development of a configuration-interaction plus all-order method for atomic calculations,” *Phys. Rev. A*, vol. 80, p. 012516, July 2009.
- [65] M. S. Safronova, W. R. Johnson, and A. Derevianko, “Relativistic many-body calculations of energy levels, hyperfine constants, electric-dipole matrix elements, and static polarizabilities for alkali-metal atoms,” *Phys. Rev. A*, vol. 60, pp. 4476–4487, Dec. 1999.
- [66] R. Pal, M. S. Safronova, W. R. Johnson, A. Derevianko, and S. G. Porsev, “Relativistic coupled-cluster single-double method applied to alkali-metal atoms,” *Phys. Rev. A*, vol. 75, Apr. 2007.
- [67] S. G. Porsev, K. Beloy, and A. Derevianko, “Precision determination of electroweak coupling from atomic parity violation and implications for particle physics,” *Phys. Rev. Lett.*, vol. 102, May 2009.
- [68] Y. G. Rakhlina, M. G. Kozlov, and S. G. Porsev, “The energy of electron affinity to a zirconium atom,” *Optics and Spectroscopy*, vol. 90, pp. 817–821, June 2001.
- [69] K. Blum, *Density Matrix Theory and Applications*. Springer-Verlag GmbH, 2012.
- [70] E. Davidson, *Reduced density matrices in quantum chemistry*. New York: Academic Press, 1976.
- [71] S. A. Kotochigova and I. I. Tupizin, “Theoretical investigation of rare-earth and barium spectra by the hartree-fock-dirac method,” *Journal of Physics B: Atomic and Molecular Physics*, vol. 20, pp. 4759–4772, Sept. 1987.
- [72] J. D. F. Richard L. Burden, *Numerical Analysis*. Brooks Cole Pub. Co., 2010.
- [73] W. Gropp, E. Lusk, and A. Skjellum, *Using MPI*. MIT Press Ltd, 2014.
- [74] W. Gropp, T. Hoefler, R. Thakur, and E. Lusk, *Using Advanced MPI : modern features of the Message-Passing-Interface*. Cambridge, MA: The MIT Press, 2015.

- [75] “Lustre.” <https://wiki.lustre.org/>.
- [76] M. S. Safronova, S. G. Porsev, C. Sanner, and J. Ye, “Two Clock Transitions in Neutral Yb for the Highest Sensitivity to Variations of the Fine-Structure Constant,” *Phys. Rev. Lett.*, vol. 120, p. 173001, 2018.
- [77] V. A. Dzuba, V. V. Flambaum, and S. Schiller, “Testing physics beyond the standard model through additional clock transitions in neutral ytterbium,” *Phys. Rev. A*, vol. 98, p. 022501, Aug. 2018.
- [78] U. I. Safronova, V. V. Flambaum, and M. S. Safronova, “Transitions between the $4f$ -core-excited states in Ir^{16+} , Ir^{17+} , and Ir^{18+} ions for clock applications,” *Phys. Rev. A*, vol. 92, p. 022501, Aug. 2015.
- [79] J. C. Berengut, V. A. Dzuba, and V. V. Flambaum, “Enhanced laboratory sensitivity to variation of the fine-structure constant using highly-charged ions,” *Phys. Rev. Lett.*, vol. 105, p. 120801, 2010.
- [80] R. T. Imanbaeva and M. G. Kozlov, “Configuration interaction and many-body perturbation theory: Application to scandium, titanium, and iodine,” *Ann. Phys. (Berlin)*, vol. 531, p. 1800253, 2019.
- [81] V. M. Shabaev, I. I. Tupitsyn, and V. A. Yerokhin, “QEDMOD: Fortran program for calculating the model lamb-shift operator,” *Computer Physics Communications*, vol. 189, pp. 175–181, 2015.
- [82] I. I. Tupitsyn, M. G. Kozlov, M. S. Safronova, V. M. Shabaev, and V. A. Dzuba, “Quantum electrodynamical shifts in multivalent heavy ions,” *Phys. Rev. Lett.*, vol. 117, p. 253001, 2016.
- [83] J. C. Berengut, V. A. Dzuba, V. V. Flambaum, and A. Ong, “Optical transitions in highly charged californium ions with high sensitivity to variation of the fine-structure constant,” *Phys. Rev. Lett.*, vol. 109, p. 070802, 2012.
- [84] V. A. Dzuba, M. S. Safronova, U. I. Safronova, and V. V. Flambaum, “Actinide ions for testing the spatial α -variation hypothesis,” *Phys. Rev. A*, vol. 92, Dec. 2015.
- [85] M. G. Kozlov, S. G. Porsev, and V. V. Flambaum, “Manifestation of the nuclear anapole moment in the M1 transitions in bismuth,” *Journal of Physics B: Atomic and Molecular Physics*, vol. 29, no. 4, pp. 689–97, 1996.
- [86] V. M. Shabaev, I. I. Tupitsyn, and V. A. Yerokhin, “Model operator approach to the lamb shift calculations in relativistic many-electron atoms,” *Phys. Rev. A*, vol. 88, p. 012513, July 2013.

- [87] V. A. Dzuba, V. V. Flambaum, and M. G. Kozlov, “Combination of the many-body perturbation theory with the configuration-interaction method,” *Phys. Rev. A*, vol. 54, p. 3948, 1996.
- [88] M. G. Kozlov, “Precision calculations of atoms with few valence electrons,” *Int. J. Quant. Chem.*, vol. 100, p. 336, 2004.
- [89] S. G. Porsev and A. Derevianko, “Triple excitations in the relativistic coupled-cluster formalism and calculation of Na properties,” *Phys. Rev. A*, vol. 73, p. 012501, 2006.
- [90] M. S. Safronova, V. A. Dzuba, V. V. Flambaum, U. I. Safronova, S. G. Porsev, and M. G. Kozlov, “Highly charged Ag-like and In-like ions for the development of atomic clocks and the search for α variation,” *Phys. Rev. A*, vol. 90, p. 042513, 2014.
- [91] M. S. Safronova, V. A. Dzuba, V. V. Flambaum, U. I. Safronova, S. G. Porsev, and M. G. Kozlov, “Atomic properties of Cd-like and Sn-like ions for the development of frequency standards and search for the variation of the fine-structure constant,” *Phys. Rev. A*, vol. 90, p. 052509, 2014.
- [92] C. C. Cannon and A. Derevianko, “Complete fourth-order relativistic many-body calculations for atoms,” *Phys. Rev. A*, vol. 69, p. 030502(R), 2004.
- [93] A. Derevianko and S. G. Porsev, ““Dressing” line and vertices in calculations of matrix elements with the coupled-cluster method and determination of Cs atomic properties,” *Phys. Rev. A*, vol. 71, p. 032509, 2005.
- [94] Yu. Ralchenko, A. Kramida, J. Reader, and the NIST ASD Team. NIST Atomic Spectra Database. Available at <http://physics.nist.gov/asd>. National Institute of Standards and Technology, Gaithersburg, MD.
- [95] A. Kramida, preliminary critical analysis of Fe XVII spectral data, private communication (2019).
- [96] K. Zhang, D. Studer, F. Weber, V. M. Gadelshin, N. Kneip, S. Raeder, D. Budker, K. Wendt, T. Kieck, S. G. Porsev, C. Cheung, M. S. Safronova, and M. G. Kozlov, “Detection of the lowest-lying odd-parity atomic levels in actinium,” *Phys. Rev. Lett.*, vol. 125, Aug. 2020.
- [97] R. Boll, D. Malkemus, and S. Mirzadeh, “Production of actinium-225 for alpha particle mediated radioimmunotherapy,” *Appl. Radiat. Isotopes.*, vol. 62, pp. 667–79, May 2005.
- [98] A. A. Kotovskii, N. A. Nerozin, I. V. Prokof’ev, V. V. Shapovalov, Y. A. Yakovshchits, A. S. Bolonkin, and A. V. Dunin, “Isolation of actinium-225 for medical purposes,” *Radiochemistry*, vol. 57, no. 3, pp. 285–291, 2015.

- [99] A. Morgenstern, C. Apostolidis, and F. Bruchertseifer, “Supply and clinical application of actinium-225 and bismuth-213,” *Seminars in Nuclear Medicine*, vol. 50, no. 2, pp. 119 – 123, 2020.
- [100] A. M. Russell and K. L. Lee, *Structure-Property Relations in Nonferrous Metals*. John Wiley & Sons, 2005.
- [101] W. Geibert, M. R. van der Loeff, C. Hanfland, and H.-J. Dauelsberg, “Actinium-227 as a deep-sea tracer: sources, distribution and applications,” *Earth. Planet. Sc. Lett.*, vol. 198, no. 1, pp. 147 – 165, 2002.
- [102] V. A. Dzuba and V. V. Flambaum, “Parity violation and electric dipole moments in atoms and molecules,” *International Journal of Modern Physics E*, vol. 21, no. 11, p. 1230010, 2012.
- [103] B. M. Roberts, V. A. Dzuba, and V. V. Flambaum, “Parity nonconservation in Fr-like actinide and Cs-like rare-earth-metal ions,” *Phys. Rev. A*, vol. 88, p. 012510, July 2013.
- [104] S. Raeder, M. Domschy, H. Heggen, J. Lassen, T. Quenzel, M. Sjödin, A. Teigelhöfer, and K. Wendt, “In-source laser spectroscopy developments at trilis—towards spectroscopy on actinium and scandium,” *Hyperfine Interact.*, vol. 216, no. 1-3, pp. 33–39, 2013.
- [105] E. Verstraelen, A. Teigelhöfer, W. Ryssens, F. Ames, A. Barzakh, M. Bender, R. Ferrer, S. Goriely, P.-H. Heenen, M. Huyse, P. Kunz, J. Lassen, V. Manea, S. Raeder, and P. Van Duppen, “Search for octupole-deformed actinium isotopes using resonance ionization spectroscopy,” *Phys. Rev. C*, vol. 100, p. 044321, Oct 2019.
- [106] M. Verlinde, S. Kraemer, J. Moens, K. Chrysalidis, J. G. Correia, S. Cottenier, H. De Witte, D. V. Fedorov, V. N. Fedosseev, R. Ferrer, L. M. Fraile, S. Geldhof, C. A. Granados, M. Laatiaoui, T. A. L. Lima, P.-C. Lin, V. Manea, B. A. Marsh, I. Moore, L. M. C. Pereira, S. Raeder, P. Van den Bergh, P. Van Duppen, A. Vantomme, E. Verstraelen, U. Wahl, and S. G. Wilkins, “Alternative approach to populate and study the ^{229}Th nuclear clock isomer,” *Phys. Rev. C*, vol. 100, p. 024315, Aug 2019.
- [107] E. P. Abel, M. Avilov, V. Ayres, E. Birnbaum, G. Bollen, G. Bonito, T. Bredeweg, H. Clause, A. Couture, J. DeVore, M. Dietrich, P. Ellison, J. Engle, R. Ferrieri, J. Fitzsimmons, M. Friedman, D. Georgobiani, S. Graves, J. Greene, S. Lapi, C. S. Loveless, T. Mastren, C. Martinez-Gomez, S. McGuinness, W. Mittig, D. Morrissey, G. Peaslee, F. Pellemoine, J. D. Robertson, N. Scielzo, M. Scott, G. Severin, D. Shaughnessy, J. Shusterman, J. Singh, M. Stoyer, L. Sutherlin,

- A. Visser, and J. Wilkinson, “Isotope harvesting at FRIB: additional opportunities for scientific discovery,” *Journal of Physics G: Nuclear and Particle Physics*, vol. 46, p. 100501, Aug. 2019.
- [108] B. R. Judd, “Low-lying levels in certain actinide atoms,” *Phys. Rev.*, vol. 125, pp. 613–625, Jan 1962.
- [109] L. J. Nugent and K. L. V. Sluis, “Theoretical treatment of the energy differences between $f^q d^1 s^2$ and $f^{q+1} s^2$ electron configurations for lanthanide and actinide atomic vapors*,” *J. Opt. Soc. Am.*, vol. 61, pp. 1112–1115, Aug 1971.
- [110] L. Özdemir and G. Ürer, “Electric dipole transition parameters for low-lying levels for neutral actinium,” *Acta. Phys. Pol. A*, vol. 118, Oct. 2010.
- [111] L. Brewer, “Energies of the electronic configurations of the lanthanide and actinide neutral atoms,” *J. Opt. Soc. Am.*, vol. 61, pp. 1101–1111, Aug 1971.
- [112] E. Eliav, S. Shmulyian, U. Kaldor, and Y. Ishikawa, “Transition energies of lanthanum, actinium, and eka-actinium (element 121),” *The Journal of Chemical Physics*, vol. 109, pp. 3954–3958, Sept. 1998.
- [113] P. Quinet, C. Argante, V. Fivet, C. Terranova, A. V. Yushchenko, and É. Biémont, “Atomic data for radioactive elements Ra I, Ra II, Ac I and Ac II and application to their detection in HD 101065 and HR 465,” *Astronomy & Astrophysics*, vol. 474, pp. 307–314, Oct. 2007.
- [114] G. Ürer and L. Özdemir, “Production energy levels and electric dipole transitions for neutral actinium ($Z = 89$),” *Arab. J. Sci. Eng.*, vol. 37, pp. 239–250, Jan. 2011.
- [115] E. Eliav and U. Kaldor, *Study of Actinides by Relativistic Coupled Cluster Methods*, ch. 2, pp. 23–54. John Wiley & Sons, Ltd, 2015.
- [116] V. A. Dzuba, V. V. Flambaum, and B. M. Roberts, “Calculations of the atomic structure for the low-lying states of actinium,” *Phys. Rev. A*, vol. 100, p. 022504, Aug 2019.
- [117] V. A. Dzuba, V. V. Flambaum, and B. M. Roberts, “Erratum: Calculations of the atomic structure for the low-lying states of actinium [Phys. Rev. A 100, 022504 (2019)],” *Phys. Rev. A*, vol. 101, p. 059901, May 2020.
- [118] A. Kramida, Yu. Ralchenko, J. Reader, and NIST ASD Team. NIST Atomic Spectra Database (ver. 5.7.1), [Online]. Available: <https://physics.nist.gov/asd> [2016, January 31]. National Institute of Standards and Technology, Gaithersburg, MD., 2019.

- [119] I. I. Tupitsyn, M. G. Kozlov, M. S. Safronova, V. M. Shabaev, and V. A. Dzuba, “Quantum Electrodynamical Shifts in Multivalent Heavy Ions,” *Phys. Rev. Lett.*, vol. 117, p. 253001, Dec. 2016.
- [120] D. J. Pegg, “Structure and dynamics of negative ions,” *Rep. Prog. Phys.*, vol. 67, pp. 857–905, 2004.
- [121] D. Leimbach, J. Karls, Y. Guo, R. Ahmed, J. Ballof, L. Bengtsson, F. B. Pamies, A. Borschevsky, K. Chrysalidis, E. Eliav, D. Fedorov, V. Fedosseev, O. Forstner, N. Galland, R. F. G. Ruiz, C. Granados, R. Heinke, K. Johnston, A. Koszorus, U. Köster, M. K. Kristiansson, Y. Liu, B. Marsh, P. Molkanov, L. F. Pašteka, J. P. Ramos, E. Renault, M. Reponen, A. Ringvall-Moberg, R. E. Rossel, D. Studer, A. Vernon, J. Warbinek, J. Welander, K. Wendt, S. Wilkins, D. Hanstorp, and S. Rothe, “The electron affinity of astatine,” *Nature Comm.*, vol. 11, p. 3824, July 2020.
- [122] T. J. Millar, C. Walsh, and T. A. Field, “Negative ions in space,” *Chem. Rev.*, vol. 117, no. 3, pp. 1765–1795, 2017.
- [123] Y. Liu, D. W. Stracener, and T. Stora, “Production of negatively charged radioactive ion beams,” *New J. Phys.*, vol. 19, p. 085005, Aug. 2017.
- [124] A. Kellerbauer and J. Walz, “A novel cooling scheme for antiprotons,” *New J. Physics*, vol. 8, p. 45, 2006.
- [125] G. Cerchiari, A. Kellerbauer, M. S. Safronova, U. I. Safronova, and P. Yzombard, “Ultracold anions for high-precision antihydrogen experiments,” *Phys. Rev. Lett.*, vol. 120, p. 133205, Mar 2018.
- [126] T. Andersen, “Atomic negative ions: structure, dynamics and collisions,” *Phys. Rep.*, vol. 394, pp. 157–313, Jan. 2004.
- [127] V. K. Ivanov, “Theoretical studies of photodetachment,” *Rad. Phys. Chem.*, vol. 70, pp. 345–370, 2004.
- [128] M. T. Eiles and C. H. Greene, “Extreme correlation and repulsive interactions in highly excited atomic alkali anions,” *Phys. Rev. Lett.*, vol. 121, p. 133401, Sep 2018.
- [129] S. J. Buckman and C. W. Clark, “Atomic negative ion resonances,” *Rev. Modern Phys.*, vol. 66, no. No. 2, p. 539, 1994.
- [130] S. J. Buckman, D. T. Alle, M. J. Brennan, P. D. Burrow, J. C. Gibson, R. J. Gulley, M. Jacka, D. S. Newman, A. R. P. Rau, J. P. Sullivan, and K. W. Trantham, “Role of Negative Ion Resonances in Electron Scattering from Atoms and Molecules,” *Aust. J. Phys.*, vol. 52, p. 473, 1999.

- [131] S. Schippers, E. Sokell, F. Aumayr, H. Sadeghpour, K. Ueda, I. Bray, K. Bartschat, A. Murray, J. Tennyson, A. Dorn, M. Yamazaki, M. Takahashi, N. Mason, O. Novotný, A. Wolf, L. Sanche, M. Centurion, Y. Yamazaki, G. Laricchia, C. M. Surko, J. Sullivan, G. Gribakin, D. W. Savin, Y. Ralchenko, R. Hoekstra, and G. O’Sullivan, “Roadmap on photonic, electronic and atomic collision physics: II. electron and antimatter interactions,” *Journal of Physics B: Atomic and Molecular Physics*, vol. 52, p. 171002, Aug. 2019.
- [132] C. Szmytkowski and P. Mozejko, “Recent total cross section measurements in electron scattering from molecules,” *Eur. Phys. J. D*, vol. 74, no. 5, p. 90, 2020.
- [133] I. Fabrikant, S. Eden, N. Mason, and J. Fedor, “Recent progress in dissociative electron attachment: From diatomics to biomolecules,” *Adv. Atom. Mol. Opt. Phys.*, vol. 66, pp. 545–657, Apr. 2017.
- [134] J. Mikosch, M. Weidemüller, and R. Wester, “On the dynamics of chemical reactions of negative ions,” *Int. Rev. Phys. Chem.*, vol. 29, no. 4, pp. 589–617, 2010.
- [135] J. Meyer and R. Wester, “Ion-molecule reaction dynamics,” *Ann. Rev. Phys. Chem.*, vol. 68, pp. 333–353, 2017.
- [136] H. Kjeldsen, “Photoionization cross sections of atomic ions from merged-beam experiments,” *Journal of Physics B: Atomic and Molecular Physics*, vol. 39, pp. R325–R377, 2006.
- [137] S. Schippers, A. Perry-Sassmannshausen, T. Buhr, M. Martins, S. Fritzsche, and A. Müller, “Multiple photodetachment of atomic anions via single and double core-hole creation,” *Journal of Physics B: Atomic and Molecular Physics*, vol. 53, p. 192001, Aug. 2020.
- [138] S. M. O’Malley and D. R. Beck, “Lifetimes and branching ratios of excited states in La^- , Os^- , Lu^- , Lr^- , and Pr^- ,” *Phys. Rev. A*, vol. 81, p. 032503, 2010.
- [139] C. W. Walter, N. D. Gibson, D. J. Matyas, C. Crocker, K. A. Dungan, B. R. Matola, and J. Rohlén, “Candidate for laser cooling of a negative ion: Observations of bound-bound transitions in La^- ,” *Phys. Rev. Lett.*, vol. 113, p. 063001, Aug. 2014.
- [140] E. Jordan, G. Cerchiari, S. Fritzsche, and A. Kellerbauer, “High-resolution spectroscopy on the laser-cooling candidate La^- ,” *Phys. Rev. Lett.*, vol. 115, p. 113001, Sept. 2015.
- [141] P. Yzombard, M. Hamamda, S. Gerber, M. Doser, and D. Comparat, “Laser cooling of molecular anions,” *Phys. Rev. Lett.*, vol. 114, p. 213001, May 2015.

- [142] R. Tang, R. Si, Z. Fei, X. Fu, Y. Lu, T. Brage, H. Liu, C. Chen, and C. Ning, “Candidate for laser cooling of a negative ion: High-resolution photoelectron imaging of Th^- ,” *Phys. Rev. Lett.*, vol. 123, p. 203002, Nov 2019.
- [143] F. Engel, T. Dieterle, F. Hummel, C. Fey, P. Schmelcher, R. Löw, T. Pfau, and F. Meinert, “Precision spectroscopy of negative-ion resonances in ultralong-range rydberg molecules,” *Phys. Rev. Lett.*, vol. 123, p. 073003, Aug 2019.
- [144] A. Perry-Sassmannshausen, T. Buhr, A. Borovik, M. Martins, S. Reinwardt, S. Ricz, S. O. Stock, F. Trinter, A. Müller, S. Fritzsche, and S. Schippers, “Multiple photodetachment of carbon anions via single and double core-hole creation,” *Phys. Rev. Lett.*, vol. 124, p. 083203, Feb 2020.
- [145] M. S. Safronova, C. Cheung, M. G. Kozlov, S. E. Spielman, N. D. Gibson, and C. W. Walter, “Predicting quasibound states of negative ions,” *arXiv:2010.02489*, 2020.
- [146] L. Pan and D. R. Beck, “Candidates for laser cooling of atomic anions: La^- versus Os^- ,” *Phys. Rev. A*, vol. 82, p. 014501, 2010.
- [147] Y. Lu, R. Tang, X. Fu, and C. Ning, “Measurement of the electron affinity of the lanthanum atom,” *Phys. Rev. A*, vol. 99, p. 062507, Jun 2019.
- [148] C. Blondel, “Comment on “measurement of the electron affinity of the lanthanum atom”,” *Phys. Rev. A*, vol. 101, p. 016501, Jan 2020.
- [149] C. W. Walter, N. D. Gibson, D. J. Carman, Y.-G Li, and D. J. Matyas, “Electron affinity of indium and the fine structure of In^- measured using infrared photodetachment threshold spectroscopy,” *Phys. Rev. A*, vol. 82, p. 032507, 2010.
- [150] C. W. Walter, N. D. Gibson, Y.-G Li, D. J. Matyas, R. M. Alton, S. E. Lou, R. L. Field III, D. Hanstorp, L. Pan, and D. R. Beck, “Experimental and theoretical study of bound and quasi-bound states of Ce^- ,” *Phys. Rev. A*, vol. 84, p. 032514, 2011.
- [151] U. Fano, “Effects of configuration interaction on intensities and phase shifts,” *Phys. Rev.*, vol. 124, pp. 1866–1878, 1961.
- [152] C. Sanner, N. Huntemann, R. Lange, C. Tamm, E. Peik, M. S. Safronova, and S. G. Porsev, “Optical clock comparison for lorentz symmetry testing,” *Nature*, vol. 567, pp. 204–208, Mar. 2019.
- [153] A. D. Ludlow, M. M. Boyd, J. Ye, E. Peik, and P. Schmidt, “Optical atomic clocks,” *Reviews of Modern Physics*, vol. 87, pp. 637–701, June 2015.

- [154] P. Schindler, D. Nigg, T. Monz, J. T. Barreiro, E. Martinez, S. X. Wang, S. Quint, M. F. Brandl, V. Nebendahl, C. F. Roos, M. Chwalla, M. Hennrich, and R. Blatt, “A quantum information processor with trapped ions,” *New Journal of Physics*, vol. 15, p. 123012, Dec. 2013.
- [155] U. I. Safronova, M. S. Safronova, and W. R. Johnson, “Forbidden $m1$ and $e2$ transitions in monovalent atoms and ions,” *Phys. Rev. A*, vol. 95, Apr. 2017.
- [156] C. F. Fischer, “Correlation in negative ions,” *Physica Scripta*, vol. 40, pp. 25–27, July 1989.
- [157] V. K. Ivanov and P. I. Yatsyshin, “Resonances in the cross section of photodetachment of $2p$ electrons from negative ions Na^- ,” *Technical Physics*, vol. 54, pp. 7–12, Jan. 2009.
- [158] R. D. Thomas, H. T. Schmidt, G. Andler, M. Björkhage, M. Blom, L. Brännholm, E. Bäckström, H. Danared, S. Das, N. Haag, P. Halldén, F. Hellberg, A. I. S. Holm, H. A. B. Johansson, A. Källberg, G. Källersjö, M. Larsson, S. Leontein, L. Liljeby, P. Löfgren, B. Malm, S. Mannervik, M. Masuda, D. Misra, A. Orbán, A. Paál, P. Reinherd, K.-G. Rensfelt, S. Rosén, K. Schmidt, F. Seitz, A. Simonsson, J. Weimer, H. Zettergren, and H. Cederquist, “The double electrostatic ion ring experiment: A unique cryogenic electrostatic storage ring for merged ion-beams studies,” *Review of Scientific Instruments*, vol. 82, p. 065112, June 2011.
- [159] E. Bäckström, D. Hanstorp, O. Hole, M. Kaminska, R. Nascimento, M. Blom, M. Björkhage, A. Källberg, P. Löfgren, P. Reinherd, S. Rosén, A. Simonsson, R. Thomas, S. Mannervik, H. Schmidt, and H. Cederquist, “Storing keV negative ions for an hour: The lifetime of the Metastable $^2P_{1/2}^o$ level in $^{32}\text{S}^-$,” *Phys. Rev. Lett.*, vol. 114, Apr. 2015.
- [160] R. von Hahn, A. Becker, F. Berg, K. Blaum, C. Breitenfeldt, H. Fadil, F. Fellenberger, M. Froese, S. George, J. Göck, M. Grieser, F. Grussie, E. A. Guerin, O. Heber, P. Herwig, J. Karthein, C. Krantz, H. Kreckel, M. Lange, F. Laux, S. Lohmann, S. Menk, C. Meyer, P. M. Mishra, O. Novotný, A. P. O’Connor, D. A. Orlov, M. L. Rappaport, R. Repnow, S. Saurabh, S. Schippers, C. D. Schröter, D. Schwalm, L. Schweikhard, T. Sieber, A. Shornikov, K. Spruck, S. S. Kumar, J. Ullrich, X. Urbain, S. Vogel, P. Wilhelm, A. Wolf, and D. Zajfman, “The cryogenic storage ring CSR,” *Review of Scientific Instruments*, vol. 87, p. 063115, June 2016.
- [161] C. Meyer, A. Becker, K. Blaum, C. Breitenfeldt, S. George, J. Göck, M. Grieser, F. Grussie, E. Guerin, R. von Hahn, P. Herwig, C. Krantz, H. Kreckel, J. Lion, S. Lohmann, P. Mishra, O. Novotný, A. O’Connor, R. Repnow, S. Saurabh, D. Schwalm, L. Schweikhard, K. Spruck, S. S. Kumar, S. Vogel, and A. Wolf,

- “Radiative rotational lifetimes and state-resolved relative detachment cross sections from photodetachment thermometry of molecular anions in a cryogenic storage ring,” *Phys. Rev. Lett.*, vol. 119, July 2017.
- [162] K. C. Chartkunchand, M. Kamińska, E. K. Anderson, M. K. Kristiansson, G. Eklund, O. M. Hole, R. F. Nascimento, M. Blom, M. Björkhage, A. Källberg, P. Löfgren, P. Reinhed, S. Rosén, A. Simonsson, R. D. Thomas, S. Mannervik, V. T. Davis, P. A. Neill, J. S. Thompson, D. Hanstorp, H. Zettergren, H. Cedergren, and H. T. Schmidt, “Radiative lifetimes of the bound excited states of Pt^- ,” *Phys. Rev. A*, vol. 94, Sept. 2016.
- [163] R. C. Bilodeau and H. K. Haugen, “Electron affinity of Bi using infrared laser photodetachment threshold spectroscopy,” *Phys. Rev. A*, vol. 64, p. 024501, Aug. 2001.
- [164] Y. Su, R. Si, K. Yao, and T. Brage, “The structure and radiative lifetimes of negative ions homologous to N^- ,” *Journal of Physics B: Atomic, Molecular and Optical Physics*, vol. 52, p. 125002, May 2019.
- [165] M. Scheer, H. K. Haugen, and D. R. Beck, “Single- and multiphoton infrared laser spectroscopy of Sb^- : A case study,” *Phys. Rev. Lett.*, vol. 79, pp. 4104–4107, Nov. 1997.
- [166] M. Scheer, R. C. Bilodeau, C. A. Brodie, and H. K. Haugen, “Systematic study of the stable states of C^- , Si^- , Ge^- , and Sn^- via infrared laser spectroscopy,” *Phys. Rev. A*, vol. 58, pp. 2844–2856, Oct. 1998.
- [167] M. Safronova, M. G. Kozlov, W. R. Johnson, and D. Jiang, “Development of a configuration-interaction plus all-order method for atomic calculations,” *Phys. Rev. A*, vol. 80, p. 012516, 2009.
- [168] G. G. Konan, L. Özdemir, and N. G. Atik, “Correlation and relativistic effects on the level structure of negative ions of atoms with half-filled p shell,” *Journal of Mathematical and Fundamental Sciences*, vol. 45, pp. 105–113, Mar. 2013.
- [169] “Caviness community cluster.” <https://sites.udel.edu/research-computing/caviness-cluster/>.
- [170] T. G. S. R. Mattson, I. Mattson, Y. H. He, and A. E. Koniges, *The OpenMP Common Core*. MIT Press Ltd, 2019.
- [171] “OpenMPI.” <https://www.open-mpi.org/>.

Appendix A

SLATER-CONDON RULES

Let us define one-particle operators as

$$\hat{F} = \sum_{i=1}^N f(\mathbf{r}_i), \quad (\text{A.1})$$

and two-particle operators as

$$\hat{G} = \frac{1}{2} \sum_{i \neq j} g(r_{ij}). \quad (\text{A.2})$$

The rules for the operator \hat{F} are

$$\langle \Psi | \hat{F} \Psi \rangle = \sum_{i=1}^N f_{ii} \quad (\text{A.3})$$

$$\langle \Psi | \hat{F} \Psi' \rangle = f_{ik} \quad (\text{A.4})$$

$$\langle \Psi | \hat{F} \Psi'' \rangle = 0, \quad (\text{A.5})$$

where Ψ denotes the determinant built from the set of spin-orbitals $\{\phi_1, \phi_2, \dots, \phi_N\}$, Ψ' differs from Ψ by replacing the spin-orbital ϕ_i by the spin-orbital ϕ_k , where $k > N$, and Ψ'' includes two of such replacements. Here we have also introduced a short-hand notation,

$$f_{ik} = \langle \psi_i | f \psi_k \rangle = \sum_{\sigma} \int d^3\mathbf{r} \psi_i^*(\mathbf{x}) f(\mathbf{x}) \psi_k(\mathbf{x}). \quad (\text{A.6})$$

The rules for the operator \hat{G} are

$$\langle \Psi | \hat{G} \Psi \rangle = \frac{1}{2} \sum_{i,j}^N (g_{ijij} - g_{ijji}) \quad (\text{A.7})$$

$$\langle \Psi | \hat{G} \Psi' \rangle = \sum_j^N (g_{ijkj} - g_{ijjk}) \quad (\text{A.8})$$

$$\langle \Psi | \hat{G} \Psi'' \rangle = g_{ijkl} - g_{ijlk} \quad (\text{A.9})$$

$$\langle \Psi | \hat{G} \Psi''' \rangle = 0, \quad (\text{A.10})$$

where Ψ''' denotes a triply substituted Slater determinant, and

$$g_{ijkl} = \langle \psi_i \psi_j | g \psi_k \psi_l \rangle = \sum_{\sigma, \sigma'} \iint d^3 \mathbf{r} d^3 \mathbf{r}' \psi_i^*(\mathbf{x}) \psi_j^*(\mathbf{x}') \frac{1}{r_{12}} \psi_k(\mathbf{x}) \psi_l(\mathbf{x}') \quad (\text{A.11})$$

Appendix B

ANGULAR MOMENTUM DIAGRAMS

In this appendix, we introduce graphical rules for angular momentum diagrams and reduction, as introduced by Lindgren and Morrison [46, 57]. When carrying out sums of products of 3-j symbols over magnetic quantum numbers, one can use a set of graphical rules to replace analytical derivations, easing the required calculations. We introduce mainly the rules that are used in the derivations in Section 2, leaving unused rules and diagrams to the source [46, 57]. We will define the basic elements of the angular momentum diagrams, then introduce the rules of summations and reduction using this diagrammatic method.

The basic element of these angular-momentum diagrams is a line segment that joins a pair of angular momentum indices

$$\overline{j_1 m_1 \quad j_2 m_2} = \delta_{j_1 j_2} \delta_{m_1 m_2}. \quad (\text{B.1})$$

An arrow attached to a line segment, or a directed line, represents

$$\overrightarrow{j_1 m_1 \quad j_2 m_2} = \overleftarrow{j_2 m_2 \quad j_1 m_1} = (-1)^{j_2 - m_2} \delta_{j_1 j_2} \delta_{-m_1 m_2}. \quad (\text{B.2})$$

The 3-j symbol is represented as

$$- \left| \begin{array}{c} j_1 m_1 \\ \hline j_2 m_2 \\ \hline j_3 m_3 \end{array} \right| = + \left| \begin{array}{c} j_3 m_3 \\ \hline j_2 m_2 \\ \hline j_1 m_1 \end{array} \right| = \begin{pmatrix} j_1 & j_2 & j_3 \\ m_1 & m_2 & m_3 \end{pmatrix}, \quad (\text{B.3})$$

where the $(-)$ sign designates that the lines are read in clockwise order, and the $(+)$ sign designates that the lines are read in counter-clockwise order, from $j_1 m_1$ to $j_2 m_2$ to $j_3 m_3$, to obtain the 3-j coefficient.

Having defined the basic elements of the angular momentum diagrams (line segment, directed line and 3-j symbol), we can introduce rules for summing over products of 3-j symbols over magnetic quantum numbers using these elements.

Summing over the magnetic quantum numbers of two line segments corresponds to connecting the vertices of the summed quantum number

$$\sum_{m_3} \frac{j_1 m_1 \quad j_2 m_2 \quad j_2 m_2 \quad j_3 m_3}{\quad} = \delta_{j_2 j_3} \frac{j_1 m_1 \quad j_3 m_3}{\quad}. \quad (\text{B.4})$$

Two arrows pointed in the same direction gives an overall phase

$$\frac{j_1 m_1 \quad j_2 m_2}{\leftarrow} = \frac{j_1 m_1 \quad j_2 m_2}{\rightarrow} = (-1)^{2j_2} \delta_{j_1 j_2} \delta_{m_1 m_2}. \quad (\text{B.5})$$

Two arrows pointed in opposite directions cancel

$$\frac{j_1 m_1 \quad j_2 m_2}{\leftrightarrow} = \frac{j_1 m_1 \quad j_2 m_2}{\leftarrow \rightarrow} = \delta_{j_1 j_2} \delta_{m_1 m_2}. \quad (\text{B.6})$$

Switching the direction of an arrow gives a factor of $(-1)^{2j}$ from the j of the initial direction

$$\frac{j_1 m_1 \quad j_2 m_2}{\leftarrow} = (-1)^{2j_1} \frac{j_1 m_1 \quad j_2 m_2}{\rightarrow}. \quad (\text{B.7})$$

Thickening a segment of the line represents a factor of $\sqrt{2j+1}$ for that line

$$\frac{j m}{\text{thick line}} = \sqrt{2j+1} \frac{j m}{\text{thin line}}. \quad (\text{B.8})$$

Changing the sign of a 3-j symbol gives an overall factor of $(-1)^{j_1+j_2+j_3}$

$$-\begin{array}{c} | \\ j_1 m_1 \\ | \\ \hline j_2 m_2 \\ \hline | \\ j_3 m_3 \end{array} = (-1)^{j_1+j_2+j_3} + \begin{array}{c} | \\ j_1 m_1 \\ | \\ \hline j_2 m_2 \\ \hline | \\ j_3 m_3 \end{array}. \quad (\text{B.9})$$

Attaching an arrow to a line segment of a 3-j symbol gives an overall factor of $(-1)^{j_1-m_1}$

$$+ \begin{array}{c} | \\ \uparrow \\ j_1 m_1 \\ \hline j_2 m_2 \\ \hline \downarrow \\ j_3 m_3 \end{array} = (-1)^{j_1-m_1} \begin{pmatrix} j_1 & j_2 & j_3 \\ -m_1 & m_2 & m_3 \end{pmatrix}. \quad (\text{B.10})$$

Attaching arrows on all 3 lines on a 3-j symbol directing outward from or inward towards the vertex has no effect on the overall phase of the 3-j symbol

$$+ \begin{array}{c} | \\ \downarrow \\ j_1 m_1 \\ \hline j_2 m_2 \\ \hline \uparrow \\ j_3 m_3 \end{array} = + \begin{array}{c} | \\ \uparrow \\ j_1 m_1 \\ \hline j_2 m_2 \\ \hline \downarrow \\ j_3 m_3 \end{array} = + \begin{array}{c} | \\ \hline j_2 m_2 \\ \hline | \\ j_3 m_3 \end{array}. \quad (\text{B.11})$$

Having listed the basic elements and diagrammatic rules, we now list formulas that are used to carry out angular reduction in Section 2. These can be derived from the rules listed above.

The Clebsch-Gordan coefficient can be written in terms of a diagram as

$$C(j_1, j_2, j; m_1, m_2, m) = \langle j_1 m_1, j_2 m_2 | j m \rangle = - \begin{array}{c} | \\ \uparrow \\ j_1 m_1 \\ \hline \text{---} \\ \hline \downarrow \\ j_2 m_2 \end{array} \cdot \quad (\text{B.12})$$

The Wigner-Eckart theorem can be written in terms of a diagram as

$$\langle j_1 m_1 | T_q^k | j_2 m_2 \rangle = (-1)^{j_1-m_1} \begin{pmatrix} j_1 & k & j_2 \\ -m_1 & q & m_2 \end{pmatrix} \langle j_1 || T^k || j_2 \rangle \quad (\text{B.13})$$

$$= - \begin{array}{c} | \\ \uparrow \\ j_1 m_1 \\ \hline \text{---} \\ \hline \downarrow \\ j_2 m_2 \end{array} \langle j_1 || T^k || j_2 \rangle.$$

The following are a list of useful identities used in angular reduction

$$\begin{array}{c}
 \begin{array}{|c}
 \hline
 j_1 m_1 \\
 \hline
 00 \\
 \hline
 j_2 m_2 \\
 \hline
 \end{array} \\
 -
 \end{array}
 = \frac{1}{\sqrt{2j_1 + 1}} \delta_{j_1 j_2} \delta_{m_1 m_2}, \quad (\text{B.14})$$

$$\begin{array}{c}
 \circ \\
 j
 \end{array}
 = 2j + 1, \quad (\text{B.15})$$

$$\begin{array}{c}
 j_1 \\
 \begin{array}{|c}
 \hline
 j_3 m_3 + \circ - j_3' m_3' \\
 \hline
 j_2 \\
 \hline
 \end{array}
 \end{array}
 = \frac{1}{2j_3 + 1} \delta_{j_3 j_3'} \delta_{m_3 m_3'}, \quad (\text{B.16})$$

$$\begin{array}{c}
 j_1 m_1 + \circ j_2 \\
 \end{array}
 = \sqrt{2j_2 + 1} \delta_{j_1 0} \delta_{m_1 0}, \quad (\text{B.17})$$

$$\begin{array}{c}
 \begin{array}{|c}
 \hline
 j_1 m_1 \\
 \hline
 j_2 + \circ j_3 \\
 \hline
 j_1' m_1' \\
 \hline
 \end{array} \\
 -
 \end{array}
 = \sqrt{\frac{2j_3 + 1}{2j_1 + 1}} \delta_{j_2 0} \delta_{j_1 j_1'} \delta_{m_1 m_1'}. \quad (\text{B.18})$$

Appendix C

HOUSEHOLDER'S METHOD OF DIAGONALIZATION

In this appendix, we introduce Householder's method of diagonalization, following Ref. [72]. Here, we focus on the details of the method, leaving proofs of theorems to the source. Given a symmetric matrix A , one can use Householder's method to find a similar symmetric tridiagonal matrix B . Suppose there is a normalized vector $\mathbf{v} \in \mathbb{R}^n$, with $\mathbf{v}^T \mathbf{v} = 1$. We define an $n \times n$ matrix

$$P = I - 2\mathbf{v}\mathbf{v}^T, \tag{C.1}$$

called the Householder transformation, which selectively zeroes out blocks of elements in vectors, or columns in matrices. It can be shown that since this transformation is symmetric and orthogonal, $P^{-1} = P$.

We begin by determining a transformation $P^{(1)}$ such that $A^{(2)} = P^{(1)}AP^{(1)}$ zeros out the elements of the first column of A beginning with the third row, i.e. $a_{j1}^{(2)} = 0$, for $j = 3, 4, \dots, n$. By symmetry, we also have $a_{1j}^{(2)} = 0$, for $j = 3, 4, \dots, n$.

Expanding the matrix, we get

$$A^{(2)} = P^{(1)}AP^{(1)} = (I - 2\mathbf{v}\mathbf{v}^T)A(I - 2\mathbf{v}\mathbf{v}^T), \tag{C.2}$$

where $a_{11}^{(2)} = a_{11}$ and $a_{j1}^{(2)} = 0$, for $j = 3, 4, \dots, n$.

Setting $v_1 = 0$ ensures that $a_{11}^{(2)} = a_{11}$. We want the transformation $P^{(1)} = I - 2\mathbf{v}\mathbf{v}^T$ to satisfy

$$P^{(1)}(a_{11}, a_{21}, a_{31}, \dots, a_{n1})^T = (a_{11}, \alpha, 0, \dots, 0)^T, \tag{C.3}$$

where the value of α is to be obtained later. To simplify notation, let

$$\hat{\mathbf{v}} = (v_2, v_3, \dots, v_n)^T \in \mathbb{R}^{n-1}, \tag{C.4}$$

$$\hat{\mathbf{y}} = (a_{21}, a_{31}, \dots, a_{n1})^T \in \mathbb{R}^{n-1}, \quad (\text{C.5})$$

and let \hat{P} be the $(n-1) \times (n-1)$ Householder transformation

$$\hat{P} = I_{n-1} - 2\hat{\mathbf{v}}\hat{\mathbf{v}}^T. \quad (\text{C.6})$$

With this notation, Eq. C.3 then becomes

$$P^{(1)} \begin{bmatrix} a_{11} \\ a_{21} \\ \vdots \\ \vdots \\ \vdots \\ a_{n1} \end{bmatrix} = \begin{bmatrix} 1 & 0 & \dots & \dots & \dots & 0 \\ \hline 0 & & & & & \\ \vdots & & & & & \\ \vdots & & & \hat{P} & & \\ \vdots & & & & & \\ 0 & & & & & \end{bmatrix} \begin{bmatrix} a_{11} \\ \hat{\mathbf{y}} \end{bmatrix} = \begin{bmatrix} a_{11} \\ \hat{P}\hat{\mathbf{y}} \end{bmatrix} = \begin{bmatrix} a_{11} \\ \alpha \\ 0 \\ \vdots \\ \vdots \\ 0 \end{bmatrix}, \quad (\text{C.7})$$

where

$$\hat{P}\hat{\mathbf{y}} = (I_{n-1} - 2\hat{\mathbf{v}}\hat{\mathbf{v}}^T)\hat{\mathbf{y}} = \hat{\mathbf{y}} - 2(\hat{\mathbf{v}}^T\hat{\mathbf{y}})\hat{\mathbf{v}} = (\alpha, 0, \dots, 0)^T. \quad (\text{C.8})$$

Defining $r = \hat{\mathbf{v}}^T\hat{\mathbf{y}}$, this gives

$$\hat{P}\hat{\mathbf{y}} = (\alpha, 0, \dots, 0)^T = (a_{21} - 2rv_2, a_{31} - 2rv_3, \dots, a_{n1} - 2rv_n)^T, \quad (\text{C.9})$$

with which we can determine all components of the vector $\hat{\mathbf{v}}$ by matching components.

Equating the components, we obtain

$$2rv_2 = a_{21} - \alpha, \quad (\text{C.10})$$

and

$$2rv_j = a_{j1}, \quad \text{for } j = 3, \dots, n. \quad (\text{C.11})$$

Squaring both sides of the equations and adding, we get

$$4r^2 \sum_{j=2}^n v_j^2 = (a_{21} - \alpha)^2 + \sum_{j=3}^n a_{j1}^2. \quad (\text{C.12})$$

Since the vector \mathbf{v} is a normalized vector, and $v_1 = 0$, the first term is simply

$$\sum_{j=2}^n v_j^2 = 1. \quad (\text{C.13})$$

Substituting, we obtain

$$4r^2 = \sum_{j=2}^n a_{j1}^2 - 2\alpha a_{21} + \alpha^2. \quad (\text{C.14})$$

From the orthogonality of P , we get from Eq. C.8

$$\begin{aligned} \alpha^2 &= (\alpha, 0, \dots, 0)(\alpha, 0, \dots, 0)^T \\ &= (\hat{P}\hat{\mathbf{y}})^T \hat{P}\hat{\mathbf{y}} = \hat{\mathbf{y}}^T \hat{P}^T \hat{P}\hat{\mathbf{y}} = \hat{\mathbf{y}}^T \hat{\mathbf{y}} \\ &= \sum_{j=2}^n a_{j1}^2, \end{aligned} \quad (\text{C.15})$$

which gives

$$2r^2 = \sum_{j=2}^n a_{j1}^2 - \alpha a_{21}. \quad (\text{C.16})$$

To ensure that $2r^2 = 0$ only if $a_{21} = a_{31} = \dots = a_{n1} = 0$, we choose

$$\alpha = -\text{sgn}(a_{21}) \sqrt{\sum_{j=2}^n a_{j1}^2}. \quad (\text{C.17})$$

Substituting α into Eq. C.16, we obtain

$$2r^2 = \sum_{j=2}^n a_{j1}^2 + |a_{21}| \sqrt{\sum_{j=2}^n a_{j1}^2}. \quad (\text{C.18})$$

With this choice of α and r , we can solve Eqs. C.10 and C.11 to obtain

$$v_2 = \frac{a_{21} - \alpha}{2r}, \quad (\text{C.19})$$

and

$$v_j = \frac{a_{j1}}{2r}, \quad \text{for each } j = 3, \dots, n. \quad (\text{C.20})$$

We then obtain

$$A^{(2)} = P^{(1)} A P^{(1)} = \begin{bmatrix} a_{11}^{(2)} & a_{12}^{(2)} & 0 & \cdots & 0 \\ a_{21}^{(2)} & a_{22}^{(2)} & a_{23}^{(2)} & \cdots & a_{2n}^{(2)} \\ 0 & a_{32}^{(2)} & a_{33}^{(2)} & \cdots & a_{3n}^{(2)} \\ \vdots & \vdots & \vdots & & \vdots \\ 0 & a_{n2}^{(2)} & a_{n3}^{(2)} & \cdots & a_{nn}^{(2)} \end{bmatrix}. \quad (\text{C.21})$$

Having found $P^{(1)}$ and computed $A^{(2)}$, this process is repeated for $k = 2, 3, \dots, n - 2$ with

$$\begin{aligned}
\alpha &= -\operatorname{sgn}(a_{21}) \sqrt{\sum_{j=2}^n a_{j1}^2}, \\
r &= \sqrt{\frac{1}{2}(\alpha^2 - a_{21}\alpha)}, \\
v_1^{(k)} &= v_2^{(k)} = \dots = v_k^{(k)} = 0, \\
v_{k+1}^{(k)} &= \frac{a_{k+1,k}^{(k)} - \alpha}{2r}, \\
v_j^{(k)} &= \frac{a_{jk}^{(k)}}{2r}, \text{ for } j = k + 2, k + 3, \dots, n, \\
P^{(k)} &= I - 2\mathbf{v}^{(k)}(\mathbf{v}^{(k)})^T,
\end{aligned} \tag{C.22}$$

and

$$\begin{aligned}
A^{(k+1)} &= P^{(k)} A^{(k)} P^{(k)} \\
&= \begin{bmatrix} a_{11}^{(k+1)} & a_{12}^{(k+1)} & 0 & \dots & \dots & \dots & 0 \\ a_{21}^{(k+1)} & \ddots & \ddots & \ddots & & & \vdots \\ 0 & \ddots & \ddots & a_{k,k+1}^{(k+1)} & 0 & \dots & 0 \\ \vdots & \ddots & a_{k+1,k}^{(k+1)} & a_{k+1,k+1}^{(k+1)} & a_{k+1,k+2}^{(k+1)} & \dots & a_{k+1,n}^{(k+1)} \\ \vdots & & 0 & \vdots & \ddots & & \vdots \\ \vdots & & \vdots & \vdots & & \ddots & \vdots \\ 0 & \dots & 0 & a_{n,k+1}^{(k+1)} & \dots & \dots & a_{nn}^{(k+1)} \end{bmatrix} \tag{C.23}
\end{aligned}$$

Repeating this process $n - 2$ times, we obtain a tridiagonal and symmetric matrix $A^{(n-1)}$, where

$$A^{(n-1)} = P^{(n-2)} P^{(n-3)} \dots P^{(1)} A P^{(1)} \dots P^{(n-3)} P^{(n-2)}. \tag{C.24}$$

Appendix D

HIGH PERFORMANCE COMPUTING

Computational problems that are too large or would take too long on standard desktop computers can be done on modern HPC architectures, such as supercomputers or clusters. Whereas a standard desktop computer would typically have a single processor, a HPC system would contain a network of nodes, each containing one or more processors. Applications that were traditionally written for serial computation have to be re-written for parallel computing. Application developers who port their codes to HPC systems must re-design their applications to run in parallel on multiple processors in order to take advantage of the available computational resources. In general, the computations would have to be broken down into parts that can be solved concurrently, and instructions from each part would be executed simultaneously on different processors.

There are three major models of parallel computing: the shared memory model, the distributed memory model, and the hybrid shared/distributed model. In the shared memory model, all parallel processes share a global memory space where data can be read and written to asynchronously. In the distributed memory model, parallel processes with their own separate segment of memory send and receive data between each other via high speed networks. The hybrid model contains properties of both the shared memory and distributed memory models; several nodes, each consisting of a set of processors sharing memory, are connected through a high speed network system. For example, the UD Caviness Community Cluster, where most of this work was done, consists of 126 compute nodes (4536 cores, 24.6 TB memory), each with 36 cores and varying amounts of memory during its first generation [169]. As of October 2020, the Caviness cluster was expanded in the Generation 2.1 initiative, now representing 265

compute nodes (10124 CPU cores, 77 TB memory) [169]. The work done in this thesis, including development and testing of parallel codes, as well as calculations done on all ions, were done primarily on the UD Caviness cluster.

Parallel codes are typically written in either C++ or Fortran, with OpenMP and MPI. OpenMP was designed for the shared memory model, whereas MPI was designed for the distributed memory model. The programs developed in this work require large amounts of processors, so MPI was the obvious choice for parallelization. After a fully optimized MPI program has been developed, OpenMP could be used to further optimize the scalability of the codes. Hybrid MPI+OpenMP parallelization is beyond the scope of this work, but is planned as a future project.

OpenMP is an API for creating code that can run on a system of threads, making it possible to write parallel code without the use of external libraries. OpenMP is typically considered more user friendly due to its use of directives, which appear as comments in the source code, to direct parallelism. However, OpenMP is limited due to the number of threads that are available on a node. On the UD Caviness Cluster, this means no more than 40 processors can be utilized with OpenMP depending on the node. OpenMP was not applied to any of the codes developed in this thesis, so more information about OpenMP will be left to the many textbooks and online resources [170].

MPI is a message passing library standard used for handling parallel processing using objects called communicators that define a group of processes that have the ability to communicate with one another. Unlike OpenMP, MPI is compatible with multi-node structures, allowing for very large, multi-node applications that are limited by the total number of processors that are available to the system. However, MPI is often less accessible and more difficult to implement due to the requirement of code restructuring. More information about MPI can be found in many textbooks and online resources [73, 74, 171]. MPI is an ongoing project, with new subroutines and functionalities being developed [171]. Here, we introduce the main concepts along with the subroutines used throughout the parallel codes.

One main concept of message-passing is the concept of a communicator. A communicator is an object that describes a group of processes that can pass messages to each other. The default communicator `MPI_COMM_WORLD` describes the group that all processes in the program starts with. In most cases, this is all that is necessary, but in some applications that utilize dynamic workload distributions and MPI windows, it is necessary to split the global communicator into sub-communicators.

The basic structure of an MPI parallel program includes initiating communicators, passing messages to communicate data between processors, and exiting from the message-passing interface. The `MPI_Init` subroutine initializes the MPI environment, then the number of processors and the id's for each processor is defined by the subroutines `MPI_Comm_Size` and `MPI_Comm_Rank`, respectively. Communications can be done using point-to-point or collective communications, or a mixture of both types. Point-to-point communication uses subroutines such as `MPI_Send` and `MPI_Recv` to send and receive data, respectively. Collective communication uses subroutines such as `MPI_Bcast` to send data from one process to all other processes in that group of communicators. The types of communicators used in the parallelization of the codes done in this thesis are mainly collective. Finally, we exit and close the MPI environment using the `MPI_Finalize` subroutine.

Next, we list a number of essential collective MPI subroutines that were used throughout the parallel codes:

- `MPI_Barrier` - This subroutine forms a barrier where no processes in the communicator can pass until all processes in the communicator reach that point of the program. This is used in all parallel programs to synchronize data before a data-dependent calculation begins, insuring all processes do in fact have the required data stored in memory.
- `MPI_Bcast` - This subroutine allows one process to send a specified data to all processes in a communicator. One of the main uses of this subroutine is to send out inputs and parameters to all processes. This is used in all parallel programs to share input data that is read from the core process to all other processes. For example, the number of configurations, array sizes and other parameters are read into the program by the master core, then it is broadcasted to all other cores with this subroutine.

- **MPI_Scatter** - This subroutine allows one process sends chunks of an array to different processes in a communicator.
- **MPI_Gather** - This subroutine is the inverse of **MPI_Scatter**. Instead of spreading elements from one process to all processes in a communicator, this subroutine takes elements from all processors in a communicator and gathers them to a single process. This is used in the **conf** program to gather the number of determinants each process has to run through for comparisons in order to calculate displacements used for subsequent collective communication subroutines.
- **MPI_Allgather** - This subroutine is essentially an **MPI_Gather** followed by an **MPI_Bcast**. Given a set of elements distributed across all processes in a communicator, this subroutine gathers all elements and gathers them to all processes. In the **conf** program, this is used to gather the number of non-zero matrix elements each process has calculated in order to calculate displacements used for writing the matrix elements out to disc.
- **MPI_Reduce** - This subroutine takes an array of elements from each process in the communicator, applies an operator to the array of elements, then returns a resultant array of elements to a single process. The reduction operators include, but are not limited to the following:
 - **MPI_Max** - returns the maximum element
 - **MPI_Min** - returns the minimum element
 - **MPI_Sum** - returns the sum of the array of elements
 - **MPI_Prod** - returns the product of all the elements

For example, in the **conf** program, this subroutine is used in the Davidson procedure after matrix multiplications. Each core has their own array of Hamiltonian matrix elements, and does multiplications with these matrix elements with eigenvectors. After multiplications, a reduction is done so the core process has the complete result for subsequent orthonormalization procedures.

- **MPI_AllReduce** - This subroutine is essentially an **MPI_Reduce** followed by an **MPI_Bcast**. An array of elements from each process in the communicator are applied with an MPI reduction operator, then the result is broadcasted to all processes in the communicator. For example, in the **conf** program, this subroutine is used to calculate the total number of non-zero matrix elements computed during the formation of the CI Hamiltonian. Each process keeps a count of the total number of matrix elements, and after each core is done their calculations, a reduction is done to sum over all counts to obtain the total number of matrix elements. It is also used to find the minimum energy of all matrix elements and then broadcast that energy to all processes.

- `MPI_Win_allocate_shared` - This subroutine creates a window with shared memory in a communicator. Introduced in MPI-3, this is MPI's solution to shared memory in a distributed parallel system. A window is created with shared memory, allowing all processes in a communicator to remotely read data from the memory allocated in the window. However, window creation is limited to each node, i.e. the windows created only exist for the communicators in the individual nodes. Due to this, each node is associated with a sub-communicator, and each sub-communicator take part in their own window. This is useful for storing a large constant array that would otherwise have to be broadcasted to every core. For example, in the `conf` program, the basis set of determinants (of dimension (N_d, N_v) , where N_d is the total number of determinants, and N_v is the total number of valence electrons) is stored in a window, and each core remotely reads the determinants during the formation of the CI Hamiltonian matrix and the \mathbf{J}^2 matrix. The core process in the master communicator broadcasts the whole 2-dimensional array of to the core processes of each sub-communicator, instead of every single process. The core processes of each sub-communicator then creates a window for the basis set of determinants for remote access by all other processes in the sub-communicator. The processes that are not labeled core processes in the sub-communicator are can then remotely read the basis set during calculations of matrix elements.